

Developing Novel Materials to Enhance Motorcyclist Safety

Michael John Robinson

31st December 2019

A thesis submitted for the degree of
Doctor of Philosophy



Summary

The number of motorcyclists in Wales has reached record highs and, while accounting for only 0.7% of the vehicles in Wales, they accounted for ~35% of the injuries categorised as killed or seriously injured. Most studies in the literature have shown that the use of motorcycle helmets reduces the probability of brain injury and death, with strong support for their use from international bodies such as the world health organisation. This work aimed to improve motorcyclist head protection by augmenting the single impact performance of existing helmets with multi-impact mitigation.

The following objectives supported this aim: An approach to improve elastomeric Fused Filament Fabrication (FFF) manufacturing quality was developed, and an equivalent porosity to injection moulding components was demonstrated. A novel accessible approach, using a uniaxial test machine to characterise elastomers dynamically, was developed. A novel computational method to generate elastomeric rate-dependent energy absorption diagrams was also developed. Additionally, the ability to scale these diagrams between different base elastomers was demonstrated.

After selecting a preliminary configuration from an energy absorption diagram, a subsequent simplified simulation of a motorcycle helmet impact enabled efficient optimisation. This approach was successfully used to predict the response of a more complex helmet assembly. A similar agreement between simulation and experimental work was observed for this approach, as was observed when simulating a fully modelled helmet assembly.

A prototype helmet, containing an elastomeric cellular structure, was shown to repeatedly pass the requirements of UNECE 22.05 while demonstrating a consistent co-efficient of restitution equivalent to that of an expanded polystyrene (EPS) helmet, even as shell failure occurred. The prototype helmet met the requirements of UNECE 22.05 at three of the four investigated locations. Additionally, it exceeded EPS' performance at one location with a liner thickness of 70% that of EPS.

Contents

Acknowledgements.....	vii
List of abbreviations.....	viii
1 Introduction	1
1.1 Research Aim	2
1.2 Research Scope	2
1.3 Research Objectives.....	3
1.4 Research Structure.....	3
2 Literature Review	8
2.1 Motorcycle helmet design and performance requirements	9
2.1.1 Established construction of motorcycle helmets.....	9
2.1.2 Helmet impact performance requirements.....	11
2.2 Designing for impact mitigation.....	19
2.2.1 Basic principles.....	20
2.2.2 Methods to select appropriate configurations.....	21
2.2.3 Identifying the optimisable performance criteria in UNECE 22.05.....	24
2.3 Cellular materials for impact mitigation	29
2.3.1 Foams.....	30
2.3.2 Cellular structures.....	38
2.4 Characterisation of materials for multi-impact mitigation.....	43
2.4.1 Resilient materials.....	43
2.4.2 Material Characterisation of Elastomers	44
2.4.3 Material modelling of AM elastomers	48
2.5 Processes for the manufacture of repeatable cellular structures	50
2.5.1 Conventional manufacturing techniques.....	50
2.5.2 Identifying AM processes for the manufacture of elastomeric cellular structures.....	51
2.5.3 SLS vs FFF.....	53

3	Methodology.....	58
3.1	Optimising FFF processing parameters to produce functional elastomeric cellular structures.....	59
3.1.1	Investigation of processing parameters.....	60
3.1.2	Assessment of component porosity	61
3.1.3	Analysis of feature accuracy	62
3.2	Establishing a novel material characterisation pathway for AM elastomers	62
3.2.1	Identification of internal strains within a cellular structure	63
3.2.2	Mechanical characterisation.....	64
3.2.3	Material modelling.....	74
3.3	Generation of a novel scalable design tool for the selection of initial SP configurations.....	76
3.3.1	Developing a meshing strategy to ensure accurate and efficient simulation.....	77
3.3.2	Investigating the effect of varying constraints on the SP structure	81
3.3.3	Approach to generate NF SP energy absorption diagram	83
3.3.4	Scaling the NF SP energy absorption diagram to alternate elastomers	84
3.4	Manufacture and analysis of a prototype SP filled motorcycle helmet	85
3.4.1	Method to propagate cellular structures within a helmet	85
3.4.2	Computational optimisation of cellular structures.....	87
3.4.3	Validation of the optimisation approach and evaluation of the prototype helmet's multi-impact performance.....	90
4	Results and Discussion	95
4.1	Optimising Fused Filament Fabrication (FFF) processing parameters to produce functional elastomeric cellular structures	95
4.1.1	Investigation of processing parameters.....	95
4.1.2	Assessment of component porosity	97
4.1.3	Analysis of feature accuracy	100
4.2	Establishing a novel material characterisation pathway for AM elastomers	101
4.2.1	Identification of internal strains.....	102

4.2.2	Mechanical characterisation approach.....	105
4.2.3	Material modelling.....	109
4.3	Generation of a novel scalable design tool for the selection of initial SP configurations	124
4.3.1	Ensuring accurate and efficient simulation	124
4.3.2	Investigating the effect of varying constraints on the SP structure	131
4.3.3	NF energy absorption diagram to predict impact behaviour	135
4.3.4	Procedure for switching the base material.....	148
4.4	Manufacture and analysis of a prototype SP filled motorcycle helmet	155
4.4.1	Computational optimisation of SP configurations for motorcycle helmets	156
4.4.2	Validation of the optimisation approach and evaluation of the prototype helmet's multi-impact performance.....	166
5	Further Discussion.....	180
5.1	Meeting the research aim.....	180
5.1.1	Comparison of EPS and SP helmets for multi-impact performance	180
5.1.2	The ability of SP filled helmet to meet the requirements of UNECE 22.05 .	180
5.2	Meeting the research objectives	181
5.2.1	Optimise processing parameters to produce functional cellular structures	181
5.2.2	Characterisation and computational modelling of AM elastomers.....	182
5.2.3	Computational generation of SP energy absorption diagram	184
5.2.4	Analysis of prototype SP motorcycle helmet.....	185
5.3	Limitations of this study.....	188
5.3.1	Optimise processing parameters to produce functional cellular structures	188
5.3.2	Characterisation and computational modelling of AM elastomers.....	189
5.3.3	Computational generation of SP energy absorption diagram	190
5.3.4	Analysis of prototype SP motorcycle helmet.....	191
6	Conclusions	193
6.1.1	Optimise processing parameters to produce functional cellular structures	193

6.1.2	Characterisation and computational modelling of AM elastomers.....	193
6.1.3	Computational generation of SP energy absorption diagram	194
6.1.4	Analysis of prototype SP motorcycle helmet.....	194
6.2	Future work.....	195
6.2.1	Use of stiffer elastomers to increase the performance of cellular structures 195	
6.2.2	Protect against concussive impacts with cellular structures	196
6.2.3	Generation of design tools for rotational criteria.....	196
6.2.4	Improving the performance of motorcycle helmet shells	197
7	Reference list	198
A	Appendices.....	209
I.	Shell element investigation.....	209
II.	Raw simulated response of the NF SP structure for the generation of energy absorption diagrams	210
III.	Raw data for the dynamic experimental compression of NF and CH cubes.....	213
IV.	Investigating shell stiffness	215
V.	Helmet reverse analysis	217
VI.	Experimental observations during testing of the helmet	218

Acknowledgements

To my wife, Caroline. Thank you. I could not have done this without your love and support.

To my mother and father, thank you for your love and support throughout my life. I am grateful for everything you've done to help me reach this point.

I want to thank both of my supervisors, Dr Peter Theobald and Dr Shwe Soe, for their help and guidance throughout this process. The time they have spent guiding me, and the lessons I have learnt have been invaluable. I also want to thank the members of my lab group who helped throughout my studies, in particular, Rhosslyn Adams and Benjamin Hanna, for sacrificing their time to assist with the processing of many...many...test specimens.

Additionally, I want to thank the technicians at Cardiff, whose help was invaluable in undertaking the experimental work presented within this thesis. Similarly, I want to thank Matt Stewart of Charles Owen for his assistance in testing the liners I developed during my studies.

This work was supported via a KESS scholarship, with part-funding from the Welsh Government's European Social Fund (ESF), and by Charles Owen.

List of abbreviations

Abbreviation	Description
ϵ_d	Strain at densification
ϵ_{pl}	Strain at plateau commencement
σ_p	Peak stress
σ_{max}	Maximum allowable stress
ABS	Acrylonitrile butadiene styrene
AE	Artificial strain energy
AM	Additive manufacturing
A	Acceleration
A_{max}	Maximum acceleration
CoG	Centre of gravity
CoR	Coefficient of restitution
CH	Cheetah filament
EF	Elastomeric foam
EPS	Expanded polystyrene
E_s	Modulus of the base material
FFF	Fused filament fabrication
HE	Hyperelastic
HIC	Head Injury Criterion
KE	Kinetic energy
l	Cell length
NF	NinjaFlex filament
SD	Standard deviation
SP	Schwarz Primitive
t	Wall thickness
t:l ratio	The ratio of wall thickness to cell length
UNECE 22.05	Motorcycle helmet standard published by the United Nations Economic Commission for Europe
VN	Vinyl nitrile
W	Energy transferred per unit volume
W_{min}	Minimum required energy transferred per unit volume
μCT	Micro X-ray computed tomography

1 Introduction

Use of motorcycles as a method of transport is becoming increasingly common and can be the primary form of transport in less well-developed countries [1]. In the United States (U.S.) alone, from 2013 to 2016, motorcyclist fatalities rose from 26x as likely as for passenger cars to 28x as likely [2, 3], with motorcyclist deaths rising from 4,692 to 5,337 for each year respectively [4]. Comparable numbers of motorcyclist deaths have been identified to occur in Europe every year, at 4,700 [5].

In 2016, the number of motorcyclists in Wales peaked at 57,414, the highest number of riders since 2009 [6]. While these users accounted for only 0.7% of the vehicular motor traffic in Wales, they accounted for ~35% of the vehicle occupant injuries categorised as killed or seriously injured (KSI) [6]. While progress has been made to make roads safer for motorcycle users, with this percentage reduced to ~26% according to the 'Police Recorded Road Accidents, 2018' report [7], there remains a clear risk to motorcyclists within Wales.

Use of motorcycle helmets has strong support from organisations such as the World Health Organisation (WHO) [8]. In a report published by the United Nations, wearing helmets had the potential to reduce severe injuries in both high and low-income countries (e.g. United Kingdom (UK) and India) by 10x [1]. This reduction in severe injury resulted in potential savings of ~2-3% of a country's gross domestic product (GDP) [1].

The majority of studies have shown that wearing a motorcycle helmet reduces the probability of brain injury and death [9]. A report from the U.S. Department of Transportation [10] suggests that the risk of any head injury is decreased by ~50% when wearing a helmet, a view supported by Rowland et al., who report death rates increased by 63% for un-helmeted riders [11], and that the risk of severe injury is reduced by more than half for helmeted riders [12]. In the U.S., from 2011 to 2015, riders wearing helmets had a consistently higher likelihood of surviving an accident and were ~20x as likely to sustain an injury vs dying, compared to only ~15x for un-helmeted riders [13]. Additionally, when comparing states in the U.S. that had universal helmet laws to those that did not, the number of un-helmeted motorcycle fatalities increases by 11.5x [14]. Furthermore, while there are a variety of potential injuries that can occur from a motorcycle accident, those to the head/facial regions continue to be the most severe/fatal [15, 16]. Therefore, these studies all support the suggestion that the use of motorcycle helmets is the most effective method of reducing motorcycle injuries [17].

The importance of helmets in reducing this risk in Wales has been recognised by the Welsh Government, with funding of £450,000 [18] to “identify innovative projects that can help the Welsh Government to reduce the number of motorcyclists killed or seriously injured on Welsh roads”. There were two winners out of an original 43 sharing this funding, one of which was developing an advanced helmet liner, from the Welsh Government’s Small Business Research Initiative (SBRI) [19]. While this will hopefully lead to improved rider safety, the risk of injury remains, and further improvements to motorcycle helmets can only be of benefit.

A real-world crash study documented 900 motorcycle accidents and, in 6.3% of the 900 cases, multiple impacts occurred at ‘the same general location’ [20]. There is much debate on the appropriateness of multi-impact requirements for helmet protection [21]. Some studies argue that the most severe impact is the primary one, and secondary impacts rarely occur in accidents [22]. However, other studies indicate this is not the case, and that multi-impact situations are most prevalent in motorcycle accidents that present a high risk of injury [23]. While the crash study highlighting the existence of these multi-impacts [20] suggested that the most severe accident was the primary one, due to the nature of accident reconstruction, it is rarely possible to ascertain which impact occurred first. For example, when staging motorcycle accidents using a dummy, in 2 out of 3 cases it was found that notable head acceleration occurred in both the primary and secondary impacts between the helmeted head and the ground/other objects [24].

1.1 Research Aim

This work aims to improve motorcyclist head protection by exploiting the mechanical benefits of cellular structures and resilient materials.

1.2 Research Scope

Existing motorcycle helmets are designed to meet the performance requirement of the UNECE 22.05 standard. This requirement is typically met by using foams that plastically yield, resulting in single impact mitigation. As multiple head impacts can occur in motorcycle accidents, the ability to mitigate this injury risk will improve rider head protection.

Therefore, this work will establish a novel computational design pathway, enabling the optimisation of cellular structures for high energy applications (i.e. exceeding the performance of existing multi-use solutions, such as the elastomeric foams used in American football helmets). These structures will be manufactured from resilient materials, to enable multi-impact performance. While an ideal helmet would be multi-collision, achieving this would involve further developing all components of a helmet for multi-impact mitigation. Therefore, this work focusses on multi-impact mitigation within a single collision event.

Further, due to the emerging nature of AM, material costs are inherently higher. Therefore, this project will not aim to produce parts at a lower cost than existing helmets and will focus on performance alone. In a similar manner, achieving a reduction in weight, at this stage of development, will also be outside the scope of this research.

1.3 Research Objectives

To achieve the research aim, while remaining within the scope of this research, a series of objectives were established:

- Computationally optimise and manufacture a novel prototype multi-impact (single accident event) helmet, with equivalent performance to existing single-impact motorcycle helmets.
- Develop a novel computational-based design pathway, to specify cellular structures for motorcycle helmets, while allowing flexibility with regards to material choice.
- Develop a novel accessible method to fully characterise a multi-use material, enabling computational generation for the design pathway and optimisation.

1.4 Research Structure

The research objectives set out in section 1.3 were broken into a series of tasks, which establish the structure of the research and therefore this thesis:

1. Optimise processing parameters to produce functional cellular structures
2. Establish a novel mechanical characterisation pathway
3. Generate a novel scalable design tool to select initial cellular configurations
4. Manufacture and analyse a prototype motorcycle helmet

In support of these tasks, a literature review was first undertaken to identify a cellular structure and material suited for multi-impact mitigation. Established structures, materials and processes were evaluated to identify novel combinations that had an equivalent performance to established impact mitigation materials (e.g. expanded polystyrene (EPS)). By selecting these from the literature, the focus could remain on the development of a comprehensive approach to helmet optimisation.

Following this review, the tasks were approached in the following manner:

1. Optimise processing parameters to produce functional cellular structures

Based on the findings of the literature review, the first piece of experimental work focussed on optimising the selected process for functionality. By minimising flaws, manufactured components will perform in line with their simulated responses. A material was also identified that, when combined with the proposed structure, could satisfy the performance requirements of motorcycle helmets.

2. Establish a novel mechanical characterisation pathway

To enable simulation of cellular structures, the base material used to produce them must first be characterised. By fitting a material model to this characterisation data, simulation software can interpret the base material's behaviour. Therefore, the second experimental component of this research developed a novel modelling pathway, as outlined below.

- i. Develop a novel method to identify the characterisation strain range

Many materials behave in a non-linear manner. Consequently, fitting a material model to the entirety of a material's response can result in a poor fit to the initial portion of the material's response. To account for this, fitting of the material model should remain focussed over the strain range that the cellular structure's base material experiences. A novel computational approach was developed to identify this characterisation strain range.

- ii. Develop a novel method to characterise the base material accessibly

For modelling of non-linear materials, collection of different strain states is frequently required. Conventionally, this data is collected using several pieces of specialised testing equipment. These make the characterisation process less accessible by incurring a

significant capital expense, in addition to requiring expertise/training for each machine. To ensure this work could be successfully transferred, an accessible approach to characterising the base material was developed.

- iii. Select an accurate material model

For most material classes, there are numerous potential material models. Therefore, applicable material models were analysed for their ability to match the characterisation data. The selected material model was also validated mechanically to ensure the simulated response was representative of the real-world response.

- 3. Generate a novel scalable design tool to select initial cellular configurations

Simulated, or mechanical, testing of a complete motorcycle helmet would be the most accurate approach to optimising the cellular structure within. However, this approach is computationally expensive and takes a significantly increased duration to reach an optimal structure. Therefore, a design tool was developed to allow selection of an approximate initial configuration, significantly reducing simulation time. Additionally, this tool made the results of this work more accessible to those with limited computational hardware, through the use of the design tool to reduce the length of a conventional experimental approach.

- i. Develop a novel meshing strategy to ensure that simulation is accurate and efficient

When simulating a component, it is common practice to find a balance between accuracy and simulation duration. Mesh size is the main contributor to these variables, so the practice of identifying this balance is known as a “mesh sensitivity study”. Mesh sensitivity studies are effective at ensuring balanced simulation; however, they are linked to the geometry on which they are undertaken. This work involves the simulation of a cellular structure with varying configurations and, consequently, many geometry changes. Therefore, a novel approach to identify mesh size based on structural features was developed to ensure any configuration was simulated accurately and efficiently. This approach was then validated mechanically, as the practice of undertaking mesh sensitivity studies inherently highlights a link between performance and mesh size.

- ii. Ensure the design tool can be utilised for varying geometrical and boundary constraints

Before the creation of the design tool, the sensitivity of the selected cellular structure was assessed. Assessing the influence of increasing the number of unit cells, or changing the external boundary conditions, is an important step to ensure the design tool could be applied to a varying geometrical constraint (e.g. a motorcycle helmet).

iii. Propagate design tool by simulating the cellular configurations

The responses of different cellular configurations were recorded at varying impact speeds. By recording these responses, the structure's rate sensitivity could be assessed, and any rate-dependent effects could be analysed. These responses were then processed into the design tool.

iv. Develop a novel approach to scale the design tool to different materials

The material selected in objective one has the potential to be unsuitable for use in motorcycle helmet protection. This potential arises due to the inherent difficulties scaling between material classes (plasticity, viscoelasticity, etc.). Additionally, standards for motorcycle helmets are continuously under review, resulting in changing impact requirements. For example, the changing impact requirements of American football helmet standards have resulted in the impact mitigating liner increasing in thickness by 340%, over the past 50 years [25]. Therefore, a novel approach to scaling the design tool by changing the base material was developed. This secondary material switching procedure was validated to ensure it was representative of real-life behaviour.

4. Manufacture and analyse a prototype motorcycle helmet

The final objective of this work was to produce a prototype helmet using the approaches developed in previous objectives. The performance of this helmet was then used to assess if the research aim had been met.

i. Develop an approach to propagate the cellular structure within the prototype helmet

Cellular structures are repeated in the X, Y, and Z axes, and consequently are cubic. This geometry introduces a challenge when incorporating cellular structures into an application with curved geometry (e.g. motorcycle helmet). Therefore, an approach to propagate the cellular structure within the prototype helmet was developed.

- ii. Develop and implement a novel approach to optimise cellular structures for motorcycle helmet protection

The most accurate way to simulate a helmet is to use the exact geometry of that helmet. However, this introduces a high computational cost, as helmets have complex curvatures and varying thicknesses. To obtain this information, scanning of the shell is frequently required and, for each type of helmet, a different shell can exist. Therefore, a novel approach was developed that simplified the shell while still being able to predict the representative performance of the helmet. This approach was combined with the developed design tool to reduce the computational expense of optimising cellular structures significantly. It was then used to identify optimised cellular configurations, at the locations and to the performance criteria, defined in the literature review.

- iii. Validate the optimisation approach and evaluate the prototype helmet's single, and multi, impact performance

The resultant optimised structures were manufactured and inserted into the prototype helmet. The helmet was subjected to the impact testing identified in the literature review and also to multi-impact testing. By comparing this testing to helmet simulation, the accuracy of the developed approach was assessed.

Additionally, the performance of the prototype helmet was experimentally compared to that of a motorcycle helmet with a conventional foam liner. By analysing this data, the ability of this work to meet the research aim was assessed.

2 Literature Review

The objectives of the literature review were:

1. Evaluate current helmet design and emerging technologies

Current helmet design and emerging technologies were evaluated. Additionally, existing legal requirements (e.g. governmental standards) and the biomechanical interaction of the head were evaluated to ensure any proposed material introduced no new issues.

2. Analyse the principles and methods of impact mitigation

Understanding the principles and techniques of impact mitigation further informs the required response of a mitigating material. This information was then used to identify specific performance requirements for optimisation during computational analysis.

3. Analyse cellular structures to identify those with equivalent performance to established foamed solutions

To ensure a cellular structure can satisfy head protection requirements, it must demonstrate equivalent performance to current materials used to mitigate impacts in motorcycle helmets. This performance was assessed by comparing existing helmet materials to promising structures, based on the requirements identified earlier in this objective.

As the functionality of a multi-impact cellular structure is conventionally achieved using elastomeric foam (e.g. American football helmets), the identified structure was also compared to an established elastomeric foam. By undertaking this comparison, the social impact of this research is increased, as elastomeric cellular structures could feasibly be implemented applications that currently utilise elastomeric foams.

4. Identify a material class for multi-impact mitigation and the requirements for computational modelling of this class of material

A material class was identified that could perform over multiple impacts. Following identification of a suitable material class, computationally modelling requirements were identified (i.e. characterisation data required).

5. Identify a process to manufacture cellular structures, from the selected material class

After establishing a structure and material class, a processing method then needs to be identified to enable manufacturing. Available processes were evaluated for their ability to manufacture cellular structures (e.g. accurate, economical). The selected process was then investigated further to identify optimisable parameters.

2.1 Motorcycle helmet design and performance requirements

This section describes the literature that was reviewed concerning current helmet design practices and emerging technologies for use in head protection. Additionally, the performance requirements for motorcycle requirements were reviewed, with helmet standards and injury criteria examined to provide greater insight into injury thresholds.

2.1.1 Established construction of motorcycle helmets

Modern helmet design has remained relatively unchanged since the 1900s [26], consisting of an external shell, an intermediate impact mitigation layer and an interior comfort layer.

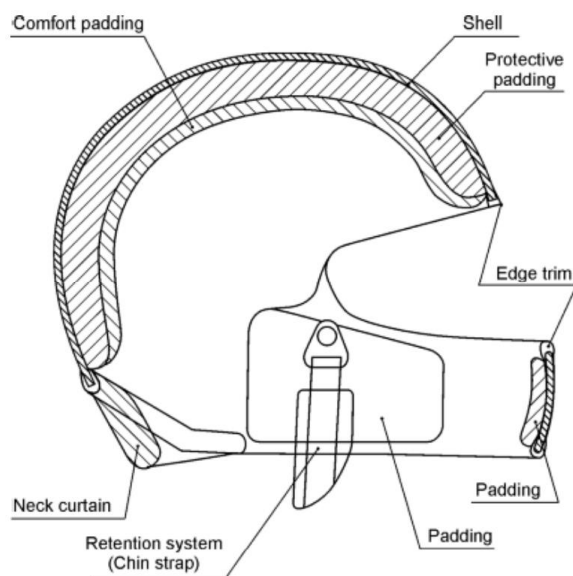


Figure 2.1. Cross-sectioned diagram of a typical modern motorcycle helmet composition, replicated from [27]

The comfort layer universally consists of a thin layer of elastomeric foam (EF). The primary purpose of this foam, as the name suggests, is to make the helmet more comfortable for day to day use. Consequently, this foam is soft and malleable, having minimal effect on

helmet performance [28], and this layer will not be considered further as it does not affect impact mitigation.

The primary purpose of the external shell is to distribute external loads to the impact mitigation layer [26]. Additionally, it serves to meet secondary performance requirements in motorcycle standards, such as penetration resistance in BS 6658 [29]. Shell materials are commonly either thermoplastic (which can be injection moulded) or composite (which are laid up in epoxy resin) [26]. The most common thermoplastic material used in motorcycle shells in the UK is Acrylonitrile butadiene styrene (ABS) [30].

The impact absorption layer in motorcycle helmets currently consists of crushable foam, with the exception of those under academic investigation, exploring the boundaries of emerging technologies. This crushable foam is commonly a layer of expanded polystyrene (EPS), with a variable thickness that allows for geometric performance tuning [26]. As this layer is the main method of mitigating energy in motorcycle helmets [26], it is the primary area explored when researching improving impact performance.

2.1.1.1 Material characterisation of the helmet

While this work intends to generate a novel liner, a review of the geometrical considerations for existing liners was undertaken. This review ensures that any proposed liner complies with the accepted geometry format.

A typical EPS liner thickness is approximately 30 – 35 mm, with examples in the literature of 36 – 39 mm [31], 20 – 50 mm [26], 25 mm [32], 10 – 50 mm [33], 28 – 40 mm [34] and 30 – 40 mm [35]. The density of the EPS foam used in motorcycles varies, but averages at 55 kg/m³, based on examples in the literature ranging from 44 – 47 kg/m³ [31], 30 – 90 kg/m³ [26], 65 – 90 kg/m³ [33], 44 kg/m³ [34] and 50 kg/m³ [35].

Of the studies which provide a matching density and liner thickness, Fernandes et al [33] highlights how the helmet thickness was inversely proportional to the density of EPS used in its construction. As the density of crushable foams is directly related to their strength, within a material class (e.g. polystyrene), there is an intrinsic link between these thicknesses and the density of the foam used (i.e. a thicker foam can be softer). This can be observed in the widely reported mechanical performance of foamed materials (e.g. EPS - section 2.3.1).

While the new liner will be developed separately, the other components of the helmet need to be modelled to enable simulation of this layer in the context of a helmet. With

regards to impact mitigation, the visor and chin straps provide limited functionality. While they are important protective measures, and the chin strap prevents the helmet from leaving the head, they do not transfer the load to the human head.

This functionality is achieved by the shell, which distributes load to the underlying impact absorption layer. Geometries of this shell vary between manufacturers, but, as covered in section 2.1.1, they are largely ABS in nature. Shells manufactured from ABS have an average thickness of ~3 mm, with examples in the literature of 3.6 – 4.4 mm [31], 5 mm [32] and 3 mm [33, 34]. Similarly, composite skin thickness averages around 2 mm, from 1.7 – 3.5 mm [31], and 2 mm [35].

In addition to an indication of geometry, material properties are required to enable the modelling of this ABS shell. ABS is a semi-rigid polymer and exhibits plasticity. However, it has been successfully implemented using a linear-elastic material model in helmet simulations [36], with resultant simulations correlating well to experimental testing. These simulations also do not implement viscoelasticity, with ABS characterisation data in the literature supporting this decision, as Young's modulus appears unchanged by varying strain rate [37].

ABS properties are inherently variable due to differences between material grades and manufacturers. Additionally, values differ between work published in the literature. Therefore, values were selected based on the agreement between helmet simulation and mechanical experimentation [33]; as recorded in Table 2.1.

Table 2.1. Material properties required for linear elastic modelling of ABS [33]

	Density /kg.m³	Poisson's ratio	Young's Modulus /GPa
ABS	1.2	0.37	4

2.1.2 Helmet impact performance requirements

In the case of a motorcycling accident, the rider can be injured in many different ways, not purely limited to head injuries. However, as the scope of this research covers mitigation of head injury alone, this section focusses on the performance requirements of the helmet.

2.1.2.1 Biomechanical considerations

There are several methods to assess helmet performance, which are based on the types of motion imparted via the helmet to the brain. These motions can be separated into two

classifications, linear and rotational. It has been shown that rotation of the skull under impact can result in severe injuries, including haematomas and diffuse axonal injury [38-40]. Meanwhile, there is a strong correlation between skull fracture/contusions and linear motion [40]. While evidence of rotational motion causing some forms of brain injury has existed in the literature for over 70 years [41], it has not been explored in significant detail until recently [42-44].

While head impacts are a complex interaction that involves the rest of the body and can occur at a variety of angles and impacts, they can be simplified into three potential motions, as shown in Figure 2.2.

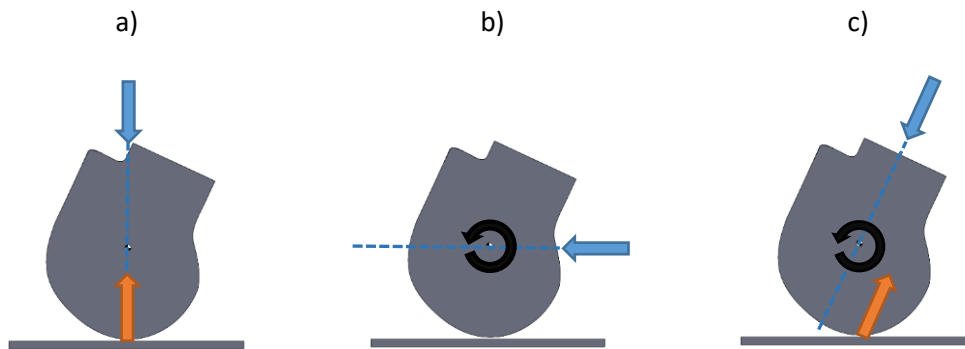


Figure 2.2. Simplified impact scenarios, with blue arrows indicating the direction of incidence, orange the reaction force, and black the resultant moment, a) linear (translation dominated), b) rotational, c) oblique (combined translation and rotation)

The motions shown in Figure 2.2 form the basis upon which most head injury criteria and helmet standards are based, as described in the following sections.

2.1.2.2 Duration-based acceleration limits

The performance criteria that informed many early injury criteria, and currently inform the majority of current helmet standards, were derived from the Wayne State tolerance curve (WSTC) (Figure 2.3)

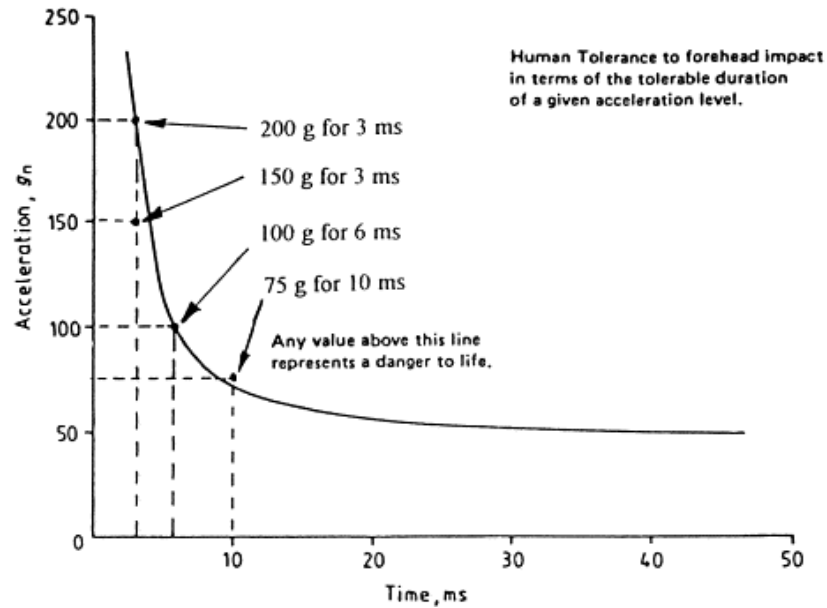


Figure 2.3 Wayne State Tolerance curve (WSTC) with example limits included for reference, replicated from [45]

From this curve, linear acceleration bound by duration limits can be derived. There exist several ways to alter the duration of an impact. The simplest way is to use softer energy absorption material over an increased thickness. This increase in liner thickness results in an increased distance over which the impact can be mitigated, resulting in lower maximum acceleration (A_{max}) and longer duration. However, when bound by thickness, the primary method of reducing the duration of periods of high acceleration is by the absorption of energy, resulting in reduced helmet rebound.

By reducing the amount of energy returned to the headform, return velocity is also reduced. This ratio of returned to initial velocity is known as the coefficient of restitution (CoR). Reduction or elimination of CoR has [46] been identified as important for the prevention of head injury [47], with a reduced CoR recommended to reduce blunt trauma to head [48].

Mild traumatic brain injury (mTBI)

Considering the current significant interest in reducing the risk of mTBI, it is pertinent also to mention it within this section. mTBI covers AIS 1-3, which consists of concussion and minor injuries [49]. Acceleration limits have been associated with these AIS scores, at 50 – 100 g, 100 – 150 g and 150 – 200 g, respectively [50]. In a similar manner to the WSTC curve, there have also been studies combining duration and acceleration limits, both rotation and linear [51].

While a concussion is perceived to be a relatively minor head injury, there are severe implications associated with them. For example, multi-impact concussion results in second impact syndrome, where the brain is at far greater risk of severe injury and death if it has not fully recovered from the initial trauma [52].

The benefits of reducing CoR is reflected further in protection against mTBI, with reducing changes in head velocity (i.e. reduced CoR) being identified as paramount to the reduction of concussion [53, 54].

However, mTBI injuries are widely deemed an unavoidable risk in motorcycle accidents. While it is difficult to ascertain accurate motorcycle speeds or energies generated during an impact [55], of the single occupancy motorcycle crashes that occurred in Iowa (US) between 2001 – 2008, 49% of the injuries occurred in areas where the speed limit was higher than 55 mph (24.5 m/s), with these injuries being of higher severity than those at lower speeds [56]. Bringing the head to a controlled stop under these kinds of speeds involves the dissipation of significant amounts of energy. Current standards reflect this, with acceleration thresholds of 250 g [29] to 275 g [27] and HIC requirements of 2400 [27], which significantly exceed the mTBI thresholds.

2.1.2.3 Injury criteria

Injury criteria are developed to predict the likelihood of injury occurring. These criteria are incorporated into standards that helmet manufacturers must meet [27, 57], and so are reviewed here in brief. The referenced articles within this section provide a more in-depth review of these criteria and their associated equations. A discussion of the linear criteria (upon which most helmet standards are currently based) was undertaken by Hardy et. al [58] and can be reviewed for a more in-depth analysis.

Injury criteria considering linear motion alone

The two most established injury criteria are the Severity Index (SI), and the Head Injury Criterion (HIC). In 1966 Gadd proposed SI [59], which was derived from the WSTC [60]. Shortly after, in 1971, Versace [61] proposed the basis for HIC, which was an iteration of the SI criterion. As an iteration, HIC maintains the relationship between time-dependent linear acceleration and head injury and augments it with the incorporation of an averaged time component.

Both criteria are actively used to assess head injury in current helmet standards. For example, SI is used in American football standards [62], while HIC is used in the motorcycle

helmet standards [27]. Due to the lack of consideration of rotation in the criteria, both have been widely criticised as inappropriate for assessment of some types of brain injury [22]. Additionally, the units of HIC have been criticised for not being directly linked to real-world variables, even though HIC does benefit from risk curves linking 15 ms HIC values to injury risk [63]. While non-ideal, these criteria have the benefit of being readily collected from existing testing equipment. Therefore, they are accessible and can easily be applied by existing helmet manufacturers. HIC is the injury criteria which has been widely adopted by many motorcycle helmet standard bodies (Table 2.2), and is calculated using:

$$HIC = \left\{ (t_2 - t_1) \left[\frac{1}{t_2 - t_1} \int_{t_1}^{t_2} a(t) dt \right]^{2.5} \right\}$$

Where $a(t)$ is the gravitational acceleration (expressed in g), while t_2 is the final time and t_1 is the initial time (expressed in seconds). These times are selected to maximise HIC, with the restriction that $t_2 - t_1 \geq 3 \text{ ms}$.

Injury criteria considering rotation

As mentioned, few impacts involve linear motion alone. In 1986, the generalised acceleration model for brain injury tolerance (GAMBIT) criterion was developed, through validation against animal and human cadaver experiments [64]. Due to the limited experimental data available at the time, there was no extensive validation of this criterion. GAMBIT was followed in 2000 by the head impact power (HIP) criterion, which used the Hybrid III headform to replicate American football impacts linked to mild brain injuries [65]. These earliest efforts to combine linear and rotational acceleration helped form the basis for future injury criteria.

In 1993, the Wayne State University head injury model (WSUHIM) was developed [66], allowing computational analysis of the deformation of the brain, with parameters within these simulations directly linked to the biomechanics of brain injury. In the years following, several other brain models have been developed, the most established of which are the Strasbourg University finite element head model (SUFEHM) in 1997 [67], the Kungliga Tekniska högskolan (KTH) brain model [43] in 2002, the University College Dublin brain trauma model (UCDBTM) in 2003 [42], simulated injury monitor (SIMon) in 2003 [44], total human model for safety (THUMS) in 2006 [68] and the global human body models consortium (GHBMC) in 2015 [69]. In most cases these models have been validated against established cadaveric test data, reducing the need for further mechanical experimentation.

Consequently, the development of new injury criteria has been eased, leading to many criteria being developed in conjunction with these head models.

Brain injury criterion (BrIC) is an injury criterion that considers rotation alone. Experimental animal head injury data was simulated using the SIMon and GHBMC head models, with brain strains being recorded. These strains were linked to the occurrence of head injury, and then risk curves were generated and correlated against the BrIC [70, 71]. Rotational injury criterion (RIC) also considers rotation alone and is based upon American football head impacts reconstructed using the THUMS head model [72]. Power rotational head injury criterion (PRHIC) takes the combined HIP criterion and removes the linear component. This angular HIP is then incorporated into the HIC equation (replacing the linear acceleration term) and validated using the same methodology as RIC [73]. These criteria demonstrate an improved correlation with traumatic brain injury (TBI) in the literature. However, linear motion can also be linked to some types of head injury [40], so its exclusion makes criteria that consider rotation alone somewhat limited.

In addition to these rotational criteria, combined criteria based on the established brain models have also been published. Notably, the Kleiven linear combination (KLC) combines HIC and angular velocity and is validated for American football concussion cases using the KTH brain model [74]. Additionally, further combined criteria based on American football concussion data were developed independently of computational brain models. The principal component score (PCS) incorporates weighted linear and rotational accelerations, in addition to weighted HIC and SI injury criteria. By combining these injury metrics, improved prediction of American football concussion data was demonstrated [75]. Also, the combined probability of concussion (CP) was developed based on both linear and rotational A_{max} . This criterion was then validated against American football and HITS concussion data [76].

As can be seen above, many of the newer criteria are validated based on concussion events, with data mainly coming from American football games. Additionally, some of the criteria are developed explicitly for the purpose of predicting concussion (e.g. CP). Arguably this brings into question their effectiveness for predicting higher-level impact events, such as those that cause skull fracture or severe brain injury.

Head model-based criteria allow for assessment of impact severity, independent of computational simulation of the brain models themselves. While this approach is inherently more accessible (as no computational skills or analysis is required), it provides

less information than the simulation of the brain models themselves. Attempts have been made to implement a brain model for injury assessment, in an accessible manner with little to no required computational skill, in the form of SUFEHM Box [77]; however, this has yet to see mainstream adoption.

2.1.2.4 Standardised testing

The injury criteria covered in section 2.1.2.3, provide an understanding of the types of motion that contribute to brain injury. However, motorcycle helmets are legally required to meet a series of performance requirements before they can be sold to consumers. These requirements are imposed by national standard bodies [29], and by regional/international bodies [27].

The performance testing prescribed by standards varies, covering a wide array of requirements such as penetration, helmet removal and fire resistance. For example, BS 6658:1985 [29] contains testing requirements for flammability and penetration; however, these are not considered in UNECE 22.05 [27]. The common and arguably most important test is for impact absorption/mitigation, as this is the primary purpose of the helmet.

While differences occur between the standards, the tests for impact absorption are all similar and have not changed significantly for a long time. The most established standards, and their impact performance requirements, are covered in Table 2.2.

Table 2.2. Summary of current motorcycle helmet testing standards

Standard	Headform mass (kg)	Velocities + anvil shapes (m/s)	Methodology	Performance requirement
BSI 6658:1985 [29]	3.1 – 5.6	Type A: first 7.5, second 5.3 (flat); first 7, second 5 (hemi) Type B: first 6.5, second 6 (flat); first 4.6, second 4.3 (hemi)	Guidewires, two impacts each site	$A_{max} < 300$ g
UNECE 22.05 [27]	3.1 - 6.1	7.5 (flat, kerbstone)	Freefall, one impact at each site	$A_{max} < 275$ g, HIC < 2400
AS/NZS 1698:2006	3.1 – 6.1	6.0 (flat), 5.2 (hemi)	Guidewires, two impacts each site	$A_{max} < 300$ g, < 200 g for impacts > 3 ms, < 150 g for impacts > 6 ms
DOT/FMVSS 218 [79]	3.5 - 6.1	5.2 (hemisphere), 6 (flat)	Guidewires, two impacts at each site	$A_{max} < 400$ g, < 200 g for impacts > 2 ms, < 150 g for impacts > 4 ms
Snell M2020D [57]	3.1 - 6.1	first 7.75, second 5.02 – 7.09 (flat, hemi – second dependent on headform mass); 7.75 (edge)	Guidewires, two impacts at each site for flat and hemisphere, one impact for edge	$A_{max} < 243$ g – 275 g (dependent on headform mass)
Snell M2020R [57]	3.1 - 6.1	first 7.7, second 5 – 6.32 (hemi – second dependent on headform mass); 8.2 (flat); 7.75 (edge)	Guidewires, one impact for flat and edge, two impacts at each site for the hemisphere	$A_{max} < 257$ g – 275 g (dependent on headform mass), HIC < 2880

In addition to the established European and American standards, several other nations develop their own helmet standards. To ensure the citizens of these countries have access to a wide variety of helmets, these nations commonly also legalise the use of other established standards. An example of this is AS/NZS 1698:2006 (included in Table 2.2) where, even though this standard has been developed, helmets manufactured to UNECE 22.05r are legal and widely used in Australia.

As can be seen in Table 2.2, all standards prescribe an A_{max} . Additionally, most prescribe a time duration to augment this, either directly specifying the period that acceleration can exceed a value or through an injury criteria. There are two approximate velocities which are used in the standards (~ 6 m/s and ~ 7.5 m/s) and two main anvil shapes (flat and hemisphere). Additionally, most of the standards utilise guidewires to control the path of the helmeted headform, which all have a mass of $\sim 3 - 6$ kg. Additionally, while not widely discussed in the literature, it can be seen in Table 2.2 that many existing motorcycle helmet standards already specify multi-impact requirements. Of the more established standards (i.e. excluding AS/NZS 1698:2006), three out of four of the standards include a multi-impact requirement.

While an ideal helmet would pass all the standards, there are inter-compatibility issues. For example, some Snell M2000 certified helmets do not pass the requirements of UNECE 22.05 [22]. This issue can be attributed to variance in test methodology (e.g. speeds), and performance criteria (e.g. A_{max}).

Additionally, arguments have been made that safer helmets can be produced by increasing the energy absorption of these standards [5]. However, this increase in energy absorption comes at an increase in A_{max} and, consequently, an increase in the severity of low energy impacts [22]. In this respect, compromises must be made to ensure a reduction in the most severe of impacts, or a reduction in the severity of the impacts that occur.

2.2 Designing for impact mitigation

This section describes the literature that was reviewed concerning the performance requirements of impact mitigation materials. By collecting this information, thresholds were then defined for the UNECE 22.05 standard.

2.2.1 Basic principles

To protect sensitive objects, impact mitigating solutions are required to mitigate all incoming kinetic energy (KE), and therefore bring the component to a stop. The most common constraint applied to this is a stated force threshold and a prescribed design envelope. In the case of motorcycle helmets, the envelope would be the thickness of the helmet, and the force threshold would be the acceleration limits.

In the simplest sense, the energy transferred to an object can be described as the force experienced by the object multiplied by the distance the object travels. Additionally, from Newton's second law, it is known that the energy required to stop a moving object is equal to the initial sum of the KE of that object. When considering Figure 2.4a, for a prescribed force threshold, the stepped response of shape 1 requires half the overall displacement of shape 2 to transfer the same amount of energy. Similarly, over a prescribed displacement, shape 3 requires half the force of shape 1 to transfer the same amount of energy.

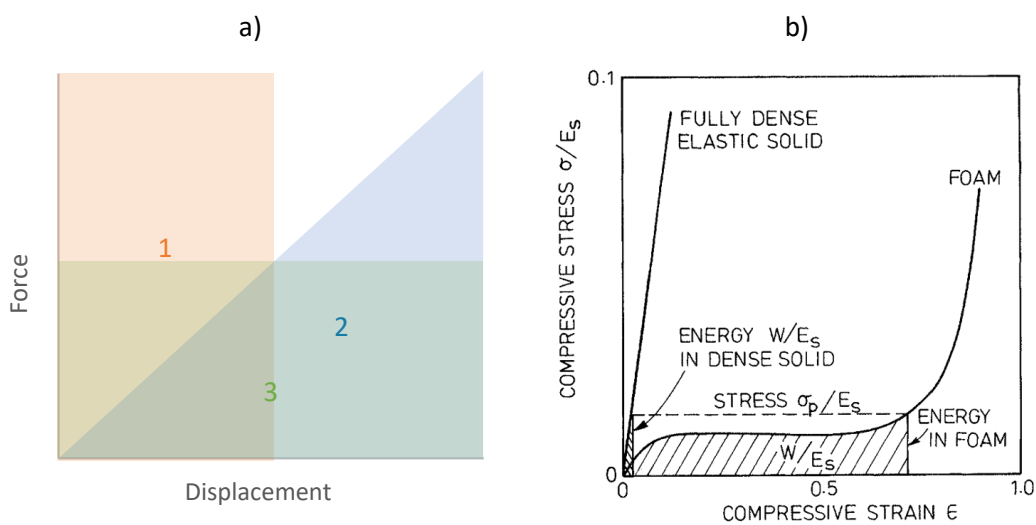


Figure 2.4 a) Three idealised step and ramp force-displacement responses, which all mitigate the same amount of energy, b) an exemplar stress-strain response of a polymeric foam (replicated from [80])

The stepped, or plateau, response (shapes 1 & 3) is typical of materials used to mitigate impacts conventionally. As seen in the example foam (Figure 2.4b) energy is stored or dissipated at a relatively consistent 'plateaued' stress, before a sharp increase in stress which is conventionally known as densification. Due to the sharp increase in stress, this densification region is not efficient when considering force thresholds. Therefore, cellular structures are only considered effective up until the point of densification.

The point at which densification commences is not well established within the literature, with several different existing approaches to its identification and is known as the densification strain (ϵ_d).

Impact mitigation is achieved by converting and storing the KE as internal elastic energy or dissipating it in some manner. For example, in conventional polymeric foams, part of the energy is stored internally as elastic energy, part of it is dissipated by the fracturing of cell walls and expulsion of the contained gasses, and part of it is dissipated through viscoelastic phenomenon within the base polymer used to produce the foam.

2.2.2 Methods to select appropriate configurations

2.2.2.1 Minimising transmitted force

One of the simplest forms of optimisation involves sweeping across a parameter and attempting to minimise/maximise an objective function. Some of the earliest performance criteria for energy absorption were based on this form of optimisation, with the objective being to minimise the force (in terms of acceleration or stress), by altering the configuration of the packaging material. For each configuration (including internal factors such as density, and geometric factors such as overall thickness) a curve is plotted where the minimum force for a given configuration can be identified. Examples of this approach include the Janssen [81] and Cushion [82] factors.

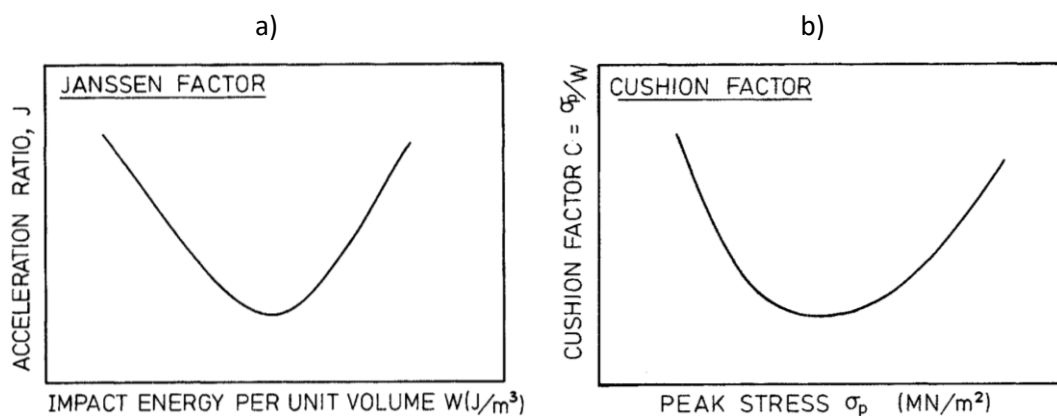


Figure 2.5. Exemplar illustrations of Janssen (a) and Cushion (b) factor curves, replicated from [80]

The Janssen factor [81] consists of plotting the ratio between the acceleration generated by a cellular structure and the theoretical acceleration that would be achieved by an idealised foam (i.e. material 1 in Figure 2.4a) across a range of impact energies (Figure 2.5a). By

utilising the Janssen factor, a foam can be investigated, and its optimal impact energy level can be identified. This approach combines strain-rate dependence and stress-strain behaviour into a single performance curve, making separate analysis challenging.

As a cellular structure is compressed, stress can both increase and decrease. By examining the material's response as compression progresses, the peak stress (σ_p) experienced by the cellular structure can be plotted against its deformation. The Cushion factor [82] relates the energy stored within the material to the amount of stress generated as the foam is compressed (Figure 2.5b). As a cellular structure compresses, the cumulative stored energy is normalised and plotted against σ_p . Plotting this allows visual identification of the point at which the material's efficiency is optimal, for a given strain-rate, and density.

While these methods provide a comparative measure between different cellular structures, they are limited as they require significant experimental data. Additionally, alteration of the cellular structure's base material requires a further series of experimentation.

2.2.2.2 *Energy absorption diagrams*

An alternate method to determine the energy dissipation capacity of cellular structures is the use of an energy absorption diagram [80, 83]. These diagrams are constructed by collecting a cellular structure's stress-strain behaviour over a range of strain-rates and configurations (e.g. density). As a cellular structure is compressed, the energy transferred per unit volume (W), and σ_p , is recorded and then normalised by the base material's solid modulus (E_s). Mitigation of incoming energy is satisfied by any configuration above the minimum required energy transferred per unit volume (W_{min}), and below the maximum allowable peak stress (σ_{max}).

While normalisation by E_s allows for comparison between materials; it does not account for non-linearity within the base material. As a cellular structure is compressed, the internal strain experienced by the material from which it is constructed (base material) increases. If a base material behaves in a non-linear manner, then normalising by a linear modulus alone can introduce issues. Therefore, any scaling of an existing diagram by changing the base material must be considered carefully.

Additionally, this does not consider any viscoelastic effects. Therefore, while energy absorption materials are a powerful tool, one does not simply scale between different material classes. For example, a highly viscoelastic material (e.g. elastomer) will have significantly more rate-dependence than a material that exhibits little viscoelasticity (e.g.

ceramics). Consequently, a highly viscoelastic material (with a low quasi-static modulus) can have a stiffer response at high speeds than a material which exhibits little viscoelasticity (with a high quasi-static modulus).

Generation and use of energy absorption diagrams

The process by which the diagrams are generated is pictorially represented in Figure 2.6.

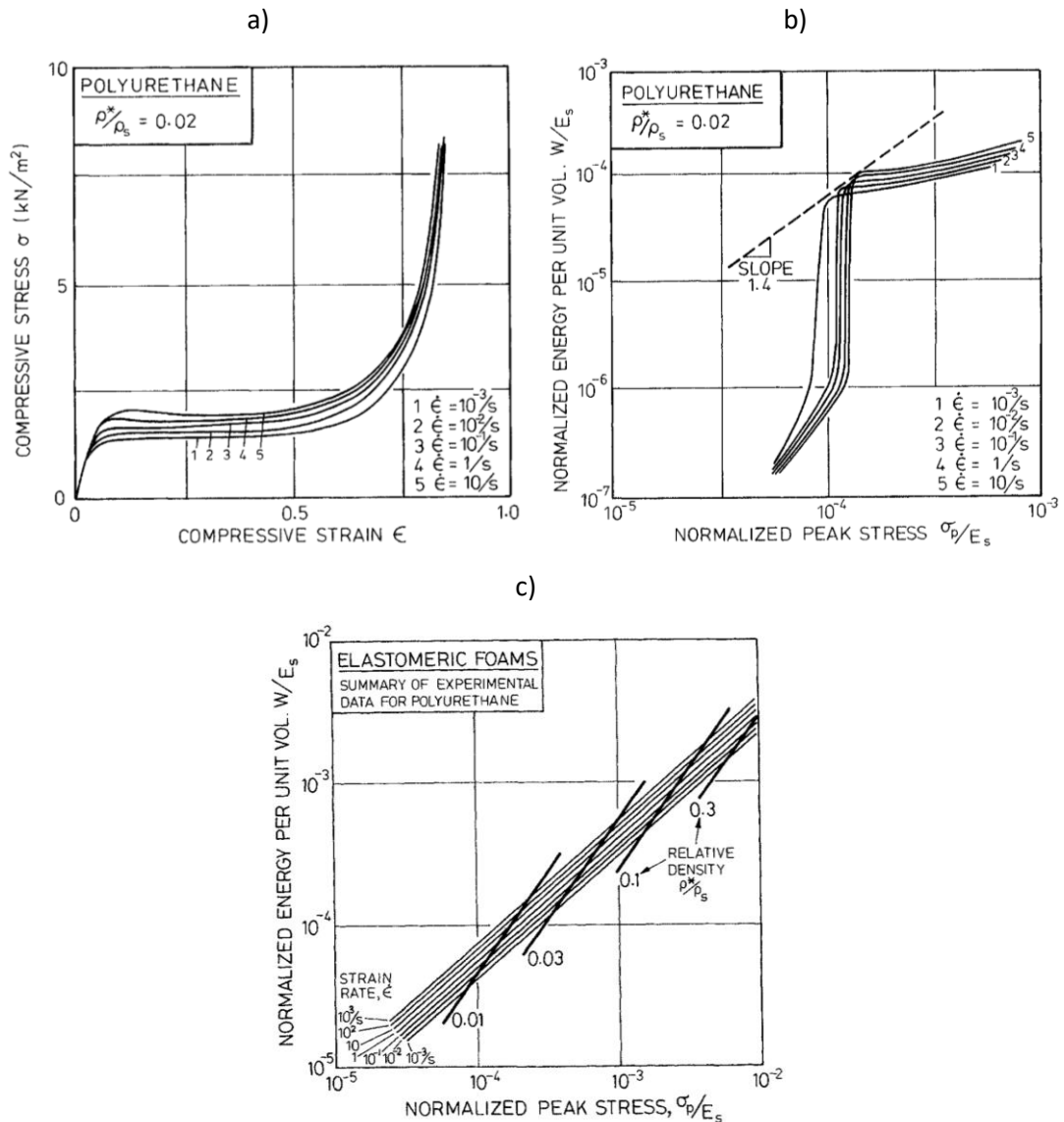


Figure 2.6 Development of an energy absorption diagram, a) experimental stress-strain behaviour of a material with a single density and varying strain rate, b) data normalised by E_s and replotted to establish envelope slope, c) combined plot incorporating replotted data for material of differing density, replicated from [80]

Identical samples of a material are compressed at different strain rates. This data is then processed into a stress-strain curve for each sample, as shown in Figure 2.6a.

Each of these stress-strain curves are then converted into a W/σ_p curve. For the σ_p axis, the maximum stress previously experienced can be progressively tabulated against strain. For the W axis, the cumulative energy per unit volume (i.e. area under the stress-strain curve) can also be progressively tabulated against strain. These datasets are then normalised by the instantaneous modulus of the base material, and plotted against one another (Figure 2.6b).

The material is most effective at the point these normalised W/σ_p curves neck. This necking can be determined by visual examination; however, a more comprehensive approach involves the calculation of curve efficiency. For each data point, the value of W is divided by σ_p . The highest resultant value can be considered the point before densification, or optimal efficiency, for the material in question. By plotting a line through these points, the optimal rate-dependent response of a material can be visualised, at a specific density (slope in Figure 2.6b).

By following this process for other densities, a series of constant density slopes can be developed. Additionally, the efficiency data used to produce the slopes of constant density can be used to produce slopes of constant strain rate as well. When these slopes are plotted together on the same graph, they form an energy absorption diagram (Figure 2.6c).

These diagrams are used to specify cellular structures based on an application's performance requirements. Commonly this is a maximum allowable transmitted force at a specified energy. The geometry of the application can be used to determine dimensional data which, in combination with the specified energy, forms the W_{min} limitation, and in combination with the maximum force forms the σ_p limitation. Any material which performs above W_{min} , and below the σ_p , will be suitable for the application in question. An example of the calculation of these limitations is shown in section 2.2.3.2.

2.2.3 Identifying the optimisable performance criteria in UNECE 22.05

2.2.3.1 Assessment of the HIC injury criteria

UNECE 22.05 has two injury requirements A_{max} and maximum HIC values. A_{max} can be directly related to σ_p in energy absorption diagrams; however, HIC is also duration-based. Therefore, HIC was investigated to assess how it would be affected by the optimisation of A_{max} .

When maximising HIC, generally the duration over which HIC is analysed has a reduced impact compared to A_{max} . This effect can be demonstrated using an example. Curves

representative of real-world responses were developed, as can be seen in Figure 2.7. Both curves were tuned to mitigate the energy of the UNECE 22.05 impact.

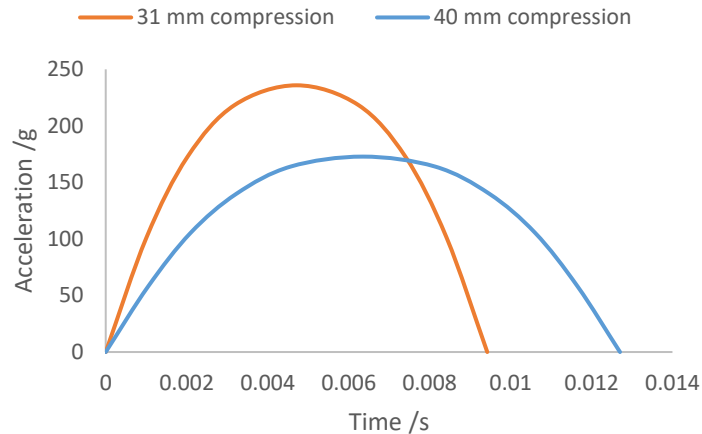


Figure 2.7. Exemplar acceleration-time histories for two responses which mitigate the same amount of kinetic energy, with the resultant maximum displacement of each response recorded in the legend

The higher curve achieved this over 31 mm of compression, resulting in a higher A_{\max} and shorter duration. The lower curve achieved it over 40 mm, resulting in a lower A_{\max} , and longer duration. When maximising HIC, the higher curve has a $HIC_{5.4ms}$ of 4772, while the lower curve has a $HIC_{6.2ms}$ of 2855. As is highlighted by the effects of changing A_{\max} , HIC is affected by several variables. However, it can be stated that a reduced acceleration appears to have a more significant effect on the magnitude of HIC than any other value.

Additionally, HIC considers the loading and unloading period of an impact. Therefore, the return velocity of the helmet inherently influences the HIC, with lower return velocities (or CoR) having reduced HIC values. A further investigation bound by UNECE 22.05 [27] was performed to demonstrate the benefit of CoR on HIC. UNECE prescribes a maximum HIC of 2400, an impact speed of 7.5 m/s and varying headform mass of 3.1 – 6.1 kg, as prescribed by EN960 [84].

This influence was investigated using three CoR values. For each CoR investigated, acceleration was decreased until the prescribed HIC of 2400 was achieved. The deceleration/acceleration period of the impact was assessed based on a ‘perfect’ step response, as discussed in section 2.2.2.2, using the mass of an average human head.

The average head mass is a difficult statistic to identify, however values have been given as 8-12 lbs (3.6 – 5.4 kg) [85], 4.5 – 5 kg [86] and 4.49 kg [87]. Taking these values into account gives an average headform weight of 4.6 kg. Examining EN 960 [84] the closest headform was the 575, with a mass of 4.7 (± 0.14) kg.

Taking this mass, and the impact speed of 7.5 m/s, a resultant KE to be mitigated of 133 J can be calculated. As most helmets are constructed from EPS [26], the required thickness of the helmet liner was calculated based on the densification strain of EPS of ~ 0.6 (section 2.3.1.1). The results of this process are displayed in Table 2.3.

Table 2.3. Idealised step responses that meet UNECE 22.05 (with a HIC of 2400), at varying coefficients of restitution (CoR)

CoR [return velocity (m/s)]	Duration of the pulse (ms)	Acceleration (g)	Displacement (mm)	EPS thickness required (mm)
0 [0]	3.6	214	13.4	22.3
0.25 [1.875]	5.2	184	15.6	26.0
0.5 [3.75]	7.0	163	17.6	29.2

Table 2.3 empirically demonstrates the relationship between displacement, acceleration and HIC. It can also be seen how HIC demonstrates the benefits of reduced CoR.

2.2.3.2 Application of UNECE 22.05 performance requirements to energy absorption diagrams

UNECE 22.05 specifies a series of points, which define the location of impact testing. Additionally, it specifies an A_{max} and a test speed. As the test speed can be converted into KE and the acceleration into a force, in combination with the cross-sectional area (CSA) of the impact points, thresholds for W_{min} and σ_{max} can be defined.

CSA for UNECE 22.05 impact points

The CSA of the impact can be defined by examination of UNECE 22.05 [27]. It specifies five impact points, four of which are relevant to liner design. These are defined as follows and are shown visually in Figure 2.8:

- Point B – “in the frontal area, situated in the vertical longitudinal plane of symmetry of the helmet and at an angle of 20° measured from Z above the AA' plane.”

- Point R – “in the rear area, situated in the vertical longitudinal plane of symmetry of the helmet and at an angle of 20° measured from Z above the AA' plane.”
- Point X – “in either the left or right lateral area, situated in the central transverse vertical plane and 12.7 mm below the AA' plane.”
- Point P – “in the area with a radius of 50 mm and a centre at the intersection of the central vertical axis and the outer surface of the helmet shell.”

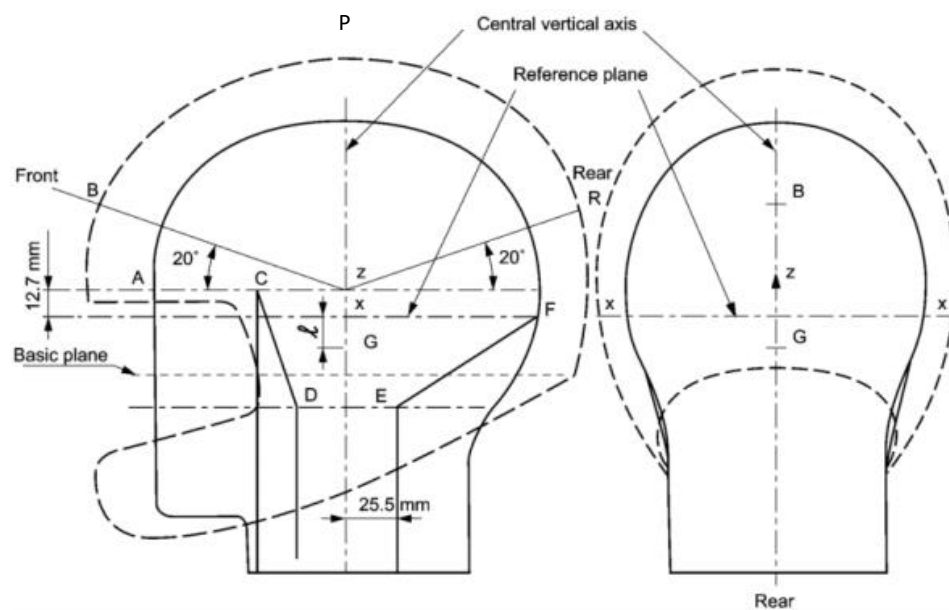


Figure 2.8. Illustration of a helmeted headform, highlighting the locations of the UNECE 22.05 impact points (B, R, X and P), replicated from [27]

In addition to the four impact points described above, point S is also specified in UNECE 22.05. This point tests the lower face region, predominately testing the energy absorption provided by the chin bar. However, this region of the helmet commonly only includes padding over the cheek areas, which means that little to none of the impact energy at this point is absorbed by liner material.

Four planes can be created, coincident to the impact locations (points B, R, X, and P) and perpendicular to the headform centre of gravity. These planes can then be projected into the headform by the proposed liner thickness (35 mm), and the area of the resultant cross-section is measured, to inform the CSA for each impact point. Note, in addition to being confined by the impact point locations, helmet design features also limited the CSA for each impact point (e.g. for point B, UNECE 22.05 states that the helmet cannot impair the

rider's vision, specifying a 7° angle, which forms a limitation, and as the headform used in the testing was a half headform, this resulted in the distinctive lower profile in Figure 2.9c).

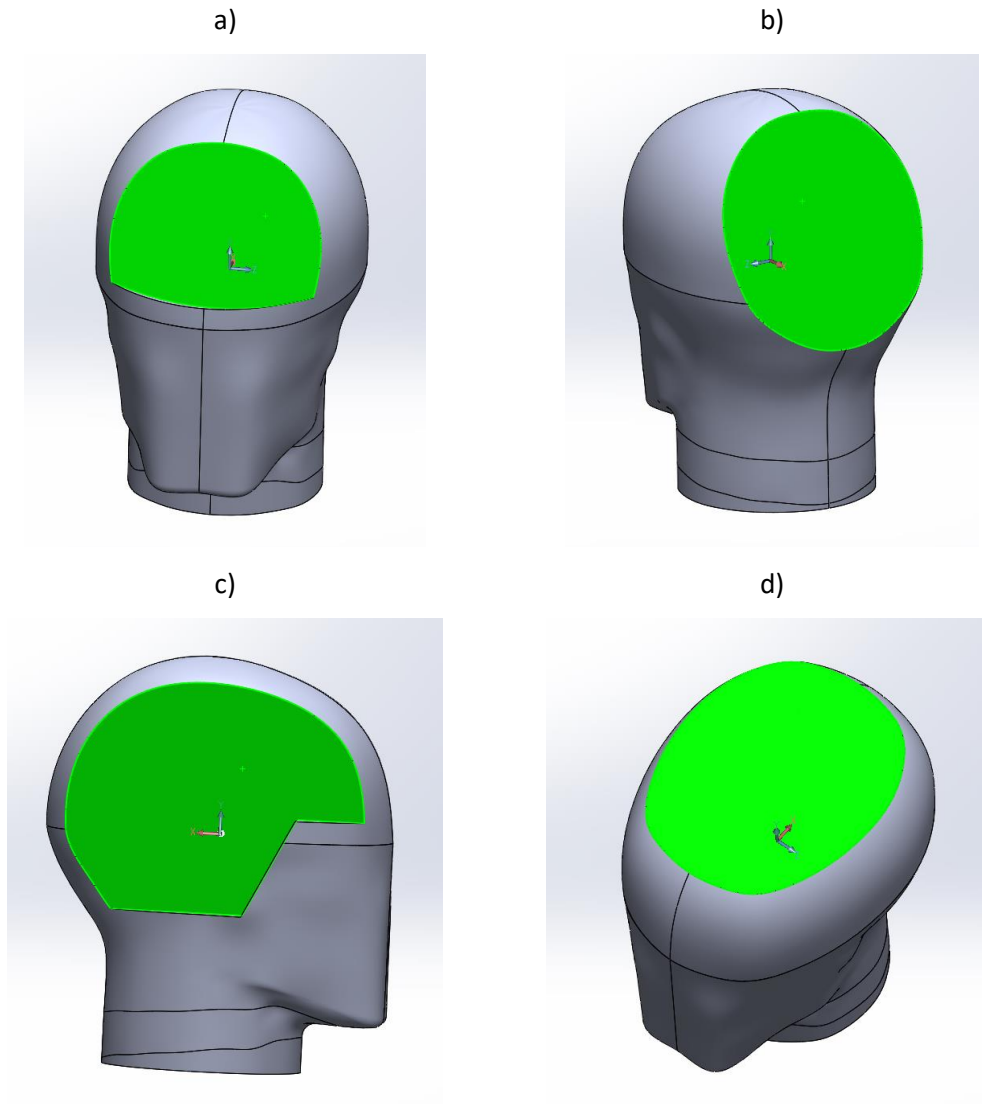


Figure 2.9. Projection of a plane, onto the EN960 575 headform, to determine the effective cross-sectional area (highlighted) for the energy absorption diagram calculations at impact points: a) B, b) R, c) X, d) P

From this process, it can be identified that at Point B, an impact CSA of 10252 mm² exists. Similarly, for point P, it was 17071 mm², for point X, it was 16877 mm², and for point R, it was 14873 mm².

Calculation of maximum allowable σ_p and minimum allowable W

A KE of 133 J was calculated in section 2.2.3.1, and a liner thickness of 35 mm can be selected based on the average thickness of motorcycle helmet liners found in section 2.1.1.

Therefore, for each impact point, the minimum value for W can be calculated as $W_{min} = \frac{3777}{CSA} \text{ J/m}^3$.

Additionally, the UNECE defines an acceleration threshold, which can be used to specify a maximum value for σ_p , as σ_{max} . The A_{max} in UNECE 22.05 is 275 g, which equals 2698 m/s², and the 575 headform has a mass of 4.7 kg. As $\sigma = \frac{F}{CSA}$, and $F = ma$, the maximum allowable stress can be calculated as $\sigma_{max} = \frac{12679}{CSA} \text{ Pa}$, for the impacts under investigation.

These equations can be used in combination with the calculated CSAs to produce Table 2.4.

Table 2.4. Required values of minimum normalised energy (W_{min}), and maximum allowable peak stress (σ_{max}), for the impact locations prescribed by the UNECE 22.05 standard

	Point B	Point R	Point X	Point P
W_{min} /kJ	368	254	224	221
σ_{max} / MPa	1.24	0.85	0.75	0.74

Out of the impact points shown in Figure 2.9, P and X had the largest CSAs. Consequently, these impact points would require a cellular structure with a reduced σ_p , and therefore density, in comparison to points B and R. These design decisions are supported by the design of the traditional helmet, where an insert of a lower density is used at point P (Appendix V). However, contrary to this example, the liner at the impact point X is of a similar thickness and the same density as that of point B, despite the apparently reduced σ_{max} in Table 2.4.

2.3 Cellular materials for impact mitigation

This section describes the literature that was reviewed concerning existing cellular materials. Due to the extensive amount of literature on cellular structures, this section was brief, to enable the selection of a preliminary structure that met the performance of EPS. As mentioned in section 1.3, this enables the focus to remain on demonstrating the approaches developed in the research presented in this thesis.

To enable the compressive response described in section 2.2.1, a structured material is required. These are collectively named cellular materials, with the foams used currently in helmet protection falling under this category. A cellular material, as its name suggests,

consists of multiple cells (or unit cells). While cellular materials have numerous applications (e.g. thermal, noise control, electrochemical [88]), this section will focus on impact mitigation. Note, for clarity when referring to cellular structures in this work, this is exclusive of foams.

Only one example of motorcycle helmet liner constructed from additively manufactured cellular structures was found in the literature. It was published in 2018 and considered a cellular structure produced from nylon [89]. The work was heavily slanted towards the cellular structure proposed by the authors, with an increased liner thickness of 44 mm, and was compared to quasi-static EPS foam data of densities up to 110 kg/m³. By comparison, the average thickness of a motorcycle helmet liner is ~20% lower, with an average density of only 55 kg/m³, as discussed in section 2.1.1.

While this piece of work demonstrates the potential for cellular structures within motorcycle helmets, it highlights the complexities of developing new helmet liners and the need to evaluate new cellular designs fairly. Therefore, this section also presents energy absorption diagrams for existing foams to allow a fair comparison to any proposed structures.

2.3.1 Foams

Foamed materials are the most common form of cellular material and are widely used in impact mitigation applications [80]. Foams can be moulded into different forms, are manufactured from a variety of materials and can be broadly classified as “open” and “closed”.

Open foams require a subsequent manufacturing step to remove the cell walls, leaving struts surrounding the irregular cells formed during the manufacture of the closed-cell foam [80]. While these are significantly lighter due to the reduced material from the secondary manufacturing step [80], they have significantly reduced mechanical performance. This reduced performance can be seen in exemplar foam in Figure 2.10.

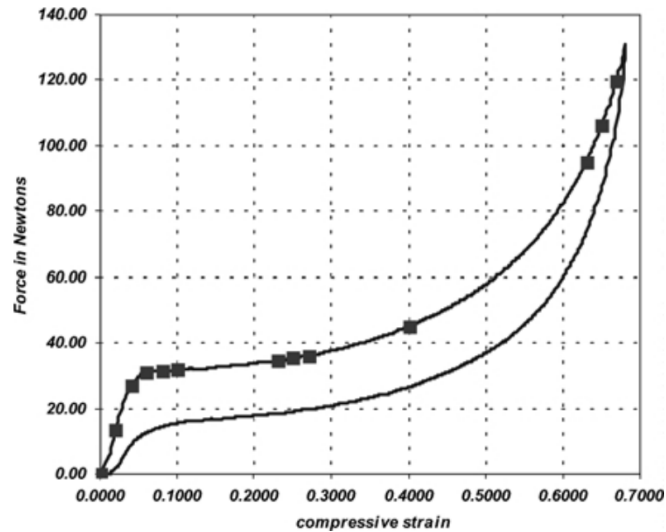


Figure 2.10. An Exemplar force-displacement response of an open-cell foam under quasi-static compressive loading, replicated from [90]

As can be seen in Figure 2.10, densification occurs at a relatively low strain 0.5, after which energy absorption efficiency begins to drop. This low densification strain, combined with an inclined stress plateau, is indicative of reduced energy absorption.

Comparatively, closed foams are more common than open-celled foams in impact mitigation. In particular, they are widely used in helmets, with crushable foam being considered the best solution, and elastomeric foams (EF) being used for multi-impact applications (American football helmets). However, while EPS is praised for its ability to reduce CoR due to its plastic deformation [91], in reality, a significant portion of the energy is absorbed elastically (Figure 2.11), in combination with any elastic energy stored by the deformation of the shell, which leads to a notable amount of the energy being returned to the head upon impact.

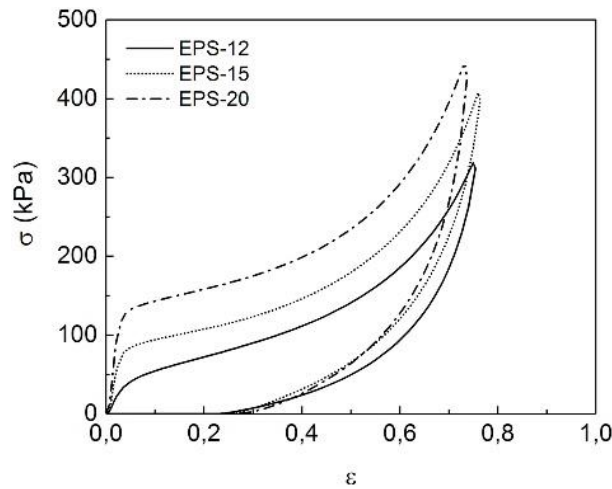


Figure 2.11 Compressive quasi-static loading and unloading response for three EPS foams, with densities of 12, 15 and 20 kg/m³, replicated from [92]

Additionally, the energy dissipated plastically is non-recoverable, leading to the helmet being ‘single-use’ and having reduced efficiency/ability to reduce CoR on subsequent impacts of any velocity. This leads to impacts at the same location increasing A_{max} , due to the loss of impact mitigation ability as the plastic failure occurs [93]

2.3.1.1 Foam performance

This section seeks to determine the performance of existing foam materials in terms of energy absorption diagrams. These diagrams allow a comparison of these foams to any proposed structures. EPS is considered as it is the gold-standard material for motorcycle helmets. As such, its performance is the main target for any energy mitigation material for motorcycle helmets to meet.

Additionally, VN is widely considered the gold standard EF and was used extensively in helmets (e.g. American football) [94]. The use of an elastomeric base material makes a comparison to EF important, to identify if any benefits to performance are purely due to material change alone. Additionally, this allows the scope to apply any structures to applications currently utilising EF.

Expanded Polystyrene (EPS)

Dynamic stress-strain data for EPS foam is limited. While there are examples of acceleration-time traces for EPS foam in the context of their applications, lack of foam dimensions/appropriate geometries means that integration of acceleration-time, to attain displacement-time, and thus stress-strain, is not feasible. The available data consisted of EPS densities of 65 – 112 kg/m³, with the lower density (65 kg/m³) being comparable to

that of the average motorcycle helmet liner density (55 kg/m^3 (section 2.1.1.1)). The resultant rate-dependent stress-strain data is presented in Figure 2.12.

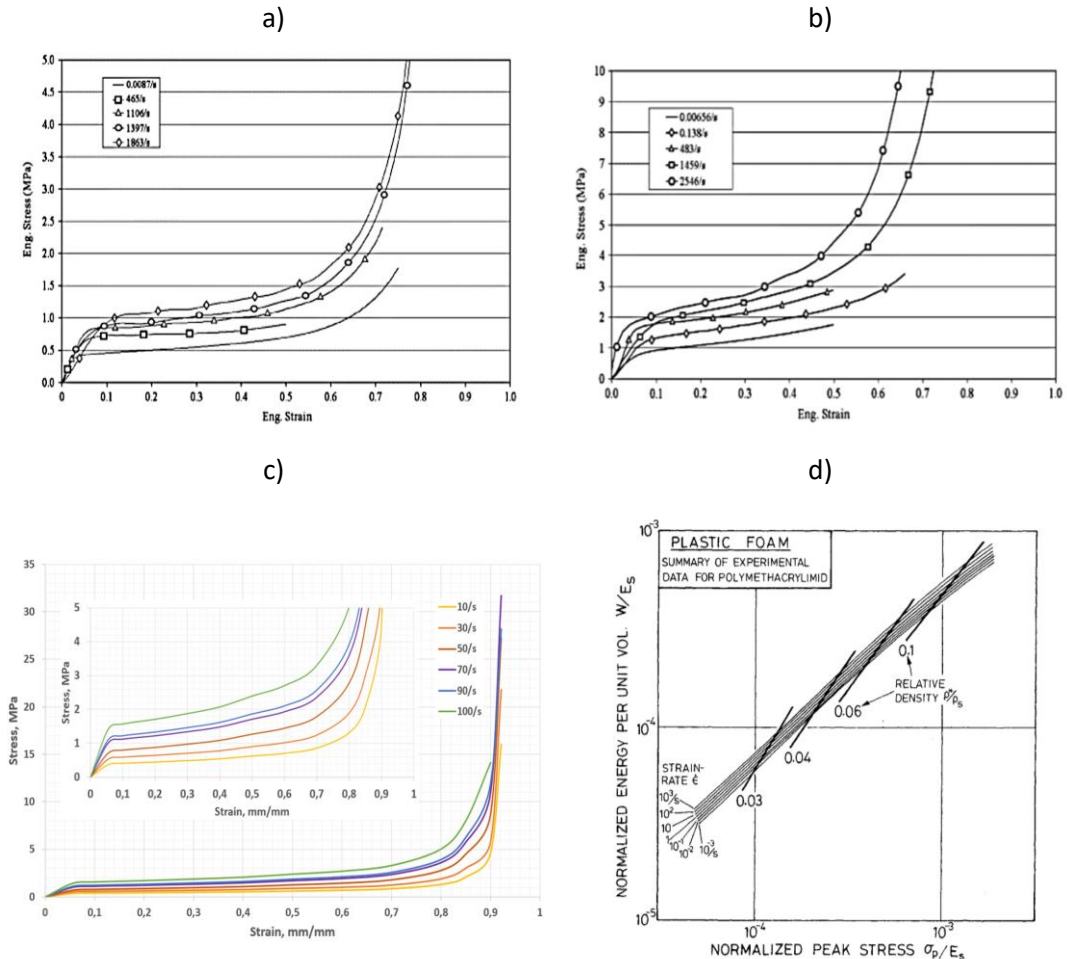


Figure 2.12. Multi-rate compressive stress-strain responses for EPS foams of differing density, a) 65 kg/m^3 from [95], b) 112 kg/m^3 from [95], c) 80 kg/m^3 from [96], d) plastic foam energy absorption diagram from [80]

In Figure 2.12a and b, mechanical test data was collected at different strain-rates through the use of a uniaxial test machine (quasi-static), a Kolsky bar (intermediate) and a gas gun (high). Some of the lower strain rate curves were incomplete, so when generating the energy absorption diagram, these incomplete curves were extrapolated to a theoretical densification point based on the profiles of the surrounding curves.

The dynamic EPS data presented in Figure 2.12c was post-processed by the authors [96]. The intention of this was to correct the change in strain rate that occurs when collecting data using conventional methods (e.g. drop tower testing).

Figure 2.12d shows the energy-absorption diagram for rigid Polymethacrylimide foam. This diagram was stated to be representative of plastic foams with $\sigma_p/E_s = 1/30$ [80]. As this book is well referenced in the literature, and the diagrams presented within it contain a wealth of potential data, the applicability of this data to be scaled to EPS was investigated.

Additionally, while not presented in Figure 2.12, quasi-static data for 0.060 kg/m³, 0.064 kg/m³ and 0.07 kg/m³ EPS foam, from [21, 97, 98], supported the quasi-static response of the 0.065 kg/m³ EPS foam [95] providing increased confidence in this data.

As the datasets in Figure 2.12 were collected independently, they did not have consistent strain rates for direct comparison. Therefore, the most similar strain rates were chosen for comparison. For Figure 2.12a and b, strain rates of 6e-3/s and 400/s were used, for Figure 2.12c, 10/s and 100/s were selected, and for Figure 2.12d, 5e-3/s and 200/s were extracted. For the derivation of the 0.08 kg/m³ foam, from Figure 2.12d, a value for E_s of 3GPa was extracted from a technical data-sheet on EPS microspheres (used for foaming into EPS) [99].

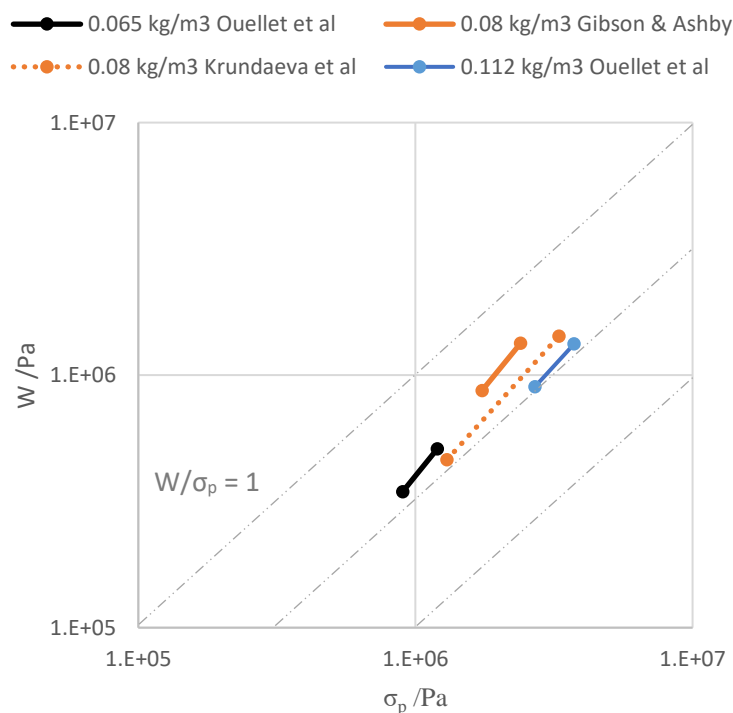


Figure 2.13. Energy absorption diagram generated from the EPS data presented in Figure 2.12. A common high and low strain rate, with a line connecting these two strain rates, is presented for each of the data sets. Also, dashed lines of constant W/σ_p are plotted to allow evaluation of efficiency.

Examining Figure 2.13, it is apparent that the derived 0.08 kg/m^3 Gibson & Ashby data [80] is not representative of EPS foam. The quasi-static energy is approximately 100% higher than logical relation to Ouellet et al. [95] and Krundaeva et al. [96] quasi-static data. Therefore, Gibson & Ashby data was not used to derive further EPS data for this study.

Additionally, the 0.08 kg/m^3 data from Krundaeva et al. [96] does not agree with the rate-dependence observed in the other literature. However, the quasi-static data appears to be in a logical relation to the Ouellet et al. data [95].

While there is a good correlation in Krundaeva et al. [96], between mechanical testing and simulated results, it was decided that the data from this work be excluded. The only evidence of this methodology is presented in Krundaeva et al. [96] and was the result of heavy post-processing. Additionally, while Krundaeva et al. [96] argues this post-processing is required, when drop-tower testing is undertaken well into the densification region, the pre-densification data is collected at a reasonably consistent strain rate [100], a fact which is highlighted within Krundaeva et al. (figure 5 - [96]).

Therefore, from this point onwards, the data from Ouellet et al. [95] was used in energy absorption diagrams when comparing to EPS.

Elastic foam (EF)

In a similar manner to EPS, dynamic stress-strain data was identified for VN600, a VN foam commonly used in American football helmets.

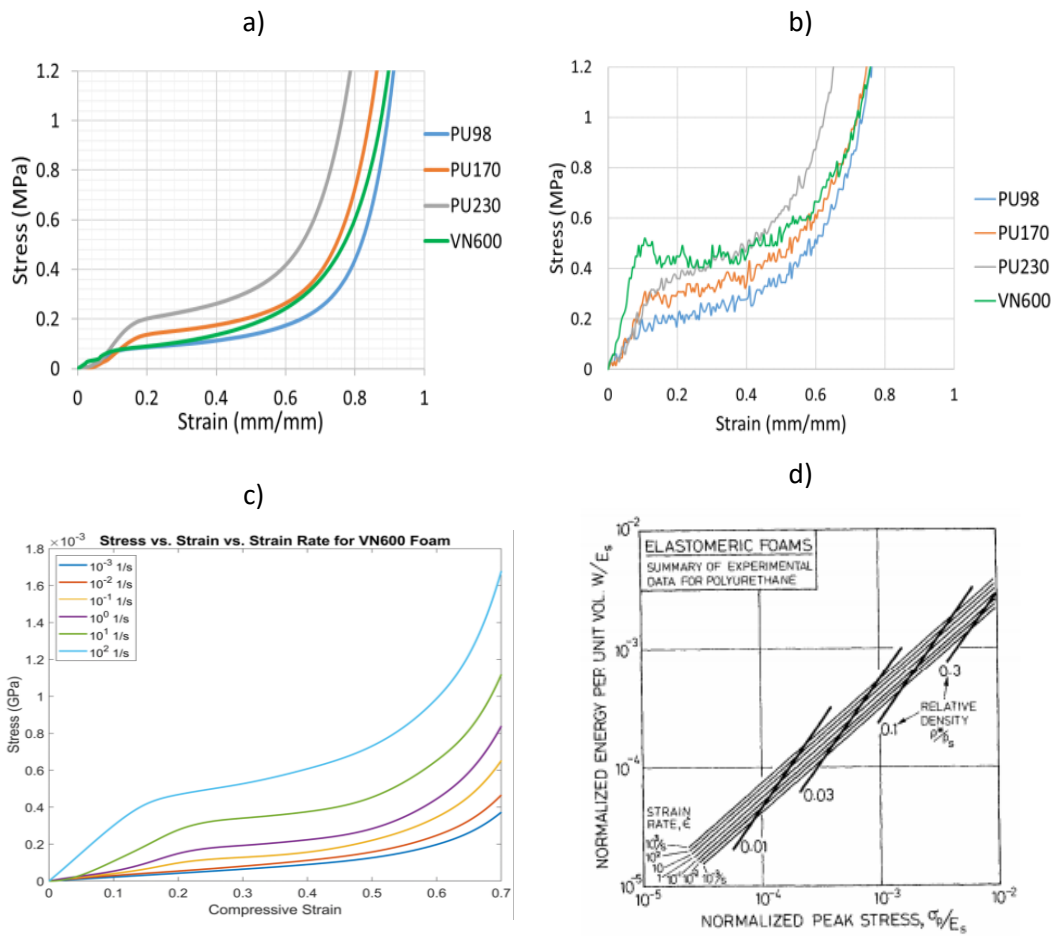


Figure 2.14. Multi-rate compressive nominal stress-strain responses for elastic foam (EF), a) quasi-static VN600 data from [100], b) dynamic (200/s) VN600 data from [100], c) VN600 data from [101], d) EF data from [80]

Figure 2.14d presents an energy absorption diagram for EF [80]. An E_s value is required to scale this energy absorption diagram. However, VN consists of a varying blend of PVC and nitrile rubber mixed by manufacturers, making the identification of E_s value for this material less straightforward than for EPS.

The two components of VN were separately explored to identify this E_s value. Nitrile rubber (NBR) is hyperelastic, and therefore highly non-linear. As a result of this, its mechanical performance is generally supplied in the form of Shore Hardness. The Shore A Hardness of NBR has been recorded at 20-95 [102]. From these values, Young's moduli can be calculated [103], resulting in an E_s range of 0.7 to 44 MPa. Meanwhile, polyvinyl chloride (PVC) comes in two grades, flexible and rigid, resulting in an E_s range of 5.52 – 7030 MPa [104, 105].

Using the EF energy absorption diagram [80], derived EF data was created with varying values of E_s . An EF density of 111 kg/m^3 was selected from which to derive the value of E_s ; as per the density of VN600 [106]. Responses for derived EF with an E_s of 0.7 MPa (lowest nitrile rubber modulus) and 7030 MPa (highest PVC modulus), were created to illustrate the potential range of results.

The data from Figure 2.14 was processed into a single energy absorption diagram and is presented in Figure 2.15.

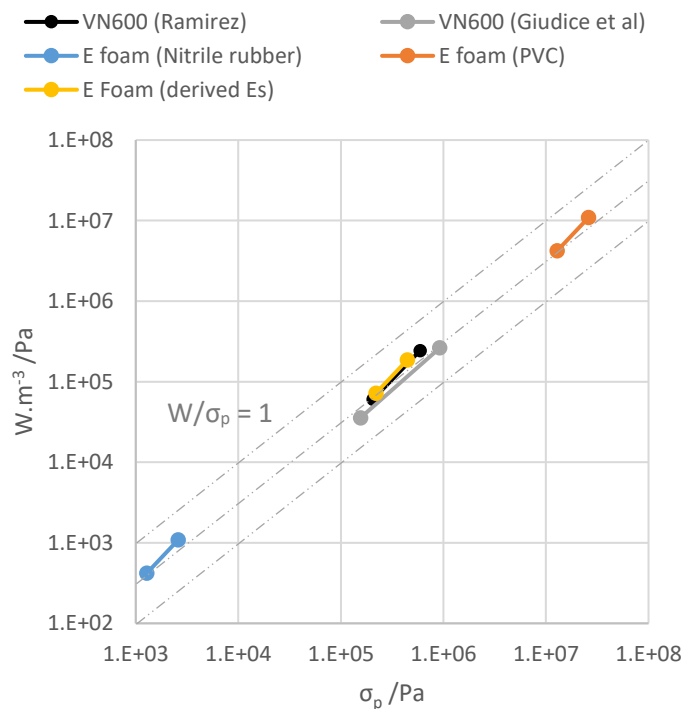


Figure 2.15. Energy absorption diagram generated from the EF data presented in Figure 2.14. A common high and low strain rate, with a line connecting these two strain rates, is presented for each of the data sets. Also, dashed lines of constant W/σ_p are plotted to allow evaluation of efficiency.

As can be seen in Figure 2.15, compared to both the derived Gibson & Ashby [80] and the data from Ramirez et al. [100] the data from Giudice et al. [101] transfers less energy and is more rate-dependent. Due to these discrepancies, the data from Giudice et al. [101] was excluded, with the data from Ramirez et al. [100] selected moving forward.

As expected, the derived EF data with an E_s of 0.7 MPa and 7030 MPa did not agree with the experimental VN600 data. The value of E_s was then varied until the derived EF curve was in agreement with the published VN600 data. When the E_s was 120 MPa , the derived EF response was similar to that of the VN600 data from Ramirez et al. [100]. Notably, lines of

constant efficiency ($W/\sigma_p = 1$) in Figure 2.15, illustrate a similar level of efficiency in both the derived EF and VN600 data [100]. Due to this agreement, the energy absorption diagram for derived EF from Gibson & Ashby [80] was used to represent EF from this point forward, allowing comparisons with a theoretical EF of any base material.

2.3.2 Cellular structures

2.3.2.1 2D

Examples include extrusions and corrugations. The most established of these are honeycombs, a well-established method of producing a lightweight material praised for their stiffness, and efficiency at filling a 2D plane. For this reason, they have been explored for use in impact mitigation scenarios. In most cases, honeycombs suffer from an initial sharp peak in force, before the structure buckles leading to a relatively flat plateau (Figure 2.16). While honeycombs have an efficient energy absorption profile and high densification, the sharp initial peak in force makes them inefficient when considering a prescribed force threshold.

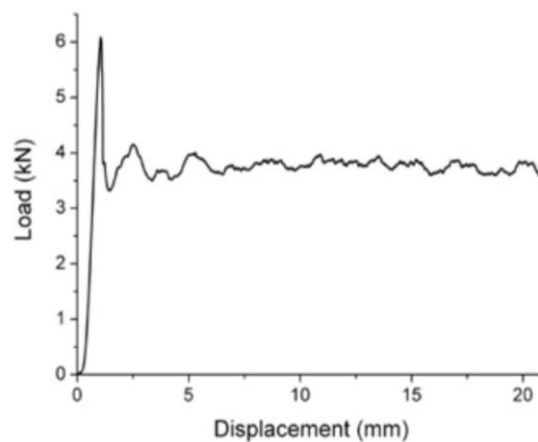


Figure 2.16 Typical compressive load-displacement response of a metallic honeycomb under quasi-static loading, reproduced from [107]

Additionally, honeycomb sandwich panels are sensitive to bonding conditions, so while both aluminium and composite honeycombs demonstrate an excellent plateau response when unbonded, within a sandwich assembly the plateau is lost [108, 109].

2.3.2.2 3D – Strut-based

Strut-based cellular structures are comparable to open cell foams from the perspective of structure. A kelvin cell is a well-known example of such a structure. The deformation of a Kelvin cell structure results in multi-stage deformation as can be seen in Figure 2.17.

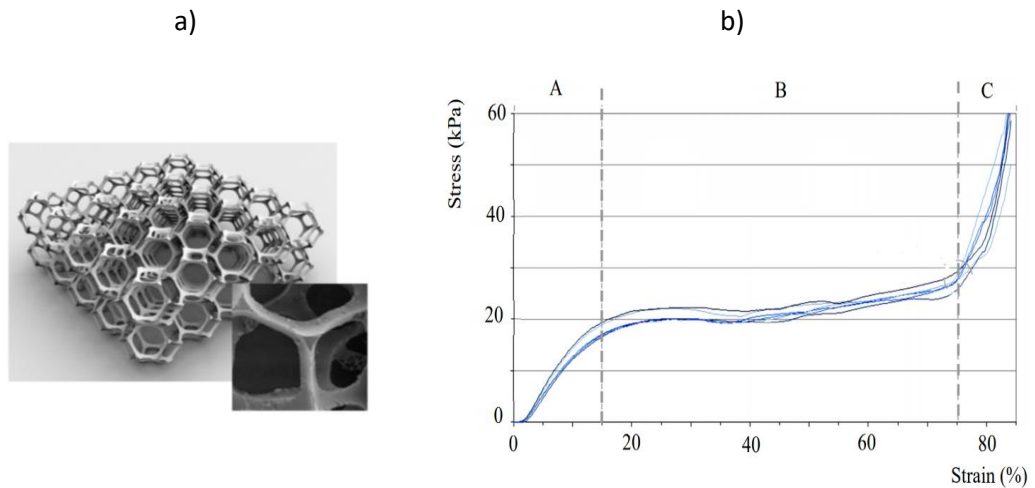


Figure 2.17 Kelvin cell a) cellular structure, b) compressive stress-strain response, under quasi-static loading, reproduced from [110]

While the Kelvin cell response initially appears impressive, further examination highlights the shortfalls of this structure. At $\sim 40\%$ strain, the plateau begins to rise. Over the range of 40-75%, where 75% is the proposed densification, the stress increases by $\sim 30\%$. This low ϵ_d is a common issue with strut-based structures.

2.3.2.3 3D – Surface-based 3D cellular structures

Surface-based structures are more comparable to closed cell foams. A simplified surface-based structure is currently used in helmets to mitigate rotation acceleration [111].

Examining the hourglass-shaped geometry, a similar branded material called Skydex® exists (Figure 2.18).

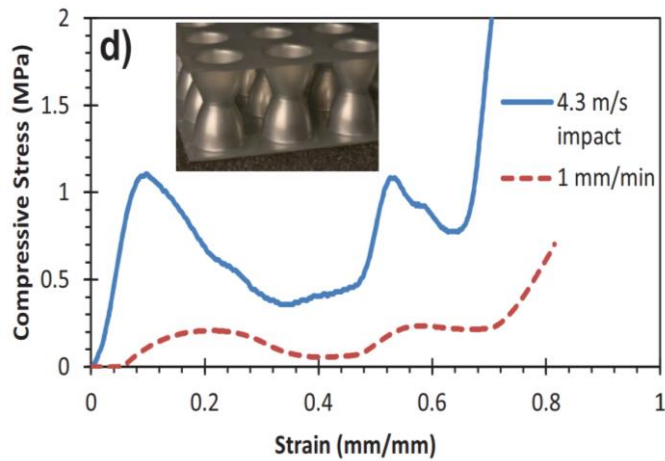


Figure 2.18 Multi-rate compressive stress-strain response of TPU Skydex® material, reproduced from [112]

Mechanical evaluation of this material shows a notably inefficient energy absorption profile; however, compared to the strut-based example, ϵ_d is notably increased.

2.3.2.4 Triply periodic surface – Schwarz primitive

Both the surface and strut-based cellular structures shown in sections 2.3.2.2 and 2.3.2.3 are challenging to compare to one another due to the different geometries used.

Therefore, to fairly compare strut- and surface-based structures, a common geometry was identified.

Desirable impact attenuating characteristics include high densification/long plateau region, as well as their suitability for manufacture (as described in section 2.2.1). The Schwarz primitive consists of supported over-hangs, making it favourable for FFF manufacture. Additionally, it can be explored as both a strut- and surface-based structure, as shown in Figure 2.19.

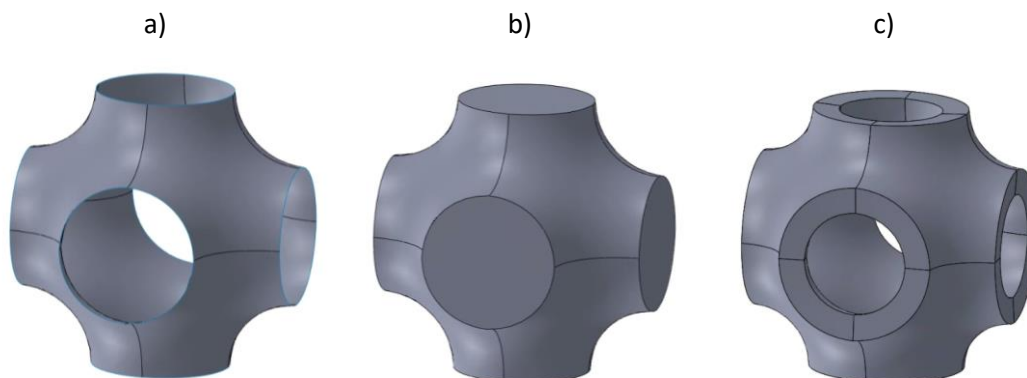


Figure 2.19. Example generation of triply periodic cellular structures, using the Schwarz Primitive (SP) geometry, a) SP surface, b) SP strut-based, c) SP surface-based

While an investigation of the strut-based SP structure was found, compared to an alternate surface-based triply surface, it had poor performance and did not plateau [113]. Comparatively, investigations into the surface-based variant of the SP structure showed promise both in terms of stress-strain response and comparison to foamed materials (Figure 2.20)

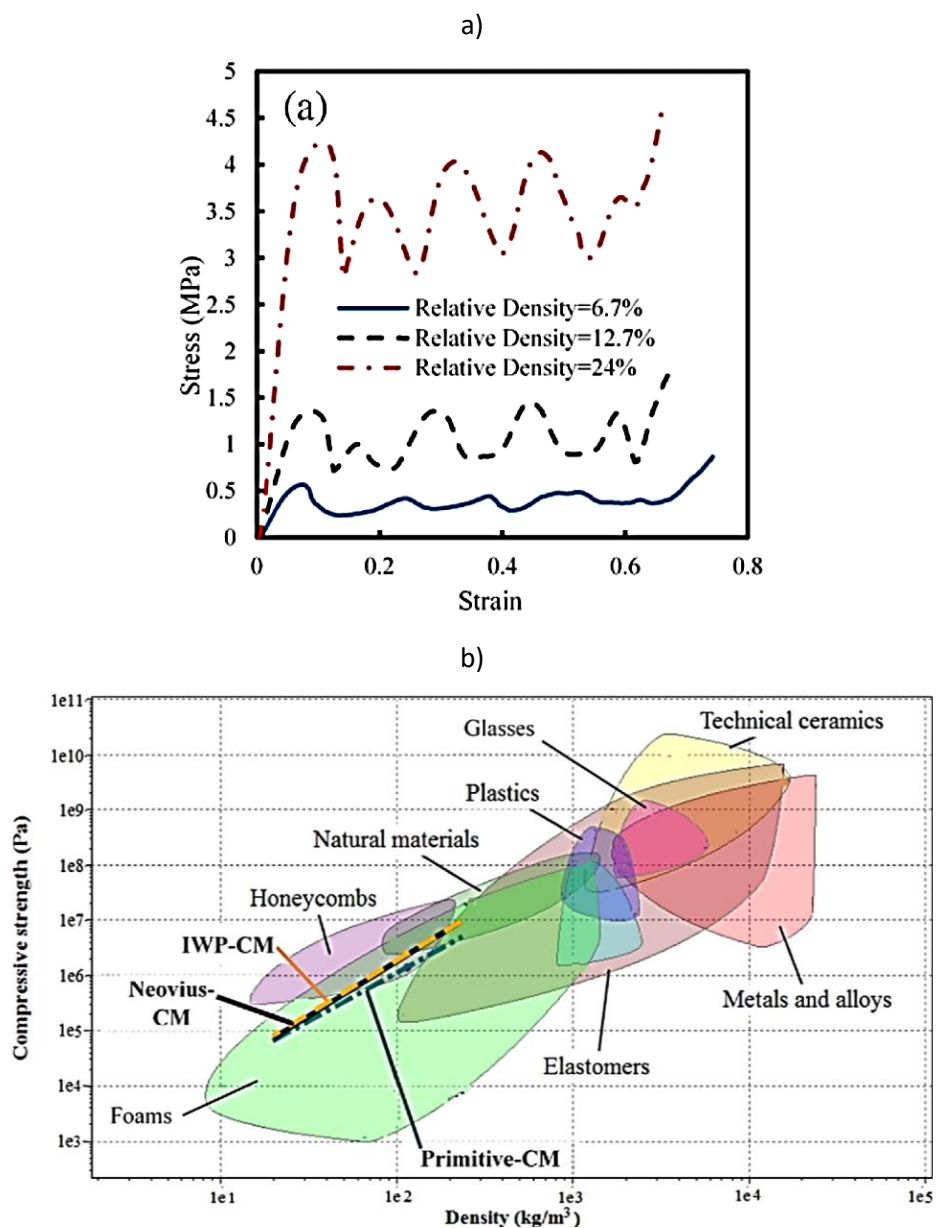


Figure 2.20. Nylon Schwarz Primitive (SP) surface-based structure, a) compressive stress-strain responses for multiple densities, b) chart of compressive strength against density for the SP (Primitive-CM) and other material classes, replicated from [114]

Comparing the general compressive stress-strain curve of the SP structure (Figure 2.20a) to that of EPS (Figure 2.12), or EF (Figure 2.14), a superior plateau and a higher ϵ_d can be observed. While EPS and EF demonstrate ϵ_d of 0.4 to 0.5, the SP structure has ϵ_d ranging from 0.6 to 0.7 at comparable relative densities. This increase of $\sim 40\%$ to ϵ_d , combined with a low ϵ_p and a plateau with constant peak stress, highlight the improved performance of the SP structure

Additionally, it demonstrates favourable performance compared to foams concerning compressive strength performance vs density (Figure 2.20b). For a given density, the Primitive-CM (SP) performs at the same level as high-performance foams (high strength:density ratio).

Schwarz primitive (SP) surface-based performance

To assess if the SP structure [114] could be used to replace EPS, its stress-strain response was converted into an energy absorption diagram. The study exploring the Nylon SP structure was tested under quasi-static loading conditions, at densities of 0.067 kg/m^3 and 0.127 kg/m^3 [114]. The SP structures were additively manufactured from nylon (PA2200), using Selective Laser Sintering (SLS). The PA2200 has an E_s of 1650 MPa according to the manufacturer's datasheet [115]. The resultant energy absorption diagram is presented in Figure 2.21.

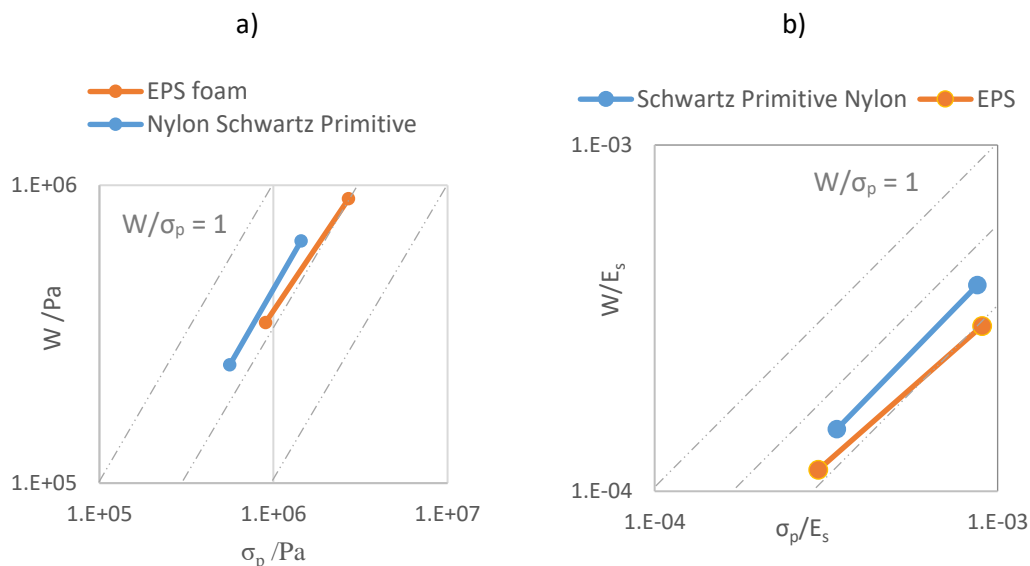


Figure 2.21. Energy absorption diagrams generated from the nylon SP (0.067 and 0.127 kg/m^3) data presented in Figure 2.20a and EPS (0.065 and 0.112 kg/m^3) data in Figure 2.12. A common high and low density, with a line connecting these two densities, is presented for each of the data sets. Also, dashed lines of constant W/σ_p are plotted to allow evaluation of efficiency. a) energy absorption diagram scaled by E_s , b) energy absorption diagram

The quasi-static data for the nylon-based SP structures are plotted alongside the EPS data (Section 2.3.1.1), in Figure 2.21a. The EPS foam data is from two densities, 0.065 kg/m³ and 0.112 kg/m³, and the SP is 0.067 kg/m³ and 0.127 kg/m³, making it a direct comparison. As can be seen in Figure 2.21a, the nylon SP provides increased efficiency over the EPS foam, while being of comparable density. Additionally, Figure 2.21b shows the EPS and nylon data normalised by their respective values of E_s . This normalisation allows for comparison independent of material. For a set σ_p , the SP stores/dissipates ~25-30% more energy when compared to EPS foam of the same density.

It should also be noted that the E_s of nylon is 1650 Mpa, while polystyrene is 3 GPa. While there will potentially be some difference in viscoelastic effects between these two materials, both are semi-rigid polymers, making them more comparable to each other than to an elastomer. Therefore, there is scope for a polystyrene SP structure to have ~2x higher σ_p and W , compared to a nylon SP structure. When scaling Figure 2.21a by 2x, the SP structure generates higher σ_p and W than EPS for the same density.

Additionally, compared to another well-documented triply periodic surface-based structure, at a set W the 0.065 kg/m³ SP structure had a σ_p ~20% lower than the Schoen Gyroid, and it achieved it at a density ~25% lower than the Schoen Gyroid [116].

2.4 Characterisation of materials for multi-impact mitigation

This section describes the literature that was reviewed concerning characterisation and modelling the identified material, with existing approaches investigated for their suitability.

2.4.1 Resilient materials

Multi-impact performance can be achieved by manufacturing cellular structures from resilient base materials. While cellular structures constructed from non-elastomeric materials have demonstrated elastic recovery [117], partial or full fracturing occurred within the structure. This fracturing indicates a significant loss of performance, supporting the assumption that non-elastic base materials cannot survive the strains experienced within cellular structures.

An investigation into the in-plane crushing of honeycomb structures has shown that internal nominal strains within cellular structures can range from ± 0.35 [94]. However, most engineering polymers experience only small strain (<0.05) elasticity, with strains above this value inducing non-recoverable plastic deformation. For example, nylon (a

common engineering polymer), demonstrates plasticity at strains of $\sim 0.03 - 0.035$ [118]. Similarly, polypropylene, a material well known for its flexibility and use in living hinges, demonstrates plasticity at strains of ~ 0.03 [119].

Comparatively, elastomers are known for their ability to be compressed to high strains (far over 0.5) repeatedly [120]. Furthermore, elastomeric cellular structures have been shown to have repeatable impact performance [94, 121], with exploratory work undertaken to explore their use in bicycle helmet design [122]. Therefore, elastomers were selected moving forward.

2.4.2 Material Characterisation of Elastomers

There is little literature covering AM elastomer characterisation [123], and only a few examples of characterising elastomers for dynamic applications [124-126].

While the rate-dependent characterisation for AM metallic structures has been reported in the literature [127, 128], rate-dependent behaviour for HE AM materials has not. Therefore, there is a need to establish a process by which they can be effectively characterised.

The success of a simulation is inherently governed by the accuracy of the material behaviour defined within the simulation. Where the material's modelled behaviour correlates poorly with its physical performance, the simulation will likely deliver an inaccurate solution.

The primary way of providing comparative mechanical performance information for any material is using standardised tests. This approach allows comparison between materials from different manufacturers, preventing values that may paint one material in a better light than another. However, this approach does not provide enough information to characterise material behaviour computationally.

In order to comprehensively characterise HE materials, it is important to consider the state(s) of stress that a simulated component will experience. In many cases, the exact states of stress within the component are unknown, usually consisting of multiple stress states. Therefore, HE material models require datasets that describe these states of stress. The most common datasets collected are uniaxial, equi-biaxial, and shear. Providing rate-dependence to the HE model is achieved through the collection of time-dependent data for viscoelastic modelling.

2.4.2.1 *Testing limitations*

Uniaxial tests follow established testing standards (tension [129] and compression [130]) and are relatively straightforward to undertake, as uniaxial test machines can be found in most testing laboratories. Tensile testing is widely understood to produce a state of pure tension within the gauge section of the test samples, making it the least contentious hyperelastic experimental method.

Comparatively, (uni-axial) simple compression testing generates friction at the platens of the testing machine. As the specimen is compressed, this friction acts on the contacting flat faces of the cylindrical specimen, preventing lateral movement and resulting in the phenomenon known as barrelling [131]. This barrelling results in a non-constant cross-sectional area and introduces a combined stress state within the specimen. This behaviour is noted even with low frictional coefficients (0.05), resulting in notable differences in the recorded stress-strain behaviour [131]. As friction is a function of multiple factors (e.g. load, strain-rate, surface roughness), it cannot be accurately compensated for during data processing.

As a result, simple compression is rarely used to collect data representative of compression for a hyper-elastic material. Instead, multi-axial data is collected, most commonly in the form of equi-biaxial tension. Collection of equi-biaxial data is mainly achieved through equi-biaxial extension and bubble inflation testing [132].

Bubble inflation testing requires sophisticated measuring equipment and specialised test apparatus to be designed and calibrated. Due to the nature of inflation, the material in question must be thin to allow suitable clamping and manageable inflation pressures. Small deviations in thickness that occur in additively manufactured specimens lead to uneven inflation, which will result in inaccuracies. Comparatively, equi-biaxial extension has fewer restrictions on specimen thickness but struggles with fatigue/cyclic testing, as many components of the jig/clamping assembly are prone to creep/slippage. Similarly to bubble inflation testing, equi-biaxial extension frequently requires additional stand-alone machinery. These machines make comprehensive hyperelastic analysis expensive to undertake, with a higher degree of training required.

For most materials, collection of shear data is conventionally achieved through simple shear testing. Simple shear testing is challenging to achieve with elastomeric materials, due to the high strains at which elastomers are tested, which can lead to these test specimens slipping out of the grips in a manner that is not feasibly controlled. Even minor slipping

would rotate the specimen, introducing a mixed stress state, making the test unrepresentative. Therefore, the more stable planar tension specimen is used to characterise hyperelastic materials.

Various test methodologies and apparatus have been developed for equi-biaxial [133], and planar [134], tests in the literature. Without any form of standardisation, this adds additional complexity for a new user. Therefore, this thesis investigates an approach that allows all testing to be undertaken on a common, widely available machine (uni-axial testing machine).

2.4.2.2 *Testing methods*

Uniaxial tensile testing is well established for the characterisation of elastomeric materials [129] and has few downsides. Tensile testing can be undertaken on bar or ring geometries; however, rings tend to have an uneven stress distribution over their cross-sectional area [129].

Equi-biaxial testing involves equal straining of a specimen around its periphery, resulting in compressive 'thinning' perpendicular to the straining direction. Due to the constant straining of the specimen around its periphery, a pure state of equal biaxial stress/strain is generated. This state is independent of the specimen thickness, or location within the specimen from which the stress/strain is recorded [135]. Equal straining commonly involves the extension of a thin disc of material via a series of tabs placed around its circumference. The combined radial force (F) is used to calculate the stress (σ) within the specimen, while a non-contact extensometer records the equi-biaxial strain. (r_d - radius of the disc, t - thickness of the disc)

$$\sigma = F * t * \pi * r_d [135].$$

As an academic exercise, equi-biaxial extension data can also be used to generate a theoretical uniaxial compressive response [131]. While this response may not necessarily be representative of that obtained during simple compression testing, it can be used as a point of comparison. For example, it can be compared to the experimental results of a simple compressive test with the caveat that the responses will likely not match, due to frictional effects and mixed stress states.

Planar tension testing involves a sheet of material that is much wider (ratio of >10:1) than its tested gauge length, which can freely contract in its thickness dimension while being constrained over its width. As a result of these restrictions, the material experiences no

rigid body rotation as it is loaded, with the extension of the specimen resulting in shear distortion alone. Rate dependent data can be provided by stress-relaxation, creep, and Dynamic Mechanical Analysis (DMA) test methods. All these test methods have their challenges and strengths, and inherently introduce inaccuracies into the process [136]. The creep and stress-relaxation tests are widely accessible and straightforward to undertake. However, the theory on which they are based requires an instantaneous strain or stress to be applied. Outside of theoretical environments, achieving this instantaneous state is not possible, due to needing to load specimens to the condition required for each test. Comparatively the DMA testing is complex to undertake and analyse, requiring additional equipment.

Analysing stress relaxation and creep testing, data needs to be back-extrapolated to a hypothetical instantaneous loading condition. Stress relaxation has been demonstrated in the viscoelastic modelling of large-strain elastomers [137], with the procedure well established in the literature, and straightforward to undertake.

2.4.2.3 Testing considerations

It is important to ensure that all data collected for the HE model is recorded at quasi-static speeds. As test speed increases, hyperelastic materials often display large degrees of rate dependence. For this reason, recording tests at different speeds can result in erroneous stiffness values when comparing different stress states to one another. When a HE quasi-static dataset has been collected, it can then be augmented with the rate-dependent data.

It is possible to fit a hyperelastic material model to experimental data erroneously. This issue commonly occurs when trying to fit a material model to a large hyperelastic data range, highlighting an issue with conventional HE modelling [121]. Polymeric testing standards were initially developed based on conventional polymers with plastic deformation regions. As elastic strains for such materials are in the region of 1-5%, and material models consist of both elastic and plastic components, pull-to-failure tests are required to collect the variance in deformation states, thus predicting this behaviour well. Additionally, as these materials fail below 100% strain, the data range is manageable, and non-linearity can be accounted for well during material modelling. However, HE materials can have strain-at-break values over 300%, and non-linearity in stress-strain behaviour is modelled alone by the HE component within the material model. As notable non-linearity in HE materials occurs at low strains <50%, this introduces an inherent favourability to fitting the material model to the larger later region of the test data (100 - 300+ %). As a

result, while fitting to the whole data range improves the prediction of large strains, the realistic strain range <50% has reduced predictive capabilities [138].

Due to the inherent flexibility of elastomeric materials, specimens are well known for creeping from even specialised gripping devices. Additionally, due to large strain elasticity, extension occurs in the stress-distribution regions of the test specimens. This further increases disparity between crosshead movement and extension in the gauge area. Therefore, strain data should be collected directly from the gauge area, as opposed to from the uniaxial machine crosshead movement.

There are two methods to account for the disparity in strain: contact and non-contact extensometry. Extensometers monitor the gauge area alone. Therefore, any disparities between the crosshead movement and specimen extension do not cause inaccuracies in strain data. Due to the low modulus of elastomeric materials, non-contact extensometry is preferred, as any surface pressure introduced by the contact extensometer may introduce experimental error. Non-contact extensometers measure the percentage increase between two markers, acting as a virtual strain-gauge.

2.4.3 Material modelling of AM elastomers

Established constitutive models can characterise the non-linear HE response of elastomeric materials. These comprise of a series of coefficients, associated with strain energy density functions, which capture the variation of stress versus strain. Curve-fitting software enables computational analysis of materials, by fitting these coefficients and allowing identification of the model with the strongest correlation to experimental data. Coefficients describing AM-produced materials typically differ from the same material manufactured using conventional processes [139, 140].

Validation methodologies for hyperelastic characterisation often involve simulation of the test piece used to collect the data. As these test pieces are created to induce a single form of stress within their test area, which the material model is matched to, simulation of these specimens returns the same data used to generate the material model. Therefore, this approach does not validate the appropriateness of the material model to simulate the material. To validate the material model, a new geometry, different from those used to generate test data, should be used. Also, the use of a geometry that induces multiple states of stress is desirable, as it allows for a more comprehensive test of the material model's predictive capacity. Cellular structures are an excellent case study for such a process. They introduce a complex mixture of stress states, challenging the predictive capabilities of the

material model, and are arguably more realistic of 'real world' loadings than specially designed specimens that induce only one form of stress.

The work presented in this thesis utilised the hyper-elastic material models available within ABAQUS; as this software was used to perform curve-fitting procedures. These were polynomial; reduced polynomial; Ogden; Arruda-Boyce; Van der Waals; and Marlow. These material models are defined using the following equations [141]:

General polynomial form

$$U = \sum_{i+j=1}^N C_{ij} (\bar{I}_1 - 3)^i (\bar{I}_2 - 3)^j + \sum_{i=1}^N \frac{1}{D_i} (J_{el} - 1)^{2i}$$

An established model using this form, which is utilised to successfully model elastomers in this thesis, is the Mooney-Rivlin model (where $N = 1$). If j is set to zero, the reduced polynomial form can be obtained

Reduced polynomial form

$$U = \sum_{i=1}^N C_{i0} (\bar{I}_1 - 3)^i + \sum_{i=1}^N \frac{1}{D_i} (J_{el} - 1)^{2i}$$

A number of well-known models utilise this form, including Neo-Hookean (where $N = 1$) and Yeoh (where $N = 3$).

Ogden form

$$U = \sum_{i=1}^N \frac{2\mu_i}{\alpha_i^2} (\bar{\lambda}_1^{\alpha_i} + \bar{\lambda}_2^{\alpha_i} + \bar{\lambda}_3^{\alpha_i} - 3) + \sum_{i=1}^N \frac{1}{D_i} (J_{el} - 1)^{2i}$$

Arruda-Boyce form

$$U = \mu \sum_{i=1}^5 \frac{C_i}{\lambda_m^{2i-2}} (\bar{I}_1^i - 3^i) + \frac{1}{D} \left(\frac{J_{el}^2 - 1}{2} - \ln J_{el} \right)$$

Van der Waals form

$$U = \mu \left\{ -(\lambda_m^2 - 3)[\ln(1 - \eta) + \eta] - \frac{2}{3} a \left(\frac{\bar{I} - 3}{2} \right)^{\frac{3}{2}} \right\} + \frac{1}{D} \left(\frac{J_{el}^2 - 1}{2} - \ln J_{el} \right)$$

Marlow form

$$U = U_{dev}(\bar{I}_1) + U_{vol}(J_{el})$$

In the models described here, U is the strain energy potential; U_{dev} and U_{vol} are the deviatoric and volumetric parts of U respectively; J_{el} is the volume ratio; \bar{I} refers to invariants of the deviatoric strain; $\bar{\lambda}$ is related to the principal stretches; \tilde{I} is related to \bar{I} ; η is related to \tilde{I} ; and N, μ, C, D, a, λ and α are material constants.

In addition to hyperelasticity, this work also modelled the viscoelastic response. Within ABAQUS this is modelled using a prony series [142]:

$$gR(t) = 1 - \sum_{i=1}^N \bar{g}_i^p \left(1 - e^{-t/\tau_i^q}\right)$$

Where N, \bar{g} and τ are material constants.

2.5 Processes for the manufacture of repeatable cellular structures

This section describes the literature concerning manufacturing processes, which are capable of producing cellular structures from elastomeric materials.

2.5.1 Conventional manufacturing techniques

2.5.1.1 Foaming

Conventionally, elastomeric foam (EF) is implemented when mitigating multiple impacts. Elastomeric foam is affordable, lightweight and demonstrates the plateauing behaviour that is key to controlled impact mitigation (Figure 2.4b). However, when compared to the EPS foam used in motorcycle helmets, the EF used in helmets has significantly reduced energy absorption (5.8 times less - Figure 2.13 and Figure 2.15), even at double the density (111 kg/m³ vs 65 kg/m³). Even if a stronger elastomeric foam could be identified, conventional methods of foaming cannot reproduce the undercuts and interior features, required in the formation of complex cellular structures. Therefore, while foaming is an important process in the field of impact mitigation, it has clear challenges that prevent its use in the production of cellular structures for motorcycle applications.

2.5.1.2 Subtractive manufacturing

Due to their low Young's modulus, subtractive machining of elastomers is challenging to achieve [143]. The predominate method to enable machinability of elastomers is the use of cryogenic machining. This process involves using liquid gas (e.g. LN₂) to cool the workpiece to below its glass transition temperature, resulting in a dramatic increase in the workpiece's Young's modulus. Cryogenic machining of elastomers is a challenging process,

requiring specialised fixturing of individual workpieces as well as additional apparatus to provide or contain the cooling fluid [143-145]. As a result, little research has been undertaken into its feasibility [145]. Additionally, subtractive based techniques are well known to be unable to produce internal voids and struggle to achieve undercuts in components. These restrictions make the manufacture of 3D cellular structures with these processes infeasible.

2.5.1.3 Addition-based processing

The most established methods for elastomeric fabrication are the use of addition-based processes [144], such as injection moulding and extrusion. These processes result in large, cost-effective production runs [146-148] that enable tight tolerances and achieve high-quality components. These processes are limited, however, by the same issues as conventional subtractive processes (e.g. no undercuts and challenging to produce multiple cavities), meaning it is not feasible to produce complex cellular structures. Additionally, these processes require a substantial initial investment in tooling, meaning that each component is of near identical-geometry and so limiting the opportunity for customisation.

2.5.2 Identifying AM processes for the manufacture of elastomeric cellular structures

Additive manufacturing helps resolve the issues seen in conventional manufacturing, enabling complex structures with internal voids. These benefits allow for the design and exploitation of cellular structures, which, in combination with digital manufacturing, allow engineers to design customised components for specific applications. These traits make additive manufacturing the only feasible process for the production of elastomeric helmet liners with complex parametrically defined structures.

Additive manufacturing is becoming a well-known process, popularised by the media, and taught at all stages of education [149]. Therefore, the base nature of the process, by which layers of material are built upon one another, can be considered to be well-known. However, except for the widely accessible Fused Filament Fabrication technology (colloquially known as 3D printing), the processes themselves benefit from further explanation.

2.5.2.1 Excluded processes

ASTM F42 [150] defines AM processes under seven categories of binder jetting, directed energy deposition, material extrusion, material jetting, powder bed fusion, sheet

lamination and vat photopolymerisation. As the goal of this work is to utilise an elastomeric material, the processes not capable of fabricating elastomers were excluded.

Direct energy deposition techniques (such as Electron Beam Melting (EBM)) predominately used metallic feedstock at the time of writing [151]. Similarly, sheet lamination was excluded as it predominately utilises paper, with edge-case uses of metallics and ceramics [151]. Therefore, these processes were not considered further.

Processes which utilise a catalyst to cure the stock material can produce components which continuously degrade as further post-cure occurs. This post-curing leads to parts becoming increasingly brittle and other performance changes. For example, in the case of vat photopolymerisation, longer post-curing exposures result in changes to mechanical properties, such as Young's modulus, ultimate tensile strength [152, 153] and reduced strain at break. Due to this inability to control the aging of material, vat photopolymerisation was also excluded.

Elastomeric components produced by material jetting have poor mechanical properties [154, 155]. For example, strain at break is mostly below that experienced in cellular structures [94, 154, 155], which would lead to any structures failing during compression. Due to this poor performance, it was excluded at this point.

Binder jetting has been used to produce predominately ceramic products, with these products being used as moulds to produce other components (e.g. sand casting). Its use in producing moulds is due to the porous nature of components binder jetting produces, which has been linked to the deposition of the binder [156]. While High-Speed Sintering (HSS) [157, 158] is demonstrating the potential for utilising polymeric powders with this technology, it is relatively young with limited material diversity, and components produced using this technology are still noticeably porous to the bare eye [159]. Therefore, it was also excluded.

The remaining two processes were material extrusion and powder bed fusion.

2.5.2.2 Material Extrusion

The most established process that involves melting and extrusion of material is Fused Filament Fabrication (FFF), also known as Fused Deposition Modelling (FDM). This process involves the melting of a feedstock filament, which is then extruded from a nozzle. The extrudate is deposited to form a 2D layer, which is then repeated to form the 3D geometry.

2.5.2.3 Powder Bed Fusion

The pre-dominant powder bed fusion process is Selective Laser Sintering (SLS). SLS involves heating a powder near its melting point. Additional energy is then provided by a laser to sinter the powder, fusing adjacent particles. This laser allows controlled sintering of the powder, with new layers of powder being added to the build chamber as it is lowered between sintering passes. The laser also sinters new layers to subsurface ones, creating the emergence of a 3D component.

2.5.3 SLS vs FFF

2.5.3.1 A comparison of SLS and FFF functionality

SLS is a well-established process that until 2014 [160] was patent protected. This protection has led to a relatively closed marketplace that has had the advantage of producing high-quality machines, with closed source materials and software meaning these processes deliver consistent components. SLS is well known to have a large amount of design freedom, as previous layers of powder provide support to new component features. These traits mean that SLS is commonly thought of as a production AM process.

Comparatively, FFF is perceived as an inferior process, which targets hobbyists/SMEs who want to produce prototype components. While some within the AM community still hold this belief, the viability of the FFF to produce functional components is increasingly being recognised [161]. Supporting this, established chemical manufacturers (such as DuPont [162] and BASF [163]) have started to produce materials for the process. Rapid developments to the underlying technology have occurred over recent years, which can in part be linked to the openness of the FFF marketplace, which has not been held back by a patent for roughly ten years [164], in contrast to approximately five years for SLS [160]. Due to the similarities between FFF and conventional extrusion, it is easier to develop materials for FFF than many of the other AM processes. This similarity leads to conventional polymers being re-purposed for FFF [165-167] and has contributed to wide material diversity compared to other AM processes.

SLS has been shown to have an issue with porosity [168], and this makes prediction of final part porosity challenging. This issue is aggravated towards the outside of a component, where the exterior material is only partially sintered. An effect of this is the change in mechanical properties observed in SLS components when exposed to moisture [169], which is commonly linked to the highly porous nature of the SLS surface [170, 171]. As cellular

structures commonly have small features, such as low wall thickness or strut diameter, this porosity becomes an important issue.

The main challenge facing FFF is control of the processing parameters. Most FFF machines are open-source and available at a lower cost than other AM technologies. The diversity of the materials and machines have meant control of processing parameters has fallen to users. Low costs and perception of the process as a method of prototyping have led to processing parameters being tuned for aesthetics rather than mechanical performance. This can be seen in the examples of functional FFF studies, where components containing unfused filament are presented as representative of FFF manufacture [172, 173].

Overall, the increased material diversity and advances that are being made in the FFF market make it attractive for niche materials such as elastomers. The challenge of achieving high density has not yet been solved for SLS, and this is a major challenge for cellular structures.

2.5.3.2 A comparison of SLS and FFF costing

In addition to comparing the difference in quality between FFF and SLS, a cost comparison was also undertaken. As there was a requirement to process elastomeric materials, and as these materials were commonly only available via third-party manufacturers, machines with closed ecosystems were excluded. However, generally, these closed-system machines were notably more expensive than their open-source alternative.

A Prodways P1000 SLS machine costs between £39,000 and £78,000 for the base model [174], has a 15kW power requirement and a build volume of 300x300x300mm. The FFF machine and extruder system used in this study was the Flashforge Creator Pro 2017, with the Diabase engineering Flexion extruder kit. This system can produce components at a comparable resolution, with a power requirement of 350 W, a build volume of 227x148x150 mm, and costs £750. If the lowest price point for the P1000 is £39,000, this same initial investment can be used to purchase 52 Creator Pro FFF machines, with an extrusion kit for each, resulting in 9.7x the build volume.

While it is difficult to comment on manufacturing time (as this is highly dependent on several factors, including geometry and processing parameters), filling the volume of one Creator Pro with the cellular structures used in this research would result in manufacturing taking 100 hours. Meanwhile, the P1000 takes 30 hours to manufacture components within its build volume, according to its technical data-sheet [175]. Therefore, while individual FFF

machines take 3x as long to manufacture the components, a farm of 52 FFF machines would result in a continuous manufacturing time 3x that of the comparatively priced SLS machine.

Electricity prices at the time of writing [176] gave electrical running costs of £1.72/hour for SLS, and £2.09/hour for the FFF farm, respectively. Material costs vary between brands; however, FFF generally has more favourable material costs, with PA12 prices of \$100/kg (\$100,000/m³) for FFF and, over \$150/kg (\$150,000/m³) for SLS [177]. Considering these prices, the running costs of the SLS machine would be ~\$4100 for materials and electricity. Comparatively, running enough FFF machines to fill the same volume would cost ~\$3950, with ~30% of the cost in the form of electricity.

As a single operator could as feasibly oversee a farm of FFF machines as an SLS machine(s), operator costs were excluded from this comparison. However, as the manufacturing time comparison above has shown, the FFF farm can produce components 3x as fast. Therefore, the per component cost of FFF operator labour will be approximately 1/3 of that of SLS.

This section demonstrates the economic viability of the FFF process when compared to a similar SLS process. It should be noted that FFF is likely more viable, as additional costs associated with the SLS process (e.g. 3-phase power and compressed air lines for post-processing facilities) have been excluded as they are dependent on existing infrastructure.

Considering the material advantages covered in section 2.5.3.1 and the porosity challenge SLS faces, this viability provides further evidence of FFF being a suitable manufacturing route moving forward.

2.5.3.3 FFF processing parameters affecting the manufacturing quality

To produce components that are fully fused, optimisation of processing parameters is required. While processing parameter guidelines are provided by both the manufacturers of FFF materials and machinery, these products are frequently developed independently from one another. As a result, a “one parameter fits all” approach is not possible, and a sweep of appropriate parameters should be undertaken to ensure components are of high density.

To ensure the optimisation of an elastomeric cellular structure is suitable for impact mitigation, the primary objective to optimise for is functionality. Therefore, the main objective for components is high levels of fusing or material contiguity. If the AM layers are not contiguous, the consequent voids will introduce points of failure. While many

parameters can influence the fusing of FFF components, the primary processing parameters that affect the quality of manufactured FFF components are:

Nozzle diameter – This affects the resolution of components and also the manufacturing time. A nozzle with a smaller diameter will allow thinner lines of the extrudate to be deposited. Therefore, higher resolutions can be achieved, as smaller features can be realised (e.g. narrower wall thicknesses). However, this increase in resolution comes at the cost of increased manufacturing time, increased chance of extrusion issues, and reduced ability to bridge over unsupported areas/those with little support. The default nozzle size on FFF machines is 0.4 mm.

Layer height – reduced layer thickness lowers the minimum feature size and allows for finer control of any features. This height is limited by machine, with minimum layer heights being in the range of 50 – 100 μm . If there is less of a gap than this, it is challenging to lay down any extrudate.

Nozzle temperature – reduced temperature results in quicker solidification of the filament after it is extruded, resulting in better feature definition and reduced drooping. If the extrudate is too cold when exiting the nozzle, blockages and interruptions occur. This results in inconsistent extrusion and gaps within manufactured components.

Printing speed – printing speed has been linked to many issues such as inconsistent extrusion [178] and layer-shifting [179]. Additionally, high printing speed has been linked to the reduced control of the extruded elastomeric filament [180].

Infill percentage/pattern – Infill pattern describes how the interior of a layer is filled. The machine first deposits an outline of extrudate around the boundary of the layer and, following this, uses an infill patterning method to fill the space inside this outline.

Extrusion multiplier – Extrusion multiplier affects the amount of material extruded by the system, too high a multiplier leads to over-extrusion and too low a multiplier leads to under-extrusion. Over-extrusion can result in issues that include distortion of features, as any excess material will expand outwards (Figure 2.22a). Comparatively, under-extrusion can result in issues such as high intra-layer porosity (Figure 2.22b), and weak interlayer bonding.

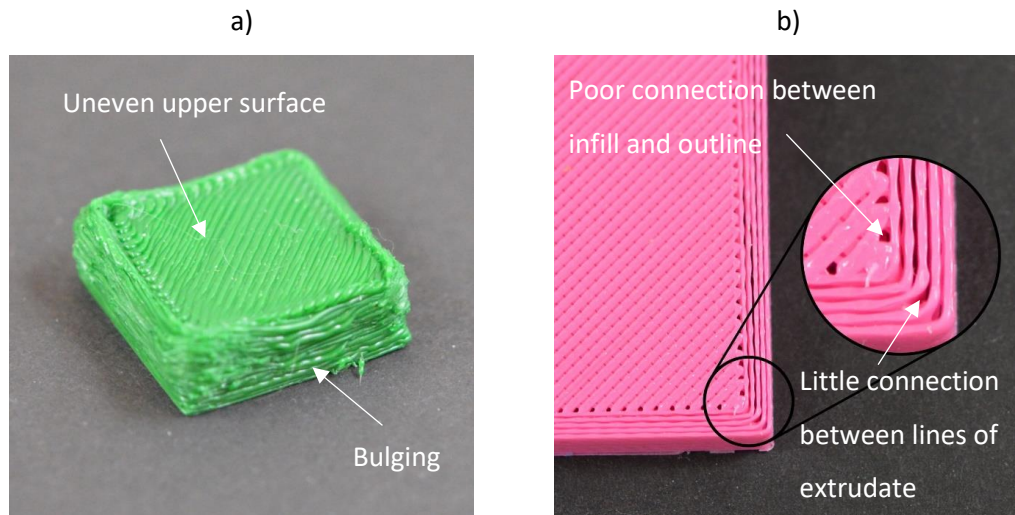


Figure 2.22 Examples of poorly processed FDM components, exhibiting a) over extrusion (excessive material), b) under extrusion (poor interlayer bonding), adapted from [179]

Therefore, an ideal component lies between these two extremes, providing low porosity without comprising feature definition. While excessive under-extrusion is immediately apparent, as gaps form between extrudate paths, it becomes harder to identify when the extrudate begins to fuse. Sectioning of the components can give an insight into whether under extrusion has occurred; however, the random nature of the physical sectioning process means this can result in a false positive. The onset of over-extrusion is more apparent when too much material is extruded, and there is not enough of a gap between the nozzle and previously extruded material. This lack of a gap leads to scarring of the upper surface of components [181], where the nozzle gouges a mark into the surface of the component as it passes over.

An additional aspect of FFF printing is the introduction of “stringing”. Due to molten polymers having a low viscosity, it can ooze as the nozzle paths between different areas within a layer. This oozing forms a fine string, which trails the FFF nozzle. When attempting to produce an aesthetic part, this material is seen as undesirable; however, due to its fine nature, it has little impact on part functionally and can be removed easily with tweezers if desired.

3 Methodology

This section describes the methodological approach to the experimental work in this research. The objectives set out in section 1.1 were addressed as follows:

1. Optimise processing parameters to produce functional cellular structures

A method for optimising the Fused Filament Fabrication (FFF) process to manufacture highly functional elastomeric cellular structures was set out. High functionality was achieved by focussing optimisation on attaining components with high density. The success of this process was evaluated using micro X-ray computed tomography (μ CT) and visual observations.

2. Establish a novel mechanical characterisation pathway

Novel methods to identify the characterisation strain range and accessibly characterise elastomeric materials were developed. The characterisation strain range was identified through computational analysis of a honeycomb and Schwarz primitive (SP) unit cell. Accessible characterisation of the elastomeric material was achieved through the development of custom test jigs, to enable full characterisation on a standard uniaxial testing machine. The approach to analysing hyperelastic material models for their agreement with this characterisation data was also developed.

3. Generate a novel scalable design tool to select initial cellular configurations

A novel method for undertaking mesh sensitivity studies was developed. This approach ensured that any investigated configuration had an acceptable level of mesh refinement, without having to undertake mesh sensitivity studies repeatedly. Also, a method of evaluating whether energy absorption diagrams could be applied to a cellular structure was developed. This evaluation examined the structure's sensitivity to external conditions and its capacity to scale to applications of different sizes. The approach to generating energy absorption diagrams was then described. Additionally, a novel method to scale these diagrams to different materials without having to repeat any simulation was then developed and validated.

4. Manufacture and analyse a prototype motorcycle helmet

A novel approach, combining the scalable design tool with complete simulation of a helmet assembly, was developed. This approach significantly reduces the number of required simulations. A mechanical testing methodology was also set out to validate the novel

optimisation approach. While developing this approach, a method to propagate the cellular structure within a helmet was also developed.

Throughout this work, computationally aided design (CAD), and computational analysis, were used as follows:

- To design additively manufactured components, and produce “.STL” files for manufacture, the CAD package SOLIDWORKS 2018 (Dassault Systems, France) was used.
- When undertaking computational analysis, ABAQUS 6.14 (Dassault Systems, France) was used. Additionally, cellular structures modelled in SOLIDWORKS 2018 were exported as “.SAT” files for meshing and analysis in ABAQUS 6.14.

3.1 Optimising FFF processing parameters to produce functional elastomeric cellular structures

This section sets out the approach for the optimisation of FFF processing parameters for elastomeric materials. Optimising these parameters serves as an essential first step, ensuring any components produced are of high performance. The goal of the optimisation process was to produce parts with minimal porosity, as porosity inherently reduces the mechanical strength of a component. A FFF machine and preliminary material were also selected to enable the investigations in this research.

The potential of the SP structure was established using an energy absorption diagram in section 2.3.2.4. However, it is not possible to scale this diagram to an elastomeric material. As discussed in section 2.2.2.2, viscoelastic and non-linear effects make it infeasible to scale from a semi-rigid polymer, such as nylon, to an elastomer. Therefore, a preliminary FFF elastomer must be selected to allow for the initial generation of an elastomeric SP energy absorption diagram. NinjaFlex (NF), a flexible thermoplastic polyurethane (TPU) [182], was selected as it had been preliminarily explored in the literature for its energy absorption capacity [183].

One of the objectives of this work is to enable replacement of the SP structure’s elastomeric base material. Therefore, an open-access FFF machine was required to broaden the material selection. A 2017 Creator Pro (Flashforge, China) was selected, alongside a Flexion extruder system (Diabase Engineering, USA) to improve extrusion

control of flexible filament. Optimisation of processing parameters was achieved through the slicing software Simplify3D (Simplify3D, US).

3.1.1 Investigation of processing parameters

Diabase engineering provided guidelines for extruding flexible filaments with their Flexion extruder [184]. Similarly, NinjaTek provided guidelines for its NF filament [185]. These two sources were used to identify the initial processing parameters for NF. While they agreed on many processing parameters, they disagreed on printing speed. Diabase recommended a printing speed of 3600 mm/min when using its Flexion extruder. Meanwhile, NinjaTek recommended a printing speed of 600-2100 mm/min. Therefore, a conservative printing speed of 2000 mm/min was selected to prevent layer-shifting and inconsistent extrusion (section 2.5.3.3).

The first variable parameter to be investigated was the nozzle temperature. As discussed in section 2.5.3.3, the extrudate must be hot enough to flow freely from the nozzle, while being of sufficiently low temperature that it quickly re-solidifies. Therefore, the filament was extruded from the nozzle, with the temperature increased by 5 °C increments until the extrude flowed freely with no stoppages or blockages.

Rectilinear and concentric infill were investigated for their ability to produce contiguous layers. These were the two 'solid' infill patterns available in Simplify3D. Test specimens were manufactured and evaluated for both patterns.

After selecting an infill pattern, the remaining processing parameter that effected functionality was the extrusion multiplier. A test specimen was manufactured at an extrusion multiplier of one, and the multiplier was increased in 5% increments, with a new specimen manufactured at each increment. This procedure was repeated until scarring was observed on the upper surface of the test specimen. This scarring is indicative of over-extrusion (section 2.5.3.3), and therefore the multiplier before this one was considered optimal.

Dumbbells (Figure 3.1a) were utilised when exploring the infill patterns and optimising the extrusion multiplier. This geometry had radii and sharp corners that introduced a challenge for the fusing of the perimeter wall and the infill pattern.

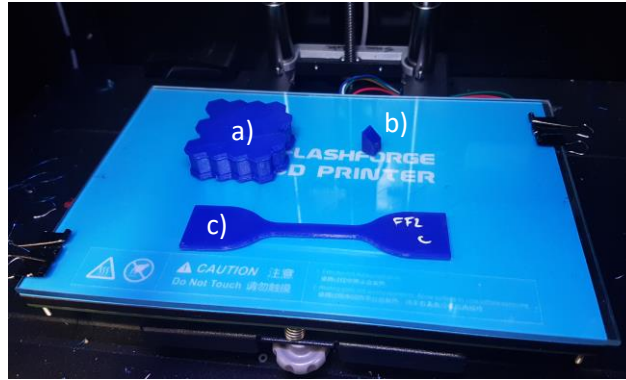


Figure 3.1. Manufacturing orientation of test components relative to FFF machine bed, a) honeycomb component, b) cuboid (note, pictured cuboid has been sectioned for analysis), c) uniaxial dumbbell

3.1.2 Assessment of component porosity

A cuboid of 7.5 x 7.5 x 20 mm (Figure 3.1b) was manufactured to evaluate the success of the optimised extrusion multiplier. These dimensions were selected to ensure the cuboid was small enough to be scanned at a high resolution, with a manageable amount of sectioning.

A Zeiss Xradia 520 (Carl Zeiss, USA) μ CT was used to scan the cuboid. The tomograms it generated were reconstructed and analysed using XMReconstructor (Carl Zeiss, USA).

Five individual scans, with a 15% overlap between each scan, were undertaken over the cuboid's 20 mm height. These were then stitched together during post-processing, enabling high-resolution imagery of the cuboid. The resultant voxel size from this process (i.e. resolution) was $\sim 11.9 \mu\text{m}$. The proportion of voids to solid material was then analysed. *Note, the boundary between material pores (< 2 voxels) cannot be accurately defined. As inaccuracies could be introduced if undertaking segmentation included these smaller pores, a threshold size of 2 voxels was implemented, with voxels below this size excluded during analysis.*

Sectioning, via scalpel, was performed after the cuboid had been examined using μ CT. This sectioning was undertaken to enable optical microscopy of the cuboid, to allow visual correlation with μ CT analysis results. A scalpel was used, as sawing and polishing of elastomeric materials is not feasible for optical examination [155]. An Olympus lab-based optical microscope was used to visually examine the sectioned cuboid, with imagery captured via a Moticam 10 (Motic, China) microscope camera.

3.1.3 Analysis of feature accuracy

The ability of the optimised profile to additively manufacture (AM) a cellular structure was also evaluated. A honeycomb component (Figure 3.1c) was scanned using μ CT to assess the ability of the optimised profile to match the input design. A honeycomb was selected, as it was the most established cellular structure whose mechanical performance had been explored in the literature. An arbitrary honeycomb was generated, with a unit cell size of 10*10*10 mm, resulting in an edge length of 5.8 mm. Additionally, a wall thickness of 0.4 mm (nozzle diameter) was selected. A configuration of 4*5 unit cells was selected, as the resultant configuration had a cross-sectional area (CSA) of approximately 50*50 mm.

By constraining the bounding volume to 50*50*10 mm, a single μ CT scan of the whole component could be taken at sufficiently high resolution to measure wall thickness accurately. Due to its increased bounding dimensions, the honeycomb component was imaged using a Nikon XT H225 (Nikon Metrology) μ CT. The larger bounding dimensions, in combination with this machine, resulted in a voxel size of $\sim 15.1 \mu\text{m}$.

CTPro version 3.0 (Nikon Metrology) was used to perform reconstructions for this system, which were pre-processed using VGStudio Max 2.1.5 (Volume Graphics, Germany). The resultant processed scans were analysed in Avizo Software (ThermoFisher Scientific, USA), which was also used to generate an “.STL” file. The consistency of the honeycomb’s wall thickness was measured by digital inspection of this “.STL” file, supported by physical measurements of the component with a Vernier calliper. *Note, these measurements were used to update the honeycomb CAD during the validation stage of the material characterisation process.*

3.2 Establishing a novel material characterisation pathway for AM elastomers

This section describes the approach for the collection of characterisation data for NF and the consequent material modelling process. Two novel methods were developed to enable this approach. Equi-biaxial and planar shear jigs were designed and manufactured to enable accessible characterisation via a standard uniaxial testing machine. Additionally, a computational approach to estimate internal strain was developed to support the selection of the characterisation strain range.

All quasi-static mechanical experimentation was performed using a Z50 (Zwick, Germany) electro-mechanical uniaxial testing machine. Additionally, a CAM028 (iMetrum, UK) non-contact video extensometer was used to collect strain data for this testing.

Dynamic mechanical testing was performed using a 9250HV (Instron, US) guided drop tower. The minimum available impactor carriage for the 9250HV had a mass of 3.53 kg. This low mass was adopted to enable testing of the NF pads at higher velocities, without overcompressing them. An in-line 8715A (Kistler, Switzerland) accelerometer was used to record the acceleration-time pulse. An SC1 (Edgertronic, USA) high-speed camera was used to record the deformation patterns during dynamic testing.

3.2.1 Identification of internal strains within a cellular structure

When modelling the behaviour of an elastomeric material, characterisation data is required. The procedure to create a material model from this data is known as curve-fitting. Curve-fitting attempts to fit a model to the provided data while remaining mathematically stable. The correlation achieved by this curve-fitting process can be high over the provided data range while being poor over certain parts of it. Therefore, even though a material model may have a high overall correlation to the characterisation data, it would not be able to accurately represent a component that experiences internal strains within the poorly correlated range.

Consequently, it is generally recommended that characterisation only be undertaken over the strain range experienced by the application. While this is straightforward to identify for simple applications (e.g. tensile extension of a rectangular strip), strains within complex applications (e.g. cellular structures) cannot be so easily identified.

3.2.1.1 *Computational approach*

A novel approach of computationally capturing the internal strains of a cellular structure was developed. The results of this exercise inform the required strain for the collection of uniaxial, planar, and equi-biaxial, characterisation data.

The honeycomb component used to evaluate the optimised processing parameters was again used here as a case study. Analysis of all internal strains within the honeycomb's 20 unit cells would require a significant quantity of data to be processed. Therefore, as this analysis is intended to be an approximation, a single unit cell was simulated to ensure data processing was manageable.

As this analysis was undertaken before characterisation testing, no HE material model existed for NF. Therefore, a linear elastic material model based on the NF datasheet (Young's modulus = 12 MPa) [182] was implemented. Hex-dominated quadratic meshing was employed, with the ABAQUS default mesh size used to seed the unit cell. The upper and lower surfaces of the honeycomb unit cell were fixed to rigid analytical surfaces. The lower analytical surface was fixed in space and, over a second, the upper analytical surface was displaced downwards. This displacement resulted in overall compression of the unit cell to 90% of its original height.

The simulation was analysed by outputting minimum and maximum nominal strain for each finite element in the honeycomb unit cell. As computational analysis is prone to error, plotting strains for all elements allows for easier identification of erroneous elements.

This process was also undertaken for an SP unit cell, to ensure the selected characterisation range was representative of the strains within the SP structure. The same bounding unit cell size of $10*10*10 \text{ mm}^3$ was used, but wall thicknesses of 0.5 mm and 1.5 mm were selected (as per section 3.3.1). Additionally, instead of hex-dominated elements, tetrahedral elements were used to mesh the SP structure.

3.2.2 Mechanical characterisation

A novel experimental approach for characterising dynamic elastomeric behaviour was pursued. Standardised uniaxial tensile testing was complemented by further multi-axial data generation. The generation of this data was achieved through a novel equi-biaxial and planar shear testing methodology. Rate-dependent datasets were also collected, with ABAQUS based curve-fitting used to identify an appropriate HE/viscoelastic material model.

3.2.2.1 *Developing accessible characterisation jigs*

Generation of hyperelastic material models requires multi-axial data generation. While uniaxial data can be collected via a conventional uniaxial test machine, collection of equi-biaxial and planar data conventionally requires standalone machines. These additional machines introduce a significant barrier to entry. Therefore, jigs were developed to allow accessible multi-axial testing within a standard uniaxial testing machine. These jigs were manufactured using a combination of different techniques and materials. Test specimens for these jigs were developed from existing designs in the literature.

Equi-biaxial tension

The equi-biaxial test specimens, identified in the literature, were initially developed for use in a custom test machine [133]. These specimens were computationally analysed when they were developed, to ensure equal strain under loading [133]. *This analysis has been re-created and is shown in Figure 3.2b, with red equivalent to maximum nominal strain and dark blue being equivalent to a nominal strain of ~ 0 .*

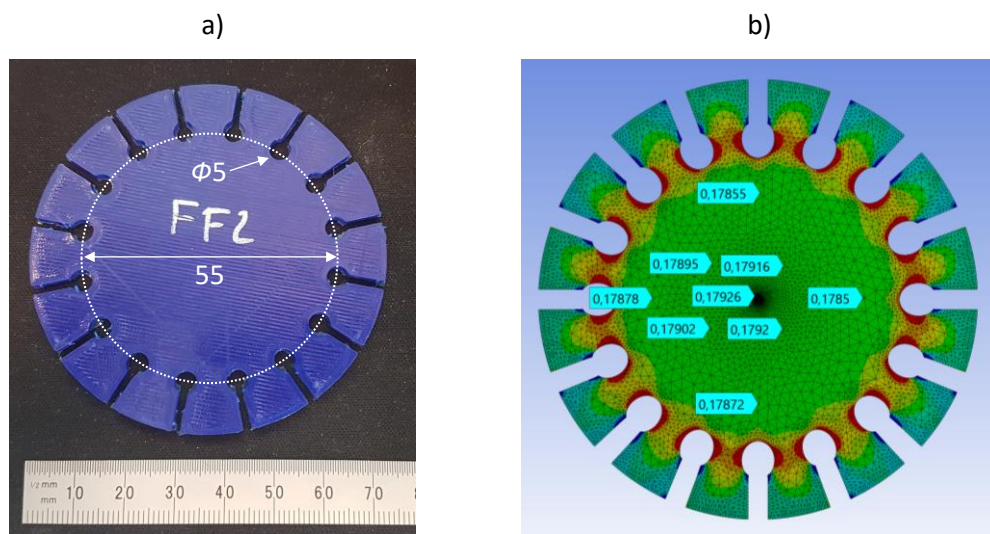


Figure 3.2: Equi-biaxial test specimen used in this research, a) dimensions (mm), b) computational analysis that was undertaken to demonstrate equal nominal strain under radial loading

Radial loading is applied via 16 clamping tabs, spaced equally around the specimen's perimeter, uniformly distributing load into the central region of the specimen. Specimens were manufactured at a thickness of 2 mm. These test specimens were adopted moving forward, and a jig was designed, which transferred vertical loading of the uniaxial testing machine into equal radial loading around the perimeter of the specimen.

The vertical loading was transferred through a series of wires into radial loading via roller bearings (Figure 3.3). Due to the jig having multiple components, assembly tolerances compounded on one another, raising difficulties in equal radial loading using wires alone. Therefore, a method of adjusting wire tension, after the specimen had been clamped, was required. This adjustment was achieved using rigging screws, which were placed in-line with the loading wires to allow independent correction.

The flexible nature of the elastomeric test specimen meant the loading wires also had to be flexible. For example, if stainless steel wires were used, the act of applying tension to the

wires would cause deformation of the specimen before the wires were pulled taut. As these wires were flexible, those under higher tension inherently deformed more, helping to balance the loading of the specimen. Therefore, they provided an additional degree of correction to the rigging screws.

A schematic of the equi-biaxial jig is shown in Figure 3.3, and an annotated photograph is shown in Figure 3.4.

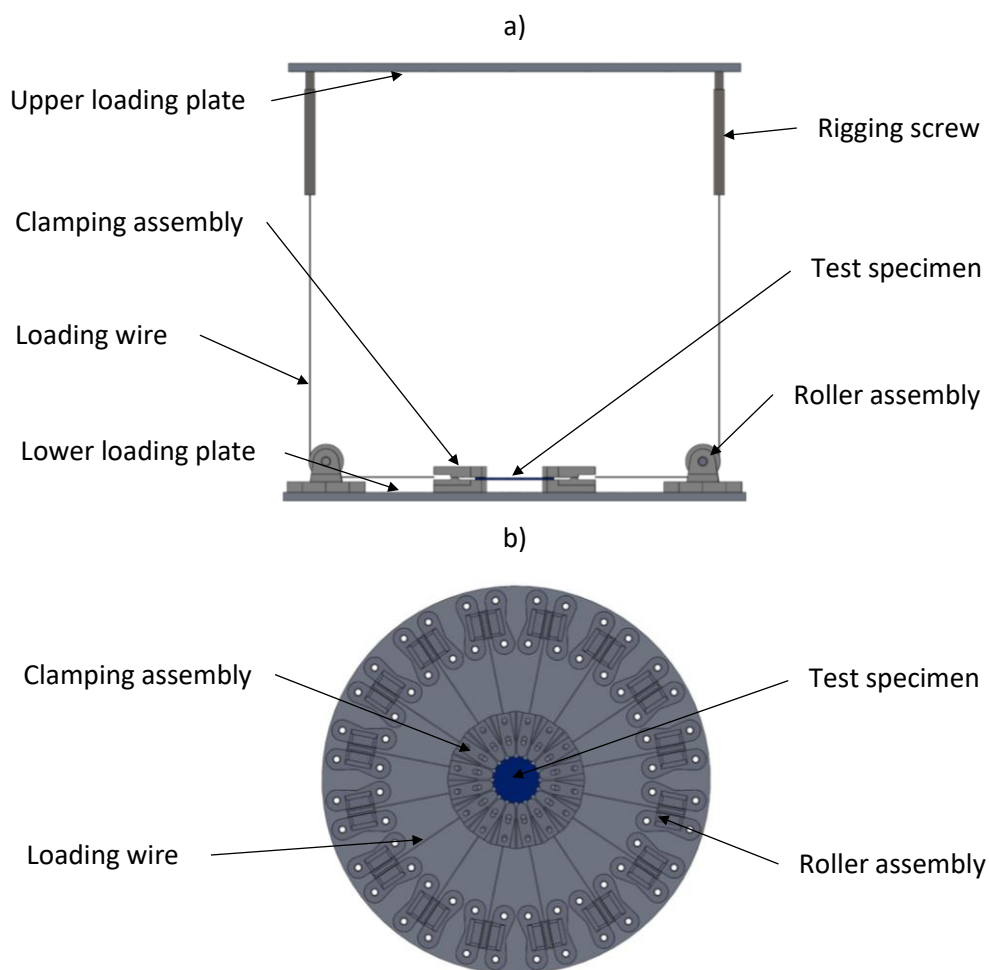


Figure 3.3. The equi-biaxial test jig developed in this research. Loading is transferred from the upper loading plate through a series of 16 loading wires. These are translated through 90° via individual roller assemblies, to the test specimen via individual clamping assemblies. a) side view, b) plan view

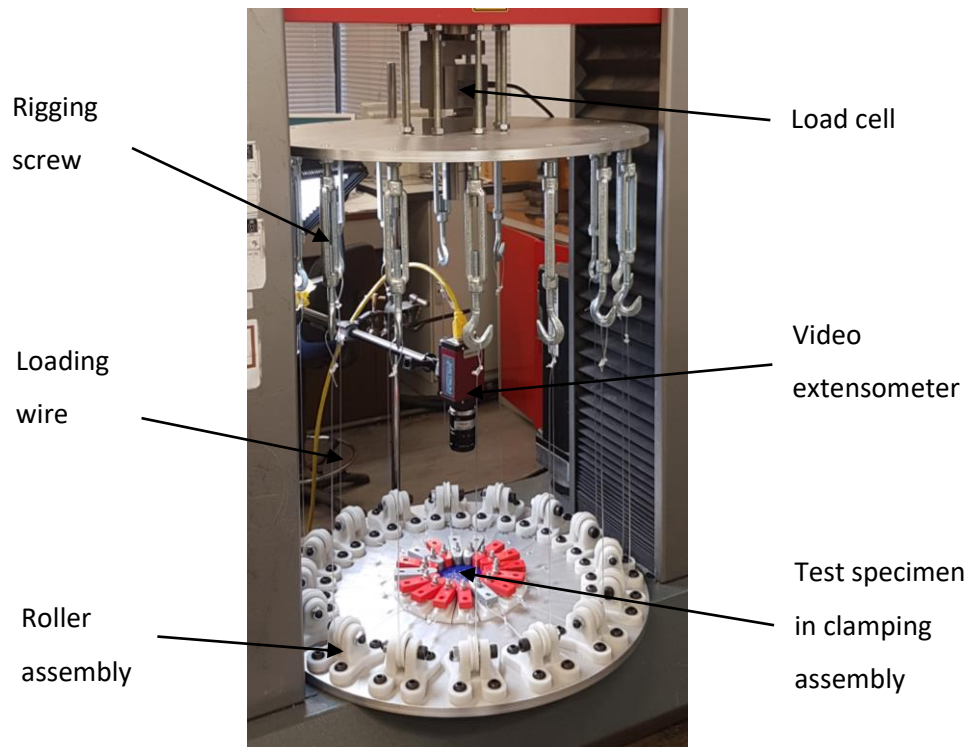


Figure 3.4. The developed equi-biaxial jig mounted within a uniaxial test machine. The aluminium loading plates are directly bolted to the test machine and transfer the load to the test assembly via a series of 16 wires. The tension in the wires is adjusted using rigging screws.

Plates were used to transfer loading from the uniaxial testing machine to the equi-biaxial jig. These were made from aluminium as it resulted in lightweight plates to minimise load cell noise, while still being stiff enough to minimise any warping induced during testing. Additionally, the machinability and availability of aluminium made it a favourable choice. The design of these plates is shown in Figure 3.5.

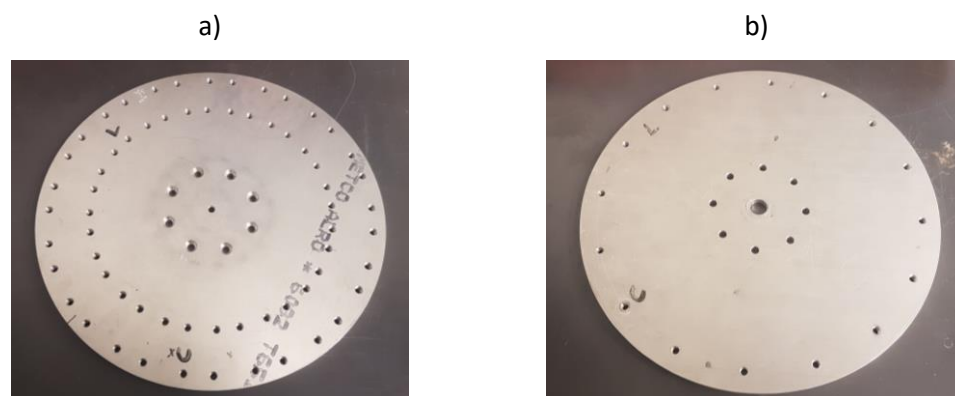


Figure 3.5. The loading plates from the developed equi-biaxial jig, showing the mounting hole patterns. a) lower plate, b) upper plate

The loading wires used to translate the uniaxial machine movement into radial loading of the specimen were nylon fishing wire. This fishing wire was capable of carrying a high load while remaining flexible. Loading wires were attached to the upper loading plate via an RS Pro rigging screw, with a hook and eye attachment. The eye was removed and replaced with a screw thread that attached into the upper loading plate. The lower hook was then attached to the loading wire by a loop, created by crimping the wire.

The loading wires individually ran over roller assemblies, which transferred the wire loading direction through 90°. The roller assemblies were manufactured using glass-filled nylon (GFN). The decision to use of GFN, instead of un-filled nylon, was made due to GFN's increased modulus, which minimised distortion. A roller mount and runner were designed using CAD, and a steel ball bearing (with rubber seals) was used in each roller assembly to reduce friction. Each assembly (Figure 3.6) was then bolted onto the lower loading plate.

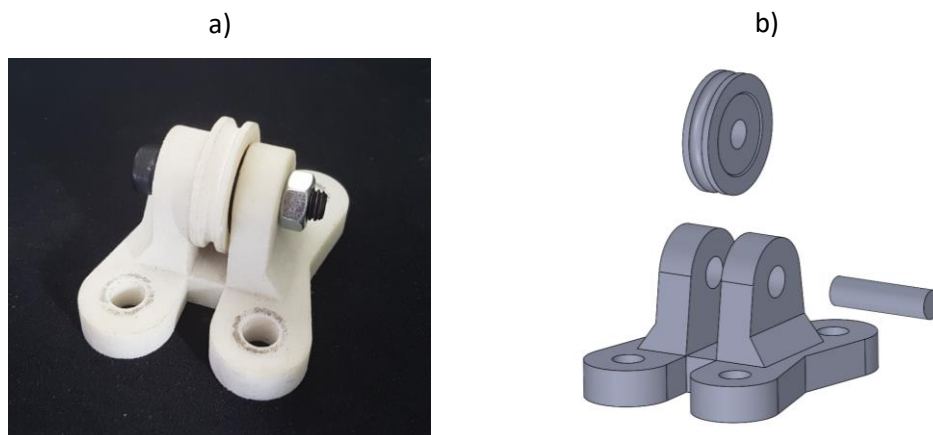


Figure 3.6. One of the 16 roller sub-assemblies from the developed equi-biaxial jig, where a roller bearing is fixtured to an additively manufactured stand using a bolt, a) complete assembly, b) exploded CAD view

The end of each wire was then attached to the lower half of a clamping assembly using another crimped loop. As the wire loading passed through the lower portion of the assembly, the upper portion was only required to provide clamping force. While the lower halves were manufactured from GFN, the reduced load requirement led to the upper halves being manufactured from Polylactic acid (PLA), as it was a more economical material. Slippage was minimised by designing a button-like extrusion where the upper and lower halves interfaced with the test specimen. The clamping assembly was tightened using a screw, which acted against a pivot point at the rear of the lower clamping component. This assembly is shown in Figure 3.7.

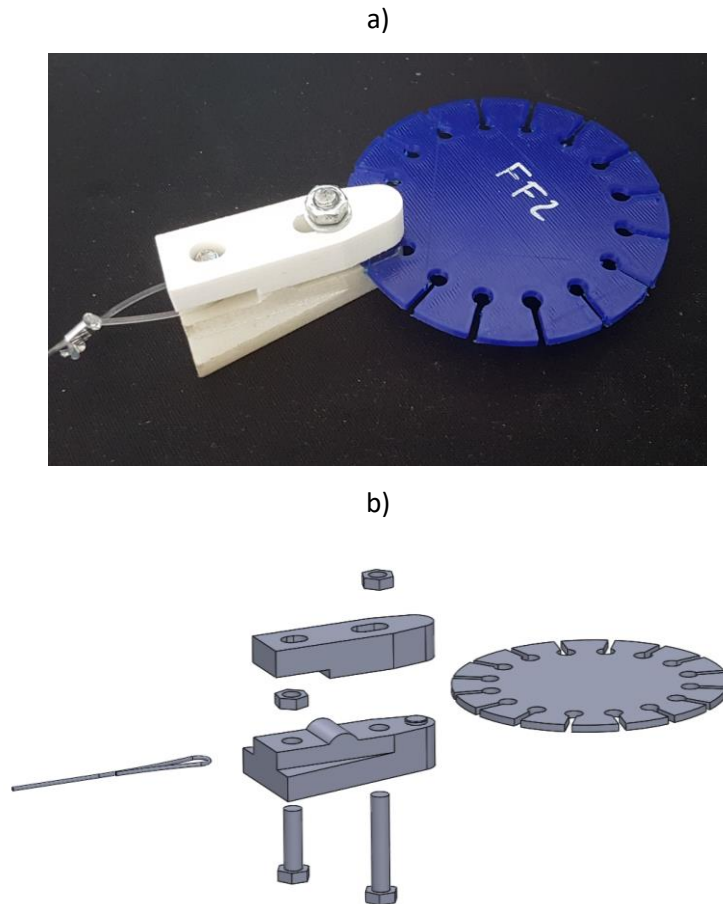


Figure 3.7. One of the 16 clamping sub-assemblies from the developed equi-biaxial jig. An upper clamping jaw pivots against a radiused feature on a lower clamping jaw to provide clamping force to the test sample. This force is controlled by adjusting the torque of a clamping bolt. The uniaxial test machine load is transferred through a wire to the lower clamping jaw via another bolt. a) sub-assembly, b) exploded CAD view

Planar tension

Planar tension specimens in the literature follow the same design and testing methodology [186, 187]. A rectangular strip of material is prepared, and metal backing plates are adhered to either side of the test specimen to inhibit lateral contraction and slippage from the grips. This approach introduces a source of error in the form of an adhesive bond. The large-strain deformation that occurs when testing elastomers results in typical adhesives (e.g. cyanoacrylate) failing due to their brittle nature. Therefore, flexible adhesives are frequently used (e.g. silicone-based). These can maintain a bond during testing but deform under loading due to their flexibility. This deformation introduces a potential source of error, as planar tension testing requires the prevention of any lateral movement.

As the test specimens were additively manufactured (AM), there was scope for a 3D specimen. Therefore, functionality was designed into the planar specimens to reduce

deformation at the grips. The gripping region of the planar specimen was thickened, and a slot was designed down its length (Figure 3.8). A set of inserts were then designed to mirror this profile, interfering with the specimen when clamped together. A two-stage compression was achieved, by increasing the level of interference along the length of the slot, to minimise lateral expansion. The reduced compression over the rest of the gripping area ensured the specimen was in full contact with the inserts. Compression of the gripping region had the potential to introduce stress-concentrations to the gauge region. Therefore, a radiused profile was incorporated from the gripping region to the gauge region, as can be seen in Figure 3.8a.

The well-established 10:1 width to height ratio [188] was adopted for the gauge area, which was 1mm thick. This new specimen is shown in Figure 3.8, and an annotated photograph showing the test jig is presented in Figure 3.9.

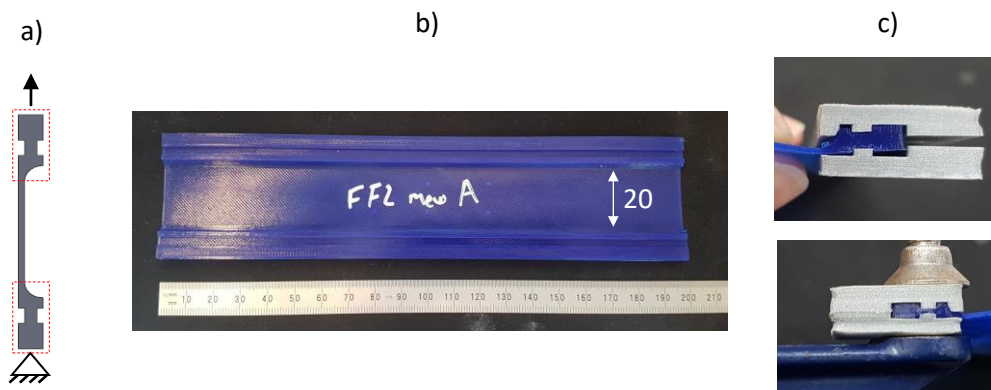


Figure 3.8: Novel planar tension specimen, a) side profile highlighting ridges and added geometry, b) dimensions (mm), n.b. gauge thickness was 1 mm, c) demonstration of clamping induced by inserts

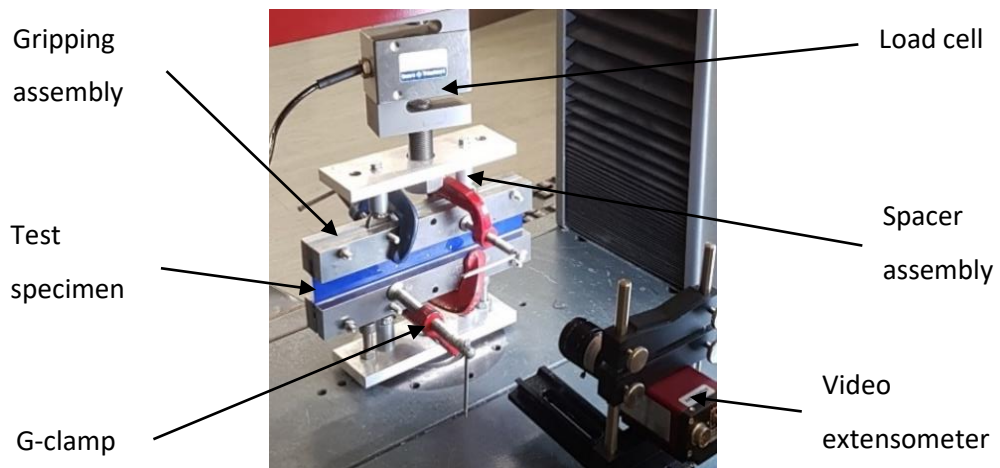


Figure 3.9. The developed planar jig mounted within a uniaxial test machine. Aluminium loading plates are bolted to the test machine and the load cell. These plates transfer the load to the test sample via two clamping assemblies, which are located using a series of bolts.

The jig was attached to the uniaxial test machine via two steel load spreading plates. The upper plate interfaced with the load cell via a single bolt, while the lower plate bolted directly onto the bed of the test machine (Figure 3.10).

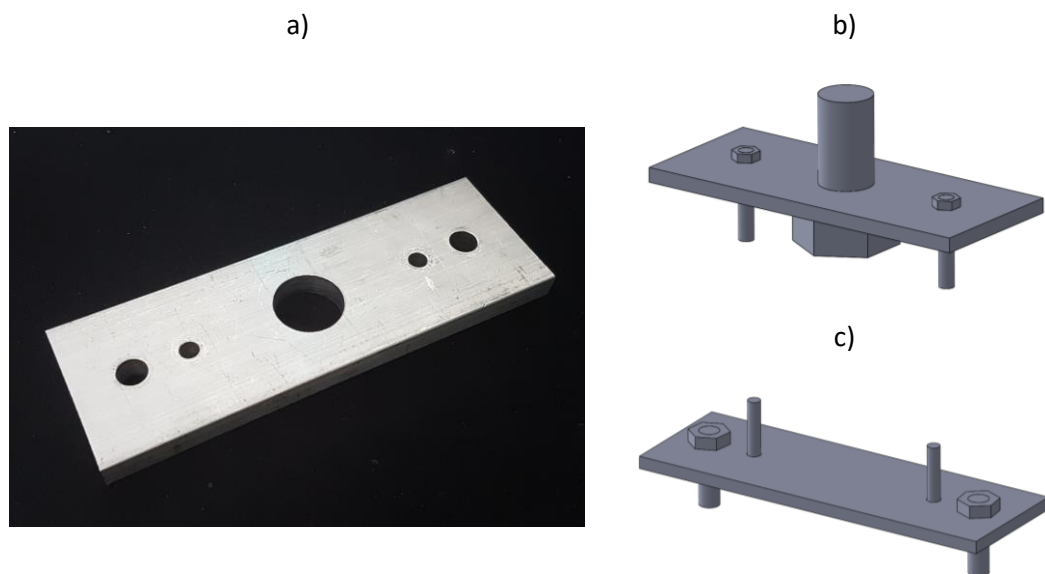


Figure 3.10. The loading plate sub-assemblies from developed planar tension jig, a) manufactured loading plate, with multiple holes allowing them to be used as an upper or lower plate, b) upper plate configuration, attaching to the load cell through a single large bolt and the test specimen clamping subassembly via two bolts, c) lower plate configuration, attaching to the test machine via two bolts and to the clamping sub-assembly via two opposing bolts.

These load plates were attached to each gripping assembly using a screw and spacer system, with the cylindrical spacers manufactured from PLA. These spacers ensured that the upper and lower portions of each gripping assembly remained parallel to one another and perpendicular to the loading direction. The spacer assembly is shown in Figure 3.11.

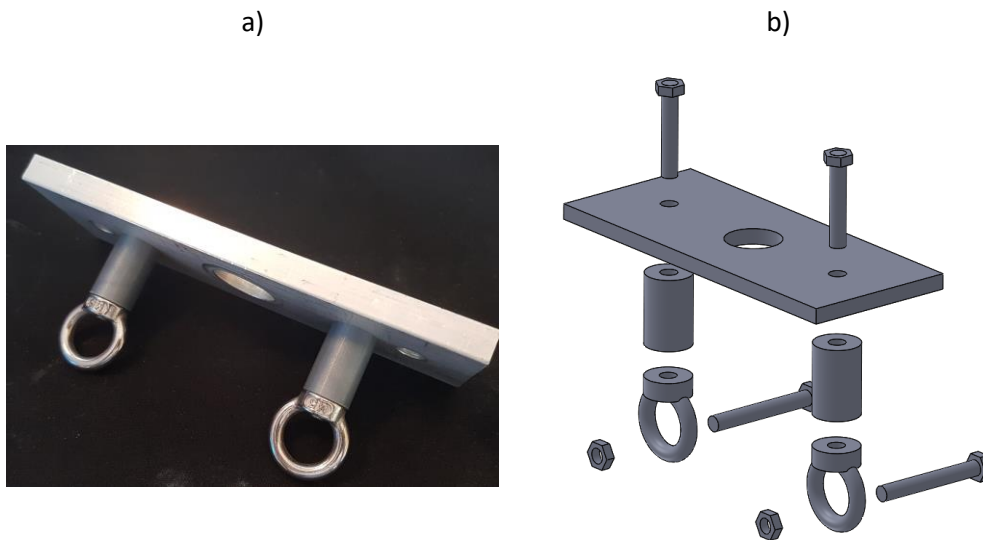


Figure 3.11. One of the spacer sub-assemblies in the developed planar jig. Two bolts pass through a loading plate into separate eyelets. The eyelets are separated from the loading plate by two identical spacers, ensuring the eyelets are parallel to the loading plate, a) sub-assembly, b) exploded CAD view

The spacer assembly (Figure 3.11) interfaced with the gripping assembly via a steel eyelet. Each gripping assembly consisted of a set of PLA inserts, which interfaced with the test specimen. Two G-clamps were then used to provide gripping force, via a set of hardened steel bars. A series of screws were inserted through the gripping assemblies, to provide alignment and transfer loading from the spacer assembly. The resultant assembly is shown in Figure 3.12.

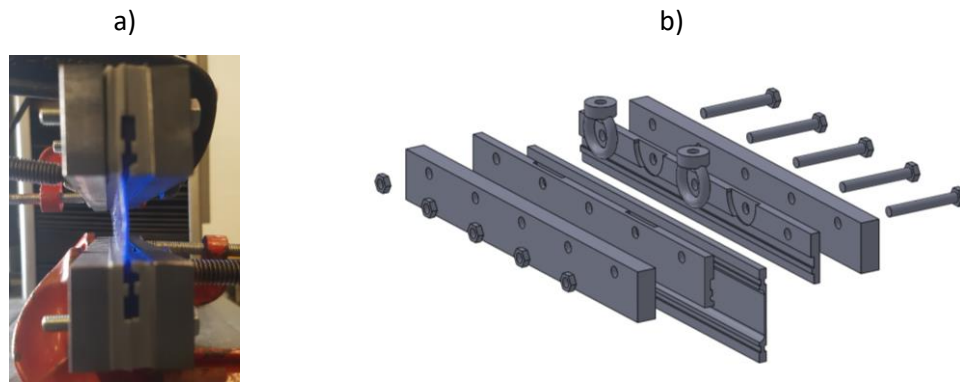


Figure 3.12. Half of the clamping sub-assembly from the developed planar jig. Two inserts interface with the test sample, with backing steel bars providing distributed loading over the inserts., a) sub-assembly, b) exploded CAD view

3.2.2.2 Test procedure

Following the creation of these testing jigs, the procedure for mechanical characterisation testing was developed. Based on section 4.2.1, specimens were tested to a nominal strain of 0.5. Five separate specimens were tested for each strain state to ensure repeatability of the collected data.

Uniaxial tensile testing was performed following ISO 37 [129], with a crosshead speed of 100 mm/min. Test specimens were designed and fabricated as per the type 1 dumbbell [129], as shown in Figure 3.13.

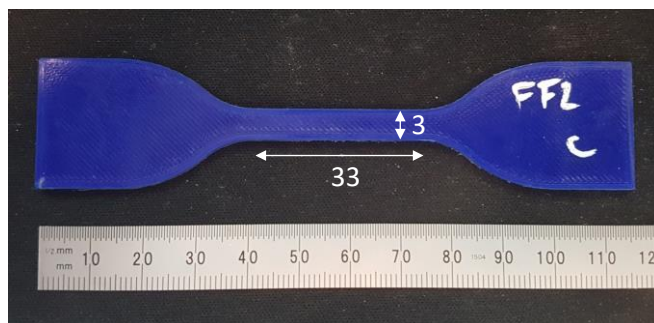


Figure 3.13. Additively manufactured NF, ISO 37 Type 1, uniaxial dumbbell specimen [129]; mm, gauge thickness = 2mm

Following an established protocol [137], these dumbbells were also used to perform uniaxial stress-relaxation tests, to collect rate-dependent data. Loading was performed at maximum available crosshead speed (600 mm/min), to a strain of 0.5, and followed by a relaxation period of 100 seconds.

As all stress states should be collected at the same strain rate, the uniaxial machine crosshead speed for the equi-biaxial and planar tension jigs was set to that of the standardised uniaxial tensile test (100 mm/min).

The manufacturing orientation of the characterisation specimens, relative to the machine bed, can be seen in Figure 3.14.

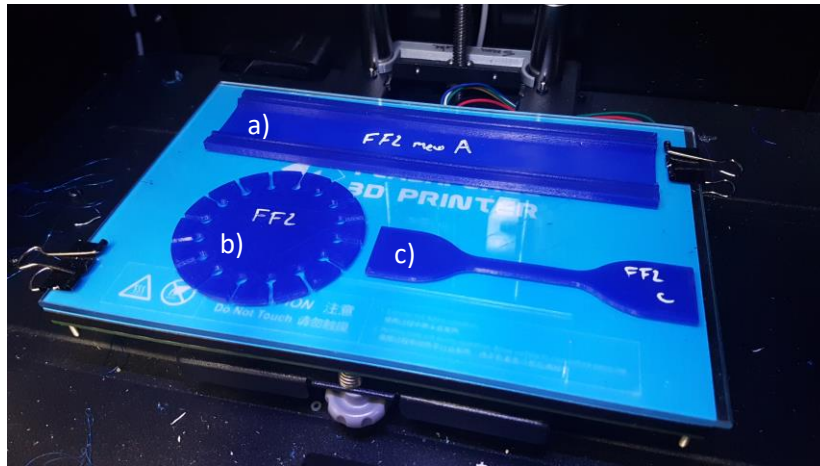


Figure 3.14. The orientation of each test sample on the FFF build platform when manufactured. a) Planar, b) Equi-biaxial, c) Uniaxial

3.2.3 Material modelling

Before computational analysis of a cellular structure can occur, a material model must be defined for the material from which it is constructed. ABAQUS was used to perform HE curve-fitting of the data collected in section 4.2.2.1, with the assumption of incompressibility (i.e. Poisson's ratio = 0.49995, as this is the maximum allowable in ABAQUS). The linear viscoelastic component of the material model was defined using normalised stress relaxation data, and a curve-fitting procedure was used to fit a Prony series (with a minimum allowable root-mean-square error of 0.001).

The HE material models investigated during this curve-fitting were those available by default in ABAQUS. This approach was taken, as the material models available in ABAQUS are frequently accessible in other commercial solvers (e.g. ANSYS), making this work more transferrable. These HE material models were analysed based on their correlation and general agreement to the experimental data, as well as their ability to predict compressive behaviour. This evidence-based approach was followed as material models can be mathematically stable while exhibiting unrealistic behaviour.

3.2.3.1 Validation

The honeycomb component used to optimise the processing parameters was again adopted here to validate the proposed material model (edge length = 5.8 mm, height = 10 mm, wall thickness = 0.4 mm). Two, 3 mm thick solid sections were designed onto the upper and lower surfaces of the honeycomb, to achieve well-defined boundary conditions. Exhaust channels (1 mm diameter) were designed into the solid lower section, enabling the release of air trapped within the honeycomb cavities during quasi-static and dynamic testing. This design is shown in Figure 3.15a, with loading performed out-of-plane, as indicated in Figure 3.15b.

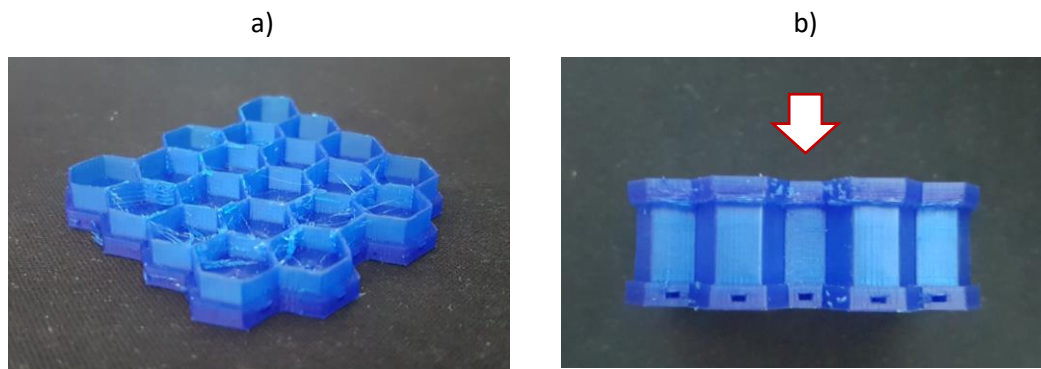


Figure 3.15. Design of additively manufactured honeycomb component used during validation testing, a) sectioned view, b) side view indicating load direction

Mechanical testing

Five separate honeycomb components were used for both dynamic and quasi-static mechanical testing.

The honeycomb component was quasi-statically compressed to densification at 100 mm/min. The solid sections were adhered to the compression platens using industrial-strength adhesive tape (Tesa 64621).

Dynamic testing of the honeycomb was investigated using a 3.53 kg impactor, at a velocity of 1.4 m/s. This velocity ensured the honeycomb compressed past the point of densification. The lower section of the honeycomb was adhered to the anvil, and the upper section was adhered to a sheet of sandpaper. Another sheet of sandpaper was adhered to the impactor, creating a sandpaper-sandpaper contact during the impact event.

Simulation

During both quasi-static and dynamic simulation, the honeycomb component was placed between two flat rigid surfaces. The lower surface was fixed in space and tied to the lower section of the honeycomb. A frictionless global contact was defined in both simulations, to prevent self-penetration of the honeycomb component.

For quasi-static compression, the upper surface was tied to the upper section of the honeycomb and was deflected 6 mm towards the lower surface, over 1 second. The viscoelastic component of the material model was suppressed, to allow a mass scaling of 20 to be implemented, reducing simulation time

For dynamic compression, the upper plate was assigned a 3.53 kg point mass and an initial velocity of 1.4 m/s towards the lower plate. A sliding frictional coefficient (CoF) of 1 was then defined between the upper section of the honeycomb and the upper plate. This value was selected as it prevented slippage at this boundary, making it representative of the sandpaper-sandpaper boundary used in mechanical experimentation.

As identified in section 4.2.3.3, when manufactured, the honeycomb component's average wall thickness grew from 0.4 mm to 0.45 mm. This increased thickness was used to update the honeycomb CAD wall thickness and also to define the size of the hex-dominated mesh. The 3 mm upper and lower sections of the honeycomb were partitioned and given an edge seed size of 0.72 mm (ABAQUS default), to reduce computational costs.

3.3 Generation of a novel scalable design tool for the selection of initial SP configurations

This section describes the approach to developing the novel design tool used to select an initial SP configuration. A method for investigating different boundary conditions, to ensure the diagram could be applied to the variable geometry of the human head, was developed. Additionally, a novel method to scale the resultant diagram to a different base material is described.

The SP structure is constrained by the mathematical surface that defines it. However, there are still several features of the structure that can be varied to investigate performance. An association between these features was pursued to reduce the number of floating variables. As cellular structures are defined by their unit cells, a link between the wall thickness (t) and unit cell length (l) is proposed. This relationship is subsequently referred

to as the $t:l$ ratio. The $t:l$ ratio is unitless; however, for both simulation and physical experimentation, discrete values for t and l are required to realise structures. Therefore, an arbitrary unit cell length of 10mm, and thicknesses of 0.5 mm, 1 mm, and 1.5 mm, were selected. These variables equate to $t:l$ ratios of 0.05:1, 0.1:1 and 0.15:1.

Transient dynamic analysis was used, due to the nature of the experimentation and as large deformations occurred. Simulations in this section were all displacement driven, to ensure a constant speed. For each simulation, a unit cell(s) was located between an upper, and lower, analytically rigid plate. The lower plate was fixed in place, and the displacement-time ramp input was used to drive the upper plate down at a constant speed. In the same manner as section 3.2.3.1, the viscoelastic component of the material model was suppressed for quasi-static simulations in this section. A time step of 0.01 seconds was used for all quasi-static simulations.

Control of the speed was achieved by varying the duration of the simulation time step (e.g. for a 25 mm tall unit cell(s), a 20 mm displacement over a 0.00267 second time step results in a speed of 7.5 m/s, or a strain rate of 300 /s). A frictionless global contact was defined to prevent self-penetration of the SP structure. Therefore, if no additional contact constraints are specified, this frictionless global contact defines the interaction properties for the whole simulation.

All quasi-static and dynamic mechanical experimentation was performed using the same equipment as in section 3.2. The results of dynamic mechanical testing are collected as an acceleration-time history by the accelerometer. However, to evaluate the success of the simulation, the stress-strain response of the structure was required. The acceleration-time curves can easily be converted to force-time curves using Newton's second law of motion. To calculate a displacement-time history the acceleration-time trace was double-integrated.

3.3.1 Developing a meshing strategy to ensure accurate and efficient simulation

3.3.1.1 *General simulation parameters*

Shell elements are preferred over solid continuum elements when undertaking computational analysis, due to their reduced complexity and consequently increased computational efficiency. However, the complexity and self-interaction in cellular structures result in shell elements poorly predicting compressive behaviour (Figure 4.22 in [189], Appendix I).

Therefore, to model the cellular structures in this work, a continuum element mesh was implemented. Quadratic elements were selected, as linear elements result in errors due to their increased stiffness [190]. Where applicable, to reduce the chance of artificial strains being generated, enhanced hourglass control was implemented.

Hexagonal elements are considered the most efficient solid continuum elements. However, when meshing complex 3D geometries (such as SP), extensive manual partitioning is required when using hexagonal elements. While sectioning enables their use, as complexity and unit cell quantities increase, manual sectioning becomes increasingly time-consuming. Therefore, a tetrahedral meshing strategy was adopted to automatically mesh the whole cellular structure, ensuring the number of operations was manageable.

To ensure the quasi-static simulations could be achieved in a manageable time, scaling was used to reduce their runtime. An undesirable result of time and mass scaling, which should be monitored for quasi-static simulation, is the artificial introduction of kinetic energy (KE) [191]. This KE can lead to erroneous results if it is above 5-10% [192], and therefore quasi-static simulations were monitored to ensure KE was below this range.

While careful monitoring can enable the use of time and mass scaling in quasi-static simulation, it is not appropriate for dynamic events. If an object is involved in a dynamic event, it will have a non-negligible KE. The use of mass scaling would artificially increase this kinetic energy, and the use of time scaling would also affect the KE by artificially increasing the impact speed. Therefore, time and mass scaling were not implemented during the simulation of dynamic events.

For the simulation of complex structures, complete elimination of all artificial energy is computationally expensive, and in many cases not possible as these energies help balance the simulation. Therefore, artificial energies must also be assessed when analysing simulation results, with acceptable values typically being in the realm of 1-2% [192]. Throughout this work, artificial energies were monitored.

3.3.1.2 Mesh sensitivity analysis

Reducing mesh size has positive and negative benefits. A downside of smaller mesh size is the increase to element count, resulting in higher computational expense. However, an increase in element count reduces the tessellation of a simulated component, leading to a potential increase to accuracy. Therefore, a mesh sensitivity study is undertaken to ensure a balance between accuracy and efficiency.

Mesh sensitivity studies are inherently linked to the geometry on which they are undertaken. Consequently, any change in geometry requires a new study. Therefore, to allow the application of a mesh sensitivity study to all potential SP configurations, a direct relation to the SP structure's geometry is required.

Mesh size is commonly linked to the shortest edge length, as a mesh seed that exceeds the shortest edge length can fail to reproduce smaller features. For the SP structure, the shortest edge length was frequently its wall thickness (t), so t was selected as the linked geometry. While this approach followed the aforementioned link to shortest edge length, it still suffers from being linked to a single dimension. Therefore, two variants of the SP structure with the same thickness, but differing unit cell sizes, would require different mesh sizes (due to changing internal radii of the SP unit cell). To account for this, a novel approach that links mesh size, to a scaling variable, is proposed. This scaling link allows an appropriate mesh to be selected for an SP structure regardless of unit cell size and wall thickness.

The relationship linking t to the rest of the SP structure is defined in section 3.3, as the $t:l$ ratio. Three $t:l$ ratios of 0.05:1, 0.1:1, and 0.15:1 were explored (where $l = 10$ mm). For each ratio, six different mesh sizes were simulated and analysed:

- 1) the ABAQUS recommended mesh size
- 2) 50% of t
- 3) 75% of t
- 4) 100% of t
- 5) 150% of t
- 6) 200% of t

The ABAQUS default mesh size was included as it is commonly adopted in place of a mesh sensitivity study. A minimum of two elements across wall thickness is widely associated with accurate resolution of bending stresses. Therefore, as discussed in section 4.3.1.1, 50% of t was investigated as it ensured this number of elements over wall thickness occurred in all the SP unit cells investigated (Figure 3.16a). The complexity of the SP unit cell results in extreme computational expense when patterned in an array. Therefore, in addition to the aforementioned smaller mesh sizes, increased mesh size was also investigated (e.g. 200% of t – Figure 3.16c). By increasing the mesh size, the number of elements per SP unit cell can be decreased, leading to a reduced computational expense.

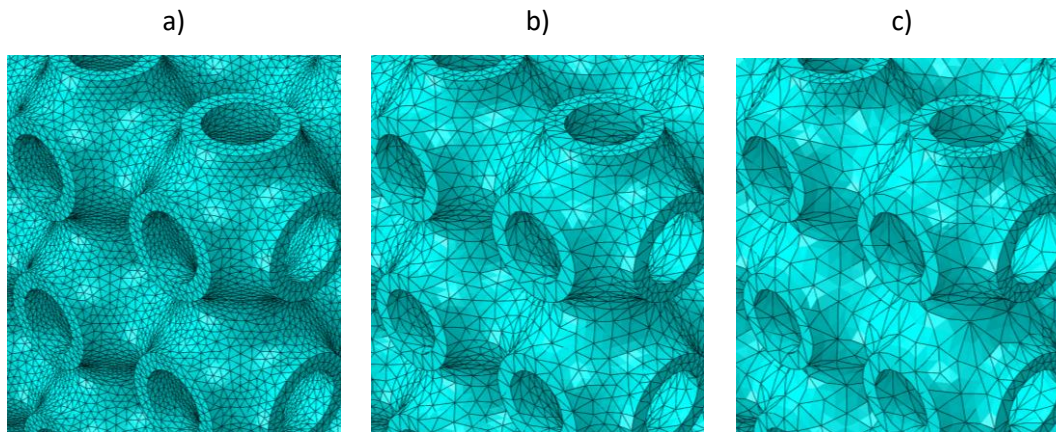


Figure 3.16. Meshing generated on an SP structure, with a 3*3*3 unit cell arrangement and a 1 mm wall thickness (t), at, a) 50% of t , b) 100% of t , c) 200% of t

The energy balance, stress, strain, and duration were recorded for each simulation. As computational power varies between users, durations were normalised for each $t:l$ ratio study. As an example, for the $t:l$ ratio of 0.1:1, option 1 had the longest duration. Therefore the durations of options 2 – 6 were normalised by that of option 1.

3.3.1.3 Validation of meshing strategy and material model

Validation was undertaken to ensure the proposed scaled mesh size resulted in simulations that were representative of real-life response. As 35 mm was identified as the average motorcycle helmet liner thickness (section 2.1.1.1), a 35*35*35 mm SP pad was investigated. A 3*3*3 unit cell configuration, with a wall thickness of 1.5 mm, was selected. This configuration was chosen as it enabled dynamic testing without resulting in excessive densification, which would risk damage to experimental apparatus (e.g. accelerometer).

Four NF SP pads were produced to this configuration (Figure 3.17), and their wall thicknesses were measured using Vernier callipers. The CAD model wall thickness was then updated to the average wall thickness of the manufactured pads. This alteration was undertaken to reduce dimensional inaccuracy between mechanical and simulated experimentation.

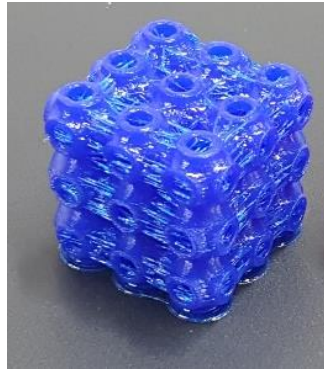


Figure 3.17. A NinjaFlex TPU SP structure pad, additively manufactured for mechanical testing validation. Stringing is visually apparent, where excess material oozes from the nozzle as it paths between printing regions.

Mechanical quasi-static and dynamic testing was undertaken, with two of the four pads being used for each type of test. For dynamic testing, SP pads were placed on a flat rigid anvil. A guided drop mass, with a flat impactor, was then released to compress the pads. The minimum drop mass (3.65 kg) was used, with a test speed of 1.7 m/s, to allow full densification of the pad. Quasi-static testing was performed by individually placing the SP pads between two flat platens, which were then compressed at a crosshead speed of 100 mm/min. To represent a frictionless boundary condition, for both quasi-static and dynamic experimentation silicone grease was used to lubricate the upper and lower surfaces, which contacted the SP pads.

3.3.2 Investigating the effect of varying constraints on the SP structure

3.3.2.1 Ensuring geometric scalability

A common concern when investigating cellular structures is the feasibility of exploring a set number of unit cells, with the assumption they will be representative of a more extensive configuration. While it has been shown that scalability of these structures under compression is feasible [114, 193, 194], there remains the scope for a new cellular structure to behave differently. Therefore, an approach to investigate this was developed.

Configurations of 1*1*1, 2*2*2, 3*3*3, and 5*5*5 unit cells were simulated. A constant $t:l$ ratio of 0.1:1 was used for all configurations (where $l = 10$ mm). The stress-strain behaviour of these configurations was then compared to assess the effects of increasing the number of unit cells.

3.3.2.2 Establishing boundary condition sensitivity

How an object interacts with the outside world can notably affect the outcomes of mechanical events. Of these interactions, boundary conditions are significant in mechanical

problems. Excluding loadings, these conditions can be separated into contact formation (e.g. friction), and geometric interactions (e.g. curved). The process of investigating these conditions was undertaken on 3*3*3 SP configurations, with t:l ratios of 0.1:1 (where l = 10 mm).

When considering contact interactions, the extremes can be defined as fixed, where surfaces cannot slide past one another, and frictionless, where no restriction exists on sliding. Simulations with fixed and frictionless boundary conditions were undertaken to explore this.

As this research focusses on helmets, a geometrical investigation is inherently linked to the human head. The 575 headform (Figure 3.18) was selected to explore geometric conditions. By measuring the headform at each impact location (defined in UNECE 22.05 [27]), and excluding the flatter side of the skull, the radius ranged from ~75 – 130 mm. Note, this excludes localised radii such as cheekbone protrusions.

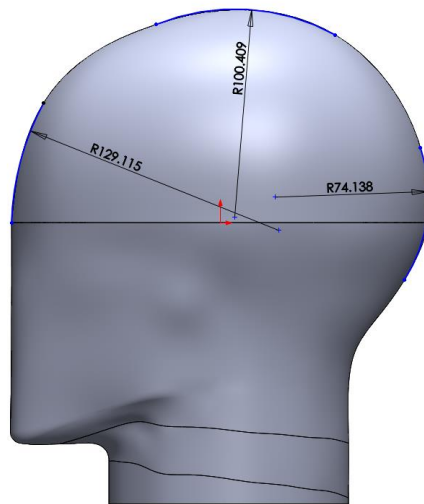


Figure 3.18. The changing radius of the EN960 575 [84] headform, used to inform the curvature with which the helmet liner interacts

The smallest radius for the 575 headform was 75 mm, and the largest radius was the side of the skull, which is representative of a flat surface. Simulated quasi-static displacement of an SP structure was undertaken using these two geometric extremes. A hemispherical surface (with a radius of 75 mm), was used to deform a cellular structure against an opposing fixed flat surface representing the anvil.

The 75 mm hemispherical surface was also used to investigate the combined effect of geometric and contact interactions. A fixed boundary was applied between the flat lower surface and the SP structure. As it is not feasible to use a fixed boundary for the curved surface (due to it progressively engaging with the SP structure), a CoF of 1 was applied between the SP and 75mm curved upper surface. This value was selected as no observable slippage occurred between the impactor and SP structure during compression. This lack of slippage resulted in a constraint that is representative of a non-sliding (or fixed) boundary.

3.3.3 Approach to generate NF SP energy absorption diagram

By developing a validated rate-dependant material model (section 3.2), energy absorption diagrams for cellular structures can be generated using computational simulation alone. By incorporating the investigatory work, undertaken in sections 3.3.1 and 3.3.2.1, the generated diagrams are also scalable to different sized unit cells. This novel combination of scalability and computation generation allows the generated energy absorption diagrams to be applied with similar flexibility to conventional foam energy absorption diagrams.

The SP structure's energy absorption diagram was generated by computationally exploring the SP structure, under quasi-static and dynamic loading. The impact speed prescribed by UNECE 22.05 [27], of 7.5 m/s, was the focus of this work. However, to populate the energy absorption diagram, the SP structure was also investigated at higher and lower speeds. Separate 3*3*3 SP configurations, with t:l ratios of 0.05:1, 0.1:1, and 0.15:1, were simulated at the following speeds (where l = 10 mm):

- 0.00167 m/s (0.0667 /s)– the speed of quasi-static testing in this work.
- 0.5 m/s (20 /s) – an example between quasi-static and 7.5 m/s.
- 2.5 m/s (100 /s) – another example between quasi-static and 7.5 m/s.
- 7.5 m/s (300 /s) – representative of, the UNECE 22.05 impact test speed.
- 13.4 m/s (536 /s) – equivalent to 30 mph, the residential speed limit in the UK.
- 20m/s (804.8 /s) – equivalent to 45 mph, an example between 30 and 70 mph.
- 31.3 m/s (1252 /s) – equivalent to 70 mph, the dual carriageway speed limit in the UK.
- Additionally, to better define the UNECE 22.05 test speed (7.5 m/s), 4 further simulations were undertaken at intermediate t:l ratios of: 0.067:1, 0.083:1, 0.117:1 and 0.133:1 (where l = 10 mm).

The stress-strain curves generated by these simulations were used to identify the energy absorbed by the structure per unit volume. σ_p and W were then normalised by the NF

instantaneous tensile modulus of 21 MPa (from section 4.2.2.1). The resultant normalised curves were plotted against one another and used to generate the NF SP energy absorption diagram, with lines of constant speed and thickness.

3.3.4 Scaling the NF SP energy absorption diagram to alternate elastomers

While the approach described in section 3.3.3 can produce geometrically scalable energy absorption diagrams, the resultant diagrams are limited to the material from which they were generated. Therefore, a novel method scaling these diagrams to different materials, without having to repeat simulations, was developed and validated.

It was desired that the NF SP energy absorption diagram, and associated material model used to generate it, be scalable to other base materials without going through a full characterisation process. As it is well-known that elastic materials have a non-linear response, and can have varying viscoelastic behaviours, consideration of moduli values (e.g. Young's modulus) from a datasheet is not adequate. Therefore, a process for changing base elastomers was developed:

1. A standardised uniaxial tensile test was undertaken on the new base material, and its response was compared to the previous base material's uniaxial tensile response. A scaling factor was then used to shift the new material curve to the original base material curve. This scaling was driven by correlation over the application strain range (e.g. $SP = \pm 0.5$, from section 4.2.1).
2. The identified factor was used to scale the original energy-absorption diagram, resulting in an approximate energy diagram for the new base material (excluding changes in viscoelastic effects).
3. A stress-relaxation experiment was performed on the new base material, to identify the viscoelastic response of the new material.
4. The previous uniaxial, equi-biaxial and planar responses were then scaled by the factor identified in step 1. Using these scaled responses, and the new stress-relaxation response, curve-fitting of a new material model was undertaken to enable simulation of the new base material.

To apply the results of this process to an application, the scaled energy absorption diagram, from step 2, is used to identify an approximate configuration. The scaled material model is then used to fine-tune the approximate configuration to the desired application.

3.3.4.1 *Switching from NF to CH*

As covered in section 4.3.3.3, it was desired that a material with a higher E_s than NF be found. Cheetah (CH) was selected to meet this requirement, as its datasheet indicated an E_s approximately double that of NF [182, 195], which was identified as suitable for application in motorcycle helmets (section 4.3.4).

Following the procedure for scaling materials set out in section 3.3.4, a scaled energy absorption diagram was created for CH. Following this step, uniaxial and stress relaxation tests were undertaken, as set out in section 3.2.2.2.

The resultant material model was validated by following the procedure described in section 3.3.1.3. The same computational and experimental approach from section 3.3.1.3 was followed for quasi-static and dynamic compression of the CH pads, except for the increase of the dynamic test speed to 2.5 m/s, to ensure densification occurred.

3.4 Manufacture and analysis of a prototype SP filled motorcycle helmet

This section describes the approach to assess whether the aim “to improve motorcyclist head protection by exploiting the mechanical benefits of cellular structures and resilient materials” had been satisfied. A method of filling a helmet shell with the SP structure was developed to enable the manufacture of the prototype helmet. A novel computational approach of optimising the SP pads for the UNECE 22.05 impact was then developed, in addition to the validation approach for said optimisation.

3.4.1 Method to propagate cellular structures within a helmet

The liner generation strategy was driven by FFF manufacturability. SP configurations were manufactured directly on the build plate to ensure successful fabrication. This approach led to the requirement for a pad-based liner (like those used in American football).

A constant liner thickness of 35 mm was selected, constraining the overall height of the SP pads. This thickness was based on the average helmet liner thickness identified in section 2.1.1.1, and the minimum thickness of the liner from the helmet used during testing (Appendix V). An initial 3*3*3 unit cell configuration was selected, based on the results of section 4.3.2.1.

The 575 headform [84] was then used to explore how pads could be arranged around the head. Attempts were made to use complete cubic pads and where this was not possible the

pads were triangulated, to ensure complete coverage of the headform. The bounding geometries created by this process are shown in Figure 3.19, with their replacement by SP pads shown in Figure 3.20.

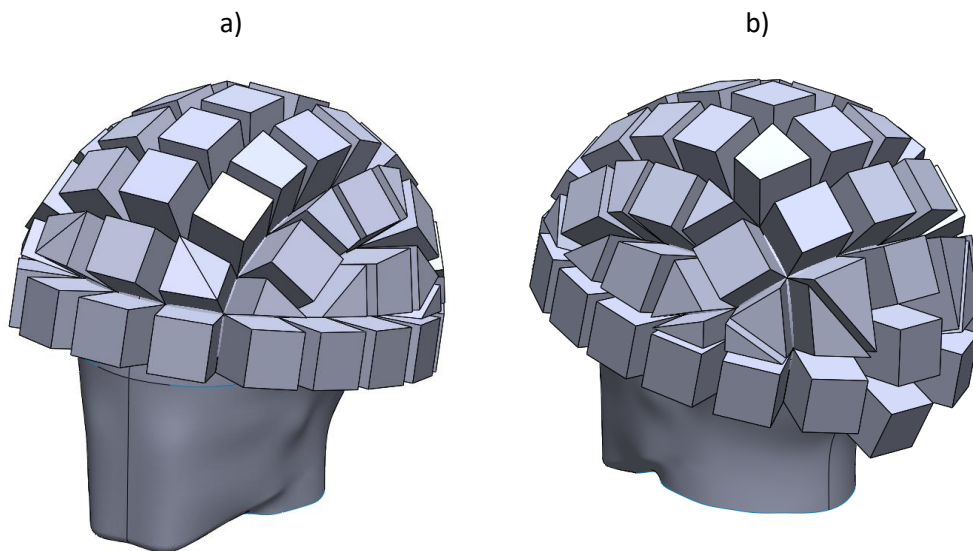


Figure 3.19. EN 960 Headform (575) with the virtual bounding regions, used to arrange the SP pads, illustrated, a) front view, b) rear view

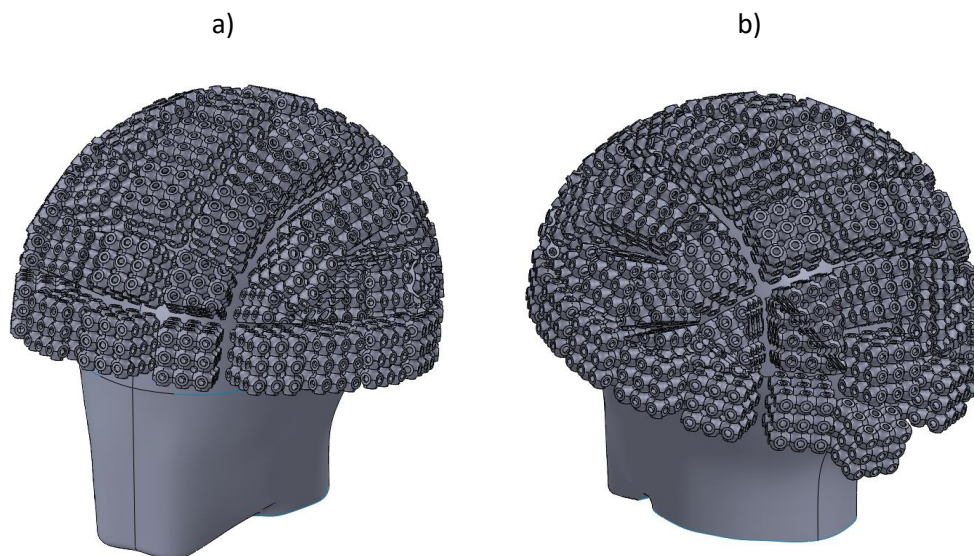


Figure 3.20. EN 960 Headform (575) with the virtual bounding regions (illustrated in Figure 3.19) replaced with SP pads cut to the size of those regions, a) front view, b) rear view

3.4.2 Computational optimisation of cellular structures

3.4.2.1 Selection of initial SP configuration from CH energy absorption diagram

Using the scaled CH energy absorption diagram, from section 4.3.4, initial configurations were selected for generation of a prototype SP liner. The performance constraints that defined the liner were the impact mitigation requirements of UNECE 22.05 [27].

UNECE 22.05 specifies an energy absorption test under freefall. However, this introduces the potential for secondary impacts at other locations. If notable secondary impacts occurred at untested locations, dissimilarities between simulated and mechanical responses could be introduced. Therefore, guidewires were used instead of a freefall condition to control this variable.

For each impact location, the performance requirements in section 2.2.3.2 were used to define bounding lines for σ_{\max} , and W_{\min} . These bounding lines were plotted on separate CH energy absorption diagrams (section 4.3.4) for each location. As discussed in section 2.2.2.2, to successfully mitigate an impact, a configuration must be above the W_{\min} line, and below the σ_{\max} line. The bounding area that satisfies these two requirements was highlighted in the diagrams, using a transparent orange box.

As the Head Injury Criterion (HIC) is influenced significantly by A_{\max} (section 2.2.3.1), the optimal configuration within the bounding area would mitigate all the incoming energy, while having the lowest possible σ_p . However, the shell inherently flexes, reducing the SP structure's ability to mitigate incoming energy. Additionally, the CH scaled diagram does not account for differences in viscoelastic behaviour between NF and CH. Therefore, the initially selected configuration was the one that laid between the σ_{\max} and W_{\min} boundaries, to account for these variables.

As the layer height of the Flashforge Creator Pro was 0.1mm, configuration wall thicknesses were defined to one decimal point. As an example, if a configuration with a t:l ratio of 0.1:1 lay at the σ_{\max} line, and a configuration with a t:l ratio of 0.15:1 lay at the W_{\min} line, an initial configuration would have a thickness of 1.3 mm if $l = 10$ mm.

3.4.2.2 Simulation of the complete helmet to optimise SP configuration

Simulation design

A simplified shell was simulated to enable load transmission from the impacting anvil to the liner pads. This shell was directly based on the pad locations, shown in Figure 3.19, and was generated as a triangulated surface (Figure 3.21).

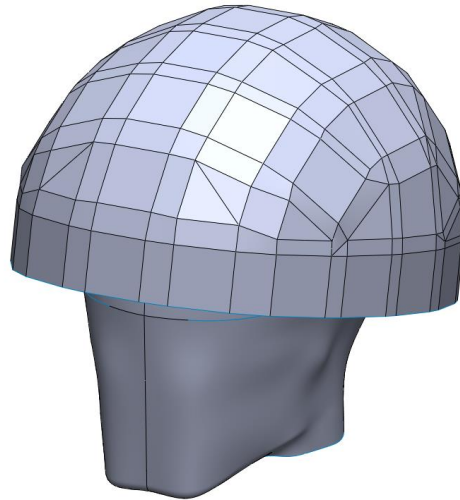


Figure 3.21. The triangulated helmet shell generated from the bounding regions shown in Figure 3.19, which are also used to arrange the SP pads

In addition to simplifying the complexity of the shell, reducing computational expense, this approach has the benefit of easing the digital assembly of pads and ensures no penetration occurs between the shell and the pads.

As the helmet shell was not involved in any self-interaction and consisted of many planar surfaces, a linear, quad-dominated, shell mesh was implemented. The ABAQUS default mesh size was used.

The helmet shell used in the physical prototype helmet was manufactured from 3 mm thick Acrylonitrile butadiene styrene (ABS) (Appendix V). Motorcycle helmet shells recorded in the literature also had an average thickness of 3 mm, and the primary material used to manufacture them was ABS (section 2.1.1.1). Additionally, as identified in section 2.1.1.1, a linear elastic material model can be used to model ABS helmet shells, with Young's modulus of 4 GPa, a density of 1200 kg/m^3 , and a Poisson's ratio of 0.37. Therefore, a 3mm thick section with these properties was applied to the simplified helmet shell.

The anvil was modelled as an analytically rigid plate, and the headform was meshed using a discrete rigid shell (using the ABAQUS default mesh seed size). The meshing strategy for the SP pads followed the same approach as in section 3.3.1.1.

The anvil was fixed in place, while the headform was restricted to only allow movement in the impact direction, representative of a guidewire restriction. The headform, helmet shell and included pads were all prescribed an initial velocity of 7.5 m/s in the direction of the impact. A global CoF of 1 was applied to the simulation, to prevent pads from slipping out

of place. A gravitational load was applied to the assembly, ensuring the simulation was representative of real-world testing.

Only the pads directly under each impact point were simulated, as pads opposite the impact point are not compressed during an impact event. As they are not compressed, they do not absorb any impact energy, only adding to the computational cost. The simulation assemblies for impact points B and R are shown in Figure 3.22.

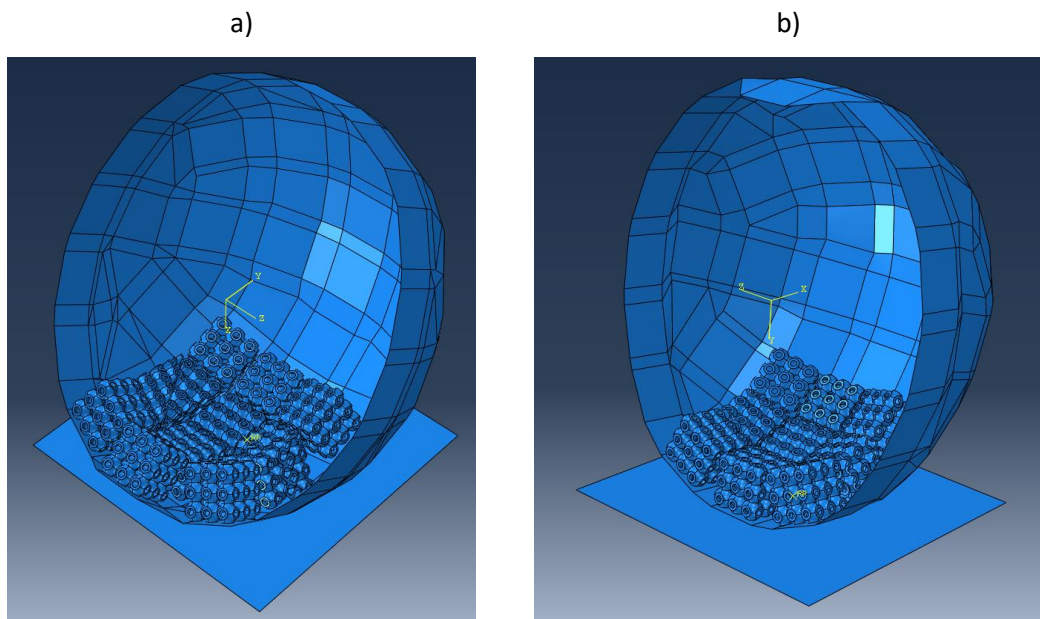


Figure 3.22. Assembly of the prototype SP helmet, used for computational analysis of the UNECE 22.05 impact at, a) point R, b) point B. Note, the 575 headform is hidden to allow viewing of the pad arrangements.

Optimisation approach

As discussed in section 3.4.2.1, the optimal SP configuration is the one that minimises the A_{\max} of the helmet. Peaks in A_{\max} can be linked to the densification of the liner, or the liner being too stiff and resulting in its underutilisation. Therefore, depending on the results of a simulation, reducing A_{\max} can be achieved in two ways: increasing wall thickness to increase the stiffness of the liner and prevent densification, or reducing wall thickness to reduce the liners stiffness and increase liner deformation to ensure effective use of the cellular structure.

Each impact location was assessed individually to identify whether an increase or decrease in wall thickness was required. First, a simulation containing the initial SP configuration (as per section 4.4.1.1) was run to assess its viability, and the resultant deformation-time pulse

was examined. If compression of the liner was >60%, densification was considered to have started, and the SP structure's wall thickness was increased to prevent it. This value was identified in section 4.3.3.1, where the SP structure densified at ~55 - 64%. However, if the liner was compressed <<60%, the SP structure was being used inefficiently, and its wall thickness was reduced to correct it. Due to the uncertainty introduced by simulation, only one 0.1 mm (as per the Creator Pro layer height) change was made to wall thickness.

Some of the pads that were compressed during an impact at point P (crown) were also active at impact points R (rear) and B (front), as shown in Figure 3.23. Therefore, before running any simulations at impact point P, simulations were run at point R and B to identify an optimal thickness for each location. The optimal overlapping pads, identified for points R and B, were then included in the simulation of point P as fixed configurations, alongside the pads being optimised.

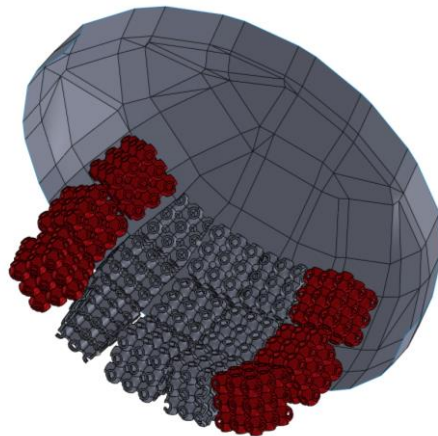


Figure 3.23. Assembly of the prototype SP helmet, used for computational analysis of the UNECE 22.05 impact at point P, with the overlapping pads from impact points B and R highlighted in red. Note, 575 headform and anvil are hidden, and the shell is sectioned to show the pads

3.4.3 Validation of the optimisation approach and evaluation of the prototype helmet's multi-impact performance

3.4.3.1 Manufacture of the SP liner

An existing helmet was selected, and its liner was replaced with SP pads. The BOX BX-1 helmet was selected as it was cost-effective, in addition to having passed UNECE 22.05. Measurement and reverse engineering, of the helmet, was undertaken to help inform the decisions made in section 3.4.3.1 (Appendix IV). In addition to the prototype helmet, with

the replacement SP liner, a separate unaltered BOX BX-1 helmet was also tested to establish its comparative performance.

The SP pads were manufactured using the optimal configurations identified in section 4.4.1.2, and the processing parameters identified in section 4.1.1.1. Due to the number of pads required for the liner they were manufactured in batches, with each impact point being manufactured in the same batch. After manufacture, loose material (stringing) was removed.

To ensure the pads remained in place during testing, they were connected using flexible Polytetrafluoroethylene (PTFE) tape. This tape allowed the consistent location of the pads relative to one another, and to the impact points. The connected pads were then inserted into the prototype helmet shell (Figure 3.24). The comfort liner was not reinserted into the prototype helmet, as it has little effect on impact mitigation (section 2.1.1). Additionally, excluding this liner eases access to the SP liner, for examination between impact events.



Figure 3.24 The additively manufactured CH SP pads (red), which form the helmet liner, a) on a representative headform, b) in place, inside the BOX BX-1 helmet shell

3.4.3.2 Mechanical experimentation

The unaltered BOX BX-1 and the BX-1 with replacement SP pads were then subjected to testing as per UNECE 22.05 [27]. A 1002 MAU 1006/CF/ALU (AD Engineering, Italy) monorail, shock absorption, drop tower was used, with data measured via an in-line 353/B17-1D (PCB, USA) accelerometer. An SC1 (Edgertronic, USA) high-speed camera was used to record the deformation patterns during dynamic testing.

Before testing, both helmets were placed onto a reference headform for marking of impact points. The fit of the helmet used for marking up is shown in Figure 3.25.

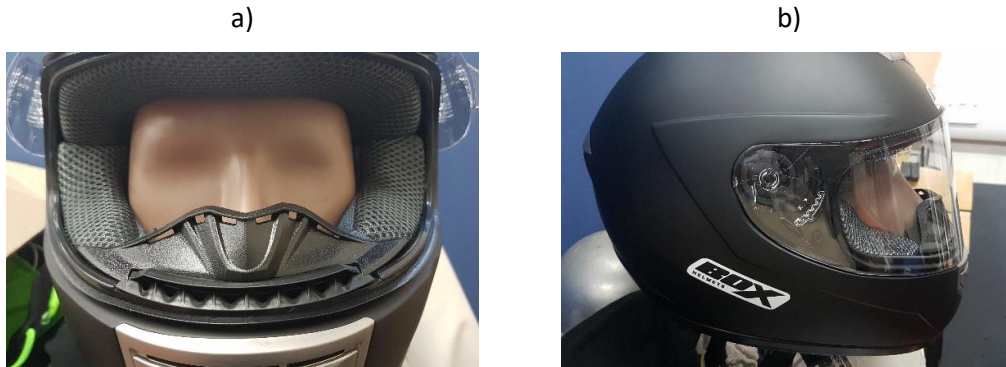


Figure 3.25. The fit of the BOX BX-1 helmet on a representative headform, a) front view, b) side view

After marking of the impact points the helmet was mounted on a 575 half headform, and the chin strap was tightened down. A half headform was used, as it allowed for mounting to a guidewire test rig. Due to the half headform, foam padding was used to provide spacing to tighten the chin strap.

Additionally, in the case of the SP replacement helmet, the consistent thickness liner resulted in looser fit between headform and helmet. Therefore, flexible PTFE tape was used to ensure the helmet did not rotate out of position before impact. The setup of point P, for the unaltered BOX BX-1 helmet, is shown in Figure 3.26.

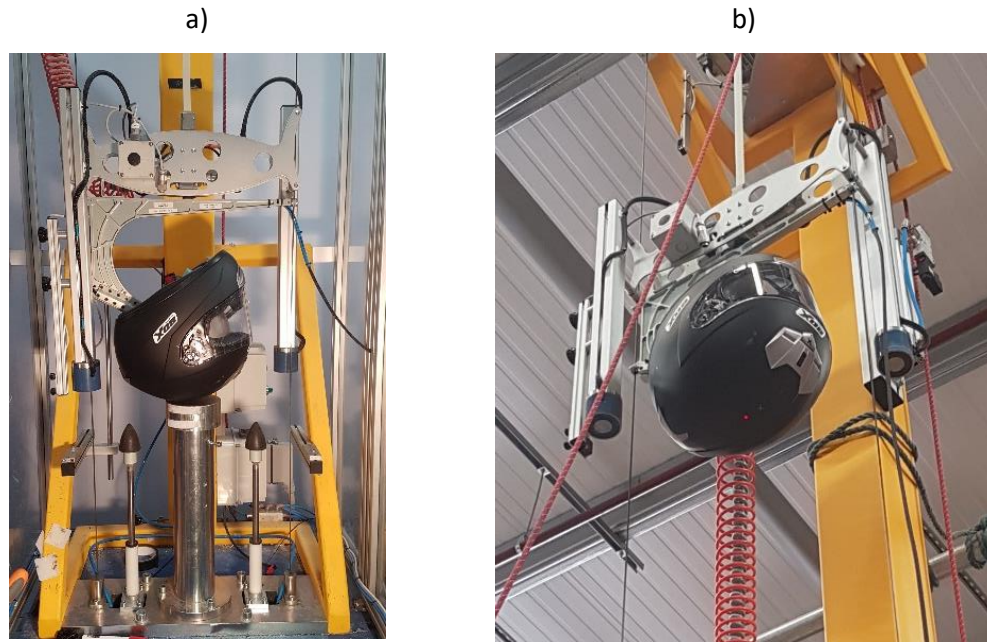


Figure 3.26. The impact drop tower, with the BOX BX-1 helmet mounted on a wire-guided headform, for an impact at Point P, a) experimental setup, b) helmet at 7.5 m/s drop height, with a red laser dot highlighting the helmet location relative to the centre of the anvil

In addition to the single impact specified by UNECE 22.05 [27], multi-impact testing was performed. As discussed in section 1, this work does not propose a solution capable of multi-collision performance; however, it aims to develop a solution capable of multi-impact performance in a single collision. Therefore, multi-impact was given preference over single impact during testing. The following impact procedure was followed for each helmet:

- 1) Point B (front)
- 2) Multi-impact at point B
- 3) Point R (rear)
- 4) Multi-impact at point R
- 5) Point X (side)
- 6) Point P (crown)

As can be seen in this testing regime, multi-impact testing was only performed at points B and R. This was due to crack propagation in the ABS shell that occurred during testing (Appendix VI). To ensure data could be collected from point P, before complete failure of the shell, multi-impacts were not performed at point X. Additionally, care was taken at point X to test on the side of the helmet where crack propagation was not visually observed. No further multi-impact testing was performed after completion of the above testing regime, due to the compromised shell leading to concern for testing equipment.

For the SP liner filled helmet, each impact point involved in multi-impacts underwent five further impacts, following the initial one. The intention behind a further five impacts was to demonstrate performance beyond the two impacts observed in several of the helmet testing standards (Table 2.2), while allowing for the lack of multi-impact performance of conventional helmet shells (as demonstrated by crack propagation in these experiments – Appendix VI)

During multi-impact testing of the unaltered BOX BX-1 helmet, very high accelerations were recorded during the second impact at point B (section 4.4.2.3). As a result of this, only two consecutive impacts were undertaken at points B and R, for the unaltered helmet. This decision was made to minimise risk to test equipment.

4 Results and Discussion

This section describes the experimental results. The objectives set out in section 1.1 were addressed as follows:

1. Optimise processing parameters to produce functional cellular structures

By optimising FFF processing parameters, high-density NF parts were achieved. This density was then proved using micro X-ray computed tomography (μ CT).

2. Establish a novel mechanical characterisation pathway

The internal strain range of a honeycomb and SP unit cell were identified computationally to inform characterisation testing. Developed equi-biaxial and planar tension jigs were shown to behave as intended, and full characterisation of NF was performed. A Mooney-Rivlin material model was found to define NF's response.

3. Generate a novel scalable design tool to select initial cellular configurations

The novel design tool was generated computationally for the SP structure. During the generation of the tool, the scalability of it to varying boundary condition was demonstrated. Additionally, the ability to scale this tool to different base materials was demonstrated.

4. Manufacture and analyse a prototype motorcycle helmet

The SP structure was computationally optimised for use in motorcycle helmets. A prototype helmet was then manufactured and experimentally tested. The results of this experimentation demonstrated the multi-impact performance of the SP structure.

4.1 Optimising Fused Filament Fabrication (FFF) processing parameters to produce functional elastomeric cellular structures

This section presents the results of the optimisation of the FFF processing parameters. It was undertaken to ensure any manufactured parts were of high functionality.

4.1.1 Investigation of processing parameters

After tuning the extrusion temperature, as per section 3.1.1, concentric and rectilinear infill patterns were investigated. While the concentric pattern inherently produces a closer

bonding between perimeter and infill, the central region where the infill pattern joins together formed a notable gap, as can be seen in Figure 4.1.

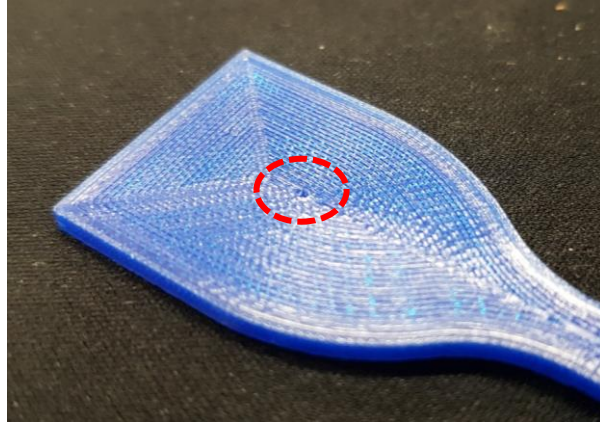


Figure 4.1 One end of a uniaxial dumbbell additively manufactured from NF TPU; with a seam defect, highlighted in red, where the concentric infill meets

Figure 4.1 highlights the worst example within the dumbbell specimen. However, less severe gaps were also introduced closer to the gauge area. While attempts were made to eliminate these gaps, they were not successful. These included increasing the temperature to lower viscosity and promote flow, as well as increasing the extrusion multiplier and extrudate overlap to deposit additional material. As no such issues occurred with rectilinear infill patterning it was adopted moving forward.

After selecting the rectilinear infill pattern, the extrusion multiplier was increased in 5% increments from a value of 1 (100%). The onset of scarring was observed at an extrusion multiplier of 1.45, as can be seen in Figure 4.2. Therefore, following the methodology set out in section 3.1.1, a multiplier of 1.4 was selected moving forward.

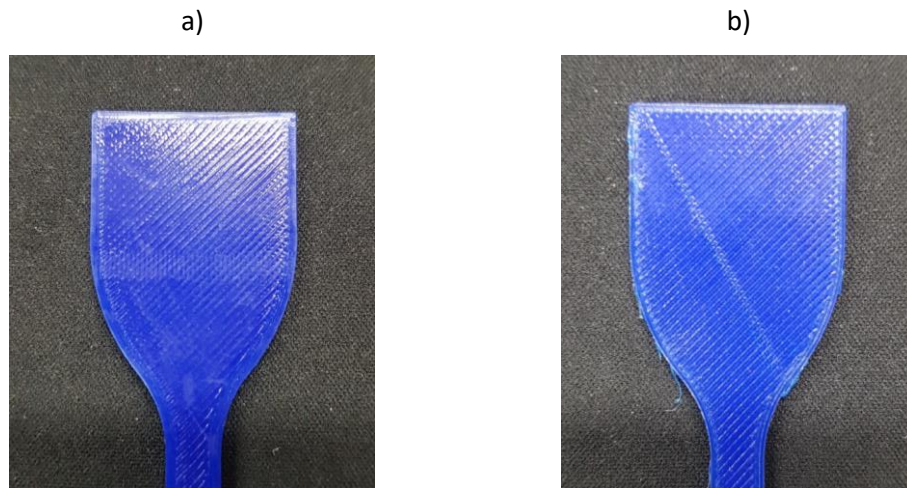


Figure 4.2 Uniaxial dumbbells additively manufactured using different extrusion multipliers a) 5% before the onset of scarring, b) onset of scarring, also note the raised ridges over the whole face area and partial distortion of the edge, at the top left of the image

4.1.1.1 Final printing parameters

The findings of section 4.1.1, and other printing parameters described in section 3.1.1, are summarised in Table 4.1. It should be noted that these values are specific to the FFF machine and accompanying hardware used in this research. For example, a minor alteration to the calibration of the thermocouples, which monitor extruder temperature, would result in a different extrusion temperature being specified.

Table 4.1. The FFF processing parameters and additional manufacturing features used to manufacture the components in this study

Nozzle Diameter	0.4 mm	Extrusion Multiplier	1.4
Printing speed	2000 mm/min	Layer Height	100 μ m
Bed Temperature	40 $^{\circ}$ C	Active cooling	Yes
Extruder Temperature	210 $^{\circ}$ C	Extruder	Flexion
Brim	5	Infill patterning	Rectilinear

4.1.2 Assessment of component porosity

The porosity of components manufactured using these optimised processing parameters was then examined. The cuboid used for this analysis can be seen in Figure 4.3.

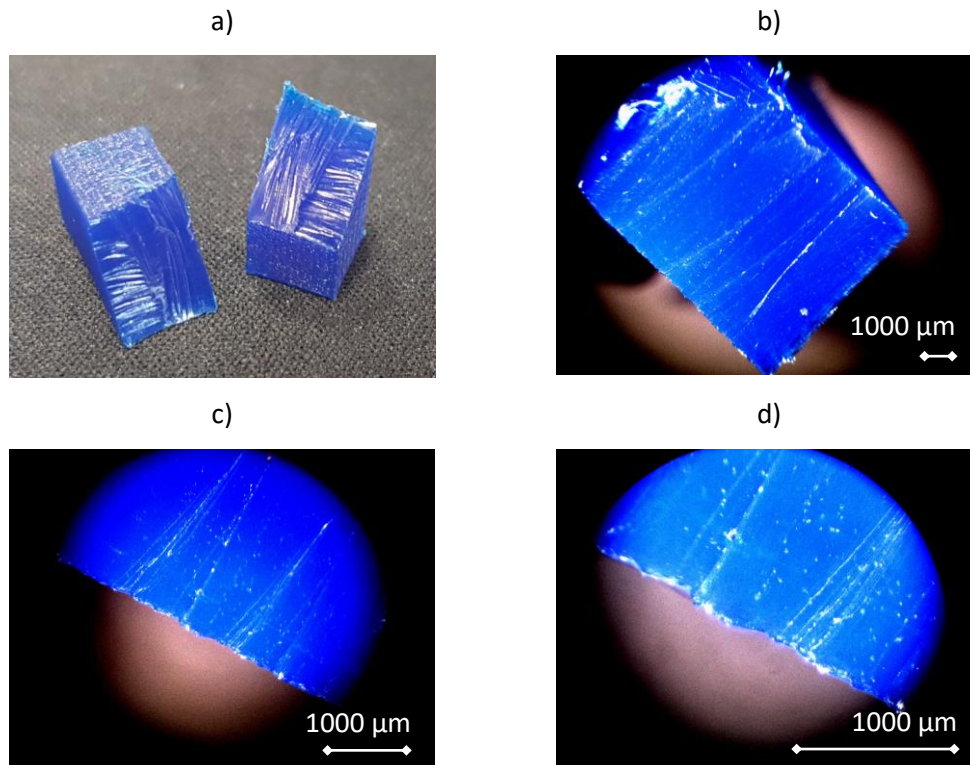


Figure 4.3. Optical microscopy of a section of the test cuboid geometry, visually demonstrating minimal porosity, a) photograph of sectioned cuboid, b) 0.7x zoom, c) 2x zoom, d) 4x zoom

Measuring the outer dimensions with a Vernier calliper, the X and Y dimensions had grown by 0.04 mm. Similarly, the X and Y dimensions of the dumbbell manufactured with this extrusion multiplier (section 4.1.1) also grew by 0.02 – 0.04 mm. This minor static growth is indicative that the optimisation process was successful, where additional material was deposited to fill voids between lines of the extrudate without altering the dimensions of the final component. Note, the striations and jagged lower edges observed in Figure 4.3 are due to the sectioning of the cuboid with a scalpel.

The rectilinear infill pattern can be observed on the upper surface of the cuboid, and individual layers can be observed in the outline extrudate on external surfaces. However, the infill pattern and outline were not visually apparent on the sectioned faces. This lack of apparent internal patterning is strongly indicative of successful extrudate fusing. These visual observations are supported by μ CT (Figure 4.4 A).

Analysis of the μ CT scan demonstrated the successful fusion of extrudate, indicating the cuboid was largely homogenous (Figure 4.4 A).

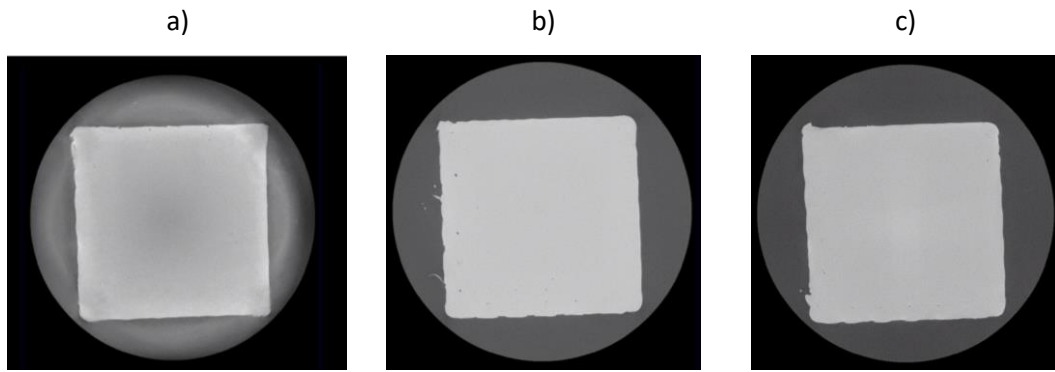


Figure 4.4 A μ CT cross-sectional scan of the test cuboid geometry. The slices show minimal intralayer voids, with the exception of some notable voids around the circumference of the slices within, a) the lower portion (closest to build plate during manufacture) of the cuboid, b) the midway up the cuboid, c) the upper region of the cuboid

The outline bounding the internal rectilinear patterning was also continuous, with no pores observed throughout its height (Figure 4.4 A). The cuboid was found to be 99.97% dense, with the average pore size being 38 μm and the maximum pore size being 119 μm . Only $\sim 10\%$ of the pores were 60-119 μm , with these larger voids being technically challenging to eliminate in FFF builds, as they exist between the rectilinear fill and bounding outline of the cuboid. This distribution of larger pores within the cuboid can be seen in Figure 4.5.

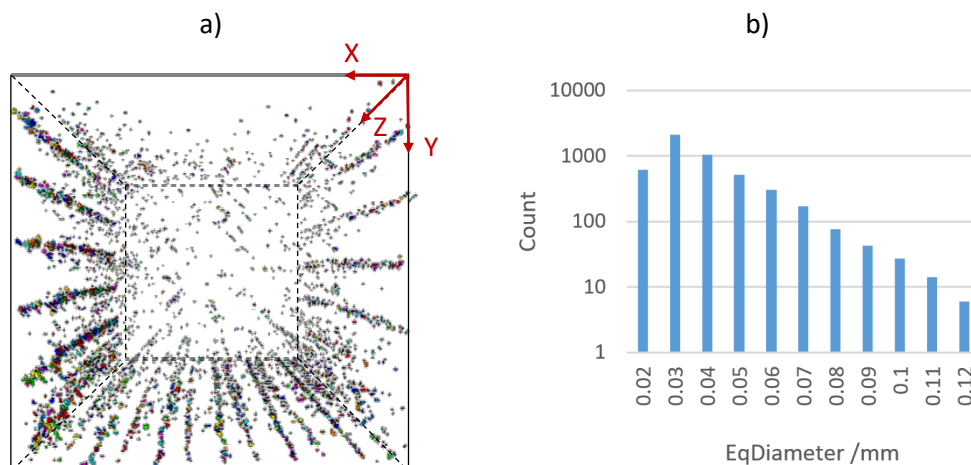


Figure 4.5 Pore distribution within the test cuboid geometry, a) perspective view down the length of the cuboid, with an approximate outline of the cuboid exterior for visualisation, b) histogram showing the effective length (eqdiameter) of the pores

A one-point perspective view down the length of the cuboid illustrates the pore distribution (Figure 4.5a). The largest pores are located at the boundary of the outline and the infill pattern, in lines running the height of the cuboid. It should be noted that 94% of

the cumulative pore volume was accounted for by these larger pores (60-119 μm). Therefore, it is unlikely that the excluded pores (with an equivalent diameter $\leq 23.7 \mu\text{m}$) would increase component porosity significantly, considering the minimal influence on porosity of the existing smaller pores.

4.1.3 Analysis of feature accuracy

During post-processing, it was identified that measurements of the honeycomb component could not be exported automatically from the μCT scan, due to the stringing of the extrudate. Therefore, these measurements were manually taken from the generated “.STL” file, as can be seen in Figure 4.6a.

Digital “.STL” measurements, and supporting physical measurements from Vernier callipers, gave an average wall thickness of 0.45 mm, with a standard deviation (SD) of 0.01 mm. Stringing, seen in Figure 4.6, was mostly focussed around the intersection of the honeycomb walls, with infrequent stringing alongside the walls. This material was fragile and only loosely attached to the walls, and therefore was excluded when measuring wall thickness. Figure 4.6b shows the wall thickness consistency, with a 0.45 mm thick honeycomb overlaid on the “.STL” scan.

The consistent growth of 0.05 mm (from the intended thickness of 0.4 mm) is similar to the ~ 0.04 mm growth observed in the cuboid and dumbbell components (sections 4.1.1 and 4.1.2). This consistency further indicates that the processing parameters are optimised to minimise porosity, without distorting features through excessive extrusion.

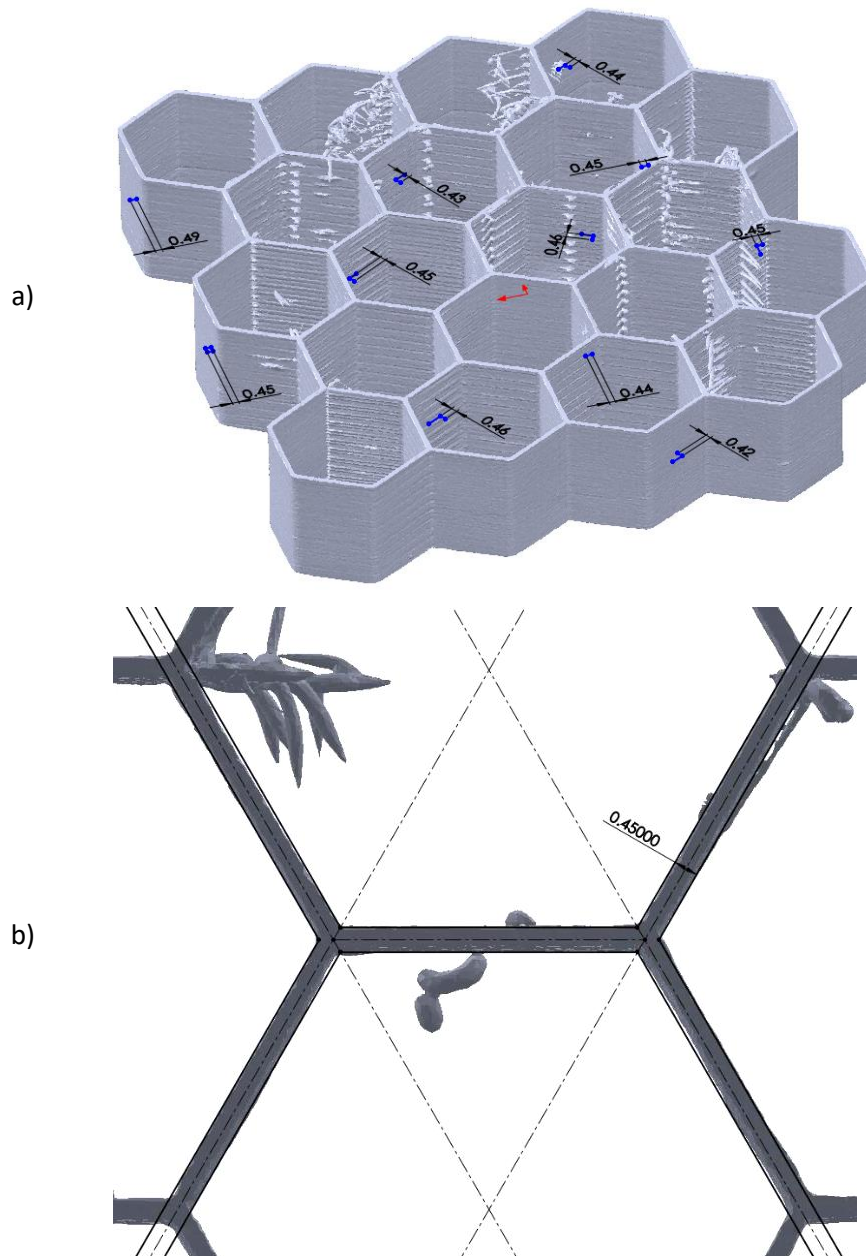


Figure 4.6. The μ CT scan of the honeycomb component was sectioned to include only the honeycomb region, a) assorted wall thickness measurements, b) out of plane view of the honeycomb, with an overlaid honeycomb pattern consisting of a 0.45 mm wall thickness, with an edge length of 5.8 mm

4.2 Establishing a novel material characterisation pathway for AM elastomers

This section presents the results of NF's mechanical characterisation and consequent computational modelling. This characterisation pathway was developed to improve the accessibility of elastomeric material characterisation and to help inform mechanical characterisation to attain an accurate material model.

4.2.1 Identification of internal strains

The honeycomb component (section 4.1.3) was again used to produce a unit cell, for development of the method to assess internal strain. The strain history for all the elements within the unit cell is shown in Figure 4.7. Figure 4.7a shows the computational compression of a single unit cell from the honeycomb test component, and the overall compressive force-time response of the unit cell itself is shown in Figure 4.7b.

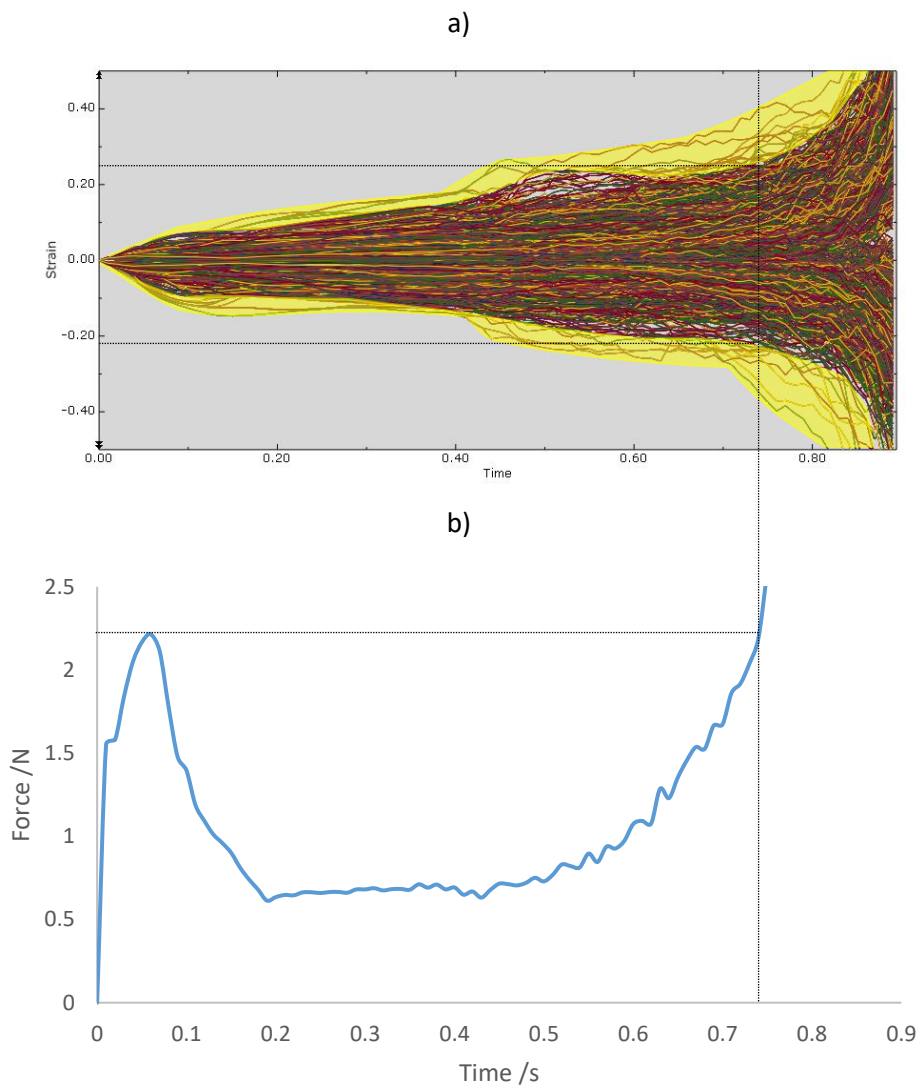


Figure 4.7 Computational compression of a single unit cell from the honeycomb test component, a) minimum and maximum nominal strains for each element in the unit cell (strain refers to nominal strain mm/mm, time is in seconds, and highlighted areas are outlying elements) b) compressive force-time response of the unit cell

Examining Figure 4.7a, outlying strain curves can be identified (as highlighted in yellow). These curves are potential examples of anomalous elements and only constitute 0.3% of

the total responses. Therefore, they were excluded from further analysis, and the resultant internal strains at densification ranged from 0.25 to -0.22.

By ~ 0.74 seconds, the unit cell had compressed 67%, and the onset of an increase to both maximum and minimum internal strains was observed in all elements. As the honeycomb unit cell compressed, the walls initially buckled and deformed into free space. However, as compression increased, the amount of free space reduced, leading to self-interaction. Densification occurred when these interactions increased to the point that the honeycomb began to act as a solid object. At this point, the walls of the honeycomb had no free space into which to deform, and the walls themselves were compressed. This compression of the walls meant that any deflection to the cellular structure had a direct influence on the internal strain of the base material. Therefore, the onset of this increase is likely linked to the ϵ_d of the honeycomb unit cell. Figure 4.9b supports this theory, showing that ϵ_d occurs at the same point.

In addition to identifying internal strains for the honeycomb unit cell, the SP unit cell was also simulated. The internal strain for an SP unit cell, with a cell length of 10mm and a wall thickness of 0.5mm, is shown in Figure 4.8.

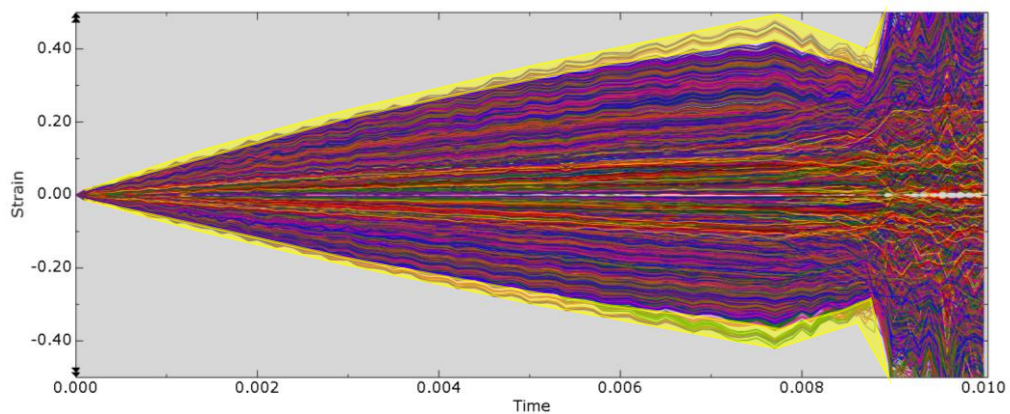


Figure 4.8. Extracted strain in each element of an SP unit cell, during its compression. The unit cell had a 0.5 mm wall thickness and a 10 mm unit cell length. (Strain refers to nominal strain mm/mm, time is in seconds, and highlighted areas are outlying elements)

As with the honeycomb unit cell, there are outlying elements in the SP unit cell, with those highlighted in Figure 4.8 accounting for $<0.5\%$ of the overall elements. Unlike the honeycomb unit cell, the internal strain curves for the 0.5 mm unit cell all had a consistent recurring jagged pattern. It should be noted that the quasi-static simulation of the SP

structure was undertaken after validation of the NF material model. In this later work, a quasi-static simulation was undertaken without mass scaling and with the incorporation of time scaling. As the energy balance indicated only non-significant artificial energy was generated, this pattern could be highlighting the onset of a time-dependent phenomenon. This behaviour also occurred in the 1.5 mm unit cell after the plateau region was reached Figure 4.9b.

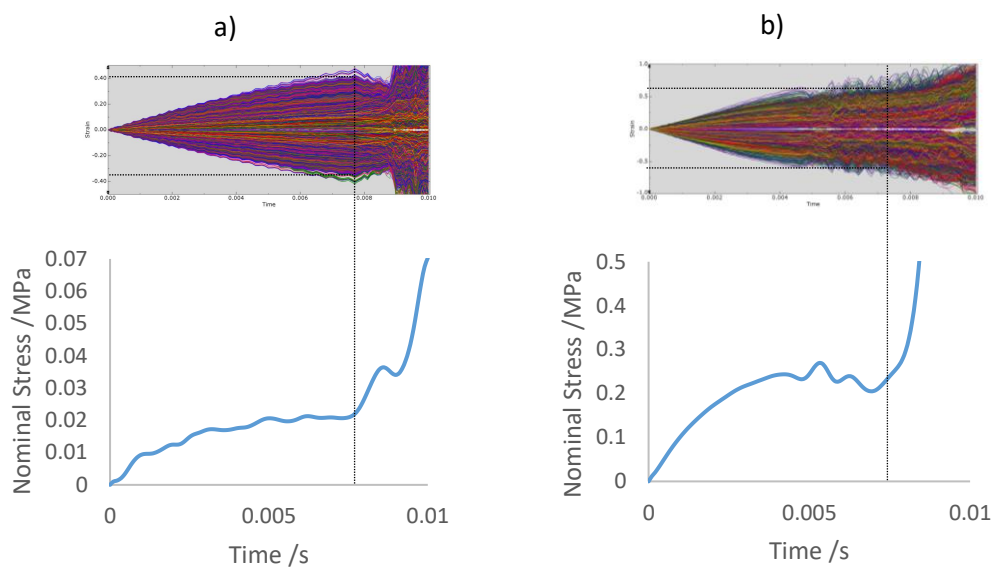


Figure 4.9. Extracted strain in each element of SP unit cells, during their compression. The unit cells had a 10 mm unit cell length and wall thicknesses of, a) 0.5 mm, b) 1.5 mm (Strain refers to nominal strain mm/mm, time is in seconds, and highlighted areas are outlying elements)

For the 0.5 mm unit cell, the internal nominal strains at densification ranged from + 0.41 to - 0.38. These rose to ± 0.65 for the 1.5 mm unit cell, indicating that higher internal strains are generated as wall thickness increases.

In Figure 4.9b, the 1.5 mm SP unit cell's internal strain profile changed from linear to a non-linear at the point of densification. However, the 0.5 mm SP unit cell (Figure 4.9a) had a linear internal strain profile up until the point of densification. After this point, instead of increasing, the internal strain decreased. During this decrease of internal strain, the overall stress-time response indicated the occurrence of a small secondary plateau. After this plateau, the stress again rose, with this secondary densification coinciding with a sharp rise in internal strain. Therefore, while this work has highlighted the potential of internal strain for identification of densification, it is likely structurally dependent. A combined review of

internal strain, and the cellular structure's stress response, is critical to ensuring ϵ_d can be identified from internal strains.

While the honeycomb and SP responses all have internal nominal strains <1 , there is still variance between different configurations. As the proposed characterised strain range is to be applied to the honeycomb and all SP structures, it was decided that a compromise between the internal strains of the 0.5 mm, and 1.5 mm, SP unit cells would be the best route forwards. Therefore, material characterisation was undertaken at a strain range of ± 0.5 .

4.2.2 Mechanical characterisation approach

4.2.2.1 Development of test apparatus to enable accessible characterisation

Loading of equi-biaxial and planar tension test specimens can be seen in Figure 4.10 and Figure 4.11. For both cases, a different specimen is shown in the photography and non-contact imagery respectively (highlighting the repeatability of the tests). The specimens in Figure 4.10 and Figure 4.11 are shown at nominal strains above the characterisation strain range, identified in section 4.2.1 (0.5), to highlight the loading of the specimens.

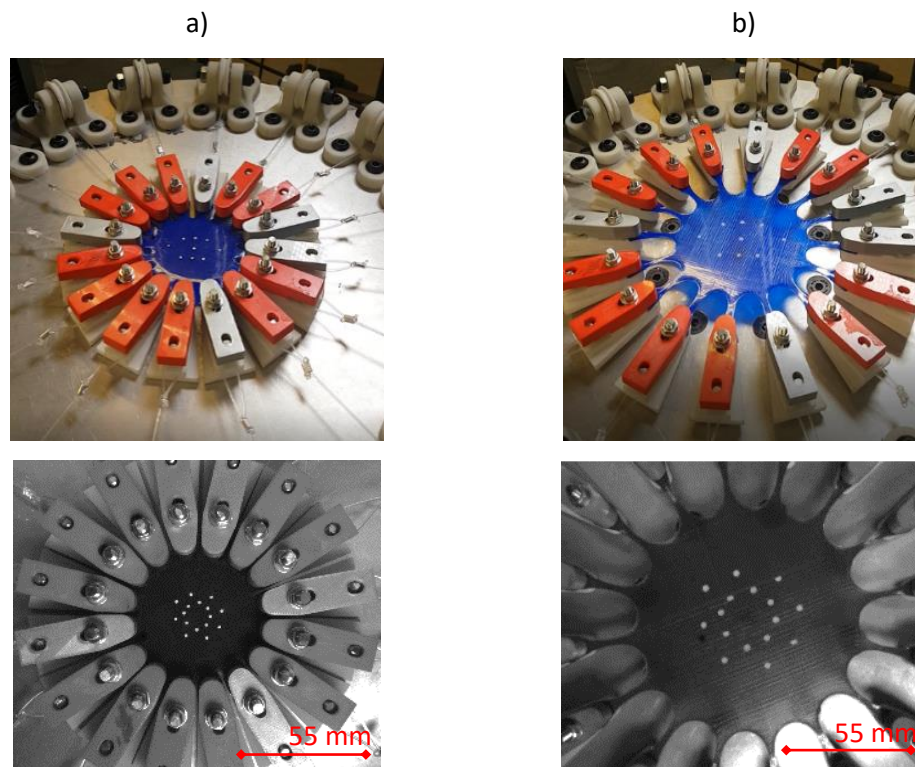


Figure 4.10. Equi-biaxial test specimen during experimental testing, showing photography (above) and non-contact imagery (below), a) at test commencement, b) under loading

One of the visual features of the test specimens was the rectilinear infill pattern used to manufacture them. In the case of the equi-biaxial specimen (Figure 4.10), the straight lines produced by this process can be seen to remain straight even when the specimen is loaded to the extent of the test jig (Figure 4.10b). This lack of change demonstrates the equal radial loading around the periphery of the test specimen, further supporting the simulated validation.

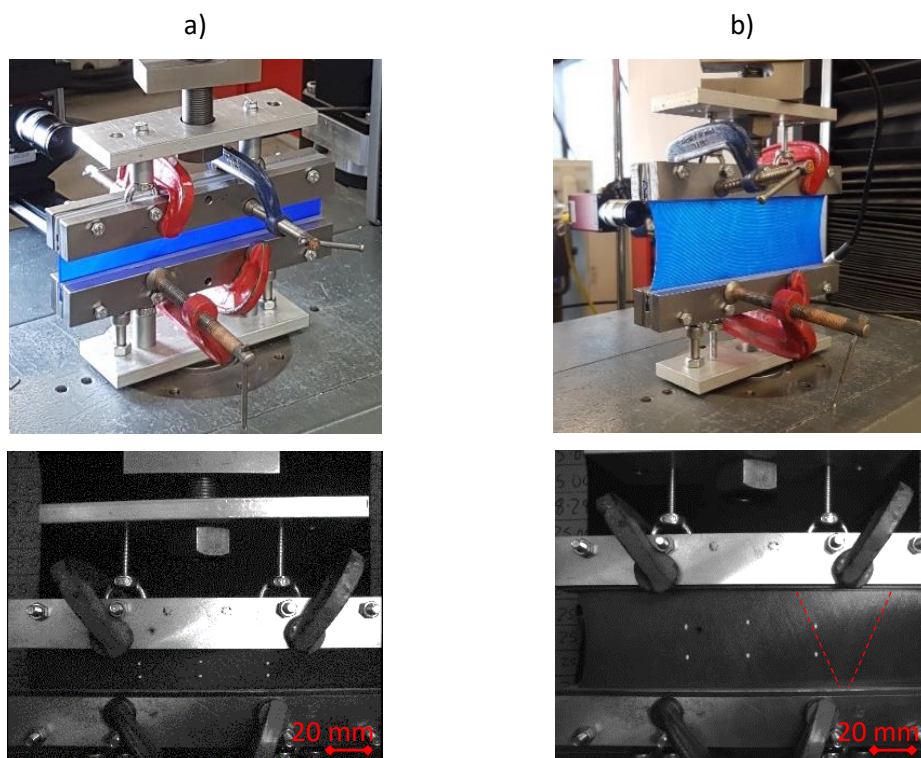


Figure 4.11. Planar tension test specimen during experimental testing, showing photography (above) and non-contact imagery (below), a) at test commencement, b) under loading (with dashed red lines highlighting rectilinear pattern)

The purpose of the planar tension test is to minimise any lateral contraction, thus ensuring the test specimen contracts over its thickness. In the case of the planar tension experiment, Figure 4.11b clearly shows the lack of lateral contraction within the gripping assembly, with the edges of the specimen ‘bowing’ inwards under loading. This bowing effect highlights why the planar tension specimen requires a ratio of 10:1.

When examining the photography in Figure 4.11b, a curved pattern can be observed. This occurs due to the bright light, used for extensometry, shining through the crossing of the rectilinear pattern. The actual rectilinear pattern in the central region remains straight even

at high extension. Evidence of this straightness is visible in the silhouetted white lines on the optical photography, as well as the highlighted straight lines in the video extensometry (Figure 4.11b), where the extensometer light reflects off the test specimen. The constant equal strain in the equi-biaxial and planar samples is further evidenced by the similar levels of strain recorded from each of the virtual strain gauges. Strain gauge data for a planar, and an equi-biaxial, sample are presented in Figure 4.12.

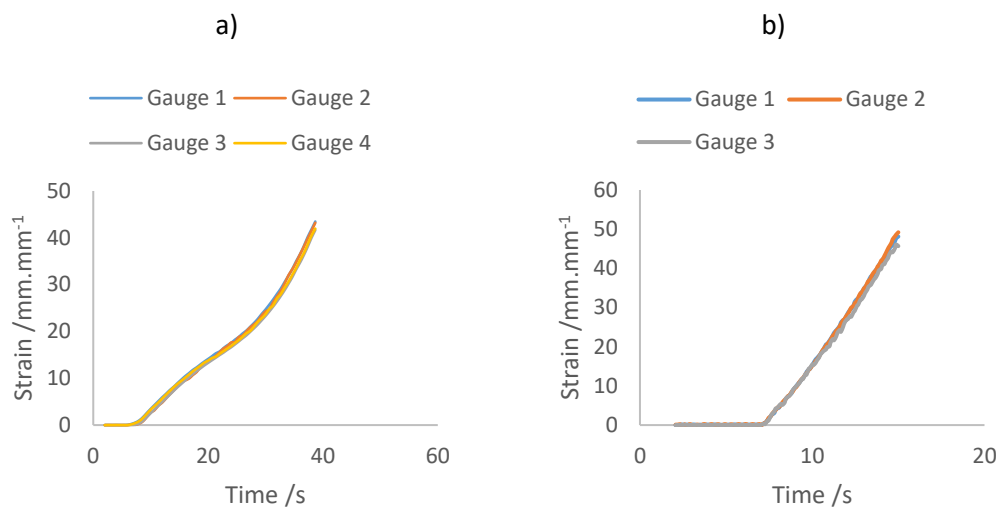


Figure 4.12. Raw strain gauge data from multiple virtual gauges over a single sample, demonstrating equal strain, a) equi-biaxial, b) planar

4.2.2.2 Mechanical characterisation data

These developed test jigs were used in combination with standardised uniaxial tensile testing to collect the characterisation data for NF. The results of each test method are displayed as a mean value, with shaded regions representing the SD, in Figure 4.13.

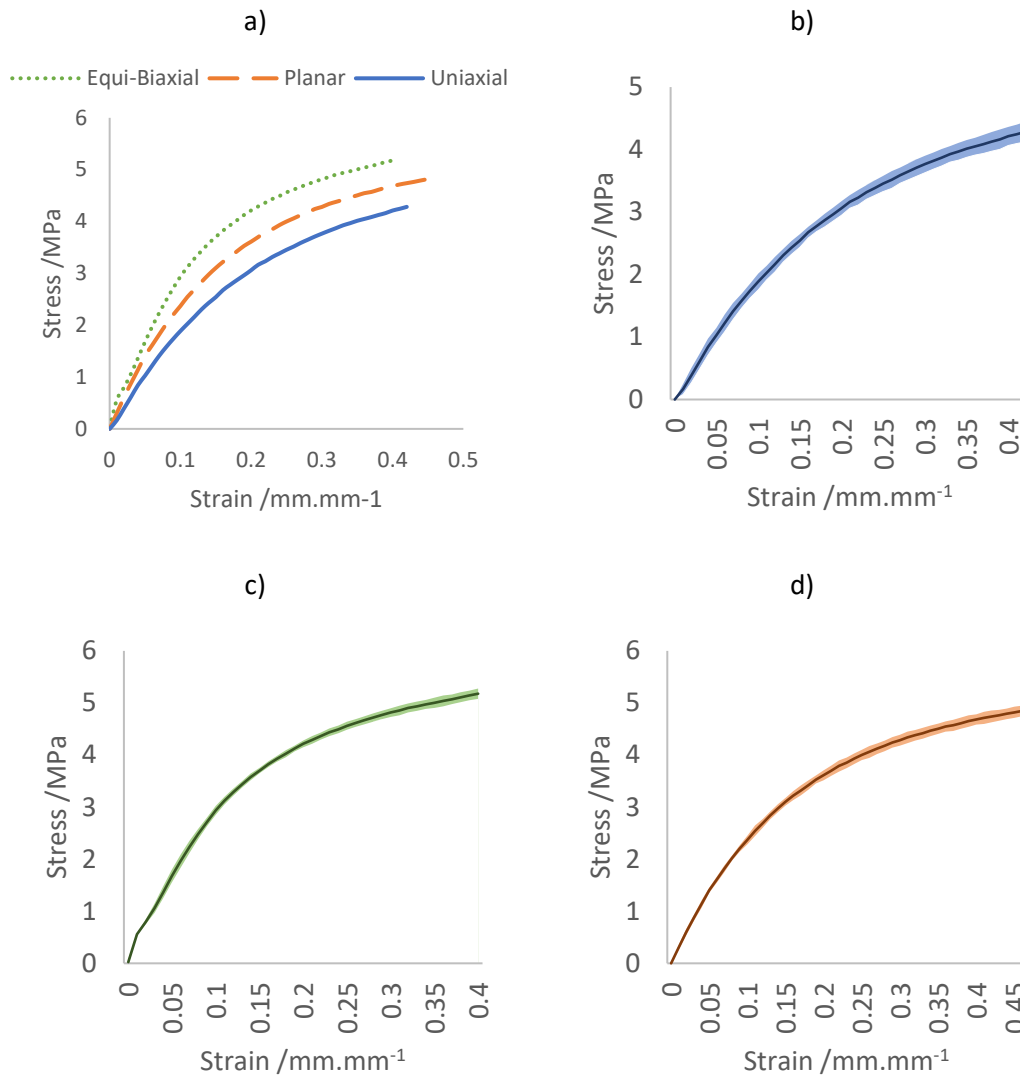


Figure 4.13 Mechanical characterisation stress-strain testing responses for the NJ TPU material, a) Combined datasets, b) Uniaxial only, c) Equi-biaxial only, d) Planar only. Shaded region = SD

All datasets demonstrated non-linear behaviour, typical of elastomeric materials.

Therefore, when identifying initial moduli, only strains from 0 to 0.05 were evaluated.

Uniaxial testing gave a mean initial modulus of 21 MPa, which is notably higher than the tensile modulus of 12 MPa stated in the NF datasheet [182]. The mean initial planar modulus was 37% greater than uniaxial, and the equi-biaxial was 63% greater. At a strain of 0.4, uniaxial stress was 4.21 MPa, planar stress was 4.68 MPa, and equi-biaxial stress was 5.18 MPa.

The discrepancy in initial uniaxial modulus could potentially be due to NinjaTek choosing to undertake their analysis at a higher strain. An inflection point can be calculated from the tensile stress-strain curve, at a strain of 0.22. Therefore, when processing data from a pull

to failure test, this strain could be considered for the evaluation of the initial modulus, as NF has an elongation at break of 660% [182]. When considering a strain of 0.22, a tensile modulus of 14.7 MPa can be calculated, much closer to the NinjaTek value of 12 MPa. Additionally, NF's uniaxial tensile modulus has been recorded as 26.5 MPa, at a strain of 0.03 [180], lending support the value recorded in this thesis.

The inability to run closed-loop control, from the non-contact extensometer to the uniaxial test machine, meant crosshead movement had to be manually tuned to achieve the required level of strain within the gauge area. Due to inconsistencies between test specimens, such as differing slippage at the grips and cross-sectional area, the maximum tested strain was not constant across specimens, ranging from 0.4 to 0.5. When taking the average performance of a set of specimens, test data was analysed up to the lowest common strain value in that test group. Therefore, while the strain identified for testing in section 4.2.1 was 0.5, the material model was developed based on characterisation data with strains of 0.46 for planar, 0.4 for equi-biaxial, and 0.42 for uniaxial.

4.2.3 Material modelling

4.2.3.1 Hyperelastic (HE) material modelling

To enable the characterisation data from section 4.2.2.2 to be interpreted by the computational analysis software, a material model must be defined. To ensure material models were accurate, they are analysed for both mathematical stability and representative behaviour. This section explores the HE material models available in ABAQUS.

Before exploring the material models, a demonstration, of how achieving the best fit to experimental data does not necessarily result in a representative material model, was performed. A superior fit can be achieved by separating datasets and undertaking curve-fitting for an individual stress state. To demonstrate this, Figure 4.14 shows a fifth-order Ogden material model that has been curve-fit to the uniaxial experimental data alone.

Note, this characterisation was performed using stand-alone software (MCalibration, Veryst Engineering, US) to tune the curve to demonstrate how experimental data can be closely tuned to a single response.

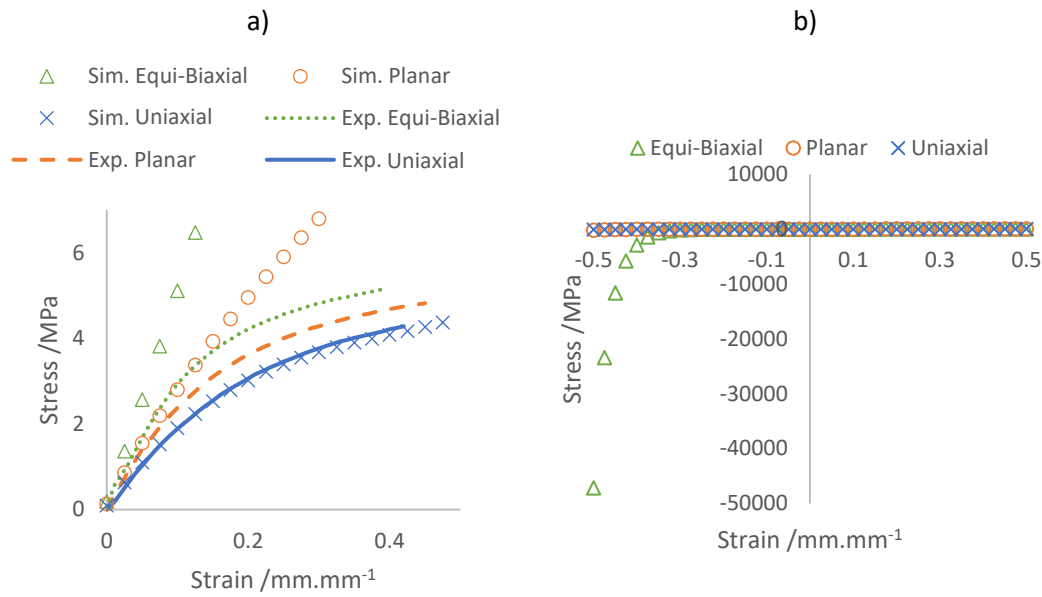


Figure 4.14. Fifth-order Ogden material model, curve-fit to the uniaxial tension response of the NF TPU material alone, a) combined graph showing the fit of the Ogden model and the experimental data, b) Ogden model extrapolated to a strain range of ± 0.5

While the correlation to the uniaxial stress state is excellent ($r^2 = 0.9975$), this behaviour is unrepresentative of NF's remaining stress states (Figure 4.14a). Additionally, Figure 4.14b highlights a state of infinite equi-biaxial compressive stress, which is generated as compressive strain tends to -0.5. Therefore, HE material models that are curve-fit to one stress state alone, or without consideration of behaviour that lies outside the experimental data range, are subject to scrutiny. When examining a material model's behaviour, it is important to examine all stress states under both compression and tension (even if tensile data alone was used to create the material model).

The HE material models available in ABAQUS were curve-fit to the characterisation data collected in section 4.2.2.2. The models were assessed over a strain range of ± 0.5 , as per section 3.2.1. The three main unrepresentative behaviours observed during this curve-fitting process were:

- 1) An increase in stress when under compressive strain, eventually leading to theoretical tensile stress at a compressive strain. The ABAQUS fitted models which demonstrated this behaviour were: Van de Waals, third and fourth-order Ogden, second-order polynomial, reduced second and fourth-order polynomial. Their responses are shown in Figure 4.15. Of note, in Figure 4.15a, the Van de Waals curve fit tends to infinite compressive stress before generating tensile stress, between compressive strains of 0.4 and 0.5.

- 2) Equi-biaxial compressive stress tending to infinity, while compressive strain was <0.5 . The least severe example of this was the reduced third-order polynomial model (Figure 4.16), which indicated a quasi-static modulus of 432 GPa between strains of 0.47 and 0.5. Comparatively, an instantaneous compressive modulus of 66 GPa has been recorded dynamically for stainless steel (during Kolsky bar experimentation [196]). The ABAQUS fitted models which demonstrated this behaviour were: fifth and sixth order Ogden, third, fifth and reduced sixth-order polynomial. The responses are shown in Figure 4.16.

- 3) Stress inverted over the explored strain range. An example of this would be tensile stresses decreasing, as the tensile strain increased. The second-order Ogden model (Figure 4.17) demonstrated this behaviour in its equi-biaxial response. This inversion was also observed in some of the models highlighted in the previous two unrepresentative behaviours (points 1 and 2) and therefore could be indicative of other issues related to curve-fitting.

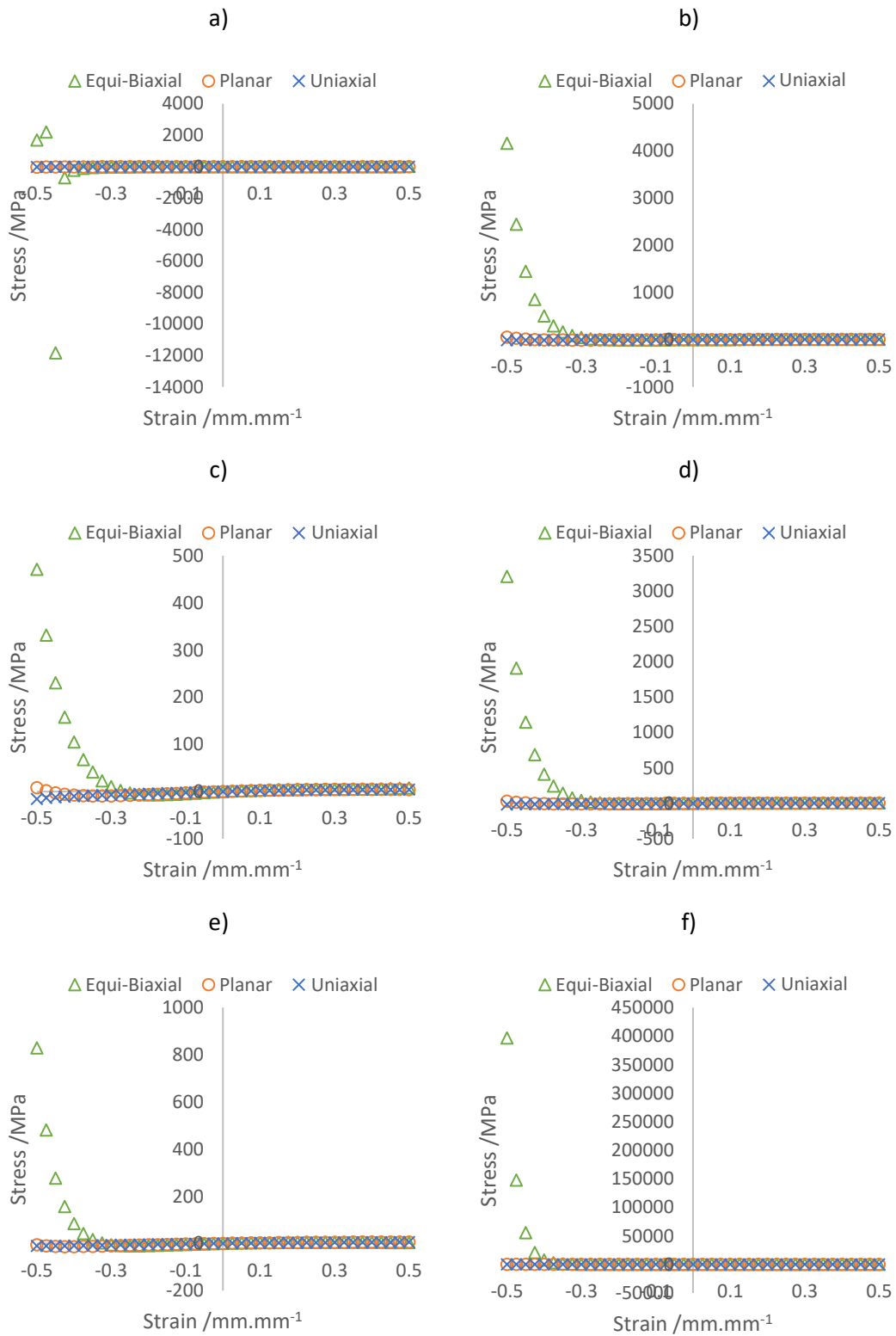


Figure 4.15. How the curve-fitting of a material model can generate theoretical tensile stress at compressive strains, in NF TPU, , a) Van de Waals, b) Ogden N3, c) Ogden N4, d) Polynomial N2, e) Reduced polynomial N2, f) Reduced polynomial N4

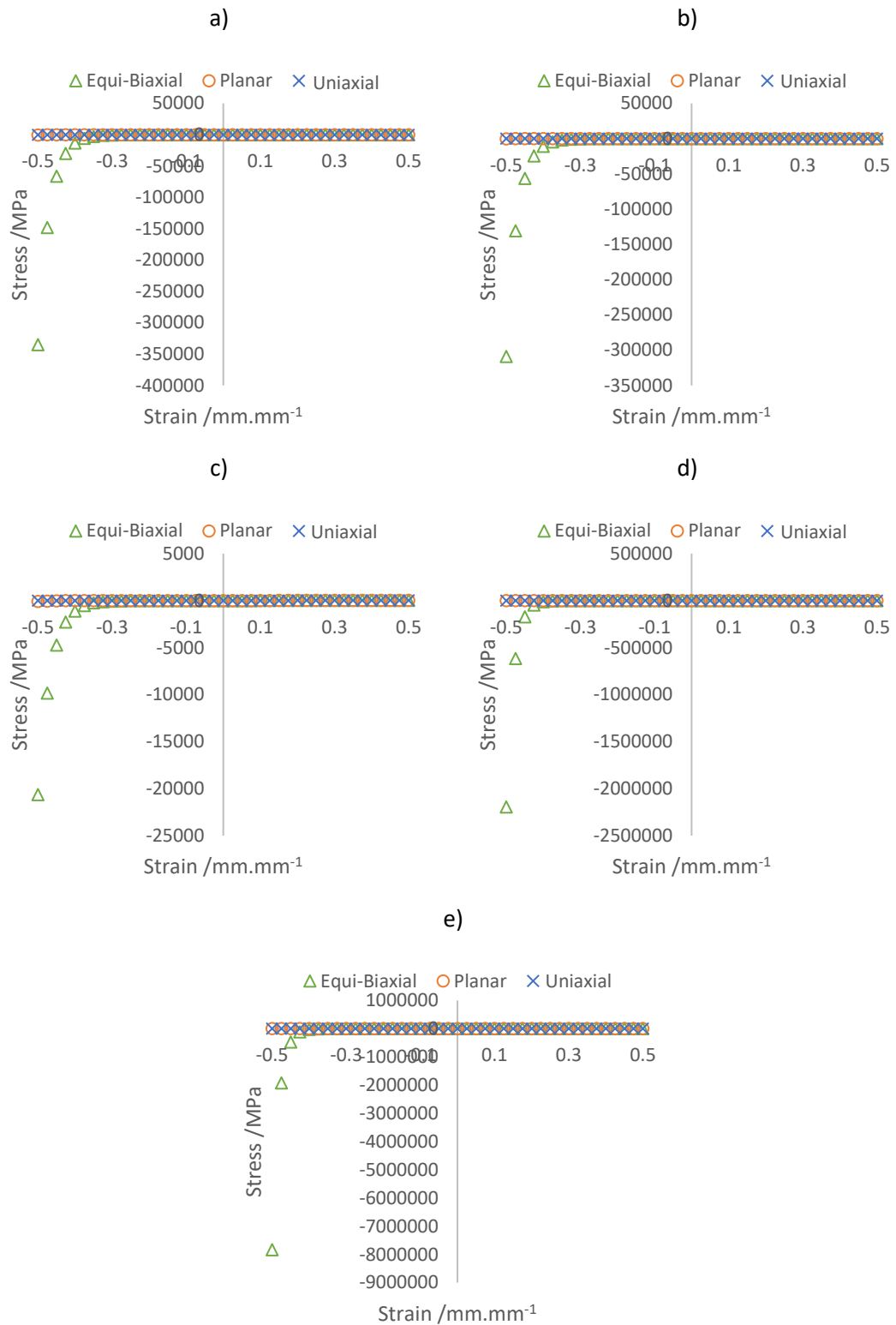


Figure 4.16. How the curve-fitting of a material model generates theoretical infinite compressive stress before 0.5 strain, in NF TPU, a) Ogden N5, b) Ogden N6, c) Reduced polynomial N3 (Yeoh), d) Reduced polynomial N5, e) Reduced polynomial N6

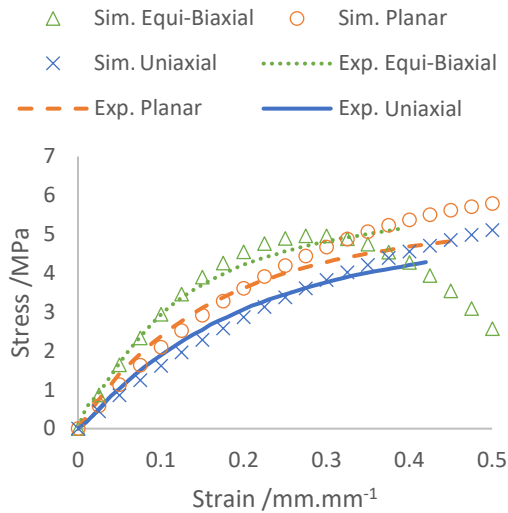


Figure 4.17. Inversion of tensile stress, as tensile strain increases, observed when fitting the second-order Ogden material model to the NF TPU experimental data

It should be noted that these instabilities have specifically arisen when curve-fitting within ABAQUS and to the strain range prescribed in section 4.2.1. Therefore, there may be instances where the models described above are more appropriate, for example, when modelling to larger data ranges or different materials.

The remaining material models that were curve-fit to the characterisation data are displayed in Figure 4.18. All these models displayed logical behaviour over the prescribed strain range (± 0.5).

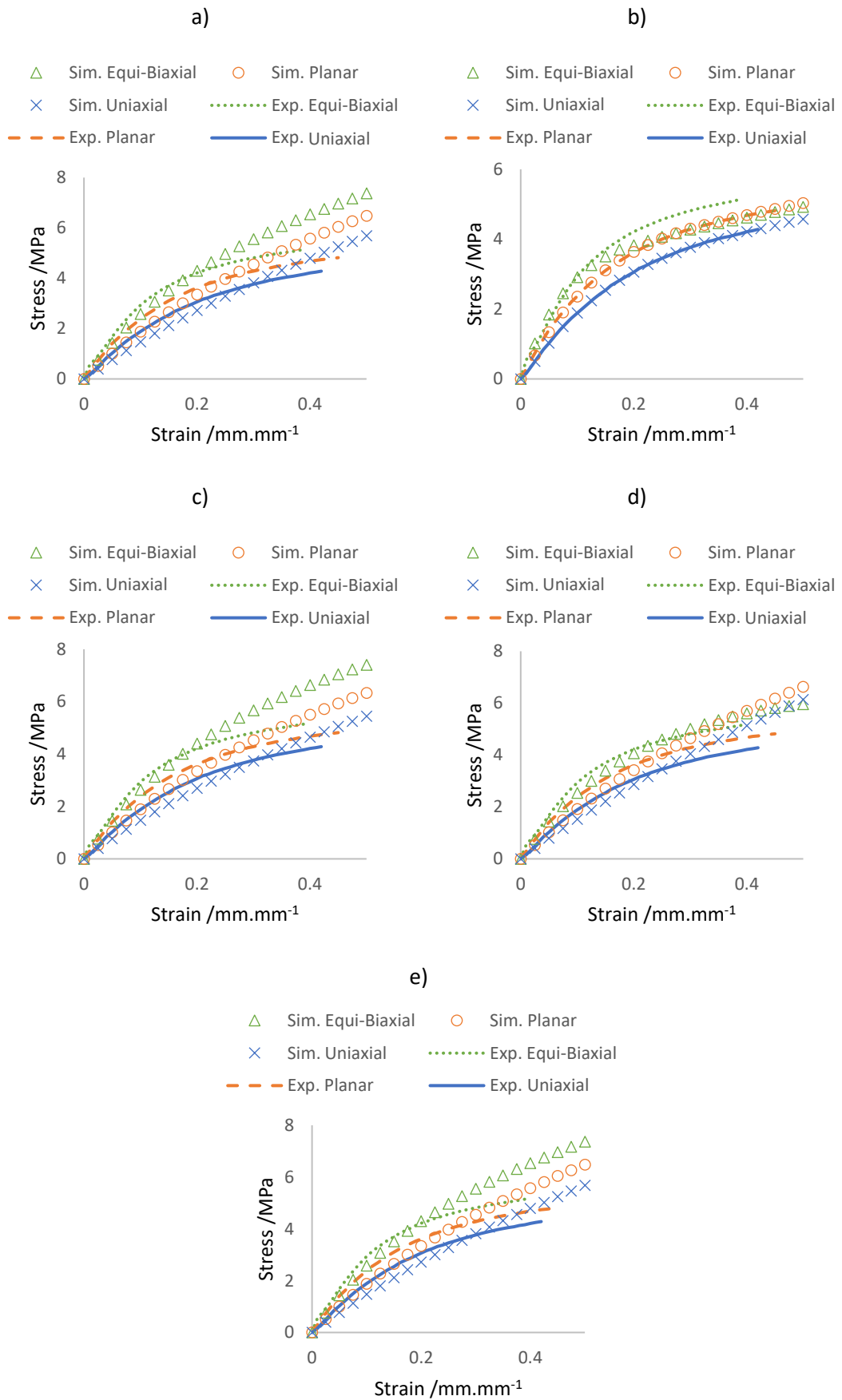


Figure 4.18. The curve-fitted response of material models to the NF TPU experimental data, a) Arruda-Boyce, b) Marlow, c) Ogden N1, d) Polynomial N1, e) Reduced polynomial N1

Nearly all these responses overshoot their respective experimental stresses, at the higher end of the strain range (0.3-0.5). An exception to this was the Marlow model and, in the case of the equi-biaxial response, the first-order polynomial (Mooney-Rivlin) model. The difference in stress between simulated and experimental responses for these material models is shown in Figure 4.19, and the correlation (r^2) between these responses is shown in Table 4.2.

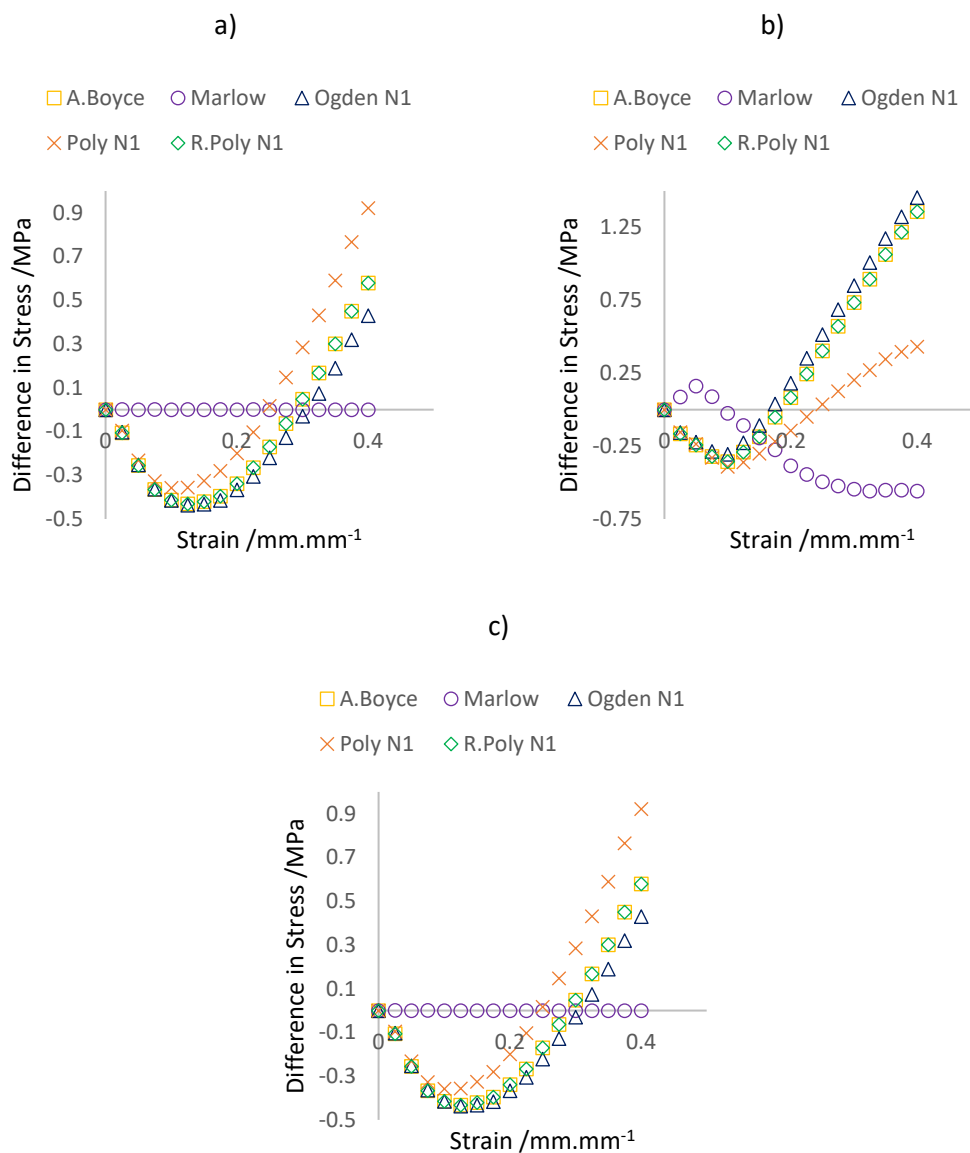


Figure 4.19. Difference between curve-fitted material models and NF TPU experimental data a) Uniaxial, b) Equi-biaxial, c) Planar

Table 4.2. Correlation (r^2) between NF TPU mechanical characterisation data and curve-fitted material models

	Uniaxial r^2	Planar r^2	Equi-biaxial r^2	Average r^2
Arruda-Boyce	0.967	0.948	0.958	0.958
Marlow	1.000	1.000	0.992	0.997
Ogden N1	0.971	0.953	0.960	0.961
Polynomial N1	0.962	0.948	0.983	0.964
R.Polynomial N1	0.971	0.959	0.961	0.964

The following material models all display similar difference values and behaviour: Arruda-Boyce; first-order Ogden; first-order polynomial (Mooney-Rivlin) and reduced first-order polynomial. As an exception to this, at 0.5 strain, the first order polynomial has a higher error in the uniaxial case (0.92 MPa vs ~ 0.5 MPa) and a notably lower error in the equi-biaxial case (0.43 MPa vs ~ 1.5 MPa). Comparatively, the Marlow model shows consistently low error for all stress states, with 0.0005 MPa, -0.55 MPa and -0.07 MPa respectively for uniaxial, equi-biaxial and planar. Considering the r^2 correlations, in addition to the difference between experimental and simulated stress, the Marlow and Mooney-Rivlin models display the best agreement to the characterisation data.

The ability of the material models to predict compressive strain was also assessed. As covered in section 2.4.2.1, equi-biaxial extension data can be converted into a theoretical uniaxial compressive response [131]. This conversion was undertaken on the mean equi-biaxial extension data. The resultant uniaxial compressive response was then compared to the five previously curve-fitted material models.

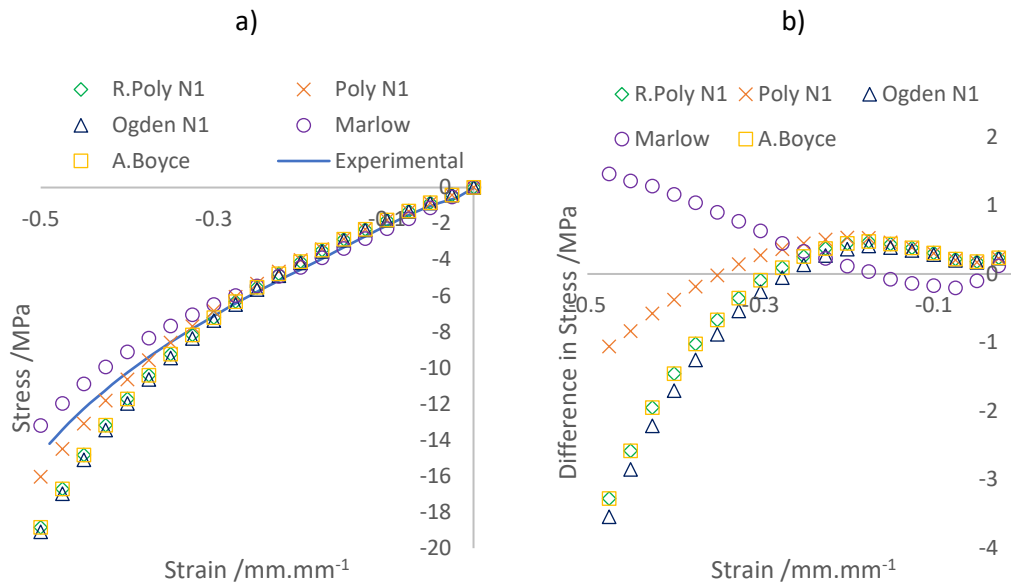


Figure 4.20. Theoretical uniaxial NF TPU compressive experimental response, derived from equi-biaxial data, alongside curve-fitted material model responses, a) combined experimental and material model plot, b) percentage difference in stress between experimental data and material models

Table 4.3. Correlation (r^2) between curve-fitted material models and theoretical NF TPU compressive experimental response

	Arruda-Boyce	Marlow	Ogden N1	Mooney-Rivlin	Neo Hookean
r^2	0.987	0.998	0.988	0.995	0.987

Figure 4.20b, and Table 4.3, show that the Marlow and Mooney-Rivlin models continue to have the best correlation to the experimental response. For the prediction of uniaxial compressive behaviour, the Mooney-Rivlin model had a lower maximum error, with +1.06 MPa vs -1.46 MPa for the Marlow model. While the Mooney-Rivlin demonstrated improved agreement and correlation to the compressive response, the Marlow model had improved agreement and correlation to the tensile response.

The Marlow model only involves fitting one of the three datasets [197]. The assumption that allows for this holds for NF when considering planar and uniaxial loadings. However, while the Marlow model still has a good agreement for the equi-biaxial dataset, it is apparent that the assumption no longer holds. Comparatively, when curve-fitting the Mooney-Rivlin model, all three datasets contribute to the fit. Additionally, the Mooney-Rivlin model is one of the most referenced models in the literature [198] and is widely available in commercial curve-fitting solvers. Therefore, the Mooney-Rivlin material model was selected moving forward.

The Mooney-Rivlin material model response is presented in Figure 4.21, and its coefficients are presented in Table 4.4. In addition to having a good correlation with the characterisation data, this model was mathematically stable over the investigated strain range.

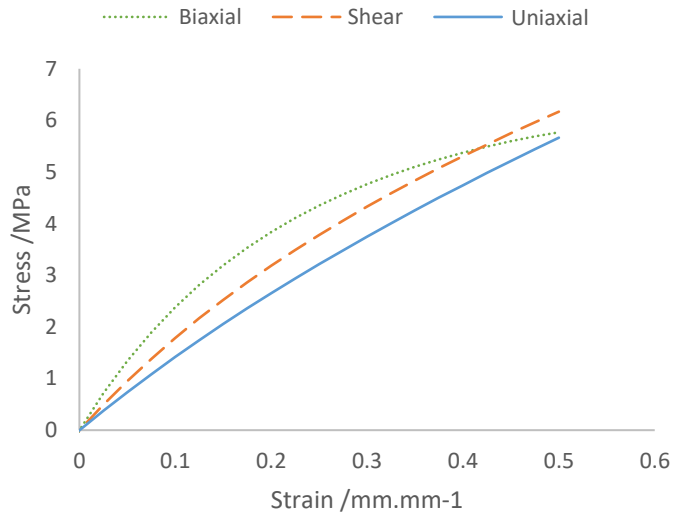


Figure 4.21. Mooney-Rivlin material model, curve-fitted to the NF TPU experimental characterisation data presented in Figure 4.13

Table 4.4. Resultant Mooney-Rivlin coefficients, fitted to the NF TPU experimental characterisation data presented in Figure 4.13

$C10$ /MPa	$C01$ /MPa
2.93	0.363

4.2.3.2 Viscoelastic material modelling

The stress-relaxation data, used to generate the viscoelastic portion of the material model, is presented in Figure 4.22a.

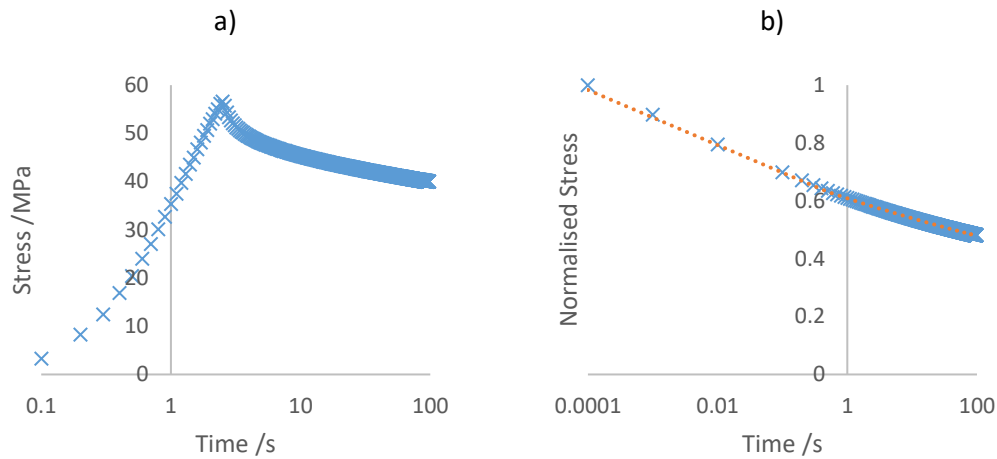


Figure 4.22. Experimental stress relaxation data, collected from NF TPU uniaxial test specimens, a) raw test data, b) processed test data, back-extrapolated to a theoretical instantaneous strain

The initial portion of the graph, from 0.1 to ~2.5 seconds, is generated by the uniaxial test machine loading the specimen to the required strain (0.5), after which the stress-relaxation test commences. Following the procedure described in [137], the loading portion of the curve was removed, and the remaining data points were manually shifted in the time domain. Back-extrapolation was then used to determine the predicted stresses approaching a theoretical instantaneous loading. This response was normalised (Figure 4.22b) and a Prony series curve-fitting procedure was performed in ABAQUS. Due to the low root mean square error (0.001) specified for the curve-fitting procedure, the viscoelastic portion of the material model closely followed the experimental response. This close agreement can be seen in Figure 4.23, with the Prony series coefficients presented in Table 4.5.

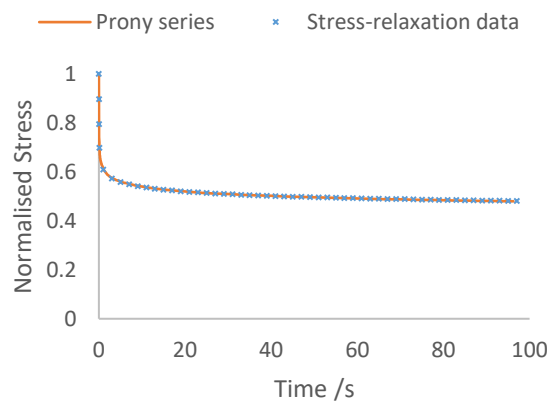


Figure 4.23. Processed, normalised uniaxial NF TPU experimental stress relaxation data; alongside the curve fitted Prony series presented in Table 4.5

Table 4.5. Prony series, curve-fitted to the NF TPU uniaxial experimental data presented in Figure 4.22

	g /MPa	τ /s
1	0.196	1.27E-03
2	0.129	8.30E-02
3	7.67E-02	0.894
4	6.03E-02	6.51
5	7.10E-02	54.6

4.2.3.3 Validation of NF material model

A honeycomb structure was simulated to validate the material model’s predictive capacity. The resultant force-displacement behaviour is presented in Figure 4.24. It should be noted that mass scaling had no notable effect on the energy balance of the simulation, with all artificial energies under the limits described in section 3.3.1.1 (e.g. kinetic energy <5%).

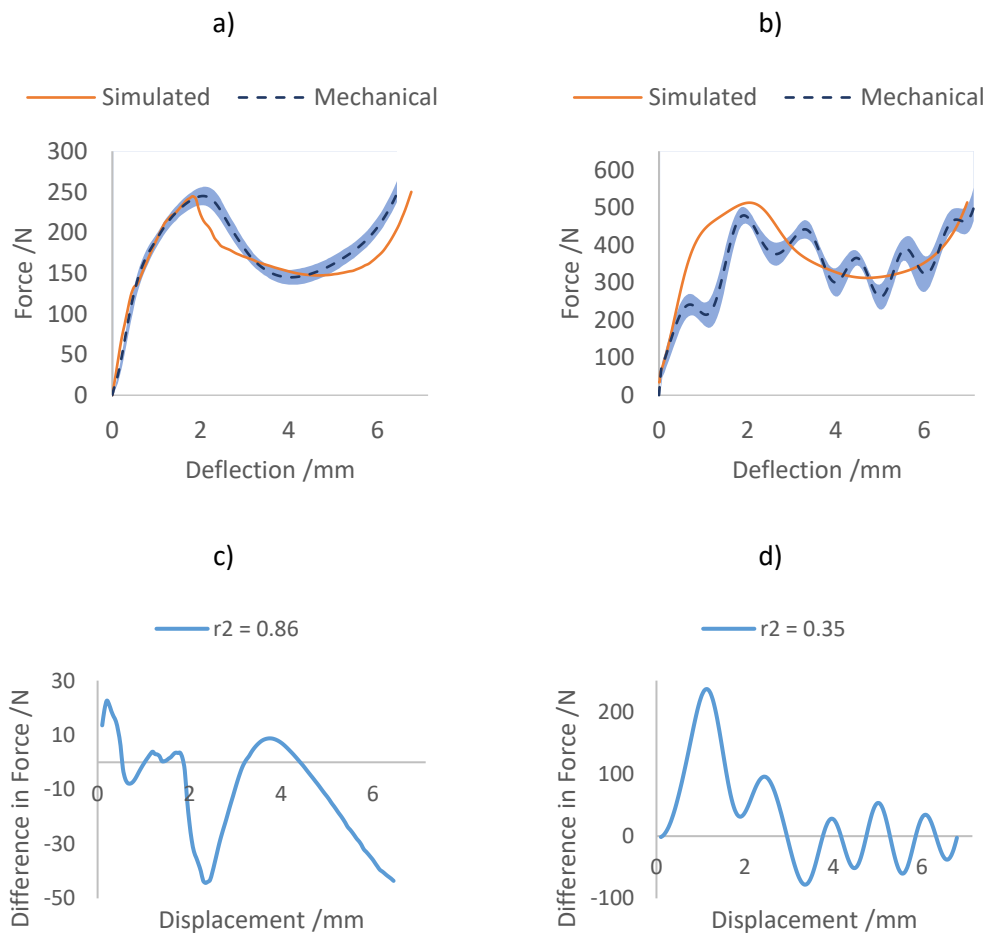


Figure 4.24 NF TPU honeycomb validation, plotting experimental compression against simulated: a) quasi-static, b) dynamic, c) difference in stress for quasi-static, d) difference in stress for dynamic, Shaded region = SD

For the quasi-static condition, the experimental densification strain (ϵ_d) had good agreement with the simulated ϵ_d (0.68 vs 0.65). The peak force (245 N) and energy transferred at densification (1.15 J) were the same for the simulated and experimental curves. In Figure 4.24a, the agreement between simulated and experimental curves is excellent up until the point of maximum force. After this point, the simulated response is smooth, while the mechanical force drops sharply. The two curves only converge again later in the densification region. Therefore, this divergence occurs when the walls of the honeycomb are predominately undergoing buckling. Despite the inherent difficulties simulating buckling behaviour, the strong agreement between key variables (ϵ_d , force, energy) indicates that the simulated quasi-static honeycomb behaviour is representative of the mechanical response.

For the dynamic condition, the experimental ϵ_d again had good agreement with the simulated ϵ_d (0.71 vs 0.70). For the simulated curve, the peak force was 513 N and the energy transferred before densification was 2.67 J. The experimental force was 7% lower, at 479 N, and energy transferred at densification was 8% lower, at 2.45 J. Examination of the curves in Figure 4.24b and d show these decreases are at least in part due to undulation observed in the mechanical response, in addition to a reduced agreement over the initial 2 – 3 mm of displacement.

The consistency of the undulation, in both duration and amplitude, indicate that it is likely a form of background noise. As the shaded region (Figure 4.24b) indicate this noise occurs consistently across all five honeycomb components, it is likely not an external noise source (e.g. electrical interference). The energy at which this test was undertaken (3.5 J) is very low, and the honeycomb tested was relatively soft. As a result, A_{max} was only ~ 12 g, making the amplitude of these undulations only $\sim 2 - 3$ g. Due to the consistency and low amplitude of this noise, it is likely due to mechanical vibration within the test setup. Despite this noise, the agreement for ϵ_d , and the visual similarity of the force-displacement curves (Figure 4.24b) suggests that the material model can be used to describe the dynamic mechanical behaviour of NF.

Further to this performance-based analysis, conventional and high-speed videography was used to analyse the honeycomb's deformation patterns, which emerged as the simulated and mechanical experiments progressed. These patterns are shown in Figure 4.25.

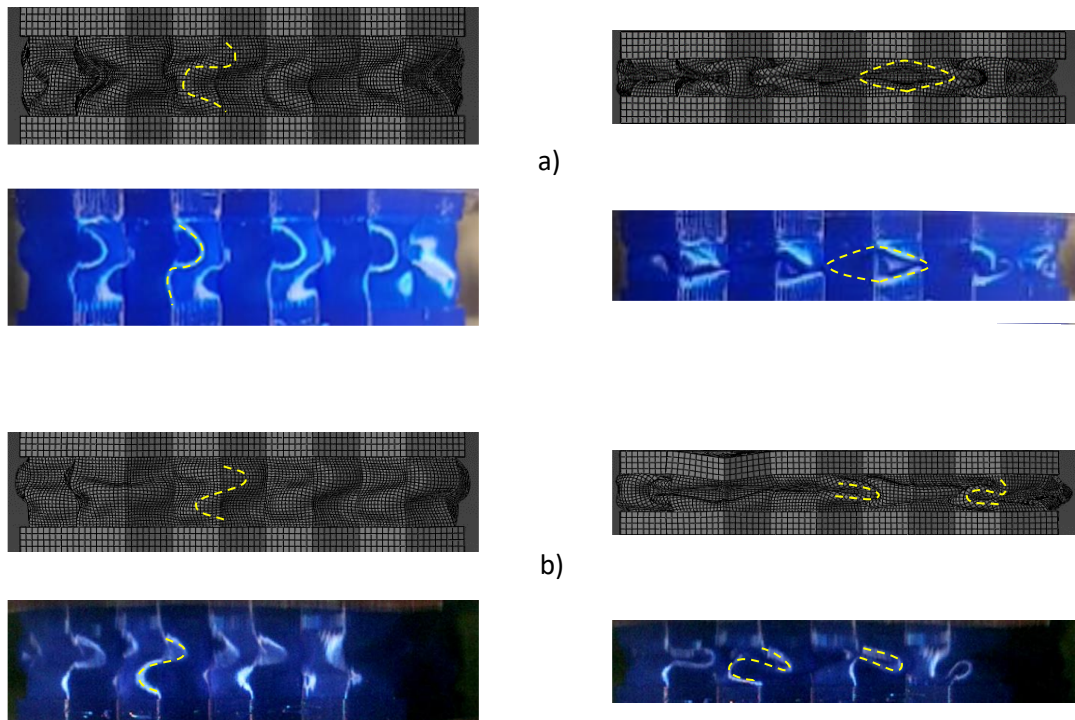


Figure 4.25 Visual comparison of simulated and experimental deformation of the NF TPU honeycomb: a) quasi-static at a nominal compressive strain of 0.2 and 0.6, b) dynamic at a nominal compressive strain of 0.2 and 0.6. Note, simulated images have been mirrored horizontally to highlight deformation patterns.

At a quasi-static nominal strain of 0.2, S-shaped deformation patterns were observed in mechanical and simulated experimentation (Figure 4.25a). When this nominal strain increased to 0.6, the structure collapsed inwards forming elongated diamond-shapes. This pattern was observed in both mechanical and simulated experimentation.

At a nominal strain of 0.2, dynamic loading also causes S-shaped deformation patterns in simulated and mechanical experimentation (Figure 4.25b). When this strain increases to 0.6, mechanical and simulated experimentation demonstrate a combination of C and S-shaped deformation patterns. However, the outer walls of the honeycomb partially collapsed inwards during simulated dynamic compression (Figure 4.25b), causing a diamond-shaped deformation pattern. This pattern was focussed under a portion of the thick upper section that displaced away from the impacting surface. As this deformation of the thick upper section was not observed in mechanical experimentation, it likely caused the emergence of the diamond-pattern. Except for the diamond-pattern (in this instance), it can be said that the deformation patterns observed in simulated and mechanical experimentation agree.

The agreement observed in the performance-based analysis is further supported by this agreement in the deformation pattern (Figure 4.25). Therefore, it can be said that the NF

material model presented in section 4.2.3.1 and 4.2.3.2 is valid for use in both quasi-static and rate-dependent computational analysis.

4.3 Generation of a novel scalable design tool for the selection of initial SP configurations

This section presents the experimental work that resulted in the production of the SP structure's energy absorption diagram. The approach to generating this diagram sought to demonstrate its applicability to variable boundary conditions and to enable scaling of the diagram to different materials.

4.3.1 Ensuring accurate and efficient simulation

4.3.1.1 Mesh sensitivity study

The results of the mesh sensitivity study, described in section 3.3.1.2, are presented here. Note, all thicknesses in this study have at least one mesh size resulting in two elements being generated across their wall thickness.

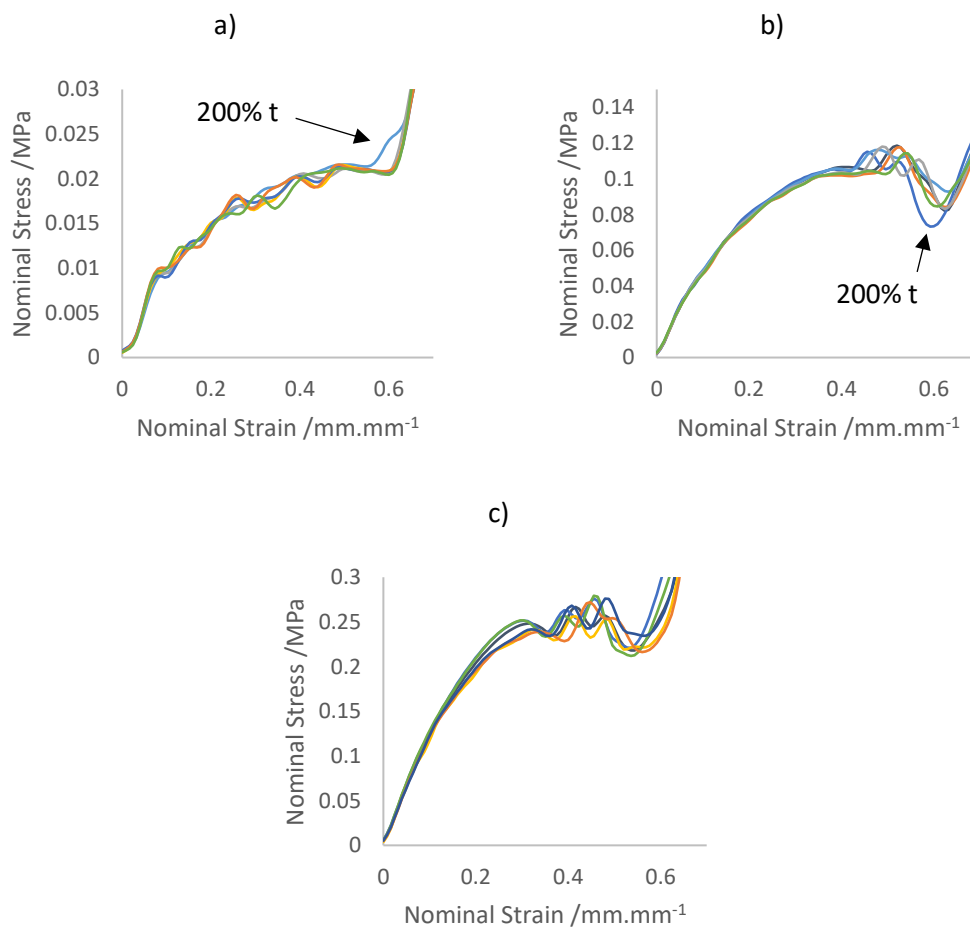


Figure 4.26. Simulated quasi-static compression of 3*3*3 SP cube configurations, with varying mesh size, $l = 10$ mm and, a) $t = 0.5$ mm, b) $t = 1$ mm, c) $t = 1.5$ mm. Note, due to data density legend is not included

While outlier curves can be identified visually (as highlighted in Figure 4.26a and b), there is no immediately apparent difference between the stress-strain responses shown in Figure 4.26. To further evaluate the stress-strain behaviour, the maximum percentage difference in stress for each mesh size was compared (Figure 4.27). The mesh at 50% wall thickness (t) was the smallest mesh size directly linked to wall thickness. As finer meshes are well known to be more accurate, 50% t was selected as the common curve from which difference in stress was calculated.

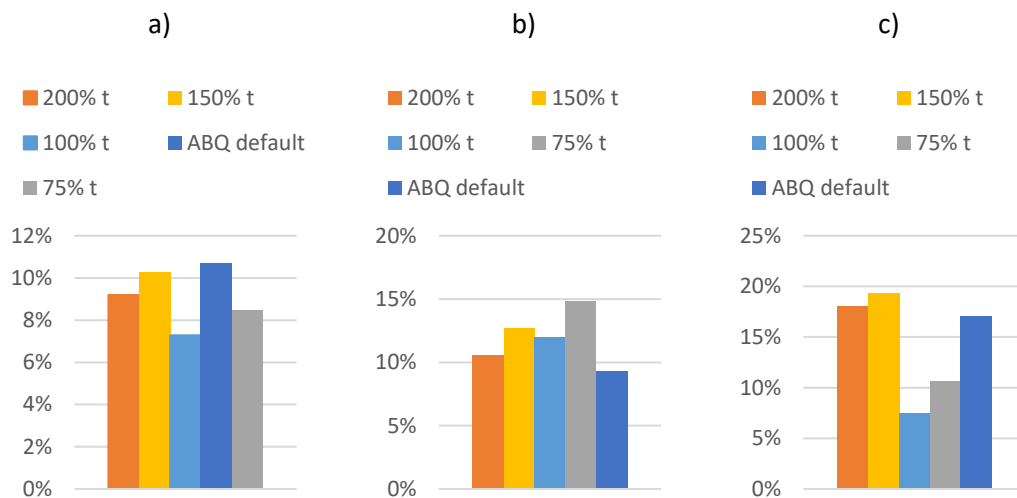


Figure 4.27. The maximum percentage difference in stress, between a mesh size 50% of t and other mesh sizes, for the quasistatic compression of a $3 \times 3 \times 3$ SP cube configuration; with, a) 0.5 mm, b) 1 mm, c) 1.5 mm; note mesh size is organised from left to right for all plots

As with the stress-strain plots (Figure 4.26), there is no discernible pattern. Similarly, when plotting average difference, or difference in terms of discrete values (instead of %), no pattern emerged. Therefore, it can be said that the SP stress-strain response demonstrates minimal mesh size sensitivity.

The energy balance was extensively investigated to ascertain if there were any other effects of altering mesh size. In the case of this investigation, three artificial energies were generated: artificial strain energy (AE), viscous dissipation energy (VD) and kinetic energy (KE).

As covered in section 3.3.1.1, KE can be introduced by time or mass scaling a quasi-static simulation. For all cases, KE was only $\sim 1\%$ of the total energy. As allowable KE is generally $\sim 5\%$ (section 3.3.1.1), and no relationship between mesh size and KE could be identified, KE

was excluded from this analysis. Additionally, for all configurations investigated, VD was <<1%. Therefore, it was also excluded from further analysis.

The final energy, AE, is associated with element distortion. It is an indicator of hour-glassing effects (non-realistic deformation of the mesh), and poor element sizing. The progression of AE within the 1 mm unit cell is shown in Figure 4.28.

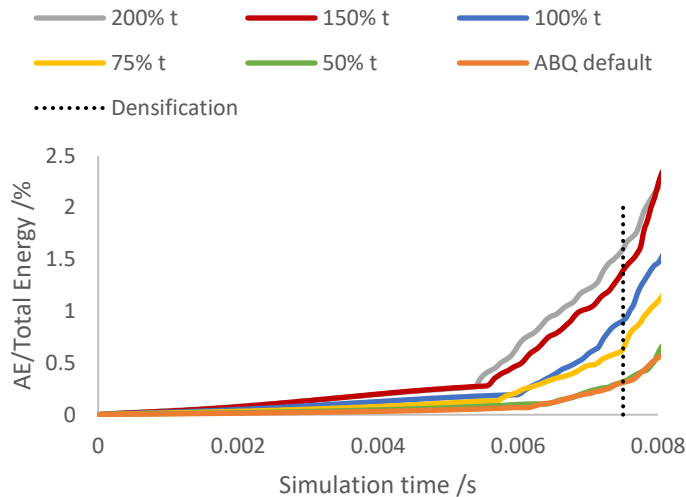


Figure 4.28. Artificial energy (AE) generated in the simulated compression of a 3*3*3 SP cube configuration, with varying mesh size, $t = 1 \text{ mm}$ and $l = 10 \text{ mm}$

Examining Figure 4.28, increases in mesh size can be directly related to an increase in AE. Additionally, as deformation increases past ϵ_d , artificial energies start to increase notably. This increase is likely due to a large number of contact problems developing as densification occurs. As AE makes up the most substantial proportion of artificial energy and is directly affected by mesh size, it was used as the quantifier in this mesh sensitivity study.

Impact mitigating materials are only considered valid up until ϵ_d ; therefore, a structure that deforms beyond this point would not be of interest. Also, as computational power can vary between users, distinct simulation durations provide little information. Therefore, AE was analysed at ϵ_d , with the time taken to complete a simulation normalised by the duration of the longest simulation, as shown in Figure 4.29.

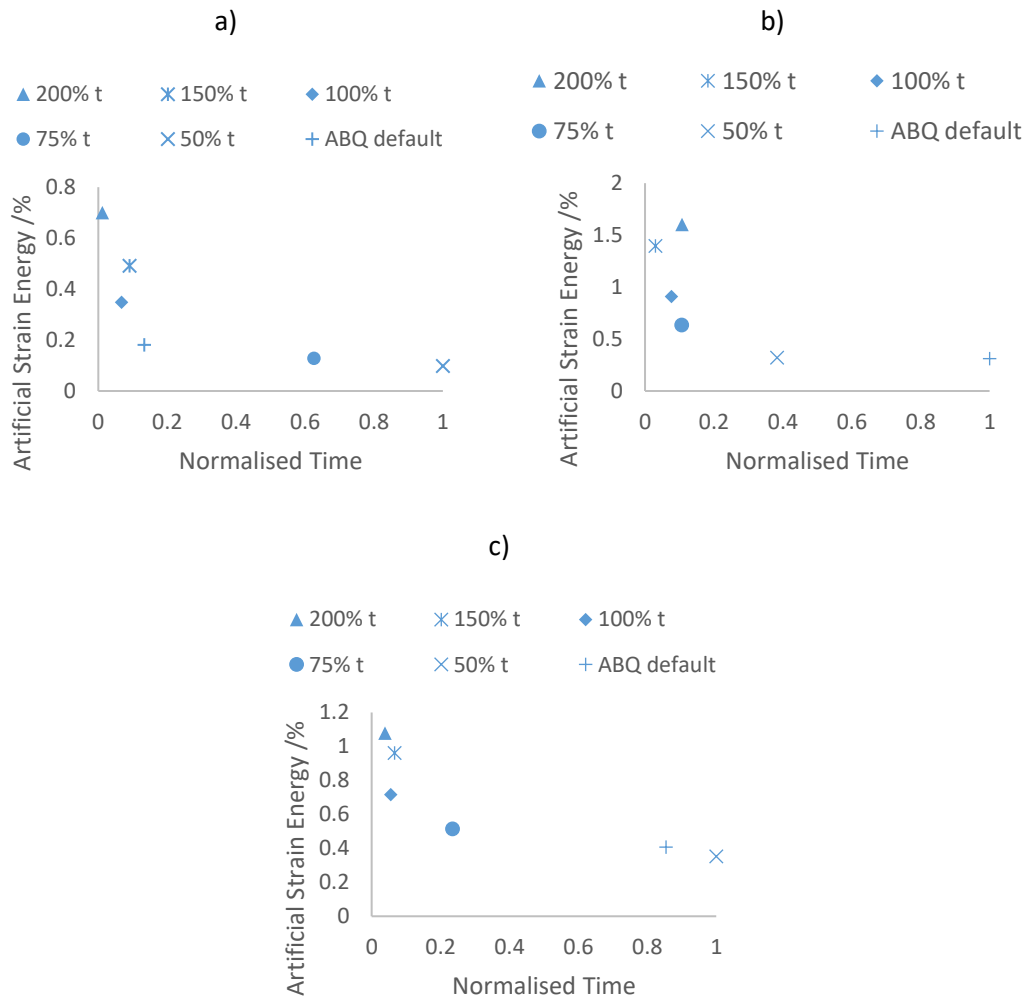


Figure 4.29. Artificial energy (AE) generated in the simulated compression of $3 \times 3 \times 3$ SP cube configurations, at the point of densification, with varying mesh size, $l = 10$ mm, and, a) $t = 0.5$ mm, b) $t = 1$ mm, c) $t = 1.5$ mm

All investigated mesh sizes generated AE below 2% (Figure 4.29). As the acceptable limit for AE is 1-2% [192], all these mesh sizes can be considered below this limit. However, for all thicknesses investigated, 150% t or 200% t result in an increase in simulation time compared to 100% t. Additionally, it can be seen in Figure 4.29b that both 150% t and 200% t have AE levels above 1%, putting them in but not above the 1-2% limit. As these larger mesh sizes provided no benefit to efficiency and had higher AE levels, they are not recommended for use.

As discussed at the beginning of this section, all wall thicknesses were explored with at least one mesh size that resulted in two elements being generated across the thickness of the wall. However, the difference in stress-strain behaviour between single and multiple elements over wall thickness is minimal, for the SP structure (Figure 4.26). Additionally, there is minimal difference in AE between single and multiple elements across the wall

thickness. For example, in Figure 4.29c, the 1.5 mm SP structure has a single element across wall thickness for 75% t and two elements for ABAQUS default and 50% t. This lack of difference would indicate that two elements across walls are not required for simulated compression of the SP structure.

Considering this, a mesh size of 100% t and 75% t were both efficient and had AE below 1%, for the three thicknesses investigated. Of these, 75% t was closer to the point of inflection, for two of the three cases investigated (1 mm and 1.5 mm). Consequently, a mesh size of 75% t was selected for the following simulations of the SP structure. However, a mesh size of 100% t would also be valid in future studies, if 75% t proved to be too computationally expensive.

4.3.1.2 Validation of meshing strategy and material model

A series of mechanical and simulated tests were undertaken to validate the simulation of the NF SP pad using this meshing approach. After manufacture, the wall thickness was measured at an average of 1.4 mm, and this value was used to update the CAD.

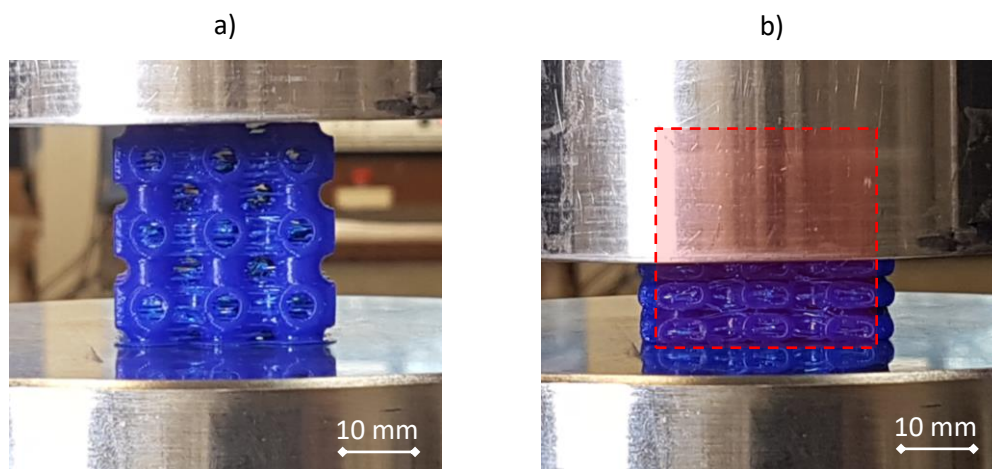


Figure 4.30. Experimental quasi-static compression of an NF SP cube a) un-deformed b) densified (showing uncompressed pad as an overlay)

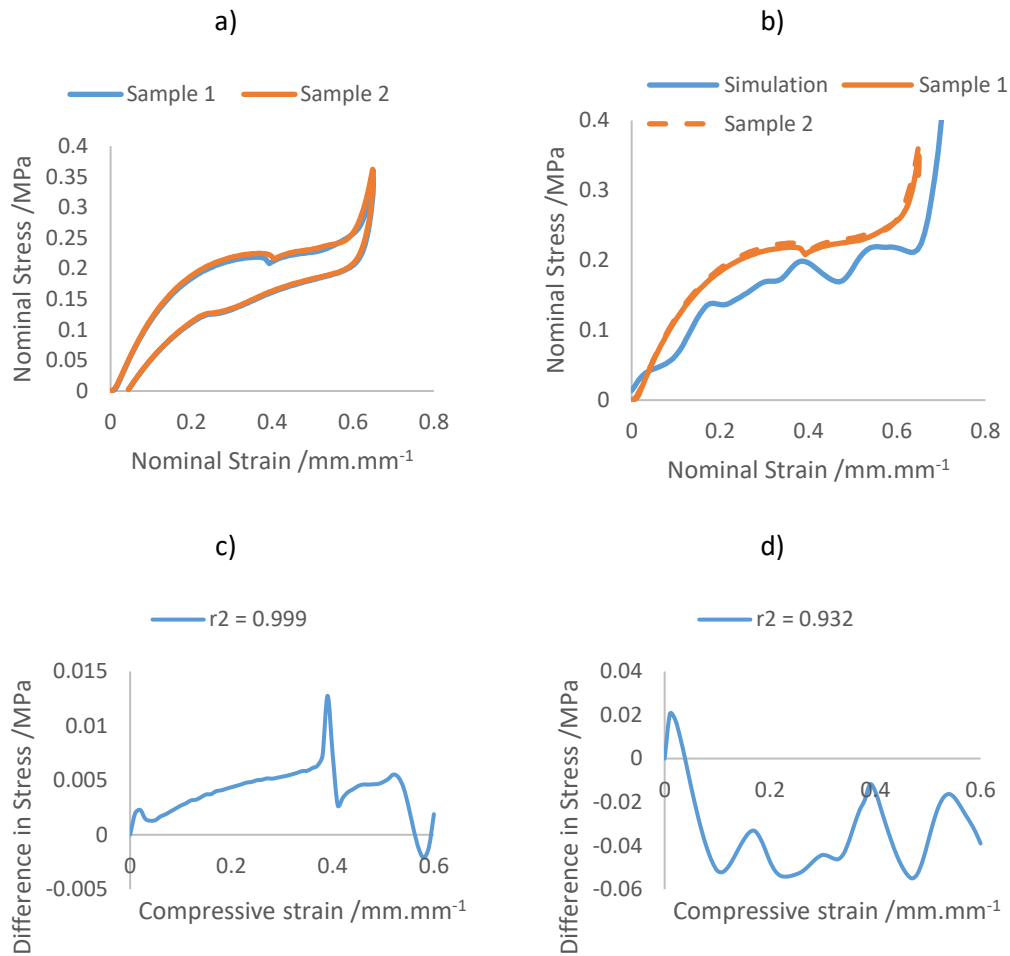


Figure 4.31. Quasi-static compression of NF SP pads, a) experimental loading and unloading, b) comparison of experimental and simulated loading, c) difference in stress between the loading of the two experimental samples, d) difference in simulated and experimental loading stress

As can be seen in Figure 4.31c, the experimental compression of the two test pads has a high degree of correlation, with $r^2 = 0.999$ and a maximum difference of 0.013 MPa. These values provide confidence in the repeatability of the manufacturing process. Figure 4.31b shows the simulated and experimental stress-strain curves for the pads. As can be seen in Figure 4.31d, the simulated and experimental data have a good correlation with $r^2 = 0.91$, and a maximum difference in the stress of 0.05 MPa. The experimental ϵ_d was 0.61, showing good agreement with the simulated ϵ_d (which was only 0.03 lower). For the simulated curve, σ_p was 0.22 MPa, which compared favourably to the experimental data (0.26 MPa). The energy transferred before densification was 4.2 J and 4.7 J, respectively.

In addition to quasi-static validation, dynamic validation was also undertaken. Full mechanical testing dynamic data for NF can be seen in Appendix II.

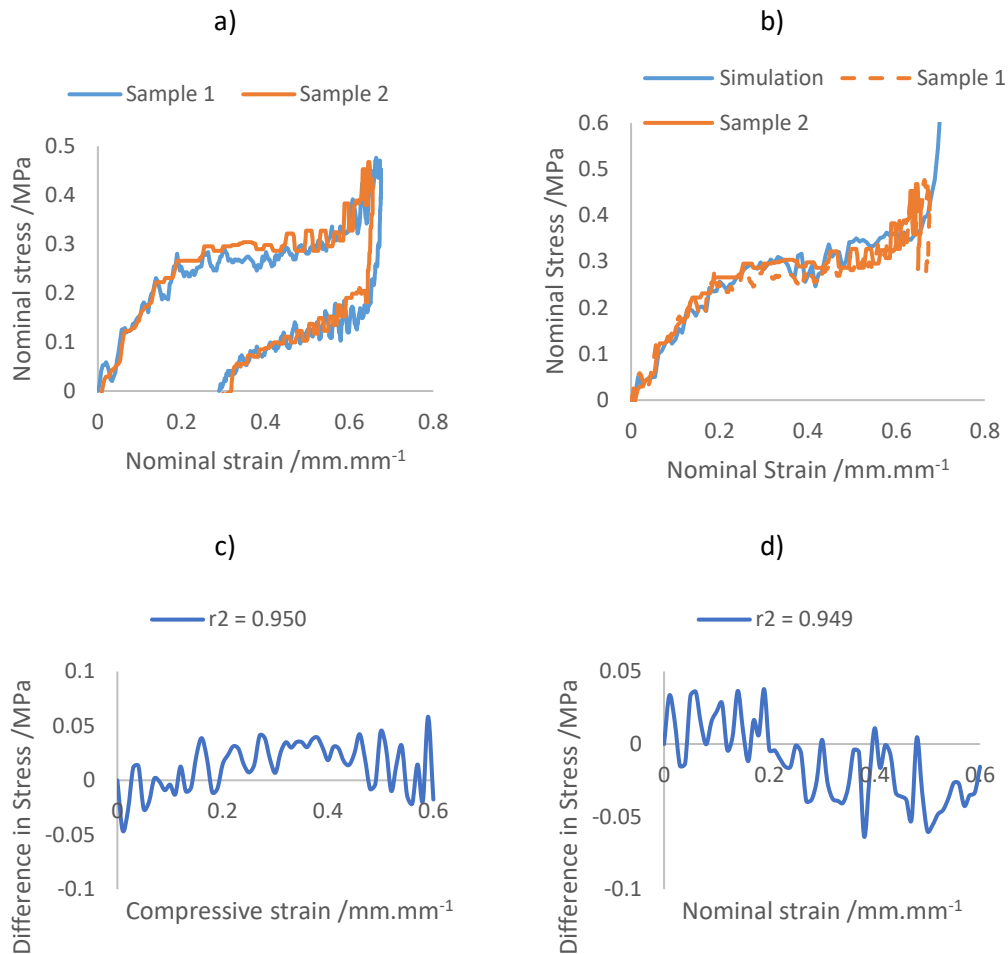


Figure 4.32. Dynamic compression of NF SP pads, a) experimental loading and unloading, b) comparison of experimental and simulated loading, c) difference in stress between the loading of the two experimental samples, d) difference in simulated and experimental loading stress

In Figure 4.32, similarly to the quasi-static testing, there is good repeatability between the two dynamic test pads, with $r^2 = 0.950$ and a maximum difference in stress 0.058 MPa. Plotting the experimental, dynamic data against the simulated data shows good correlation, with $r^2 = 0.949$ and a maximum difference in stress 0.064 MPa. The mechanical data has a ϵ_d of 0.58, and the simulated data had a ϵ_d of 0.63. The energy transferred before densification was 6.4 J for the mechanical tests and 7.1 J for the simulations, while the σ_p was 0.34 MPa and 0.36 MPa, respectively.

Stringing can be observed on the NF SP pads (Figure 4.9). Examination of the high correlation and agreement in stresses observed here would suggest that this stringing has minimal influence. However, there is a difference in recorded ϵ_d for the simulated and experimental response, both quasi-statically and dynamically.

4.3.2 Investigating the effect of varying constraints on the SP structure

4.3.2.1 Ensuring geometric scalability

Configurations of 1*1*1, 2*2*2, 3*3*3, and 5*5*5 were investigated to ensure the performance of one configuration stress-strain performance was scalable. As the 5*5*5 structure had the largest unit cell count, it can be said to be the most representative of higher unit cell counts. Therefore, it was selected to identify correlation and the difference in stress for the other unit cell configurations.

The stress-strain performance, the time required to simulate the configurations, and the difference in stress, are all presented in Figure 4.33.

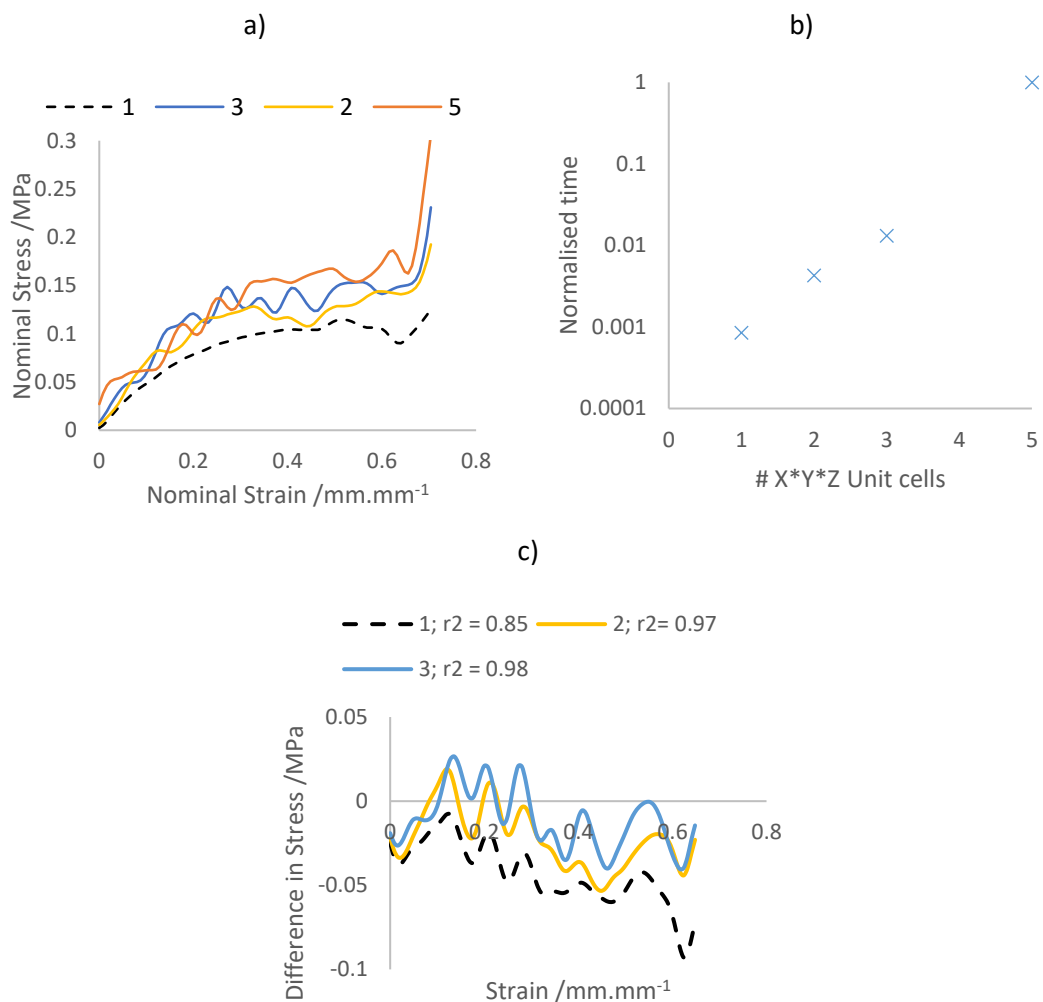


Figure 4.33. Simulating the effect of changing unit cell count a) Stress-strain curves for X*Y*Z configurations of 10 mm unit cell, with a t:l ratio of 0.1:1 (e.g. curve '5' indicates a pad consisting of 5*5*5 unit cells), b) Relationship between X*Y*Z unit cells and the time taken to simulate compression to densification, d) difference in stress between 5*5*5 unit cells and other X*Y*Z configurations

Regardless of the configuration investigated, ϵ_d remains relatively constant at ~ 0.65 , as can be seen in Figure 4.33a. Additionally, while the $1*1*1$ configuration is significantly different from the other configurations investigated, the $2*2*2$ and $3*3*3$ configurations demonstrate good agreement with the $5*5*5$ configuration. Overall, as long as a configuration was greater than $2*2*2$ unit cells, equivalent stress-strain behaviour to larger configurations was observed.

In addition to ensuring equivalent performance, computational efficiency was also investigated. By examining Figure 4.33b, a non-linear relationship between unit cell count and simulation time can be identified. Figure 4.33b was further analysed to explore this relationship, with the results presented in Table 4.6.

Table 4.6. Increase in time taken to simulate the compression of a $1*1*1$ SP unit cell configuration compared to alternative SP unit cell configurations ($2*2*2$, $3*3*3$ and $5*5*5$)

	$2*2*2$	$3*3*3$	$5*5*5$
# of unit cells	8	27	125
Increase to simulation time (from $1*1*1$)	5x	15x	1173x
Increase per unit cell	0.63x	0.56x	9.38x

Table 4.6 shows a significant increase in time associated with the simulation of multiple unit cells. While these increases are significant, the $2*2*2$ and $3*3*3$ configurations have increased efficiency in simulation, on a per unit cell basis. However, this increased efficiency was not observed for the $5*5*5$ configuration, with the per unit cell efficiency dropping by $\sim 15x$. Of these configurations, the $3*3*3$ had the highest efficiency per unit cell.

Considering these effects of unit cell count on efficiency, and the highest agreement being between the $5*5*5$ and $3*3*3$ configurations, the $3*3*3$ configuration was selected for future simulation of the SP structure.

4.3.2.2 Establishing boundary condition sensitivity

When manufacturing a helmet, an SP pad may be adhered to another component, enforcing a fixed boundary. Alternatively, the SP pad may be placed inside a low friction bag, allowing it to compress with minimal restrictions on lateral movement. Therefore, it is important to understand the effects of varying boundary conditions, to establish if the

energy absorption diagram could be applied to both of these cases. Additionally, the inclusion of frictional sliding results in significant increases to simulation time. Therefore, if comparable performance exists between frictionless and frictional boundary contact, frictionless contact can be used to improve simulation efficiency.

The extremes of boundary contacts were explored in this study, with these being frictionless and fixed. These contact boundaries were chosen as all other contacts (such as frictional sliding) should lie between these two contact conditions. A combined condition, where one side of the SP pad was fixed, and the other was frictionless, was also investigated. The results of this investigation are presented in Figure 4.34.

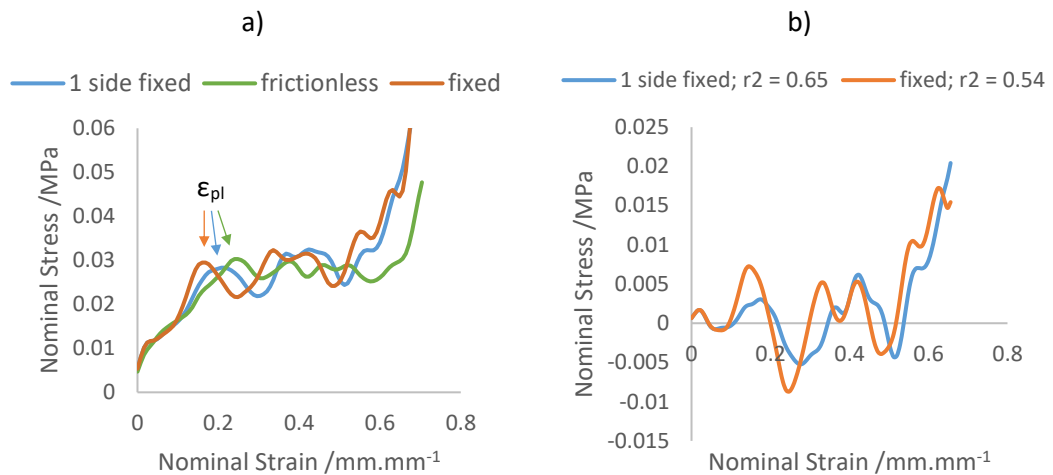


Figure 4.34. Simulated compression of a 3x3x3 NJ SP configuration, with a t:l ratio of 0.05:1 and varying boundary constraints, a) stress-strain curves, b) difference in stress vs frictionless

When examining Figure 4.34a, it is apparent that ϵ_{pl} commences earlier when fixed boundaries are introduced, with ϵ_{pl} decreasing from 0.24 (frictionless) to 0.19 when one side is fixed and 0.16 when both are. Also, ϵ_d decreases when fixed boundaries are introduced, from 0.65 (frictionless) to 0.59. As a result of both ϵ_d and ϵ_{pl} changing, the energy absorbed at densification remains relatively constant, with 0.43 J at frictionless, 0.40 J (93%) with one side fixed and 0.41 J (95%) with both sides fixed.

The fixed boundary contacts have an average correlation with the frictionless data ($r^2 = 0.65, 0.54$); however, the similar energy absorbed, in addition to comparable stress-strain curves in Figure 4.34, suggests good agreement between the different contact conditions. This agreement is supported when evaluating correlation up to a nominal strain of 0.55,

where r^2 values increase to 0.83 and 0.67. Examination of Figure 4.34a also highlights this improved agreement up to a strain of 0.55.

As the SP pad is intended to be used in a helmet, the SP pads will be in contact with a geometric boundary of varying curvature. In a similar manner to the boundary contacts, the extremes of the curvature were explored. The smallest radius on the 535 headform was at the rear (75 mm), and the largest was at the side (roughly flat). The effect of combined curvature and boundary contact was also explored, using the 75 mm radiused surface with frictional contact. The results are presented in Figure 4.35.

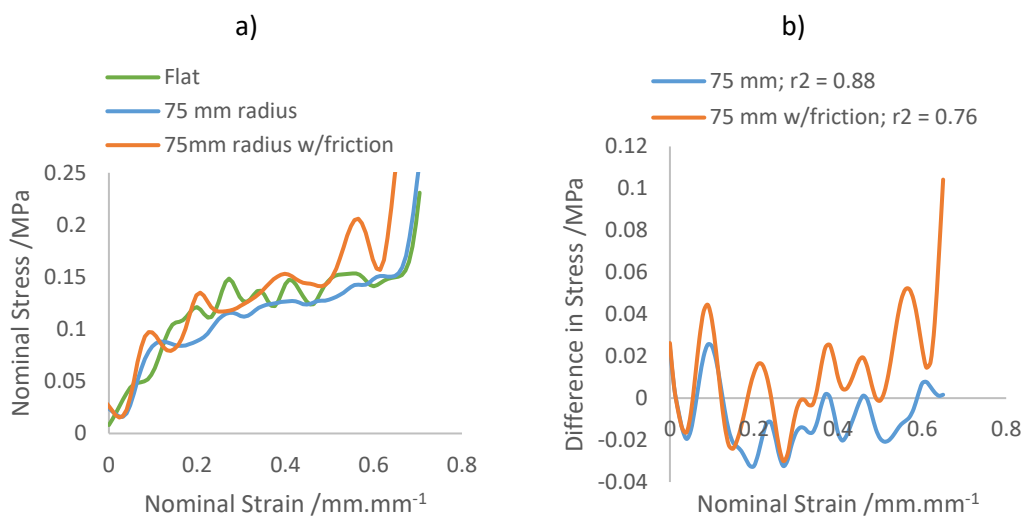


Figure 4.35. Simulated compression of a 3x3x3 NJ SP configuration, with a $t:l$ ratio of 0.05:1 and varying geometric constraints, a) stress-strain curves, b) difference in stress vs frictionless

Examining Figure 4.35a, it is apparent that good agreement exists between the three conditions investigated. The flat and 75 mm radiused boundaries had similar levels of ϵ_d (0.65 flat, 0.64 curved) and energy transferred at densification (2.1 J flat, 2.0 J curved). Meanwhile, the combined 75 mm radiused frictional boundary had a reduced ϵ_d (0.61), but the energy at densification was equivalent to that of the flat boundary (2.1 J). Compared to the investigation into boundary contacts alone, there was no identifiable change in ϵ_{pl} between the three boundary conditions.

Figure 4.35b shows good correlation ($r^2 = 0.88$ and 0.76) and agreement between the flat, frictionless boundary and the 75 mm radius with friction. Similar levels of energy at densification and ϵ_d further support this agreement. Therefore, it can be said that the SP

structure demonstrates little geometric sensitivity in the context of motorcycle helmet design.

4.3.3 NF energy absorption diagram to predict impact behaviour

4.3.3.1 *Collection of simulated stress-strain behaviour*

The responses of different SP configurations were collected at varying speeds for the generation of the energy absorption diagram. An NF SP pad, with a 3*3*3 unit cell configuration and $l = 10$ mm, was computationally compressed past the point of densification. The results of this process for $t:l$ ratio of 0.05:1, 0.1:1 and 0.15:1 are shown in Figure 4.36.

For all the $t:l$ ratios investigated in Figure 4.36, the quasi-static response had the lowest peak stress, and increases in speed led to increased stress. SP pads compressed at 0.5 m/s and 2.5 m/s demonstrated notable agreement in their stress-strain response. Meanwhile, the 7.5 m/s stress-strain curve diverged from the close agreement between 0.5 and 2.5 m/s.

Examining Figure 4.36, it can be seen that the ϵ_d values for the simulated pads are consistent from quasi-static to 2.5 m/s. Additionally, there is little difference in ϵ_d as speed increase from quasi-static (0.65), to 7.5 m/s (0.64), for $t:l$ ratios of 0.05:1 and 0.1:1. However, for a $t:l$ ratio of 0.15:1, ϵ_d reduces when the speed of compression increases from 2.5 m/s (0.62) to 7.5 m/s (0.55).

For a $t:l$ ratio of 0.05:1, ϵ_{pl} occurs at ~ 0.15 , for a ratio of 0.1:1 it occurs at ~ 0.2 and for a ratio of 0.15:1 it occurs at ~ 0.3 . While this indicates a link between increases to ϵ_{pl} and increasing wall thickness, examining Figure 4.36 indicates ϵ_{pl} is unaffected by the increasing speed. In addition to ϵ_{pl} increasing as wall thickness increases, the stress-strain plateau becomes increasingly inclined as the SP structure's wall thickness increases.

These changes to ϵ_{pl} , plateau behaviour and ϵ_d result in reduced energy mitigation efficiency, as wall thickness increases.

As specified in section 3.3.3, these SP configurations were also simulated at higher test speeds (Figure 4.37).

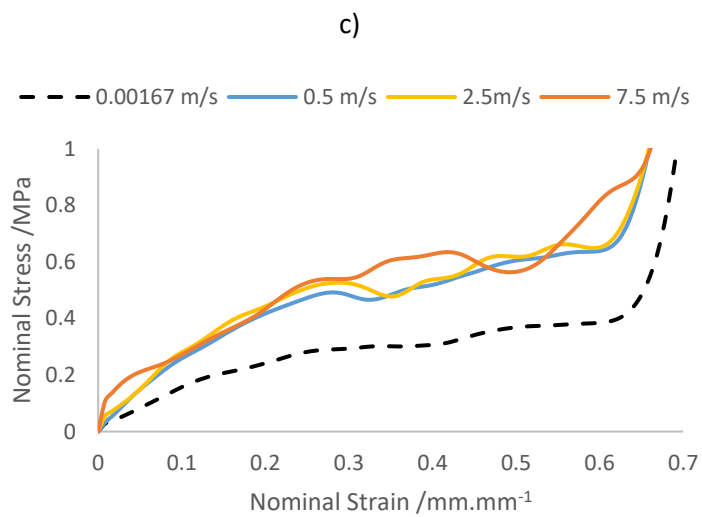
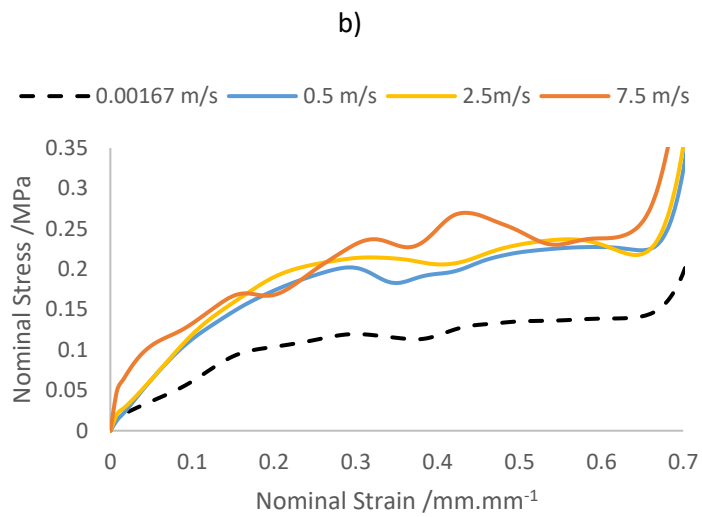
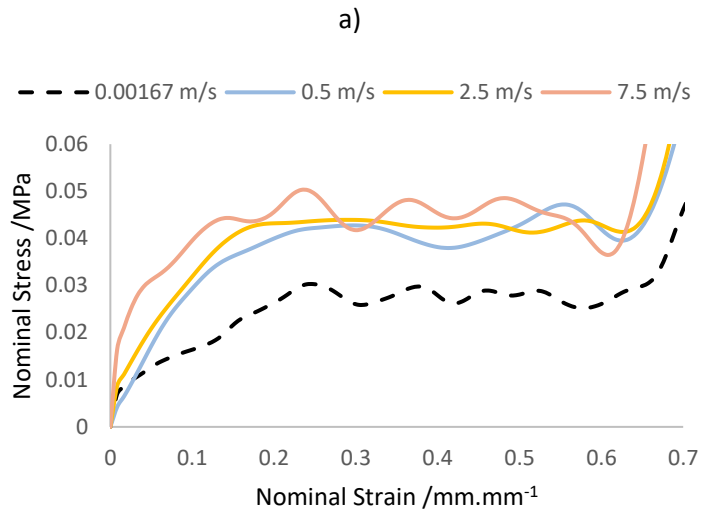


Figure 4.36. Simulated compression of 3*3*3 NF SP pads, from speeds of 0.00167 – 7.5 m/s: a) $t:l = 0.05:1$, b) $t:l = 0.1:1$, c) $t:l = 0.15:1$

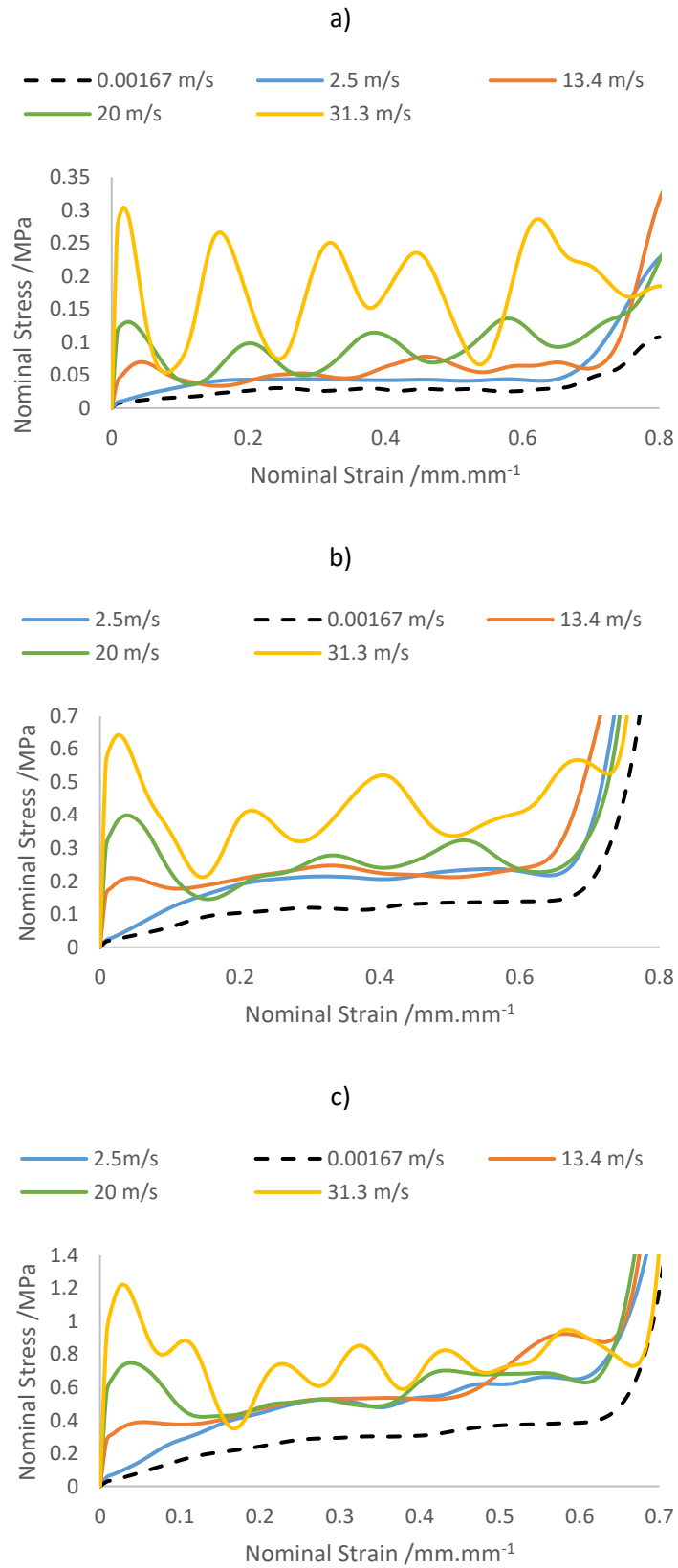


Figure 4.37. Simulated compression of 3*3*3 NF SP pads, from speeds of 0.00167 – 31.3 m/s: a) $t:l = 0.05:1$, b) $t:l = 0.1:1$, c) $t:l = 0.15:1$

The SP configuration with a t:l ratio of 0.05:1 had an increase in the amount of energy stored by 9.3x, from quasi-static to 31.3 m/s. Comparatively, the SP configuration with a t:l ratio of 0.1:1 increased by 4.5x, and the configuration with a t:l ratio of 0.15:1 only increased by 3.1x. Therefore, rate-sensitivity appears to increase, as the t:l ratio decreases.

Figure 4.36 highlighted a reduction in ϵ_d between 2.5 and 7.5 m/s, while Figure 4.37 shows significant increases to ϵ_d as the speed increases past 7.5m/s. This pattern of increasing ϵ_d is observed as low as 13.4 m/s for a t:l ratio of 0.05:1, while it is only observed at higher speeds (31.3 m/s) for t:l ratios of 0.1:1 and 0.15:1. Changes in ϵ_d are recorded in Table 4.7.

Table 4.7. *Densification strain (ϵ_d) of 3*3*3 SP pads, when compression is simulated for different speeds and t:l ratios*

t:l ratio	0.05:1	0.1:1	0.15:1
ϵ_d (0.0017 - 2.5 m/s)	0.65	0.65	0.62
ϵ_d (7.5 m/s)	0.64	0.64	0.55
ϵ_d (31.3 m/s)	>0.83	0.76	0.67

Examining Figure 4.37, a high degree of undulation is observed in the stress-strain curves at 31.3 m/s. While this undulation could be attributed to noise within the simulation, an examination of the simulated deformation highlights this is unlikely. The changes in deformation pattern are shown in Figure 4.38, for an SP structure with a t:l ratio of 0.05:1. Note, Figure 4.38 and Figure 4.40 display deformation in the direction of compression, with red being maximum (~ 10 mm) and dark blue being minimum (~ 0 mm).

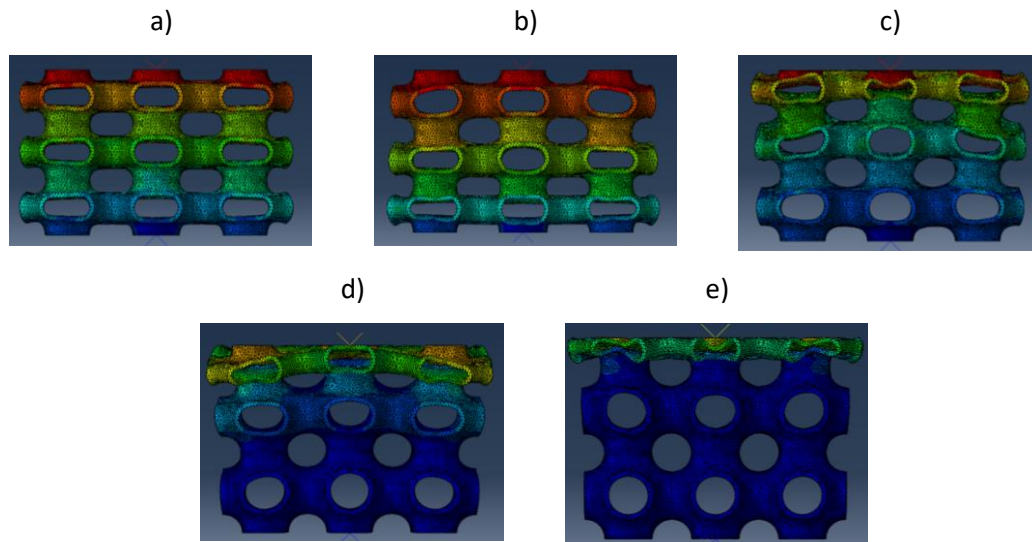


Figure 4.38. Deformation pattern observed in a simulated 3*3*3 NF SP pad at a nominal compressive strain of 0.33, with a t:l ratio of 0.05:1, under varying loading speed, a) quasi-static to 2.5 m/s, b) 7.5m/s, c) 13.4 m/s, d) 20 m/s, e) 31.3 m/s

At a t:l ratio of 0.05:1, the deformation observed at ≤ 2.5 m/s is equally spread over the height of the SP structure (Figure 4.38). However, increasing the speed to 7.5 m/s results in deformation appearing to be focussed towards the base. By examining the simulation, it was identified that this was the result of the deformation oscillating up and down the SP structure as it compressed. From 13.4 m/s onwards the deformation appeared focussed towards the top of the structure, with the upper unit cells compressing before the lower ones. This focus at the top of the SP structure was observed throughout these higher compressive speeds. At a speed of 31.3 m/s, the lower sets of unit cells had minimal compression until the upper cells had densified. Further breakdown of the deformation pattern at 31.3 m/s is shown in Figure 4.39, with red being equivalent to ~ 0 mm of deformation and dark blue being equivalent to maximum deformation.

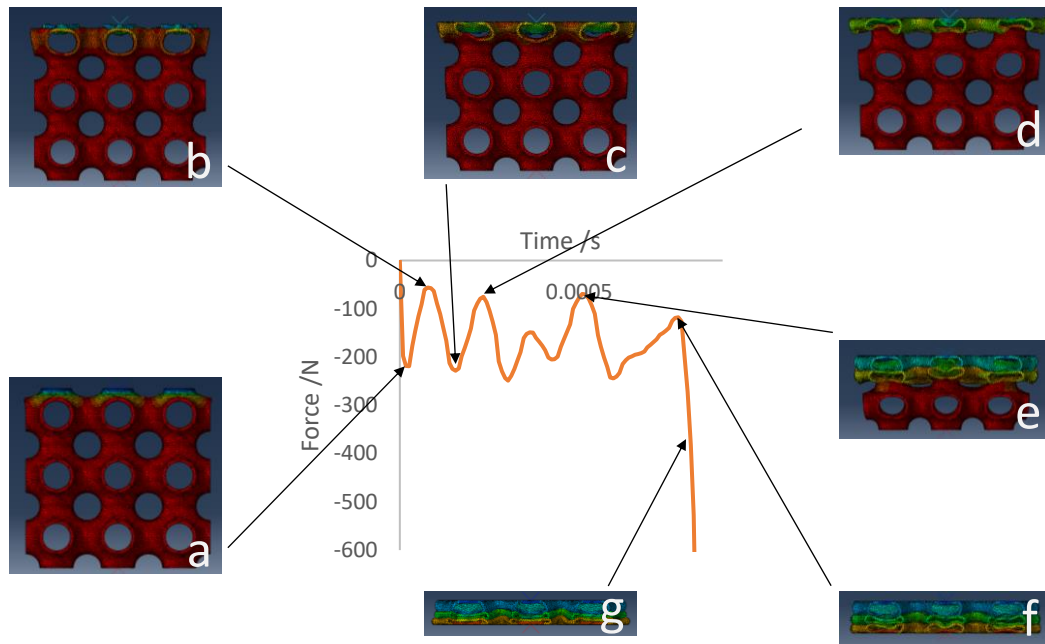


Figure 4.39. Stages of compression observed when a 3*3*3 NF pad undergoes a simulated 31.3 m/s compressive impact, with a t:l ratio of 0.05:1 (l = 10 mm)

When examining Figure 4.39, the peaks and troughs of the undulation can be directly linked to collapse behaviour. The initial compression of the upper half of the unit cell results in a peak in force (Figure 4.39a). Following this peak in force, ‘snap-through’ mechanic occurs in the upper half of the unit cell, resulting in a reduction in force (Figure 4.39b). Following this, the lower half of the unit cell is compressed by the densified upper section, resulting in another peak in force (Figure 4.39c). This is followed by another ‘snap-through’ mechanic and associated reduction in force (Figure 4.39d). This pattern repeats until all cells are densified. As each set of unit cells effectively densifies before compressing the unit cells below it, the densification of the final layer of unit cells occurs at a higher ϵ_d than for the lower test speeds. Similar behaviour can be observed when the t:l ratio increases to 0.15:1 (Figure 4.40).

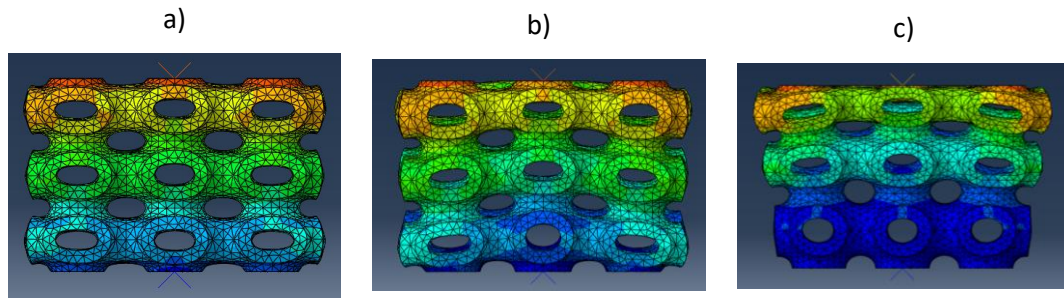


Figure 4.40. Deformation pattern observed in a 3*3*3 NF SP pad under a simulated nominal compressive strain of 0.33, with a t:l ratio of 0.15:1, under varying loading speed, a) quasi-static to 7.5 m/s, b) 20 m/s, c) 31.3 m/s

As with a t:l ratio of 0.05:1, 0.15:1 also demonstrates rate-sensitive deformation patterns (Figure 4.40). However, these do not occur until speeds exceed 7.5 m/s. The same behaviour observed in the 7.5 m/s impact for a t:l ratio of 0.05:1 (unit cells oscillating) only becomes apparent at 20 m/s. Similarly, the concentration of compression at the top of the structure observed at 13.4 m/s for a t:l ratio of 0.05:1 only began to emerge at 31.3 m/s for a t:l ratio of 0.15:1.

Rate-dependence occurs in cellular structures, becoming apparent at higher-speed experimentation, with different deformation behaviour developing compared to quasi-static experimentation [199]. This behaviour is commonly only seen in cellular structures during extremely high-speed compression. For example, a metallic strut-based structure demonstrated rate dependence at 9126 s^{-1} [199]. However, this work has shown that for a t:l ratio of 0.05:1, rate dependence begins to occur in the SP structure by 7.5 m/s, equivalent to 250 /s . This low speed rate-dependence brings into question the current practice of defining energy absorption diagrams by strain rate alone. While potentially appropriate in legacy applications (e.g. foams), emerging cellular structures that demonstrate significant rate-sensitive effects would be better linked to discrete speeds than strain rates.

4.3.3.2 Processing stress-strain data into an energy absorption diagram

After simulating the compression of the SP configurations (section 4.3.3.1), the resultant stress-strain curves need to be converted for use in the energy absorption diagram. The results of this process, for SP structures with t:l ratios of 0.05:1, 0.1:1 and 0.15:1 are presented in Figure 4.41.

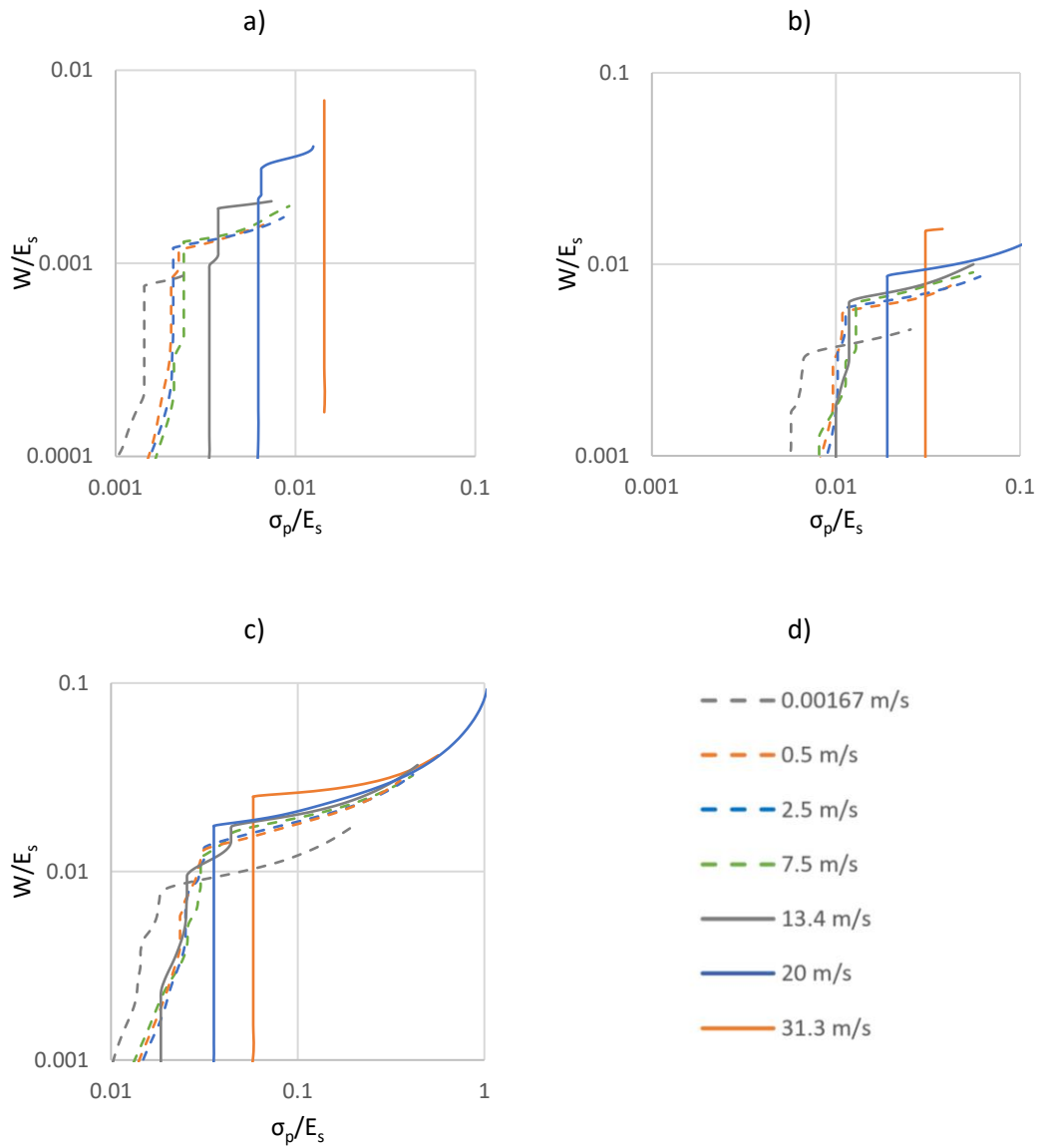


Figure 4.41. Simulated compressive $W-\sigma_p$ curves for $3*3*3$ SP pads, over varying speeds (0.00167 – 31.3 m/s), with different densities ($t:l$ ratios), a) $t:l = 0.05:1$, b) $t:l = 0.1:1$, c) $t:l = 0.15:1$, d) legend

The inflection point, indicative of efficient use of the SP structure, was then identified for each W/σ_p curve. Each set of inflection points, from diagrams shown in Figure 4.41, were then processed into a combined energy absorption diagram (Figure 4.42).

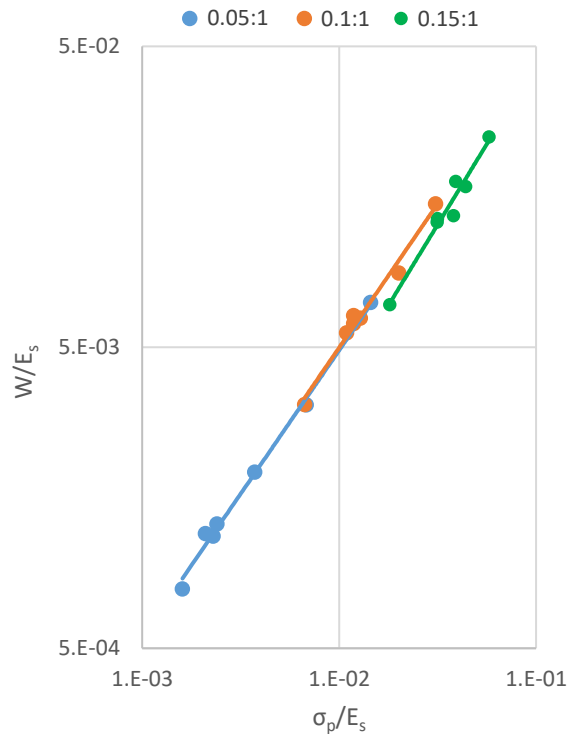


Figure 4.42. Combined normalised W - σ_p plot for the NF SP structure, from speeds of 0.00167 – 31.3 m/s and $t:l$ ratios of 0.05:1, 0.1:1 and 0.15:1

Lines of constant density were plotted to the inversion points using power curves, as this provided the best fit to the collected data.

4.3.3.3 Comparison of NF SP structure to established motorcycle liner materials

The SP surface was selected as it exceeded the energy mitigation performance of expanded polystyrene (EPS) when manufactured from nylon (section 2.3.2.4). To ensure this performance was retained when changing the base material, the normalised curves of elastomeric and nylon SP structures were compared. The nylon SP structures were only tested quasi-statically in the literature (section 2.3.2.4), so this comparison does not explore rate dependence. The stress-strain responses of the nylon SP structure were provided in terms of density, rather than wall thickness (0.127 and 0.24). Therefore, NF SP structures with $t:l$ ratios closest to these densities were selected for comparison, at: 0.05:1 (density = 0.117) and 0.1:1 (density = 0.232). The resultant energy absorption diagram is shown in Figure 4.43.

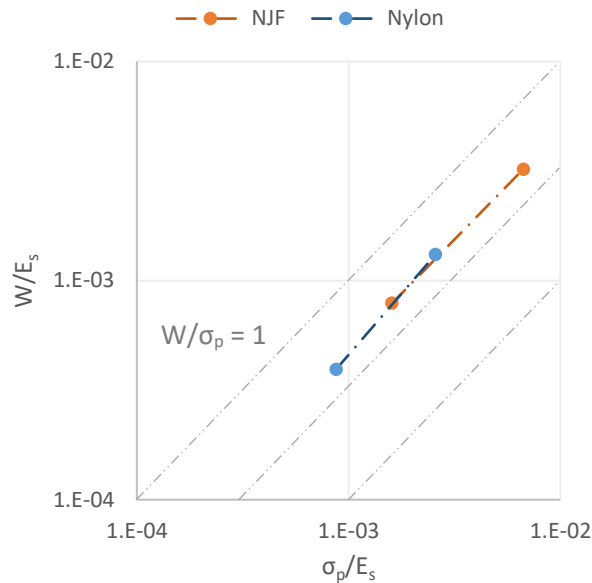


Figure 4.43. Comparison of quasi-static compression of NF ($\rho = 0.117$ and 0.232), and nylon ($\rho = 0.127$ and 0.24), SP structure W - σ_p performance

As can be seen in Figure 4.43, the NF SP structures demonstrate increased normalised energy transferred and σ_p , compared to nylon SP equivalents. This increase could be due to the E_s value chosen to normalise the nylon SP response in section 2.3.2.4. Depending on processing parameters, this value can vary. Additionally, the E_s was taken directly from a datasheet, which may have calculated a higher E_s . While there are changes to the SP response, the overall efficiency is unchanged (i.e. both NF and nylon SP structures sit on a common “ $W/\sigma_p = 1$ ” line).

In section 2.3.2.4, it was noted that the nylon SP stress-strain response undulated significantly. Comparatively, the NF SP structure did not exhibit this behaviour until dynamically loaded (Figure 4.36). This undulation inherently reduces the efficiency of energy transferred in the nylon variant. For both NF and nylon SP structures, ϵ_d was similar, at 0.65 (NF) and 0.64 (nylon). Therefore, the lack of change in efficiency (common “ $W/\sigma_p = 1$ ” line), despite the nylon SP structures having undulation, is likely due to the ϵ_{pl} for the nylon SP structures beginning at ~ 0.1 . This ϵ_{pl} was less than half that of the NF SP structures (~ 0.25). Therefore, the nylon SP structure offsets the loss in energy efficiency by reaching the stress plateau earlier.

After assessing the performance difference between an SP structure made from a semi-rigid polymer and an elastomer, the full elastomeric SP diagram (Figure 4.42) was plotted alongside two established energy mitigation materials (EPS and EF, from section 2.3.1.1).

The inflection points from Figure 4.42 were removed to reduce data density, leaving the power curves that defined constant density. Also, for each class of material (EPS, EF, SP), lines of constant speed were plotted using power curves. The lines of constant density are solid/dashed, while fainter dotted lines indicate maximum (31.3 m/s) and minimum (quasi-static) speeds. Note, data for EF and EPS was provided at strain-rates as opposed to speeds, so was converted into speed-dependent data by assuming a foam thickness of 30 mm.

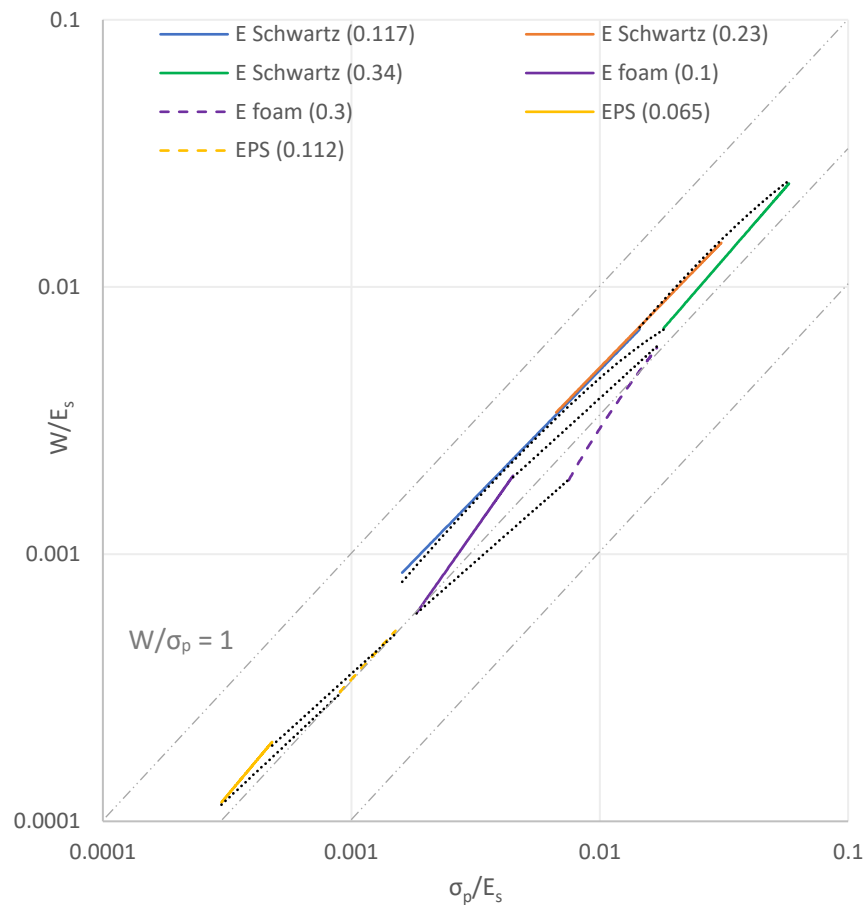


Figure 4.44. Energy absorption diagram for the NF TPU SP structure, alongside inferred elastic foams (EF), and mechanical test data for EPS foams

Examining Figure 4.44, the SP structure is more efficient than the plotted EPS and EF densities. Examining the “ $W/\sigma_p = 1$ ” lines, for comparable relative densities EPS (0.112) has a lower efficiency than EF (0.1), which has a reduced efficiency compared to the SP structure (0.117). There is also a pattern of reduced efficiency with increasing relative density for all materials plotted here. As an exception to this, when the relative density of the SP structure is increased from 0.117 to 0.23, there was little change to the efficiency.

This lack of change indicates that up to relative densities of ~ 0.23 , the SP structure has consistent levels of efficiency.

By scaling the energy absorption curves shown in Figure 4.44, by their base material E_s (assuming EF was also produced from NF), Figure 4.45 was produced. This scaled diagram displays the real-life performance of the structures.

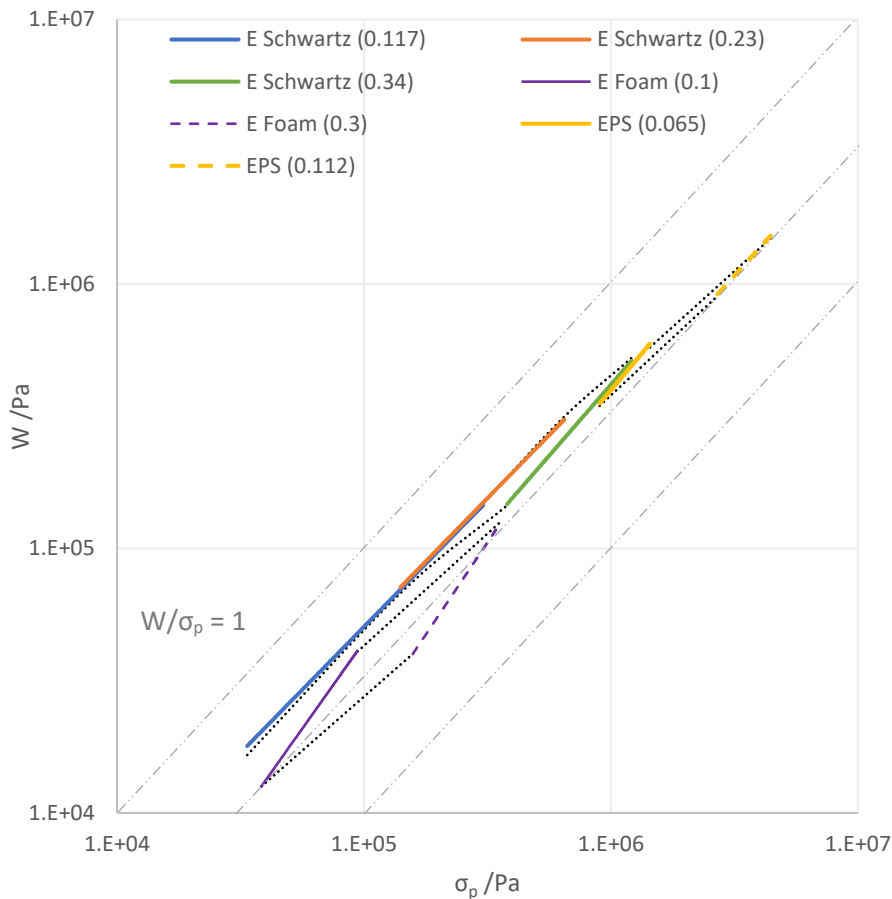


Figure 4.45. Energy absorption diagram for NF SP, NF EF, and EPS, scaled by their respective E_s values

As can be seen in Figure 4.45, while the efficiency of the structures does not change, EPS generates significantly increased W and σ_p compared to NF EF and SP configurations at equivalent densities. For example, the 0.065 EPS curve has similar levels of W and σ_p to the 0.34 NF SP curve. While this indicates that NF SP structure of ~ 0.34 should be similar in performance to the average density EPS used in motorcycle helmets (0.055), it leaves a narrow margin of error.

Markers were plotted for each material class to further investigate their performance at the UNECE 22.05 test speed (7.5 m/s). The lines of constant speed and density were then removed to improve data clarity. For the SP structure, markers were plotted for t:l ratios of 0.05:1, 0.067:1, 0.083:1, 0.1:1, 0.117:1, 0.133:1, 0.15:1. These are equivalent to relative densities of: 0.117, 0.156, 0.193, 0.23, 0.271, 0.307, 0.34

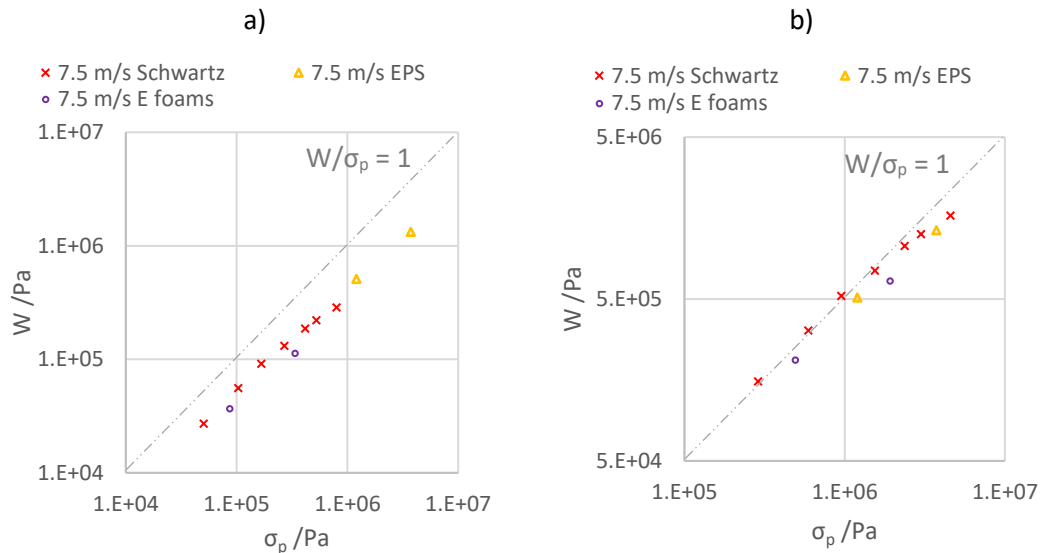


Figure 4.46. Densification ($W-\sigma_p$) markers for SP, EPS, and EF at 7.5 m/s, a) E_s scaled energy absorption diagram, using $NF E_s$ to scale SP and EF, b) E_s scaled energy absorption diagram, using 120MPa E_s to scale SP and EF

Further to the analysis of Figure 4.45, Figure 4.46a demonstrates the NF SP structure (0.34) cannot meet the performance of EPS foam (0.065) due to its low E_s (21 MPa). While the 0.34 NF SP structure could potentially meet the performance of the average motorcycle helmet EPS foam (0.055), there is a narrow margin of error. This narrow margin indicates an elastomeric base material with a higher E_s value is required to comfortably exceed the performance of EPS. Additionally, it is desirable to have a higher E_s , as this enables the use of low-density SP structures, which are more efficient. For example, when E_s is increased to that of the derived Vinyl Nitrile (VN) modulus (120 MPa – section 2.3.1.1), configurations of the SP structure mitigate higher energies for any given σ_p value, compared to both elastomeric foam (VN) and semi-rigid foam (EPS) (Figure 4.46). Note, between 20th – 23rd May 2019 [162], after the completion of the experimental work in this research, DuPont™ began selling a commercial FFF material with a modulus of 130 MPa [200]. This development provides confidence that the performance in Figure 4.46b will likely be achievable in future research.

4.3.4 Procedure for switching the base material

Section 4.3.3.3 highlighted that meeting the requirements of UNECE 22.05 would be challenging for even the higher density NF SP structures. However, Figure 4.46b demonstrated how improving E_s could allow the SP structure to exceed these requirements comfortably. Therefore, an alternative material with a higher E_s was identified.

Cheetah (CH) is a TPU [195] manufactured by the same company that produced NF, but it had double NF's modulus according to technical datasheets [182, 195]. Therefore, the NF energy absorption diagram (Figure 4.44) was scaled 2x, resulting in a scaled energy absorption diagram for CH (Figure 4.47).

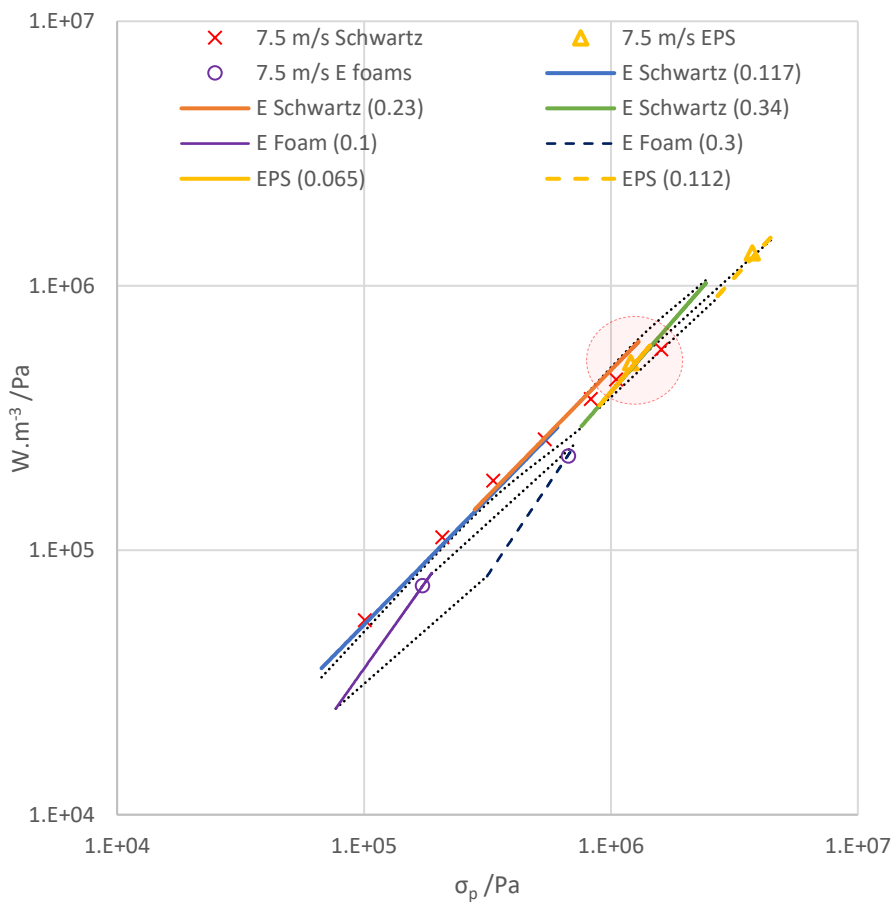


Figure 4.47. Energy absorption diagram for CH SP, CH EF, and EPS, scaled by their respective E_s values

As highlighted in Figure 4.47, at 7.5 m/s a CH SP structure with a t:l ratio between 0.133:1 and 0.15:1 has a similar performance to a 65 kg/m³ EPS foam. As the average density of EPS foam used in motorcycle helmets is 55 kg/m³ (section 2.1.1), this would suggest that a CH could be used to produce an SP liner that would meet the performance requirements of

UNECE 22.05. Note, as discussed in section 3.3.4, the energy absorption diagram (Figure 4.47) is independent of any changes in viscoelasticity between NF and CH.

To ensure the effective E_s of CH was double that of NF, uniaxial tension testing was undertaken as per section 3.2.2.2. The results are shown in Figure 4.48.

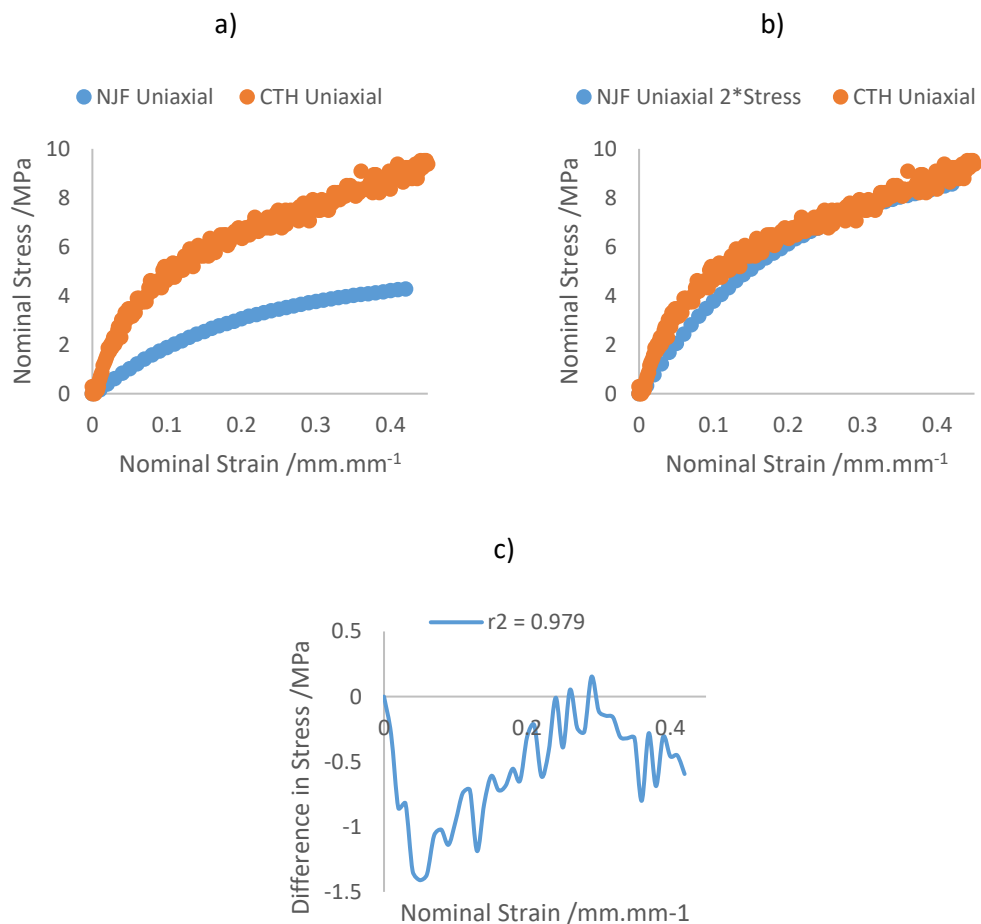


Figure 4.48. Mechanical tensile testing of uniaxial samples, a) CH and NF, b) CH and doubled NF, c) difference in stress between doubled NF and CH, with r^2

Examining Figure 4.48b, if CH's E_s were to be directly determined from the CH uniaxial response, it would be 61 MPa. As E_s was used to normalise the NF energy absorption diagram, this would suggest that 61 MPa should scale the diagram to CH. However, if this E_s is used to scale the NF energy absorption diagram, it results in CH SP configurations having 2.95x the performance of equivalent NF SP configurations. This increase in performance is ~50% higher than the relative uniaxial performance would indicate (doubled NF E_s – Figure 4.48b), making it unrepresentative of CH's actual performance. As σ_p and W are both

calculated from stress-strain curves, the overall difference in response between stress-strain curves was used to scale energy absorption diagrams instead.

Figure 4.48b demonstrates how scaling the NF stress-strain data by 2x results in a good correlation to the CH stress-strain data ($r^2 = 0.979$), with a maximum difference in the stress of 1.41 MPa. When comparing the amount of energy transferred (W/m^3), the CH stress-strain curve mitigates similar levels of energy (97.5%) as that of the doubled NF stress-strain curve.

Generally, the overall agreement between the stress-strain curves, the close correlation and agreement in transferred energy, suggest that doubling of the NF E_s (from 21 MPa to 42 MPa) is representative of CH quasi-static performance. Therefore, a new HE material model was curve-fit for CH, using doubled NF tensile, biaxial, and shear test data. The coefficients for this model are presented in Table 4.8.

Table 4.8. Hyperelastic coefficients, for the scaled CH Moony-Rivlin material model

C10 /MPa	C01 /MPa
6.63	-1.06

In addition to re-characterising the HE component of the material model, the viscoelastic response of CH needs to be characterised. Following the same approach as in section 4.2.3.2, the viscoelastic response of CH was collected from the stress relaxation of a uniaxial tensile dumbbell. This response was then processed to remove the loading ramp and manually shifted in the time domain (as per NF in section 4.2.3.2). The resultant normalised CH stress-relaxation data is presented alongside that for NF (Figure 4.49). A Prony series was curve-fit to the CH viscoelastic data, and its coefficients are presented in Table 4.9.

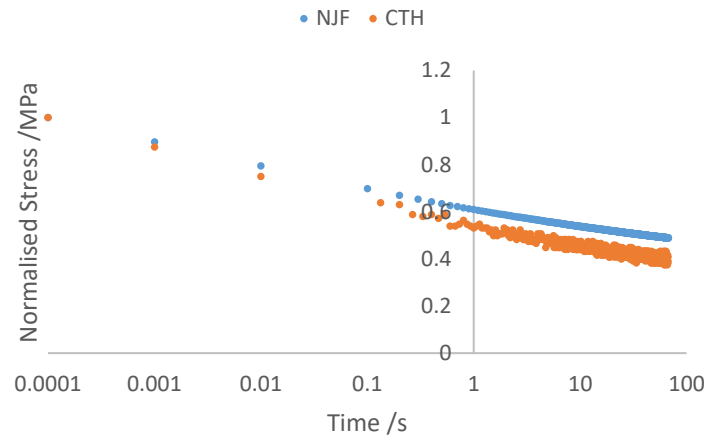


Figure 4.49. Normalised experimental uniaxial tensile stress relaxation data, for CH, and NF

Table 4.9. Prony coefficients, from CH stress relaxation experiments

	G /MPa	K /MPa	tau /s
1	0.477	0.0000	1.21E-02
2	0.125	0.0000	15.82

When comparing the extrapolated normalised stress-relaxation curves for NF and CH (Figure 4.49), a notable difference can be observed. The long-time normalised stress (100 seconds) of CH is ~25% lower than of NF. This increased difference indicates CH has increased viscoelasticity and therefore rate-dependency over NF, in addition to having a higher E_s .

The combined CH HE and viscoelastic material model was then validated. A CH SP configuration was arbitrarily selected and a series of mechanical and simulated tests were undertaken. After manufacture, the wall thickness was measured at an average of 1.5 mm and this value was used to update the CAD.

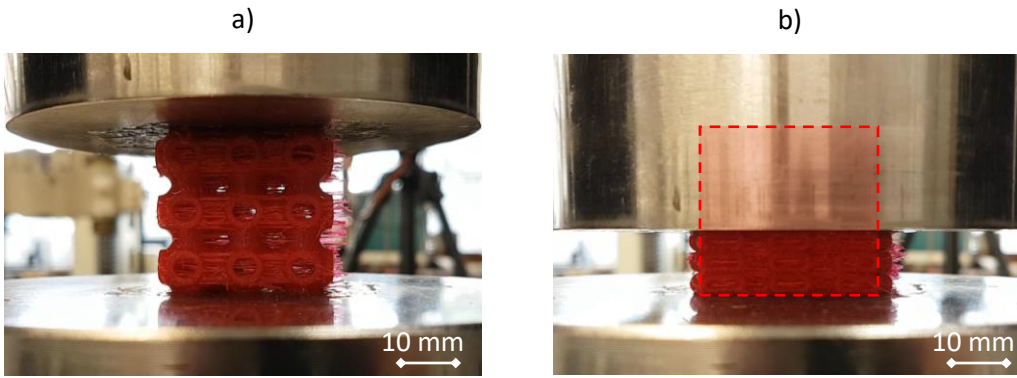


Figure 4.50. Experimental quasi-static compression of CH SP pad a) un-deformed b) densified (showing uncompressed pad as an overlay)

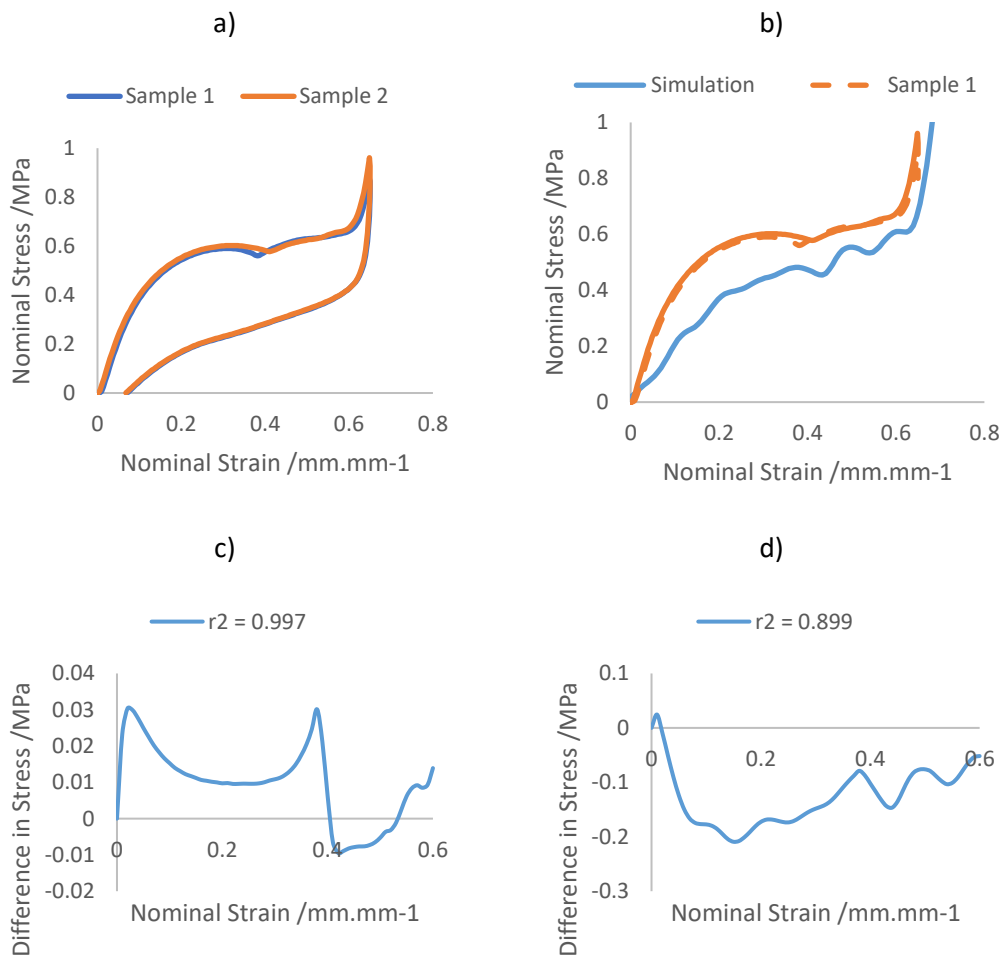


Figure 4.51. Quasi-static compression of CH SP pads, a) experimental loading and unloading, b) comparison of experimental and simulated loading, c) difference in stress between the loading of the two experimental samples, d) difference in simulated and experimental loading stress

As with the NF SP pads, the quasi-static testing of the CH SP pads shows good repeatability, with a high correlation of $r^2 = 0.997$ and a maximum difference in the stress of 0.03 MPa, for the loading phase. The experimental ϵ_d was 0.6, and the simulated ϵ_d was 0.64. The simulated and experimental data also have a good correlation with $r^2 = 0.899$ and a maximum difference in the stress of 0.21 MPa. For the simulated and experimental curves, σ_p was 0.61 MPa and 0.66 MPa respectively. Additionally, the energies mitigated were 11.0 J and 13.6 J, respectively.

In Figure 4.51d, the difference in stress for the CH SP structure drops from 0.2 MPa to 0.075 MPa over a nominal strain range of 0 to 0.6. Comparatively, the NF SP structure had a consistent difference in the stress of ~ 0.045 MPa over the same strain range. This changing difference in stress implies that the CH material model has reduced agreement between experimental and simulated stress-strain responses before ϵ_{pl} .

The reduced agreement can be explained by the reduced E_s of the doubled NF uniaxial data, compared to the actual CH uniaxial data. Between a nominal strain of 0 and ~ 0.25 the doubled uniaxial NF data, which was used to scale the HE material model, had a lower instantaneous modulus than the actual CH uniaxial data (Figure 4.48). Additionally, the internal strains experienced by the SP structure before ϵ_{pl} are 0.11 (at a t:l ratio of 0.15:1) to 0.28 (at a t:l ratio of 0.05:1), as shown in Figure 4.9. Therefore, at compressive strains below ϵ_{pl} , internal strains were within the strain range that the doubled NF model underestimated the actual CH stress response.

As with NF SP pad validation (section 4.3.1.2), dynamic validation was also undertaken, as presented in Figure 4.52. Full mechanical testing dynamic data for CH can be examined in Appendix III.

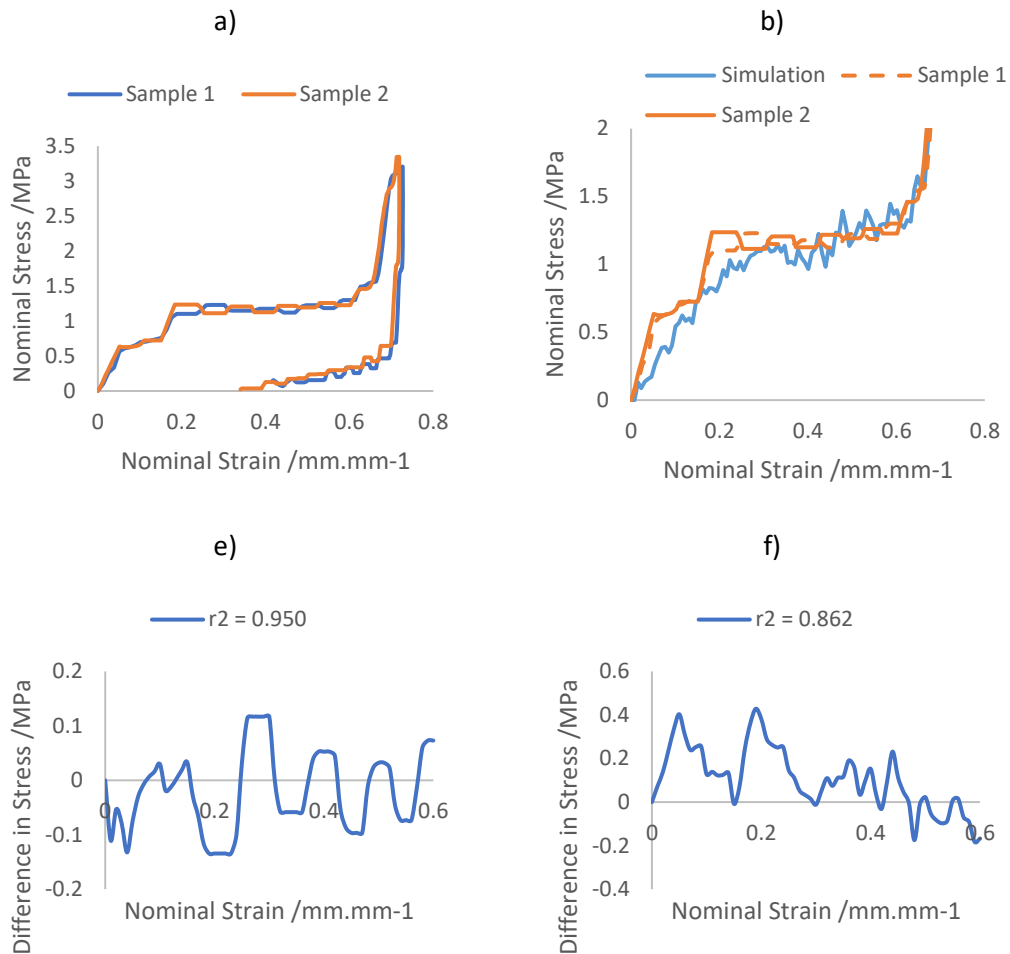


Figure 4.52. Dynamic compression of CH SP pads, a) experimental loading and unloading, b) comparison of experimental and simulated loading, c) difference in stress between the loading of the two experimental samples, d) difference in simulated and experimental loading stress

As with the NF dynamic testing, there is good agreement between the two CH SP pads, with a correlation of $r^2 = 0.950$ and a maximum difference in stress was 0.134 MPa. Figure 4.52b also highlights how the mechanical and simulated compression agreed well, with $r^2 = 0.862$ and a maximum difference in the stress of 0.429 MPa. While the experimental and simulated stress-strain curves have a good agreement, a larger difference in stress can be seen between 0 and 0.3 strain. As with the quasi-static compression of the CH SP structure, this is likely due to the difference in instantaneous modulus between CH and the scaled NF uniaxial responses (Figure 4.48).

Additionally, there is a difference between the plateau region of the simulated and mechanical dynamic compression. Mechanical testing had a slight incline to this plateau, while the simulated plateau was far more horizontal. However, simulated and mechanical

compression commenced at the same ϵ_{pi} (~ 0.25) and had similar levels of energy transferred at 0.6 strain, with the simulation at 23.6 J and experimental at 23.4 J.

As with the NF SP pads, in section 4.3.1.2, stringing occurred in the CH SP pads during manufacture. Unlike the NF SP pads, there was a reduced difference in ϵ_d for the quasi-static scenario and strong agreement in the ϵ_d values for the dynamic scenario.

4.4 Manufacture and analysis of a prototype SP filled motorcycle helmet

This section presents the optimisation and resultant experimentation of the prototype SP filled motorcycle helmet. The goal of this section is to provide experimental confirmation that the aim of this research has been met. Additionally, it serves to assess the validity of the optimisation approach.

The following excerpt from section 2.2.3.2 is included, to provide an easier reference to the impact points defined in UNECE 22.05:

- Point B – “the frontal area, situated in the vertical longitudinal plane of symmetry of the helmet and at an angle of 20° measured from Z above the AA' plane.”
- Point R – “the rear area, situated in the vertical longitudinal plane of symmetry of the helmet and at an angle of 20° measured from Z above the AA' plane.”
- Point X – “either the left or right lateral area, situated in the central transverse vertical plane and 12.7 mm below the AA' plane.”
- Point P – “the area with a radius of 50 mm and a centre at the intersection of the central vertical axis and the outer surface of the helmet shell.”

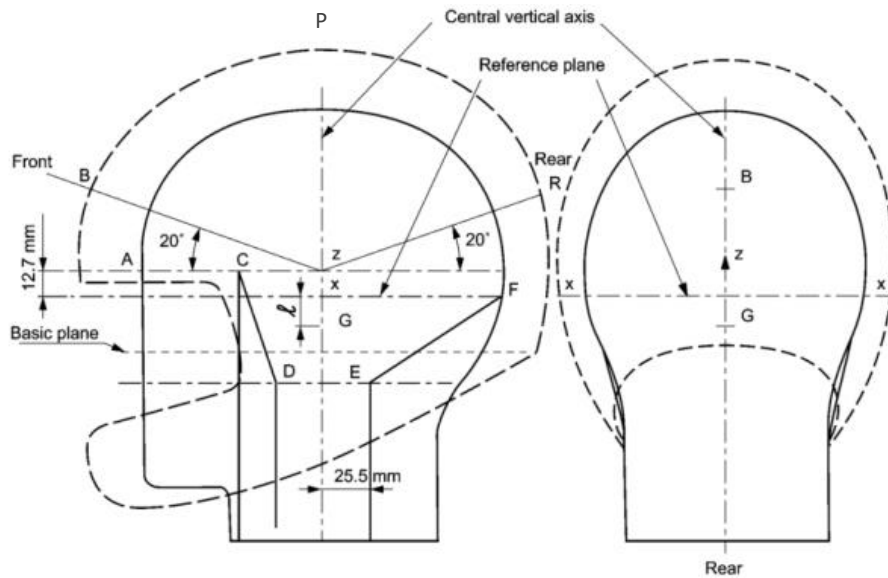


Figure 4.53. Illustration of a helmeted headform, highlighting the locations of the UNECE 22.05 impact points (B, R, X and P), replicated from [27]

4.4.1 Computational optimisation of SP configurations for motorcycle helmets

4.4.1.1 Selection of initial SP configuration from energy absorption diagrams

In section 2.2.3.2, the requirements of UNECE 22.05 were converted into W_{\min} and σ_{\max} values for each impact location. Lines of W_{\min} and σ_{\max} were plotted on a CH energy absorption diagrams (Figure 4.47), to identify configurations that met these requirements for each of the impact points defined by UNECE 22.05. These diagrams are presented in Figure 4.54 to Figure 4.56. Note, a single diagram is shown for points X and P due to their similar CSA (16877 and 17071 mm²) resulting in almost identical boundary lines.

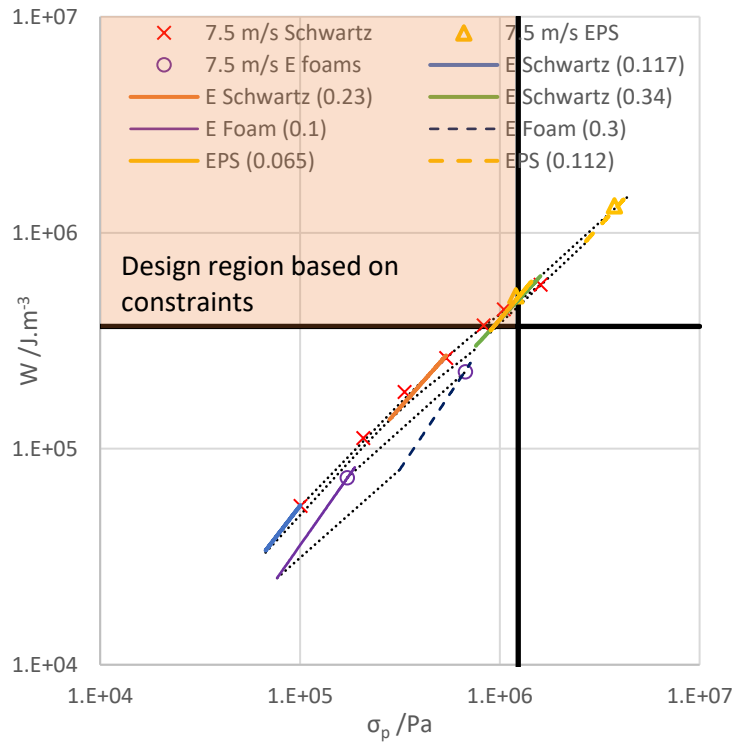


Figure 4.54. Energy absorption diagram for CH SP, CH EF foam and EPS foam with bounding lines, highlighting the minimum energy absorbed and maximum allowable stress, for impact point B (bounding lines for CSA = 10252 mm²)

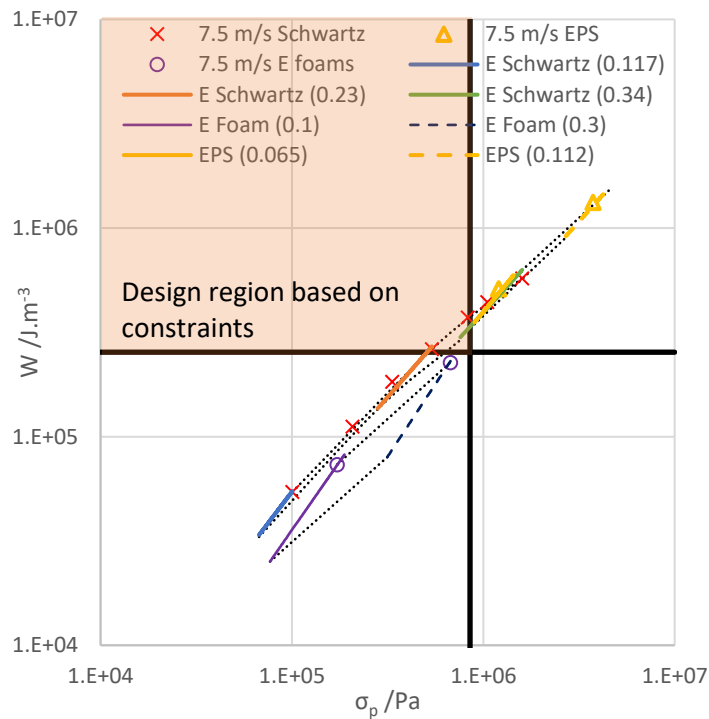


Figure 4.55. Energy absorption diagram for CH SP, CH EF foam and EPS foam with bounding lines, highlighting the minimum energy absorbed and maximum allowable stress, for impact point R (bounding lines for CSA = 14873 mm²)

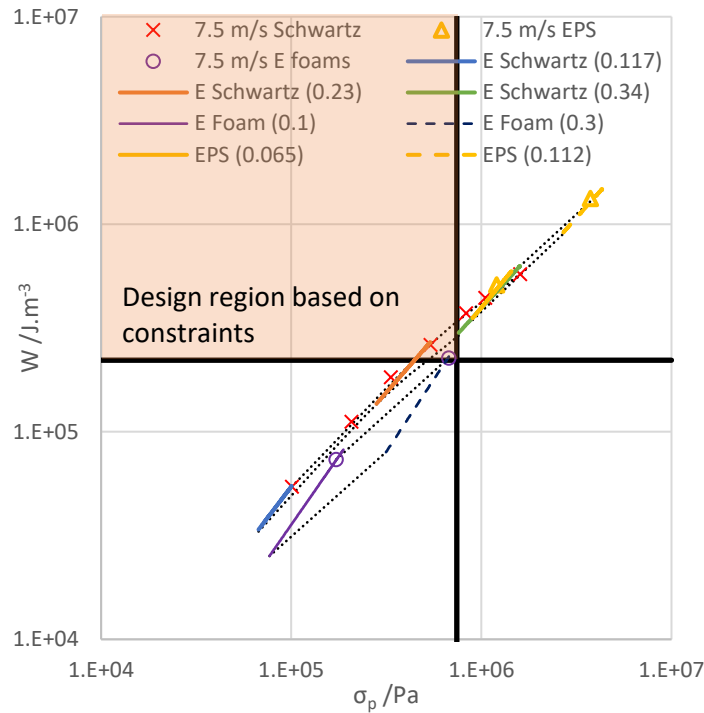


Figure 4.56. Energy absorption diagram for CH SP, CH EF foam and EPS foam with bounding lines, highlighting the minimum energy absorbed and maximum allowable stress, for impact points X and P (bounding lines for CSA = 16877 and 17071 mm²)

The configurations that lay on the W_{\min} and σ_{\max} lines were identified from Figure 4.54 to Figure 4.56. These were used to identify an intermediate configuration for each impact point, as presented in Table 4.10.

Table 4.10. Initial liner thickness selections for the CH SP structure, at impact points B, R, X and P; established from energy absorption diagrams

	Point B	Point R	Points X and P
T:l ratio range	0.12:1 – 0.14:1	0.1:1 – 0.12:1	0.09:1 – 0.11:1
Thickness range /mm	1.40 – 1.63	1.17 – 1.40	1.05 – 1.28
Resultant thickness /mm	1.5	1.3	1.2
Relative Density	0.30	0.26	0.24

4.4.1.2 Simulation of the complete helmet to optimise configurations

After the selection of the initial configurations from the energy absorption diagrams (Table 4.10), the optimisation approach specified in section 3.4.2.2 was followed. Optimisation at points B and R were undertaken first, as some of these pads were included at point P. After

the initial simulation, all configurations required a change in thickness (maximum of ± 0.1 mm as covered in section 3.4.2.2). Following these optimisations point X was addressed.

Impact point B

The acceleration-displacement plots for the initial 1.5 mm SP simulation at point B can be seen in Figure 4.57.

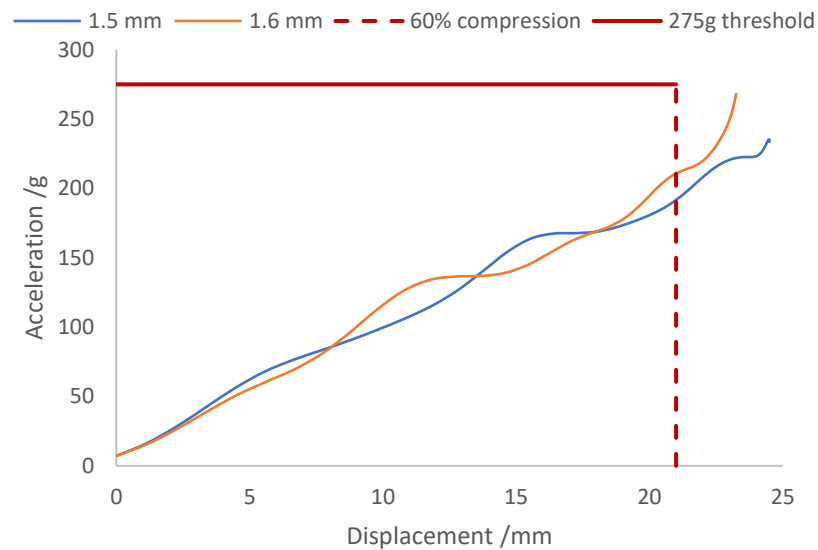


Figure 4.57. Simulated compressive 7.5 m/s impact on CH SP liner-filled helmet, at impact point B; with SP wall thicknesses of 1.5 mm and 1.6 mm

When simulating the impact at point B with 1.5mm SP pads, a compression of 24.5 mm (70%) and an A_{\max} of 235 g was recorded. As this compression is notably above the densification level of 60% compression specified in section 3.4.2.2, the thickness of the SP structure was increased. At 1.6 mm, A_{\max} of 269 g and compression of 23.3 mm (67%) was recorded. While still above the specified deformation limit, both traces were below the acceleration limit (275 g) set by UNECE 22.05. As the 1.6 mm configuration was the closest to the specified compression, this thickness was selected for point B moving forward.

Impact point R

The acceleration-displacement plots for the initial 1.3 mm SP simulation at point R can be seen in Figure 4.58.

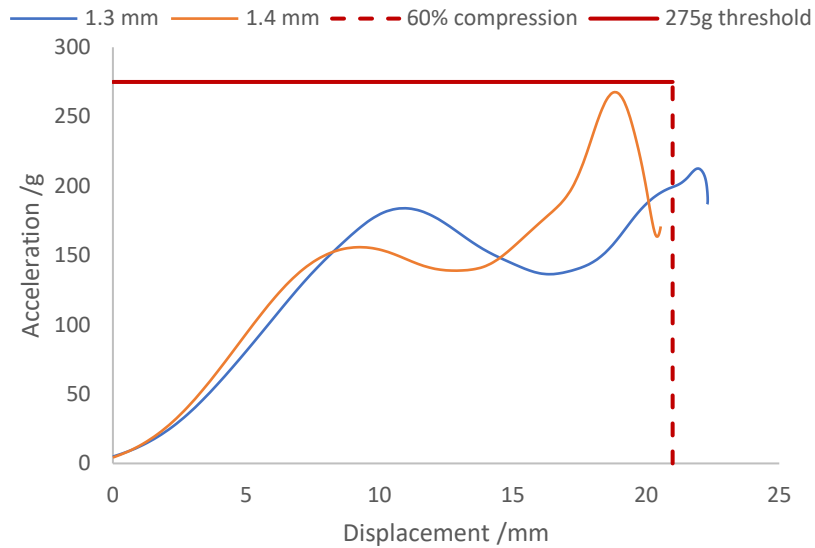


Figure 4.58. Simulated compressive 7.5 m/s impact on CH SP liner-filled helmet, at impact point R; with SP wall thicknesses of 1.3mm and 1.4mm

When simulating the impact at point R, the 1.3 mm SP configuration resulted in 22.3 mm of compression (64%) and an A_{max} of 212 g. Therefore, as with point B, the thickness was increased by 0.1 mm to 1.4 mm, resulting in A_{max} of 267g and compression of 20.6 mm (59%). Both responses were below the A_{max} limit of UNECE 22.05, and therefore the 1.4 mm configuration was selected as it was closer to the specified compression of 60%.

Impact point P

The acceleration-displacement plot for the initial 1.2 mm SP simulation at point P can be seen in Figure 4.59.

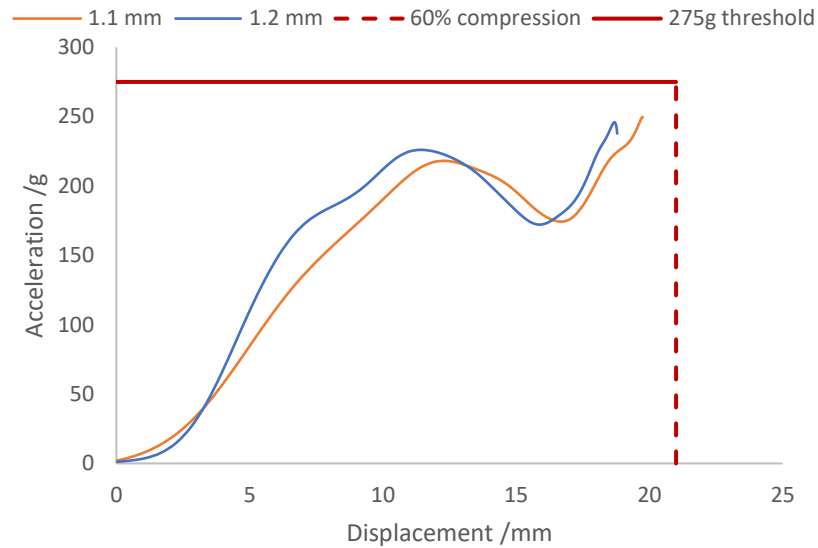


Figure 4.59. Simulated compressive 7.5 m/s impact on CH SP liner-filled helmet, at impact point P; with SP wall thicknesses of 1.1mm and 1.2mm

When simulating the impact at point P, a compression of 18.8 mm (54%) and an A_{\max} of 246 g were recorded for the 1.2 mm SP configuration. As this compression is notably below the densification level of 60% compression specified in section 3.4.2.2, the thickness of the SP structure was decreased. At 1.1 mm, A_{\max} of 250 g and compression of 19.7 mm (56%) were recorded. Both responses were below the A_{\max} limit of UNECE 22.05, and therefore the 1.1 mm configuration was selected as it was closer to the specified compression of 60%.

Impact point X

When analysing point X, the simulation terminated prematurely. The simulated deformation was examined to assess why this had occurred and to ensure no issues, such as self-penetration, had occurred. The visual deformation of the SP liner at maximum compression for each impact point is shown in Figure 4.60; where red colouring is equivalent to maximum deformation and dark blue is equivalent to minimum deformation or, in the case of the shell buckling inwards, negative deformation.

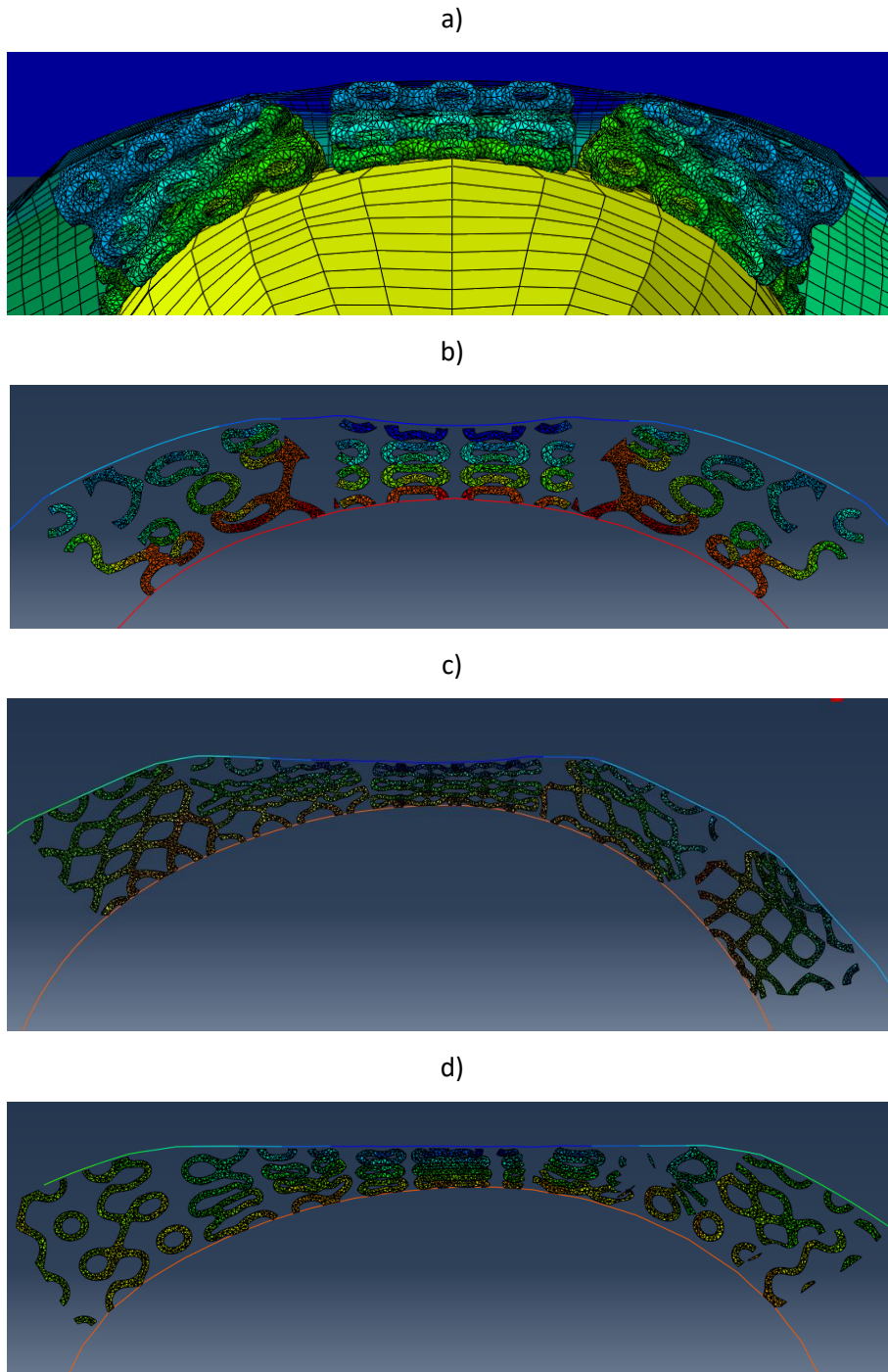


Figure 4.60. View of SP pads, at maximum dynamic compression (impact speed = 7.5 m/s), at a) Point B, b) Point R (section cut), c) Point P (section cut), d) Point X (section cut)

Pads remained in place throughout the simulation and all contact problems appeared to resolve successfully, with no penetration occurring. The deformation patterns give an insight into the effectiveness of the pads at each location. For points B and R (Figure 4.60a and b), the shell distributes the impact load into all the SP pads under the impact point. This distribution is visually apparent, as all pads undergo similar levels of compression,

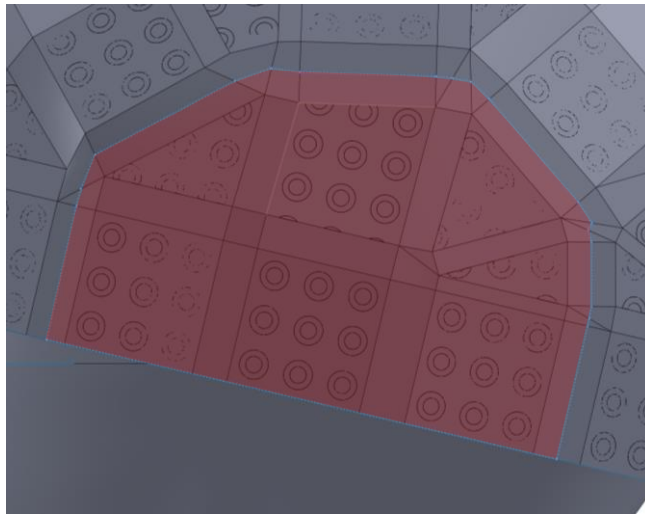
while still having the highest levels of compression directly under the impact point. Comparatively, the shell appears to less effectively distribute load at points P and X (Figure 4.60c and d).

For the impact at point P, this reduced effectiveness is in part due to liner generation strategy (section 3.4.1). Due to points B, R and P sharing pads, optimisation was undertaken at points B and R first. Optimisation of point P was then undertaken with these overlapping pads at a fixed thickness (as specified during optimisation of points B and R). After optimisation, the thickness at point B was 1.6 mm, at point R it was 1.4 mm. As the optimised thickness for the remaining pads at point P was 1.1 mm, the overlapping pads from points B and R were notably thicker. This increased thickness of the overlapping pads inherently results in the central pads deforming at notably lower loads than the outlying ones.

Meanwhile, for the impact at point X (Figure 4.60 d), only the central SP pads appeared to carry any load, with the outer pads under negligible compression. This behaviour contrasts with the other impact points, where all pads were engaged to some degree. This poor load distribution is noted in other helmets in the literature [201] and explains the discrepancy observed in section 2.2.3.2.

Considering the lack of deformation in the outlying pads, the cross-sectional area at point X was re-adjusted to exclude the non-functional outlying pads, as highlighted in Figure 4.61a. This area was then projected back to the headform, as per section 2.2.3.2, and the resultant CSA was measured at 10078 mm². The updated energy absorption plot is shown in Figure 4.61b.

a)



b)

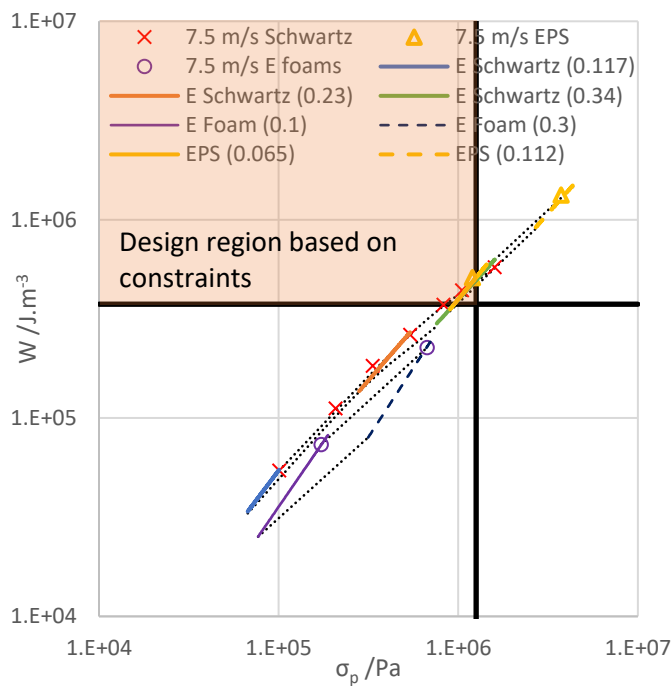


Figure 4.61. Correction undertaken for impact point X, a) Adjusted CSA, b) accompanying energy absorption diagram with updated bounding W_{min} and σ_{max} lines

From the energy absorption diagram shown in Figure 4.61b, an updated initial configuration for point X can be identified. At the σ_{max} line, the t:l ratio was 0.14:1, and at the W_{min} line it was 0.12:1. For the 35mm 3*3*3 SP pad, this results in an intermediate thickness of 1.5 mm, with a relative density of 0.30. The acceleration-displacement plot for the initial 1.5 mm SP simulation at point X is displayed in Figure 4.62.

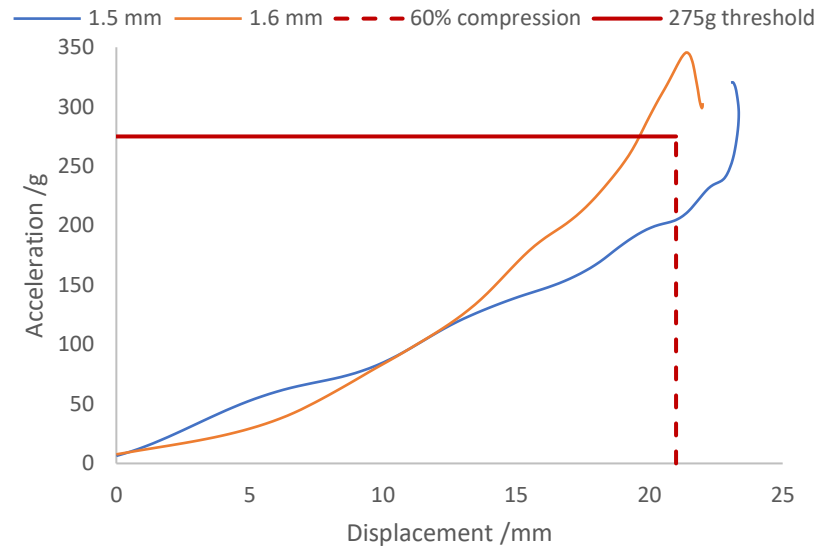


Figure 4.62. Simulated compressive 7.5 m/s impact on CH SP liner-filled helmet, at impact point X; with SP wall thicknesses of 1.5 mm and 1.6 mm

When simulating the impact at point X, with 1.5 mm SP pads a maximum compression of 23.4 mm (67%) and an acceleration of 293 g were recorded. However, as the helmet rebounded from the anvil, the acceleration continued to climb to an A_{max} of 320 g. As this compression is notably above the densification level of 60% compression, specified in section 3.4.2.2, the thickness of the SP structure was increased to 1.6 mm. At this thickness, A_{max} of 346 g and compression of 22.0 mm (63%) were recorded. Both responses were notably above the acceleration limit (275g) set by UNECE 22.05, in addition to being above the specified level of compression. As the 1.6 mm configuration was the closest to the specified compression, its thickness was selected for point X, with the understanding that it would likely not meet the acceleration requirements of UNECE 22.05.

Summary of final configurations

The optimised thicknesses for each impact point are shown in Table 4.11. *Note, all thicknesses are specified for 35*35*35 mm³ pads, in a 3*3*3 unit cell configuration.*

Table 4.11. Optimised liner thickness selections for the CH SP structure, at impact points B, R, X and P; established from helmet simulations

	Point B	Point R	Point X	Point P
Resultant thickness /mm	1.6	1.4	1.6	1.1
Relative Density	0.32	0.28	0.32	0.22

When manufactured, these SP pads had a total mass of 840 g. Therefore, compared to the 238g EPS liner (Appendix V), the liner mass was increased by 253%. However, most of the mass in current motorcycle helmet designs are in components other than the liner (e.g. the shell). This distribution of mass was also observed in the BOX BX-1 helmet, with an overall helmet mass of 1486 g. Therefore, the increased mass of the SP liner only contributed to an increase in the helmet mass of 41%. While this is a non-trivial increase in mass, it is not as severe as the relative increase in liner mass would suggest.

4.4.2 Validation of the optimisation approach and evaluation of the prototype helmet's multi-impact performance

4.4.2.1 *Validation of helmet simulation approach*

The SP configurations for each impact point were then manufactured and placed inside the surrogate BOX BX-1 helmet. Following the methodology set out in section 3.4.3.2, this helmet was then subjected to a series of impacts. The results of this mechanical testing are presented alongside their associated simulated responses in Figure 4.63. Additionally, their comparative performance is quantitated in Figure 4.64.

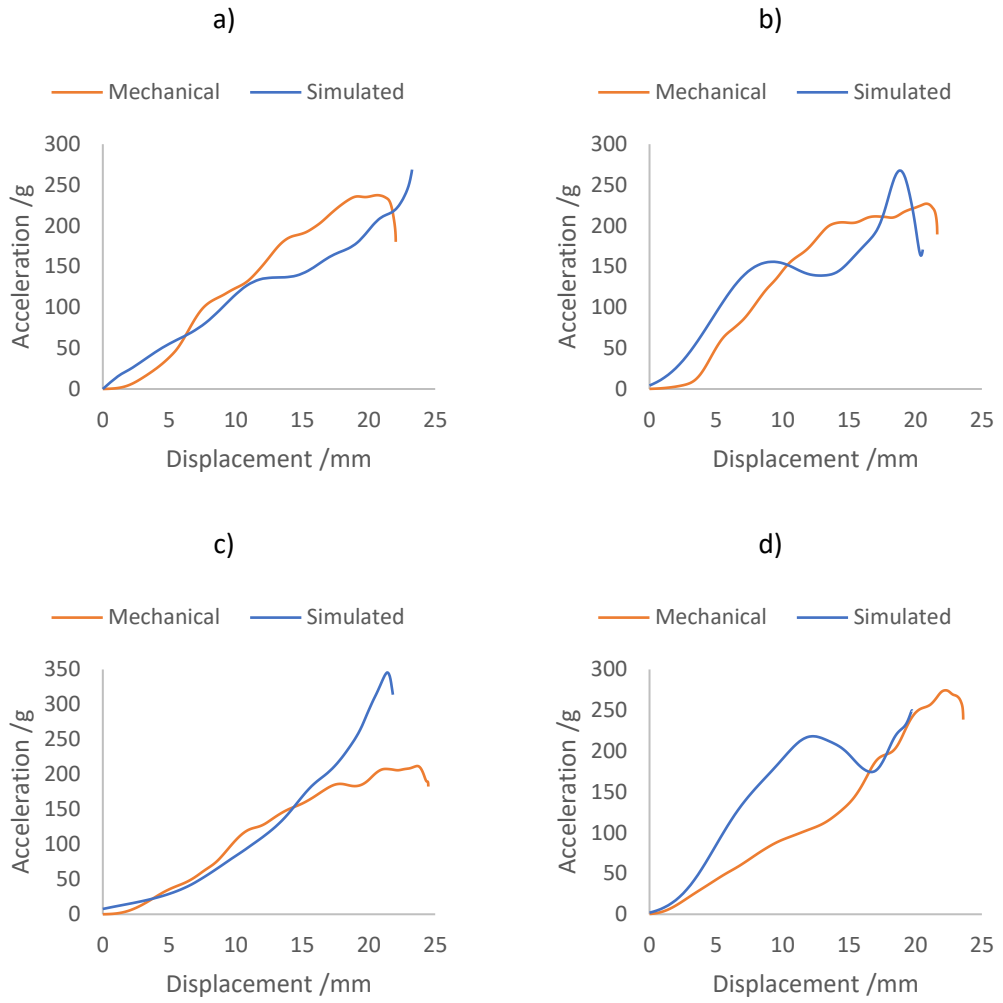


Figure 4.63. Comparison of the simulated and experimental loading responses for the CH SP filled helmet, during a 7.5 m/s impact, at, a) Point B, b) Point R, c) Point X, d) Point P

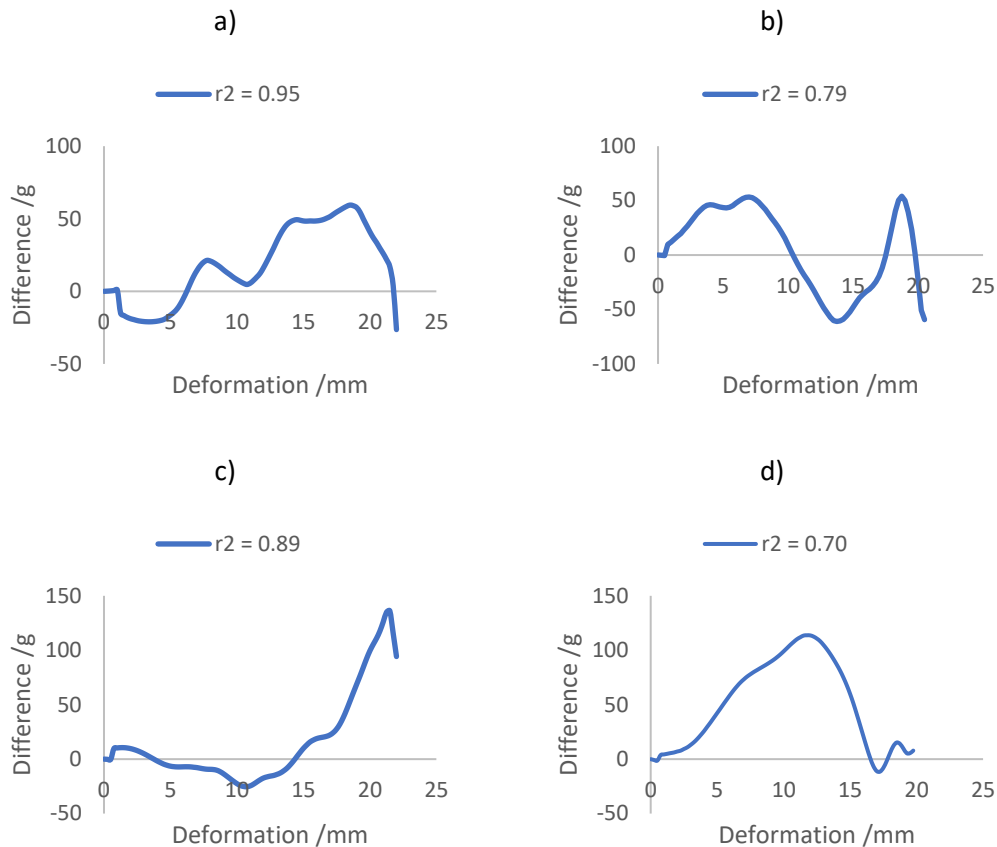


Figure 4.64. The difference in acceleration over deformation for the simulated and experimental loading responses of the CH SP filled helmet, during a 7.5 m/s impact, with accompanying r^2 values, a) Point B, b) Point R, c) Point X, d) Point P

Points B and R demonstrate the best agreement between simulated and mechanical responses, with $r^2 = 0.95$ and 0.79 , respectively. Additionally, the differences in acceleration (57g and 61g) are the lowest out of the four impacts. For both points, the simulated and mechanical deformations were within 5% of each other.

While having good correlation between simulated and mechanical responses, points X ($r^2 = 0.89$) and P ($r^2 = 0.7$) demonstrated poorer agreement overall. Point X has high agreement up until 17.5 mm (with the difference in acceleration being ± 25 g), however past this point simulated and mechanical responses deviate dramatically, resulting in a maximum difference in acceleration of 136 g. Due to this increase in acceleration, the simulated liner required reduced deformation (11% lower) to absorb the same amount of energy.

Conversely, point P demonstrated reduced agreement between mechanical and simulated response initially (difference in acceleration = 114 g), but this agreement improved approaching maximum compression (at 17-20 mm compression, the difference was ± 15 g).

Due to these larger initial accelerations at Point P, the incoming energy was dissipated over a shorter distance. Therefore, densification was 16% lower than mechanical testing.

Further examination of the acceleration-displacement response was undertaken to assess this reduced correlation. For the simulation of point X (Figure 4.63c), the acceleration-displacement response is indicative of an exponential relationship, while the mechanical response is tending to a logarithmic relationship. The pure compressive response of the EPS and SP liners (outside of a helmet environment) both tend to logarithmic, with a plateau after an initial rise in stress. Therefore, the effective use of this material should also have this response. For example, this can be identified as a distinct plateau in the mechanical response at point R (Figure 4.63b). As the simulated response at point X is exponential, it would imply that the load distribution within the physical helmet was better than that in the simulated one. Applying this logic to the responses at the other points:

- Point B (Figure 4.63a) demonstrates a linear relationship, and therefore has relatively ineffective load distribution, in both simulated and mechanical responses. This ineffectiveness is likely due to the visor opening reducing the rigidity of the shell in this region.
- Point R (Figure 4.63b) demonstrates effective load distribution for both simulated and mechanical responses. While there are undulations in the simulated response, the general initial loading slope followed by a plateau can be identified in both curves. This is reflected in Figure 4.60, where point R appears to load the SP pads most equally.
- Point P (Figure 4.63d) demonstrates superior load distribution in simulation than it does in mechanical testing. When point P was tested, the helmet shell had extensive fractures at the front and rear of the helmet (Appendix VI). This reduction in the overall integrity of the helmet shell could contribute to an inferior load distribution during mechanical testing. The link between loss of performance and degradation of shell integrity is explored in section 4.4.2.3, where multi-impacts lead to shell damage and progressive reduction in initial stiffness.
- As discussed, the simulated response of point X (Figure 4.63c) has poor load distribution, which could be due to the simulated shell. This shell covered all the pads over the head and was approximately hemispherical. However, the mechanically tested helmet was a full-face helmet, which included a chin bar. This chin bar would likely increase the shell rigidity at point X, improving load distribution. Similarly, while the foam in the chin bar was not involved in the

impact (as the half headform did not engage with the liner in that region), it could potentially increase the rigidity provided by this chin bar.

The simulation in this work was developed to simulate the loading portion of the impact response. This decision was made as the loading portion ultimately defines the energy absorption diagram. Therefore, undertaking the loading portion alone halves the simulation time. However, three out of four of the fully simulated acceleration-time traces agreed with the experimental data (Figure 4.65).

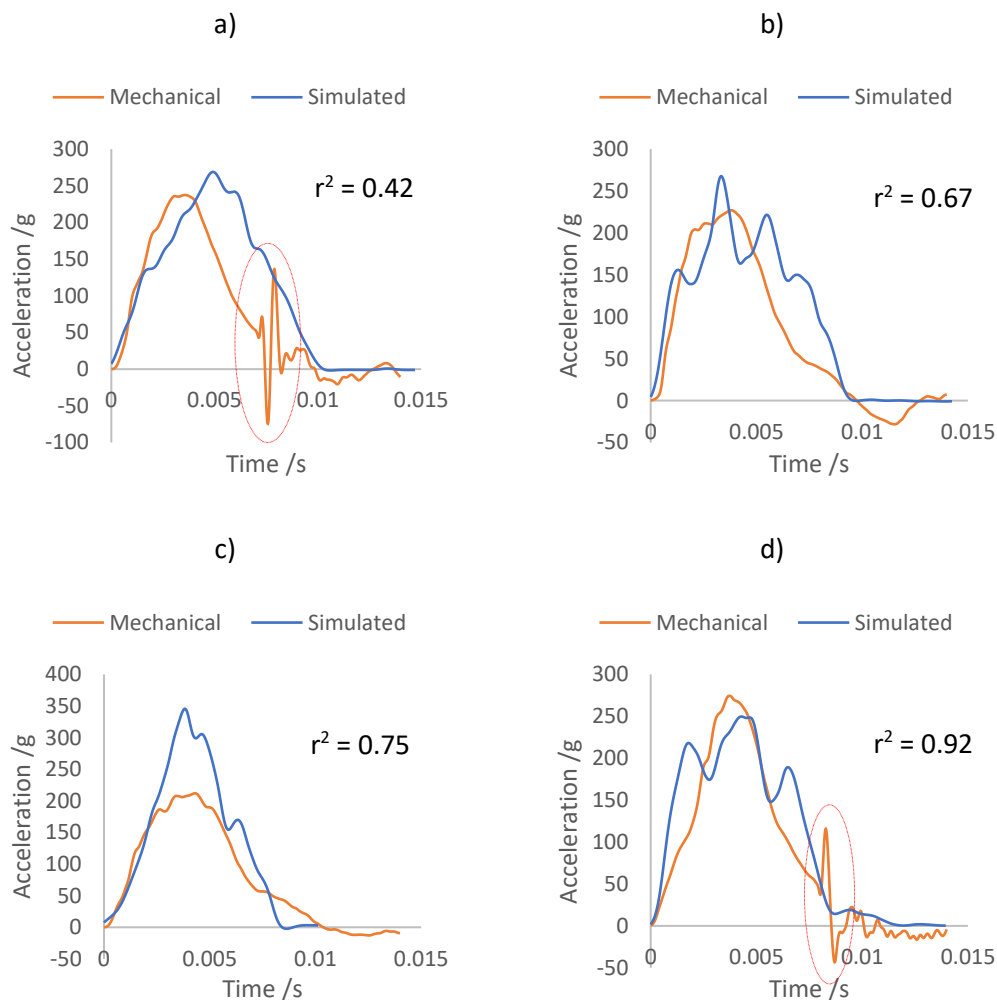


Figure 4.65. Comparison of the simulated and experimental responses for the CH SP filled helmet, during a 7.5 m/s impact, at, a) Point B, b) Point R, c) Point X, d) Point P

The duration of both simulated and experimental pulses for points B, R and P, agreed at ~ 10 ms. However, for the simulation at point X, the duration of the simulated pulse was only 8.7 ms, compared to the mechanical pulse at 10.1 ms. This decrease is likely due to the increased A_{\max} of the simulated response, which requires a lower deformation to mitigate the same KE and, therefore, the combination of the two would lead to reduced duration.

While point R, X and P had a good correlation between mechanical and simulated experimentation (0.67, 0.75 and 0.92 respectively), point B had reduced correlation, at only 0.42. This correlation highlights the reduced agreement of the rebound at point B, as the compression at this location had a high correlation at 0.96 (Figure 4.64a). Conversely, the correlation at point P notably improved when mapping the full compression and rebound (from 0.7 to 0.92).

Additionally, in Figure 4.65a & d, an unusual fluctuation can be observed in the mechanical acceleration-time pulse. This fluctuation occurred during rebound of the helmet and is highlighted on the pulses. The effects of this fluctuation appear to propagate into the remainder of the acceleration-time curve as a jagged response. Examination of high-speed videos identified this was due to the light gate connecting with a metal flag that activates it. This collision occurred due to lateral deformation of the carriage assembly, induced during helmet rebounding from the anvil. It is also present in the sixth impact displayed in Figure 4.70.

4.4.2.2 *Assessment of the motorcycle helmet to meet the requirements of UNECE 22.05*

This section compares the performance of the CH SP liner and an established EPS motorcycle helmet liner. The impacts at the locations specified in UNECE 22.05 are shown in Figure 4.66, with HIC and A_{\max} values for these impacts in Table 4.12.

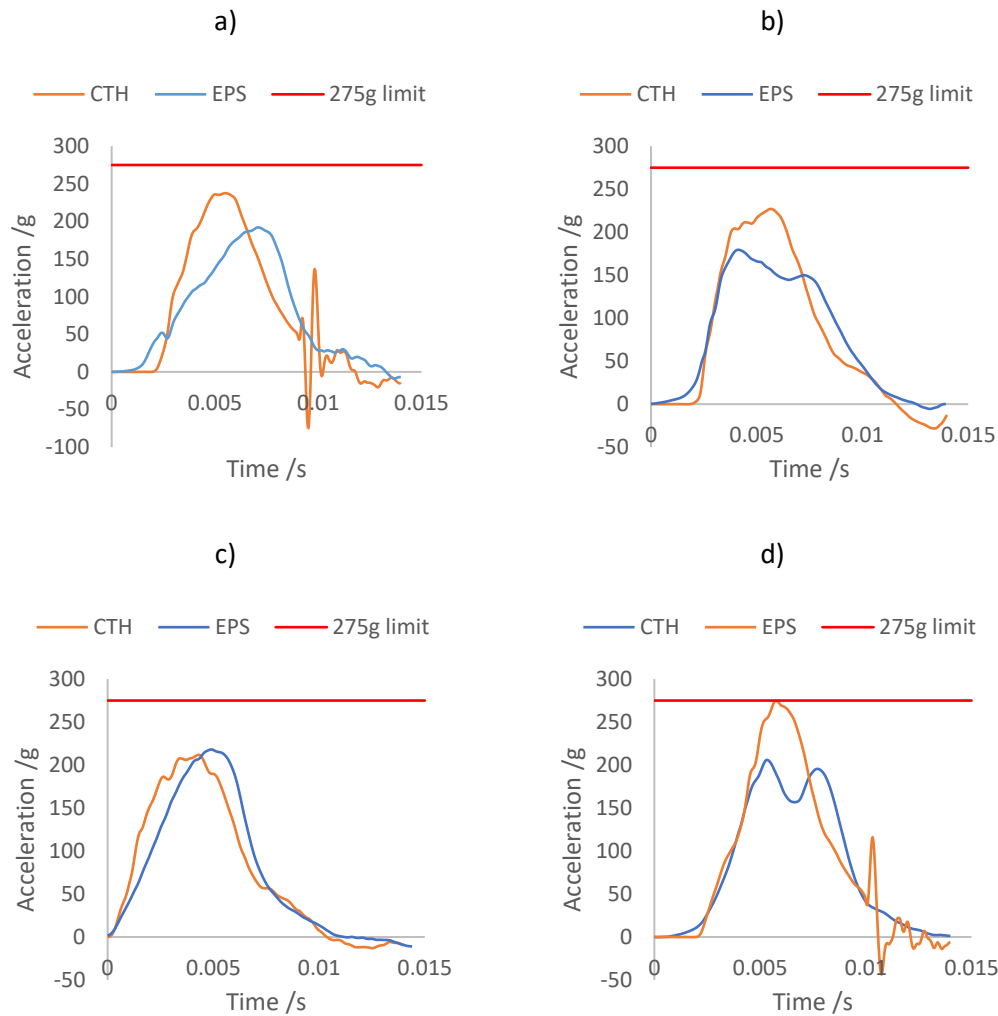


Figure 4.66. Comparison of the experimental responses for CH SP and EPS foam filled helmets, during a 7.5 m/s impact, at, a) Point B, b) Point R, c) Point X, d) Point P

Table 4.12. Comparison of experimental A_{max} and HIC for CH SP and EPS foam filled helmets, during a 7.5 m/s impact, at points B, R, X and P

	Point B	Point R	Point X	Point P
SP - A_{max} /g	237	227	212	274
SP – HIC (HIC duration)	2235 (4 ms)	2232 (5 ms)	1748 (5 ms)	2687 (5 ms)
EPS - A_{max} /g	192	179	218	206
EPS - HIC	1492	1612	1905	1935

Examining Figure 4.63, the maximum compressive strains for the SP pads were between 0.57 and 0.67 for all impacts points. When compared to the ϵ_d of the SP structure (0.55 to 0.64 – Table 4.7), the selected pads appear to be used effectively in the prototype helmet.

At three of the four impact points, the SP filled helmet satisfied the requirements of UNECE 22.05, with $HIC < 2400$ and $A_{max} < 275$ g. The exception to this was point P, where the SP filled helmet passed the A_{max} requirement of UNECE 22.05 but exceeded the maximum HIC value.

At impact point X, the SP liner had a lower HIC and A_{max} than the EPS liner. Additionally, this improved performance was achieved over a reduced liner thickness (24.5 mm vs 30.2 mm for EPS). At the remaining impact points (B, R and P), the EPS liner had lower HIC and A_{max} than for the SP liner. Examination of the results at these points highlights avenues to improving SP performance in the future.

For points R and P, reduced performance can be attributed to the significant increase in EPS liner thickness at these points, with the EPS liner at point P being approximately 120% of the CH liner, and at point R 143%. This increased liner thickness allows increased deformation, resulting in a lower A_{max} . However, the EPS liner at point B varied in thickness from 35 to 40 mm, making it more comparable to the SP liner thickness (at 35 mm) than the other impact points. Therefore, while SP pads of equal thickness to the EPS liner at points P and R would likely result in improved performance, the use of a CH SP structure at point B requires further review.

In addition to evaluating the SP and EPS helmets' ability to meet the performance metrics prescribed by UNECE 22.05, their coefficient of restitution (CoR) was also examined. One potential perception of elastomeric liners is that they will be more 'elastic' than EPS and return significantly more of an impact's energy to the head (instead of absorbing it). Figure 4.67 displays the change in velocity over impact duration.

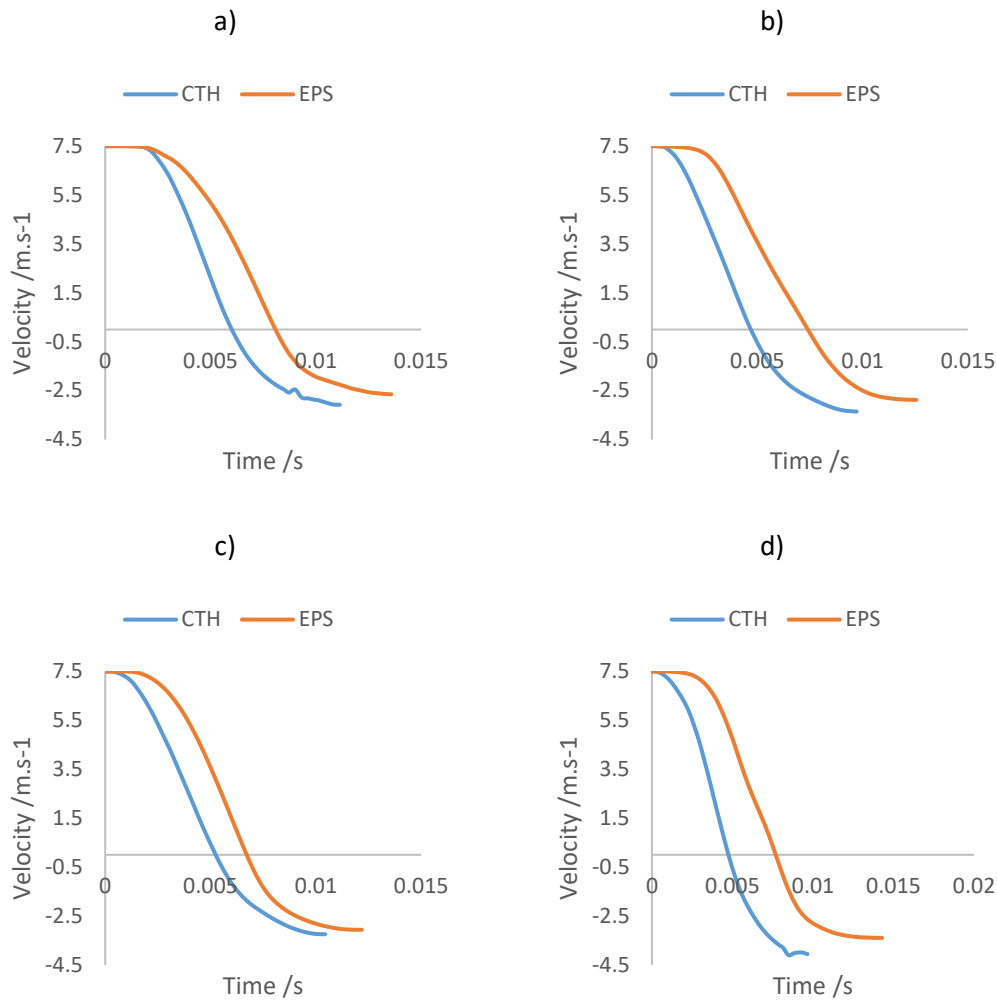


Figure 4.67. Comparison of the experimental change in velocity of the CH SP and EPS foam filled helmets, during a 7.5 m/s impact, at, a) Point B, b) Point R, c) Point X, d) Point P

Assessment of the impact points (Figure 4.67) shows a similar CoR for both SP filled and EPS filled helmets (e.g. at point X, SP CoR = 0.43, EPS CoR = 0.40). This similarity would suggest that the EPS and SP liners both absorb similar levels of energy. EPS is commonly believed to return little of the incoming energy, due to internal plastic deformation. While the comparable CoR could be attributed to the shell returning energy as it unloads, an examination of the hysteresis in EPS' stress-strain curve (Figure 2.11) indicates this CoR may be due to EPS' response alone. This CoR is explored further in section 4.4.2.3.

4.4.2.3 Multi-impact performance of SP, and EPS, liners

The acceleration-time response for multi-impacts of the SP liner helmet, at point B, is shown in Figure 4.68.

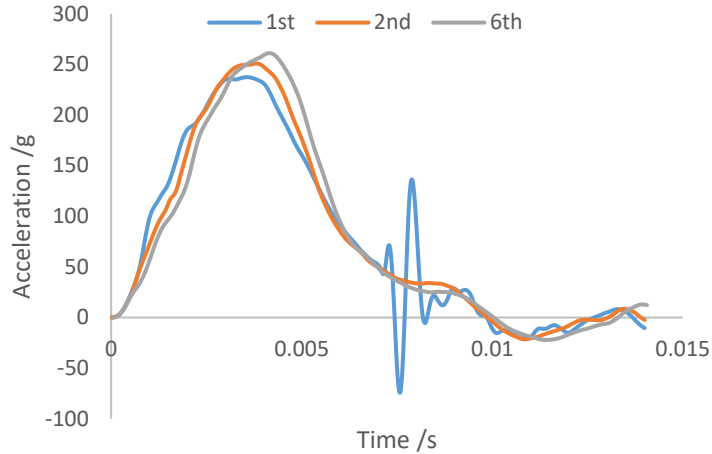


Figure 4.68. Comparison of the difference in experimental responses when the CH SP filled helmet undergoes multiple 7.5 m/s compressive impacts, at point B

Throughout the six impacts at point B, the A_{max} of the SP filled helmet increased from 237 g to 260 g (+10%). For the first to the fifth impact, A_{max} remained under the 275 g limit, with HIC values < 2400 (the first impact had $HIC_{4ms} = 2235$). However, while the sixth impact remained under A_{max} limit, it exceeded the HIC limit ($HIC_{4ms} = 2545$). The duration of all impacts remained unchanged at 10 ms. This relatively consistent performance is notable considering the helmet shell fractured at point B during the first impact (Appendix VI).

Figure 4.69 shows the first and second impact at point B for the unaltered EPS helmet.

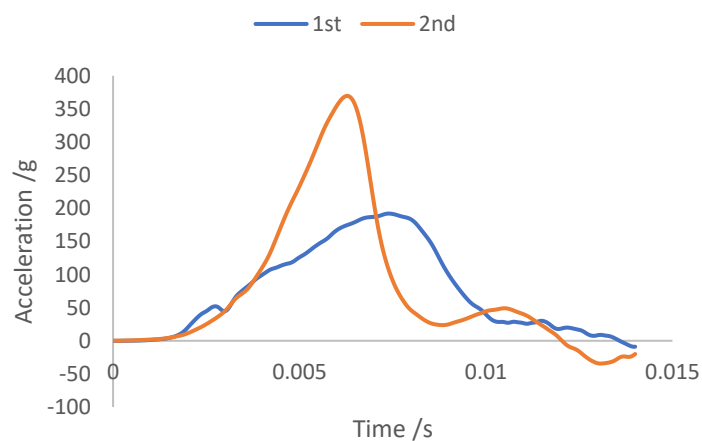


Figure 4.69. Comparison of the difference in experimental responses when the EPS foam filled helmet undergoes multiple 7.5 m/s compressive impacts, at point B

At point B, the first impact on the EPS filled helmet had an A_{max} of 192 g, a duration of 13 ms and $HIC_{5ms} = 1492$. For the second impact, A_{max} and HIC increased, to 370 g (+93%) and $HIC_{5ms} = 3156$, far over the A_{max} (275 g) and HIC (2400) limits of the UNECE 22.05 standard. Existing testing standards with multi-impact requirements (section 2.1.2.4) prescribe accelerations remain below a set value for all the impacts. Therefore, if UNECE 22.05 had a multi-impact requirement, the EPS liner would likely not meet it at this location.

Figure 4.70 shows the acceleration-time curves for multi-impacts on the SP lined helmet, at point R.

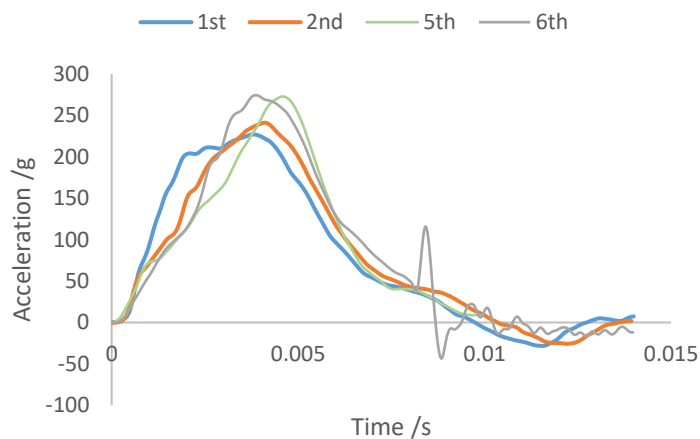


Figure 4.70. Comparison of the difference in experimental responses when the CH SP filled helmet undergoes multiple 7.5 m/s compressive impacts, at point R

The first impact had an A_{max} of 227 g and $HIC_{5ms} = 2232$, with a duration of ~10 ms for all impacts. While impacts remained below the 275 g limit (with the sixth impact = 274 g), the sixth impact exceeded the maximum allowable HIC of UNECE 22.05, with $HIC_{4ms} = 2738$. Note, the 5th impact had $HIC_{4ms} = 2301$.

A similar pattern of increasing A_{max} with successive impacts is observed in Figure 4.70 and Figure 4.68. However, the increase in A_{max} is higher than for Point B, with an increase of 13% from first to fifth impact and 21% from first to sixth. The damage to the shell at point R was more significant than point B (Appendix V). Therefore the sixth impact is likely where the shell integrity had decreased to the point that it could no longer sustain performance. This loss of integrity would explain the more comparable difference in A_{max} between the first and sixth impact at point B (10%) and the first and fifth impact at point R (13%).

While the SP helmet performs less capably at point R than point B, Figure 4.70 and Figure 4.68 would suggest an SP filled motorcycle helmet to be capable of multi-collision mitigation (in addition to multi-impact mitigation within a single collision). However, damage to the helmet's structural integrity (i.e. shell fracturing) highlights that further work needs to be undertaken to produce a multi-collision motorcycle helmet. All components of the helmet would need to be developed for multi-collision mitigation, and extensive testing would need to be conducted to ensure no secondary issues arose.

Examining Figure 4.68 and Figure 4.70, it appears that crack propagation (Appendix VI) leads to a reduction in initial helmet stiffness. This reduction can be seen in the divergence at the beginning of the acceleration-time curve, as the impact count progresses. This proposal is supported by the increased divergence observed at point R (Figure 4.70), which had more severe damage than point B. Therefore, if this damage to the shell was prevented, it is likely that the SP filled helmet would continue to meet the requirements of UNECE 22.05 in subsequent multi-impacts.

Figure 4.71 shows the first and second impacts at point R for the EPS filled helmet.

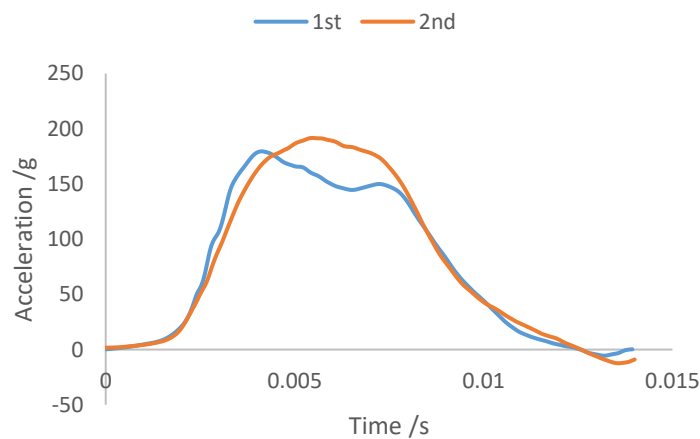


Figure 4.71. Comparison of the difference in experimental responses when the EPS foam filled helmet undergoes multiple 7.5 m/s compressive impacts, at point R

The first impact had an A_{\max} of 179 g, a HIC_{6ms} = 1612, and a duration of 12 ms. The second impact had an A_{\max} of 192 g, a HIC_{5ms} = 1915, and the same duration.

Unlike the SP filled helmet, the first impact on the EPS filled helmet did not result in crack propagation from the rear vents. This lack of shell failure explains the lack of divergence in

the acceleration-time traces from the first impact to the second. For the second impact, the increased difference in the acceleration-time curve, between 4.7 and 5.6 ms, is indicative of the onset of densification. This proposal is supported by a 15% increase in deformation observed between the first and second impacts.

As observed in Appendix VI, significant damage was incurred to the SP filled helmet's shell during the multi-impacts at points B and R. As this damage inherently affects the integrity of the shell, the influence of this cracking on helmet CoR was investigated. The change in velocity for the SP filled helmet at points B and R is shown in Figure 4.72.

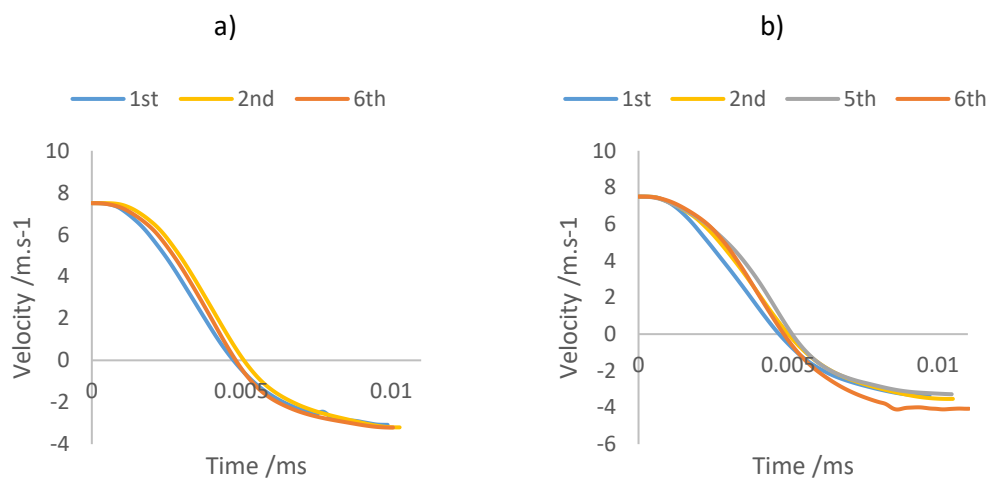


Figure 4.72. Comparison of the experimental change in velocity when the CH SP filled helmet undergoes multiple 7.5 m/s impacts, at, a) point B, b) point R

Examining Figure 4.72a shows that after six impacts, the SP filled helmet's CoR at point B changed negligibly. For the SP filled helmet, multi-impacts at point B resulted in extensive fracturing of the shell (Appendix V). This lack of change is also observed in the first five impacts at point R (Figure 4.72b), where even more significant crack propagation occurred. Note, the CoR at point R increases for the sixth impact. This sixth impact is linked to shell integrity failure during the analysis of Figure 4.70. Therefore, even significant damage (short of complete loss of integrity) of the shell seems to have little effect on helmet CoR. This finding supports the analysis of the SP and EPS liner CoR, undertaken in section 4.4.2.2, where it was postulated that the helmet shell had little effect on CoR.

In addition to the calculation of CoR for the SP filled helmets, this analysis was also undertaken for the EPS helmet. While the inherent plastic deformation that occurs in EPS

means that influence of the shell on CoR cannot be identified, the lack of change in CoR observed for multi-impacts of the SP helmet (Figure 4.72) indicates that any changes to CoR would be due to EPS alone. In particular, for point R, this is further supported by the lack of fracturing in the shell occurred after the first or second impact. The results of this process for points B and R are presented in Figure 4.73.

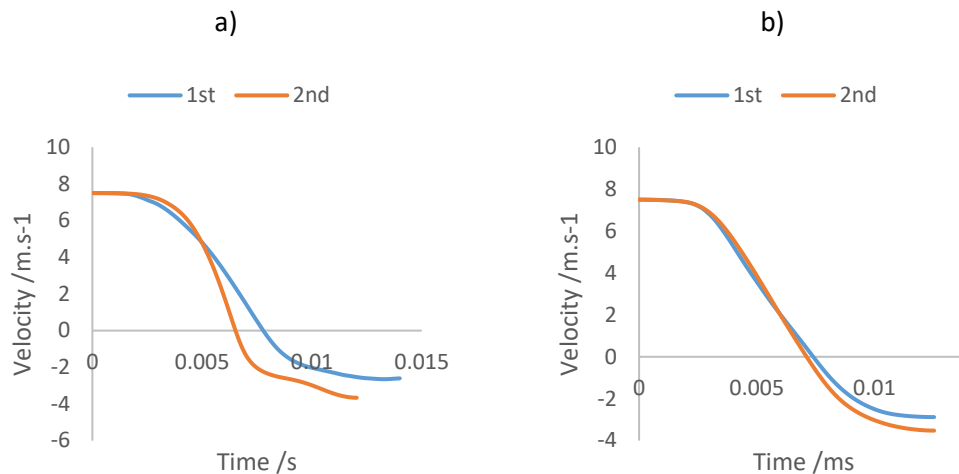


Figure 4.73. Comparison of the experimental change in velocity when the EPS foam filled helmet undergoes multiple 7.5 m/s impacts, at, a) point B, b) point R

At point B, the CoR changes from 0.35 for the first impact to 0.49 for the second and at point R, it changes from 0.38 to 0.5. A change in CoR of ~25% is significant and indicates that even though the second impact at point R was within the UNECE 22.05 limits, the safety of this multi-impact performance is questionable. This similar CoR change for EPS, between points B and R, supports the analysis of Figure 4.71; where it was suggested that even though the second response was still within the UNECE 22.05 limits, it was strongly indicative of the onset of densification. Therefore, even though point R survived two impacts, any further impacts would likely result in high densification, as per point B (Figure 4.69).

5 Further Discussion

5.1 Meeting the research aim

This work aimed to improve motorcyclist head protection by exploiting the mechanical benefits of cellular structures and resilient materials. This aim is achieved by enhancing motorcycle helmet performance through mitigation of multiple impacts (within a single collision) while meeting the current level of single-impact motorcycle helmet performance (i.e. passing UNECE 22.05).

5.1.1 Comparison of EPS and SP helmets for multi-impact performance

Compared to EPS, the ability of the SP structure to improve motorcyclist safety by providing multi-impact mitigation has been demonstrated.

The EPS filled helmet demonstrated the ability to mitigate two impacts to the requirements of UNECE 22.05 at point R (Figure 4.71), and one at point B (Figure 4.69); however, this came with an associated increase in CoR (Figure 4.73). An increase in CoR can be linked to increased head injury severity [47, 48, 53, 54]. Therefore, even though EPS can mitigate two impacts at one location due to the significant thickness of the liner (50 mm from Appendix V), its second mitigation is less safe. Therefore, this study highlights the lack of multi-impact performance in EPS.

Comparatively, the SP structure met the requirements of UNECE 22.05 up to five times (Figure 4.71), with a negligible change to CoR for impact points B and R (Figure 4.72). Notably, this mitigation performance persisted past the point of shell failure, resulting in the SP liner protecting the head even in the event of shell failure. Visual observations (Appendix VI) indicate that the sixth impact failing to meet UNECE 22.05 is linked to severe helmet shell damage.

5.1.2 The ability of SP filled helmet to meet the requirements of UNECE 22.05

The ability of the SP filled helmet to meet the requirements of UNECE was demonstrated for points B, R and X (section 4.4.2.2). However, while the SP liner passed the A_{max} requirement of UNECE 22.05 for point P, it failed to meet the HIC requirement of < 2400 , with $HIC_{5ms} = 2687$ (Table 4.12).

Considering the prototype nature of the helmet, the satisfaction of UNECE 22.05 at three of the four locations, in addition to partial conformance at one of the locations, demonstrates the potential for the SP structure to produce a helmet that meets UNECE 22.05. The SP

liner also achieved this at a thickness of only 70% to 87.5% that of the respective EPS liner (section 3.4.1, Appendix V), except for point B, where the liners were of equivalent thickness. This reduction in liner thickness resulted in the SP liner having less available deflection over which to mitigate incoming energy. Therefore, if the thickness of the SP liner at point P were variably increased by 12.5% to 25%, in line with the thickness of the EPS liner, it is highly likely that the SP liner would meet the requirements of UNECE 22.05 at point P.

Meeting or exceeding the impact mitigation performance of EPS is a desirable outcome for the commercial implementation of the SP structure in motorcycle helmets. However, at this early stage of research, it was unlikely that the SP liner would exceed the performance of the EPS liner. Therefore, it is notable that the SP liner managed to exceed the A_{max} and HIC performance of EPS at point X (Table 4.12). This achievement is even more notable considering the constant SP liner thickness adopted for the prototype helmet, resulting in the SP liner at point X achieving a reduction in A_{max} of 3%, over a liner thickness only 70% that of EPS (section 3.4.1, Appendix V).

This initial empirical demonstration of the SP liner outperforming EPS shows its promise, with an examination of the generated SP energy absorption diagrams highlighting further potential. For example, at the same relative density, the SP structure (0.117) is significantly more efficient than EPS (0.112), as highlighted in section 4.3.3.3. Therefore, with a base material of a higher E_s , the SP structure should notably outperform EPS (Figure 4.46).

5.2 Meeting the research objectives

In addition to assessing if the research aim had been met, an analysis of the novel approaches developed in this work was also undertaken.

5.2.1 Optimise processing parameters to produce functional cellular structures

A common perception is that FFF produces components of poor quality, which at least in part is due to the inferior components examined in the literature [172, 173]. These studies explore unfused test specimens, leading to weak mechanical performance and also a poor perception of the quality of FFF components. Even studies that indicate superior FFF density present parts with clearly visible inter-layer bonding, and non-consistent layer height [180].

The potential of FFF to produce high-quality components is demonstrated in this research, with NF components of exceptionally high density (section 4.1.2 - 99.97%). This value exceeds those reported in the literature for Selective Laser Sintering (SLS) of elastomeric components (~95%) and is comparable to those recorded for injection moulded components [202].

This high density was achieved without loss of feature accuracy, as shown in Figure 4.6, with the primary method to achieve it being incremental increases to the extrusion multiplier. Raising this multiplier increases the quantity of material that is deposited. An alternative approach to increase the quantity of extruded material was explored previously for FFF elastomers [180]. However, as this study explored honeycombs, which were manufactured using a single line of extrudate, the quantity of material appeared only to be increased until inter-layer voids were eliminated, without any further control or consideration of components consisting of multiple lines of extrudate.

Controlling excess deposition is essential to ensure the intra-layer voids are successfully filled (Figure 4.4 A), without causing over-extrusion. Increased over-extrusion results in increases to distortion and multiplicative growth [179]. No distortion occurred in this research, with the only growth being static at 0.03 to 0.05 mm, in components of varying exterior dimensions (section 4.1). This static growth can be attributed to the extrudate forming the outline of components, which barrels as the excess material has no voids to fill on the exterior of the components. Due to this lack of distortion and multiplicative growth, the static increase can be corrected for in slicing software or compensated for in the CAD model itself.

5.2.2 Characterisation and computational modelling of AM elastomers

By achieving the high density described in section 5.2.1, manufactured components have high inter- and intra-layer bonding. This bonding inherently increases homogeneity, and due to the thin walls and struts that occur in cellular structures, this is essential for the prevention of failure points being 'built-in' to components. The success of this manufacturing optimisation process is further demonstrated by the validation of the NF material model using the SP structure (4.3.1.2) and the honeycomb component (4.2.3.3).

This material model was created through the successful development of a novel, accessible and transferable material characterisation approach. The equi-biaxial and planar rigs developed for this work help to demonstrate how a uniaxial test machine can be used to characterise elastomers dynamically. Validation of this approach, by the comparison of

simulated and mechanical responses (Figure 4.24) and deformation patterns (Figure 4.25), demonstrates accurate prediction of complex HE buckling events over multiple speeds and states.

While the validation process in this research demonstrated a high level of agreement between mechanical and simulated responses (Figure 4.24), a comparison was sought to contextualise it. No studies investigating the dynamic compression of elastomeric honeycombs were found. However, studies exploring the quasi-static out-of-plane compression of elastomeric honeycombs were identified [203, 204], as presented in Figure 5.1. These studies undertook no quantitative analysis; therefore, to enable a qualitative comparison of its agreement, the validation in this research (Figure 4.24) was also included in Figure 5.1.

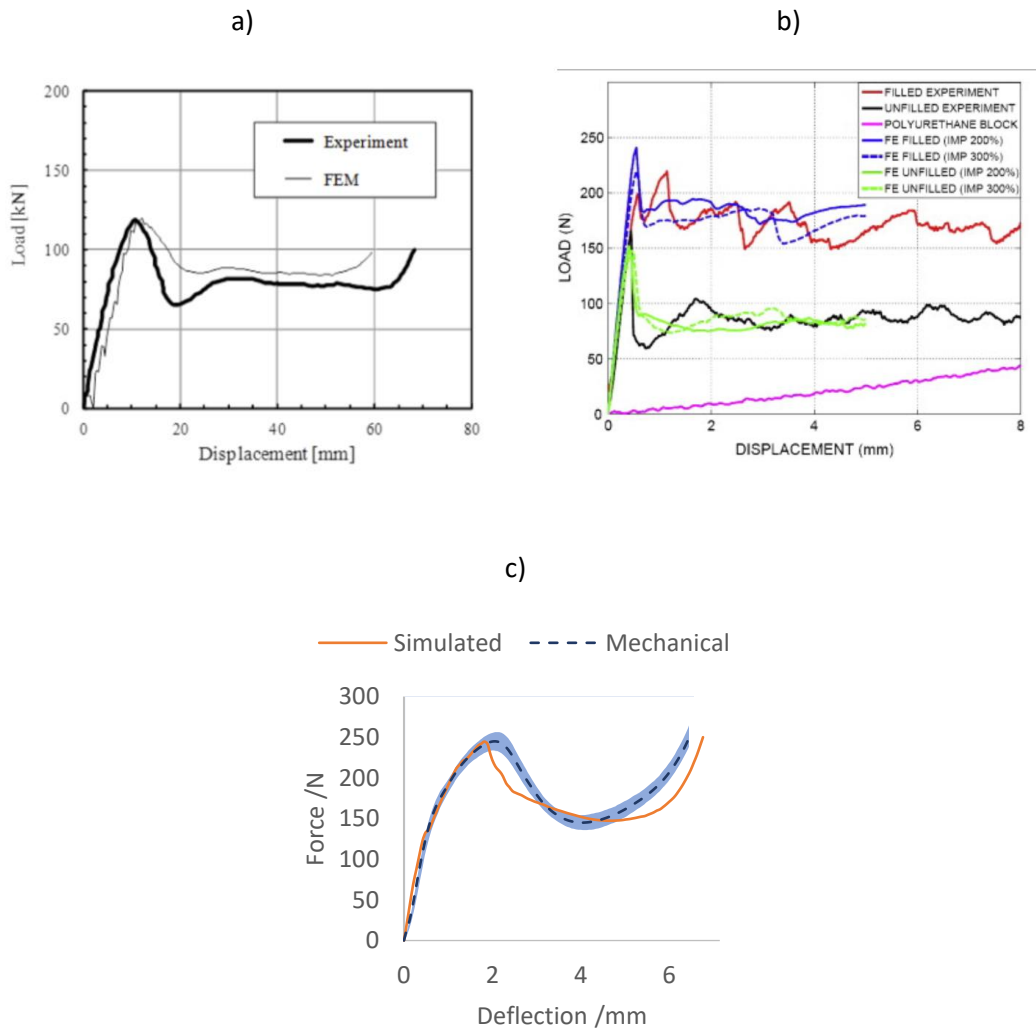


Figure 5.1. Quasi-static compression of honeycomb structures consisting of an elastomeric component, a) elastomeric honeycomb arrangement from [203], b) circular polycarbonate honeycomb, with elastomer fill from [204], c) elastomeric honeycomb simulated in this work (Figure 4.24)

The study presented in Figure 5.1a explored a similar honeycomb unit cell arrangement as this research, while Figure 5.1b presents the validation of circular polycarbonate honeycombs, filled with an elastomer. It is visually apparent that the work presented in this research (Figure 5.1c) has a superior agreement to both of the other studies (Figure 5.1a and b).

Additionally, the novel approach developed in this research has been used to characterise two different materials (Luvosint [205] and NinjaFlex [121]), which were then used to accurately simulate the multi-rate compression of three separate cellular structures (Miura Ori [205], Honeycomb [121], and SP (section 4.3.1.2)). The novel contributions presented in these journal papers, and this thesis, will help enable future studies of dynamic elastomeric structures. Additionally, they improve confidence that the approach proposed in this research can be applied to alternate materials and structures.

5.2.3 Computational generation of SP energy absorption diagram

A novel method to generate energy absorption diagrams, using computational analysis, has been developed (section 4.3.3). The SP structure has been successfully implemented in these diagrams, and equivalent efficiency has been demonstrated to the quasi-static performance of nylon-based SP structures [114] (section 4.3.3.3). This equivalency improves confidence in the generated diagrams.

This approach is the first known example of utilising computational analysis to generate rate-dependent energy absorption diagrams for elastomeric cellular structures. While an example of an elastomeric energy absorption diagram for a honeycomb was identified [180], the study did not explore rate-dependence and adopted an empirical approach to diagram generation. Note, this group has recently separately empirically investigated rate-dependence of functionally graded honeycombs; however, only stress-strain behaviour was analysed [206].

Additionally, this is the first known approach for scaling energy absorption diagrams between different base elastomeric materials. By performing uniaxial tension and stress relaxation testing of standardised uniaxial dumbbells, scaled energy absorption diagrams and a comprehensive scaled material model were developed (section 4.3.4). The resultant material model was then successfully mechanically validated. The lack of other examples in the literature highlights the novelty of this approach.

5.2.4 Analysis of prototype SP motorcycle helmet

A method of propagating the SP structure inside a helmet, without distorting its features, was successfully demonstrated (section 3.4.1). While coverage of the headform required the sectioning of some SP pads, the ability of this liner to meet the requirements of UNECE 22.05 highlights its success (section 4.4.2).

This work has developed and demonstrated a novel approach, combining an energy absorption diagram and computational analysis, to select cellular structure configurations for use in motorcycle helmets. After selecting a preliminary SP configuration from its energy absorption diagram (section 4.4.1.1), a subsequent simplified approach to the simulation of a motorcycle helmet impact enabled efficient optimisation (section 4.4.1.2). This approach has successfully been validated through mechanical testing, demonstrating good predictive capability (section 4.4.2.1).

To further assess the success of this simplified approach, its agreement was compared to that achieved by simulation of fully realised helmets. Only one example was found that performed computational validation of a motorcycle helmet with cellular structures [207]. This study investigated the placement of aluminium honeycomb inserts into an existing EPS motorcycle helmet, with the simulated geometry generated through CT scanning of the resultant helmet. The results of this study are presented in Figure 5.2. Additionally, a motorcycle helmet simulation using EPS alone was used as a point of comparison [36]. The generation of the simulated geometry in this second study came from CAD files supplied by the helmet's manufacturer. The results of this study are presented in Figure 5.3. Note, both of these examples were performed to the requirements of UNECE 22.05.

Both studies identified in the literature did not undertake any quantitative analysis [36, 207]. Therefore, their responses are presented next to those from the equivalent impact points in this research (Figure 4.65), in Figure 5.2 and Figure 5.3. Note, in the honeycomb helmet [207] point X was not investigated, and due to the inaccuracies described in section 4.4.2.1, point X was also not compared against the EPS only helmet [36].

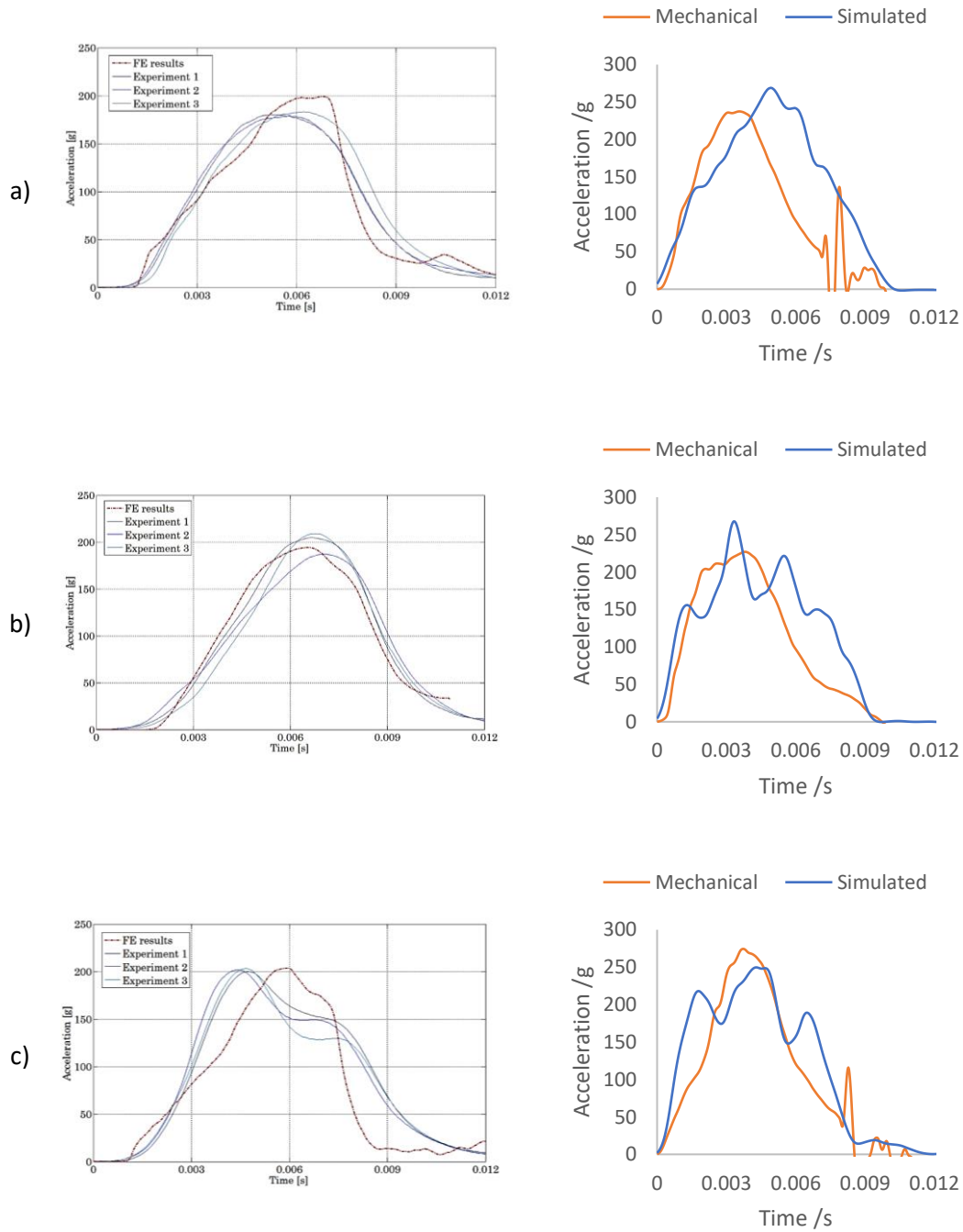


Figure 5.2 Comparison of simulated and experimental acceleration-time curves for an EPS lined helmet with metallic honeycomb inserts (left) replicated from [207], alongside the experimental and simulated responses of the SP helmet (right) presented in this thesis (Figure 4.65), at point a) B, b) R, c) P

The simulation of the honeycomb helmet has improved agreement between simulated and experimental data, at point R (Figure 5.2b), when compared to the results achieved by the SP helmet in this work. This is evidenced by the agreement in the general shape of the honeycomb acceleration-time curves, and the observed peak acceleration, between “FE results” and “Experiment 1” through “Experiment 3”. However, at points B and R (Figure

5.2a and c), the agreement observed between simulated and experimental loading responses of the honeycomb helmet is more comparable to that of the SP helmet; with similar differences in peak acceleration and deviation observed between experimental and simulated curves.

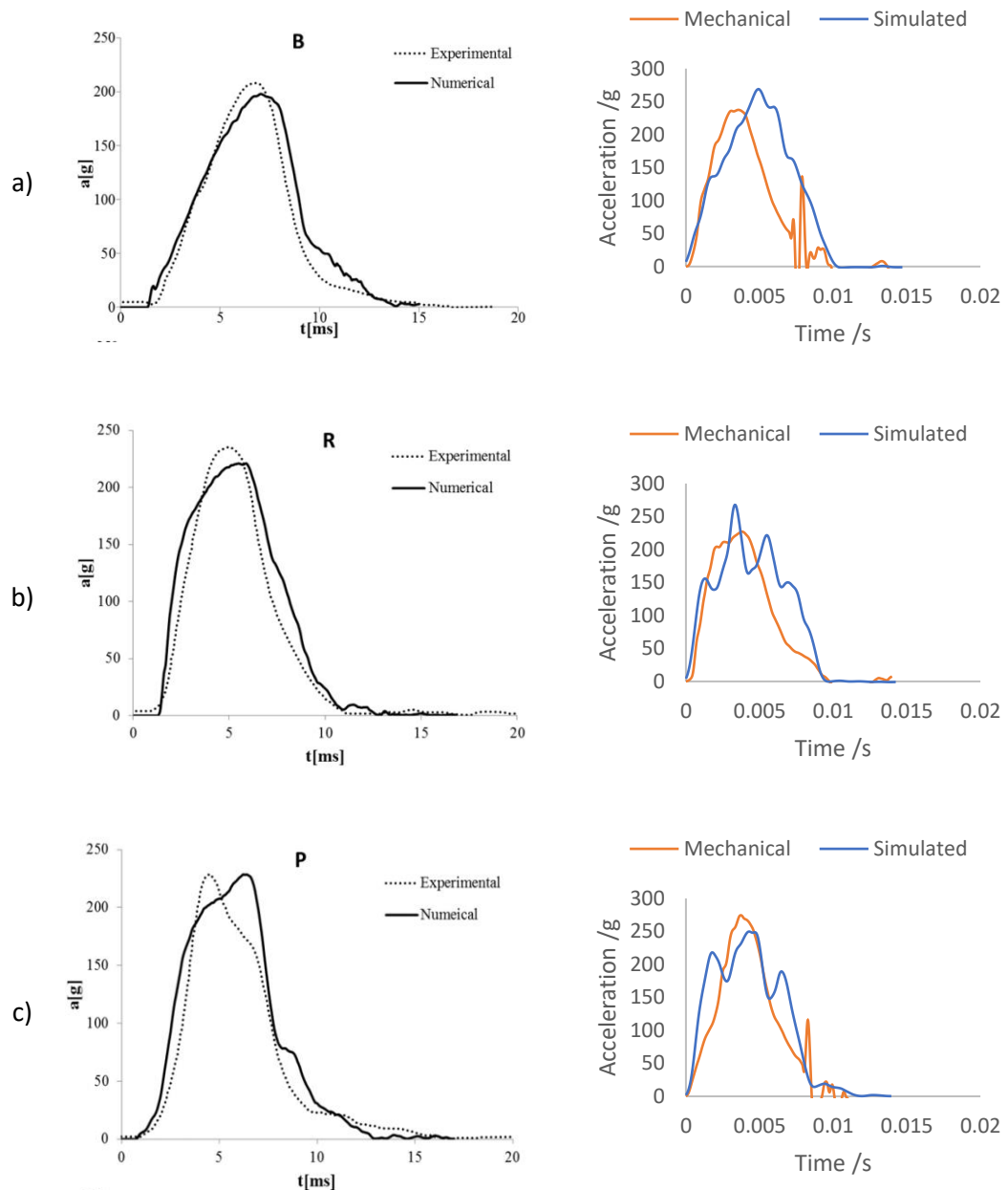


Figure 5.3 Comparison of simulated and experimental acceleration-time curves for an EPS lined helmet (left) replicated from [36], alongside the experimental and simulated responses of the SP helmet (right) presented in this thesis (Figure 4.65), at point a) B, b) R, c) P

Both the honeycomb and SP filled helmets (Figure 5.2) appear to have reduced agreement between experimental and simulated curve shape when compared to the EPS only helmet, shown in Figure 5.3. However, this is partially due to the scaling of the time axes as can be seen by the rescaling of the SP data from this research (Figure 5.3). While the EPS helmet arguably has reduced deviation between experimental and simulated results (compared to the SP structure), deviation and differences in peak acceleration can still be observed.

While the comparisons in Figure 5.2 and Figure 5.3 demonstrate the potential for improvement in the simulation of the SP structure (through the use of scanned geometry), they also highlight the comparable predictive power of the simplified approach presented in this thesis.

5.3 Limitations of this study

The limitations of this research are addressed in this section to provide insight into the challenges that will need to be met in future work.

5.3.1 Optimise processing parameters to produce functional cellular structures

The early stages of the research served to enable the later ones. Therefore, they were inherently limited in nature. Selection of the structure, limitation to commercially available filaments and a truncated optimisation process were all undertaken to allow the focus to remain on the objectives that followed them.

Therefore, other cellular structures have the potential to outperform the SP structure.

While the SP structure has been successful in meeting the requirements of this project, it was not explicitly developed for AM or impact mitigation. This research has provided the tools for evaluating the performance of new structures, relative to the SP structure, which will enable the identification of promising structures in the future.

Commercial filaments introduce an inherent restriction on material availability. While the development of high-performance polymers has been ongoing since the inception of Bakelite in 1907 [208], the focus of major chemical companies has not moved to FFF until recent years [162, 163]. Therefore the material selection in this research was limited.

The optimisation process undertaken in this research was limited in nature. It focussed primarily on achieving high-density components to reduce the inconsistencies between simulation and mechanical testing. For the implementation of this work into an industrial

environment, a more comprehensive optimisation approach may be desirable. For example, the extent to which each processing parameter affects cellular structure manufacturability could be investigated, in addition to optimising the material density.

5.3.2 Characterisation and computational modelling of AM elastomers

Collection of additional characterisation data has the potential to improve the material models presented in this thesis. However, incorporation of this data adds complexity and reduces accessibility. The first two features that could be considered for modelling of helmets are:

Temperature – UNECE 22.05 specifies conditioning tests at three separate temperatures [27]. In this research, testing was only undertaken at an ambient temperature condition, with low/high temperatures being excluded. As changes in temperature are well-known to affect the performance of materials, a temperature dependant HE model would be beneficial when specifying an elastomeric cellular structure for UNECE 22.05.

Hysteresis – Despite the lack of a hysteresis component, the unloading phase of the helmet impact was partially predicted in this research (section 4.4.2.1). This predictive capacity was likely due to the viscoelastic portion of the material model, which is known to provide a limited hysteresis effect [137]. However, incorporation of a dedicated hysteresis portion to the material model could improve this predictive capacity further. Care would need to be taken to ensure the proposed hysteresis component did not conflict with the hysteresis effect that was provided by the viscoelastic component.

Future modelling of temperature and hysteresis effects could allow for the simulation of edge cases, further minimising the suite of physical testing required for helmet certification, at the cost of reduced accessibility. Additionally, should computational power or techniques develop to the point that the parametric optimisation of helmet impacts is feasible, modelling of these effects will ensure a parametrically optimised helmet can satisfy all the requirements of UNECE 22.05.

Two other well-known HE effects, which should also be mentioned, are anisotropy and non-linear viscoelasticity. These effects are challenging to implement and additionally are less relevant for the simulation of helmet impacts, in light of the success demonstrated in this research.

Anisotropy – It is known that the layer-by-layer AM build process produces component anisotropy, with this behaviour frequently noted to alter mechanical performance under

loading perpendicular to deposited layers [209-211]. This work has shown a good correlation between experimental and simulated results, without anisotropy. However, alternate tensile dominated loading scenarios can benefit from its inclusion.

Viscoelasticity – While the use of non-linear visco-hyperelastic models may improve prediction of dynamically loaded elastomers, their modelling ability is questionable [212]. Additionally, they require a diverse range of strain-dependent characterisation, which reduces their accessibility further. Consequently, they are rarely incorporated into commercial curve-fitting packages and instead are implemented through custom material models [213]. Considering the validation presented in this thesis, they also arguably provide little benefit for the effort and additional computation cost required for their implementation.

5.3.3 Computational generation of SP energy absorption diagram

The approach presented in this thesis, to generate energy absorption diagrams, applies well to repeatable structures with limited variable parameters. Structures that are less constrained will be challenging to implement, without establishing restrictions on their parameters. For example, origami structures with several parameters may require an approach consisting of multiple cross-referenced energy absorption diagrams [189]. Therefore, complex structures may limit the application of this approach in the future.

During the exploration of higher speeds, the emergence of rate-dependent effects was noted. The effects of this rate-dependence on the stress-strain behaviour varied depending on thickness, with lower thicknesses having a far more undulating response than higher thicknesses. The potential reason for this rate-dependence was not explored. Therefore, it could be due to the $t:l$ ratio, to discrete wall thicknesses or some other mechanical effect. This effect should be further explored before applying the higher speed regions of the energy absorption diagram to other applications. Future work exploring why this undulation occurs, and how to leverage it, would help resolve this uncertainty and could provide a potential route to a highly rate-dependent helmet (section 6.2.2).

Power curves were shown to represent the rate-dependence of SP configurations well on energy absorption diagrams (section 4.3.3.2). However, in section 4.3.3.1, it is noted that the undulating response at higher speeds was significantly less efficient than the plateaued response at lower speeds. Therefore, if the SP structure was explored at a wider variety of speeds, a more appropriate mapping of this behaviour may require separate curves, maybe

including a transition curve. Without this more in-depth modelling, the accuracy of the energy absorption diagrams is reduced.

This work adopted a planar cross-sectional area, to specify the requirements of each impact point. Logically, a curved surface area would seem to be more suited to the specification of a helmet assembly (as the shell and headform are curved). If a curved surface area were to be used, the CSA of the impact points would increase non-uniformly from 19 to 29%. However, even when adopting a planar assumption, a stiffer structure was required when undertaking further optimisation (section 4.4.1.2); implying a need for a reduction in effective CSA, as opposed to the increase observed when transitioning from planar to curved CSA assumptions. This is likely due to the flattening of the helmet shell during impact (Figure 4.60), resulting in the mitigating liner being compressed between a more planar impacting surface and the curved headform. This flattening effect could occur due to several factors, which would vary for each impact point; including the changing radius of the headform, shell geometry, and stiffness of the padding. Comparably, non-uniformity was less apparent when adopting a planar assumption. Therefore, a planar CSA provided a good starting point for this research. However, there is scope for future work to explore the use of curved CSAs and scaling factors, to potentially improve these initial predictions.

5.3.4 Analysis of prototype SP motorcycle helmet

To ensure the testing of the helmet was controlled, guidewires were used during drop testing. The use of these wires meant the helmet testing was not fully in-line with the prescribed conditions of UNECE 22.05 (i.e. under freefall). This discrepancy means the results in this research are not directly equivalent to those that strictly followed the specification of UNECE 22.05. It should also be noted that the introduction of guidewires is a more severe test than freefall [214], as they restrict dissipation of energy through the rotation of the helmet.

A general trend of steadily increasing A_{max} and HIC, with increasing impact count, was observed at points B and R for the SP helmet (Figure 4.68 and Figure 4.70). It is argued in this thesis that this is linked to the steady failure of the shell, with this supported by visual observations (Appendix V) as well as changes in the acceleration-time pulse (section 4.4.2.3). This behaviour is observed at point R from the first to the sixth impact, with a steady increase in A_{max} and HIC as impact count increases. Additionally, it is observed in the progression from the first to the second and then to the sixth impact at point B.

However, as discussed in section 4.4.2.1, the primary impact for the SP helmet at point B resulted in the light gate connecting with the metal flag that activated it. While the fluctuation in the acceleration-time trace this caused was noted on the data acquisition device, the reason it occurred was not identified until later. The second impact was recorded as expected, but the third impact was not recorded. It was assumed that this was due to the testing equipment, so it was restarted and a manual check of the light gate was performed, indicating it was working correctly. Therefore, the fourth impact was performed; however, it also failed to record any data. After this, the machine was restarted, and the SP helmet was removed. A low-speed impact test using a sacrificial test helmet was performed, to check if triggering was occurring correctly. On its success, the SP helmet was replaced, and a fifth impact was attempted. During this impact, the weakened metal flag fully detached from the drop carriage assembly, highlighting that it had been damaged. The high-speed video was reviewed, and the flag was identified to be causing the triggering issue. Subsequent impacts were monitored for light gate contact, and the light gate was checked/replaced as necessary from this point forward. As a result of this, the acceleration-time traces for the third through fifth impacts at point B cannot be analysed in this thesis.

The mass of the SP liner is significantly higher than that of the EPS liner (+253%), leading to an increase in the overall helmet mass of 41%. It has been suggested that increased helmet mass results in an increased chance of neck injury [215]. While this suggestion appears logical, empirical studies of hospital submissions dispute it. One study found no existence of any link between increased helmet mass and serious neck injury [216], while another went as far as to assert that helmets reduced the occurrence and severity of neck injury [12]. Therefore, while this increase in mass is a potential challenge for market adoption, as riders understandably prefer a to wear lighter helmets, there is not a clear link between increases to helmet mass and decreases to rider safety.

When selecting SP configurations for the prototype helmet, all impact points required at least one additional step to reach an optimised configuration. Several factors likely contribute to this, including the lack of a viscoelastic scaling in the energy absorption diagram, the sectioning of the helmet (which was required to ensure full coverage of the head) and the poor load distribution of the shell. While the optimisation method was developed to compensate for this disparity, there is no clear way to accommodate it within the energy absorption diagrams presented in this thesis.

6 Conclusions

As discussed in section 5, the research aim (section 1.1) was achieved through the development of new methods (section 3) and demonstrated through experimentation (section 4). A summary of this discussion is covered in this section, framed by the research objectives (section 1.3).

6.1.1 Optimise processing parameters to produce functional cellular structures

- Optimisation of processing parameter enabled the manufacture of high-quality elastomeric FFF components.
 - An exceptionally high component density of 99.97% was achieved (section 4.1.2). This value exceeded that reported for successful SLS of elastomers (~95%) and was comparable to injection moulded elastomers (~100%) [202].
 - Controlled deposition of extra material ensured intra-layer voids were filled (Figure 4.4 A), without causing over-extrusion. Due to the high inter- and intra-layer bonding, cellular structures were reproduced accurately (Figure 4.6).
 - The high-quality achieved demonstrates the applicability of FFF to produce functional applications, disputing the perception that it produces inferior components.

6.1.2 Characterisation and computational modelling of AM elastomers

- A novel dynamic HE characterisation approach was developed.
 - Through the design and manufacture of equi-biaxial (Figure 4.10) and planar (Figure 4.11) test jigs, the ability to use only a uniaxial testing machine to collect multi-rate and multi-strain state data for an AM elastomer was demonstrated (section 4.2).
- Accurate rate-dependent simulation of complex HE buckling events was demonstrated, validating this characterisation approach.
 - Simulated and mechanical responses (Figure 4.24), in addition to deformation patterns (Figure 4.25), were shown to have high levels of agreement.
 - The agreement achieved in this validation (Figure 5.1) also demonstrated the success of the novel approach developed to identify the characterisation strain range (section 4.2.1).

6.1.3 Computational generation of SP energy absorption diagram

- A novel method to generate elastomeric rate-dependent energy absorption diagrams through computational analysis was developed.
 - This approach was then demonstrated through the successful implementation of the SP structure (section 4.3.3).
 - The ability of the SP structure to outperform EPS and VN was demonstrated by higher efficiency in energy absorption diagrams (Figure 4.44).
- An approach to scale an energy absorption diagram to different elastomeric materials was also developed.
 - Using only uniaxial tension and stress relaxation testing, the scaling of an energy absorption diagram, in addition to the creation of a comprehensive scaled material model, was demonstrated (section 4.3.4).
 - The resultant dynamic material model was successfully mechanically validated (Figure 4.51 and Figure 4.52).

6.1.4 Analysis of prototype SP motorcycle helmet

- This work has developed and demonstrated a novel approach, combining an energy absorption diagram and computational analysis, to select cellular structure configurations for use in motorcycle helmets.
 - After selecting preliminary SP configurations from an energy absorption diagram (section 4.4.1.1), a subsequent simplified approach to the simulation of a motorcycle helmet impact enabled efficient optimisation (section 4.4.1.2).
 - This approach has successfully been validated through mechanical testing, demonstrating good predictive capability (Figure 4.63 and Figure 4.65) and comparable agreement to that observed by simulation of fully modelled motorcycle helmets (Figure 5.2 and Figure 5.3).
- The single impact performance of a helmet liner manufactured from elastomeric cellular structures was demonstrated.
 - The SP filled helmet was shown to meet the requirements of UNECE 22.05 at three separate impact locations (Table 4.12).
 - This capability was achieved over a reduced liner thickness compared to EPS (section 5.2.4), with the prototype cellular helmet exceeding the

performance of EPS at one impact point (Table 4.12), with a liner thickness 70% that of EPS (section 5.2.4).

- This work demonstrated the ability of the SP structure to improve motorcyclist safety by providing multi-impact mitigation for a single collision.
 - A prototype helmet passed the requirements of the ECE 22.05 standard five times in a row (Figure 4.70), with a repeatable CoR over these five impacts (Figure 4.72)
 - The CoR of the prototype helmet was equivalent to that of the EPS helmet, despite the elastic nature of the cellular structure within (Figure 4.67)
 - Protection was provided even after cracks propagated through the helmet shell (Appendix VI).
 - Compared to the prototype helmet, the EPS failed to survive more than two impacts (Figure 4.69 and Figure 4.71), and even at the location where this was achieved, CoR was increased by ~25% (Figure 4.73).

6.2 Future work

6.2.1 Use of stiffer elastomers to increase the performance of cellular structures

At 7.5 m/s, when the SP energy absorption diagrams are scaled to an E_s of 120 MPa, an SP configuration (relative density of 0.193) transfers the same levels of energy as EPS (relative density of 0.065). While this requires an SP configuration with a density of 3x that of EPS, the resultant σ_p is ~25% lower. This reduced σ_p highlights the potential of combining the SP structure with emerging elastomeric filaments of even higher E_s (e.g. Dupont Hytrel [200]).

In addition to exploring materials with a higher E_s , exploring those with a lower E_s may also result in improved performance. Examining Table 4.7 and Figure 4.37 through to Figure 4.40 highlighted the existence of rate-dependence within the SP structure. It is well-known that wave speed (c) through solid materials can be linked to the base materials modulus (E)

and density (ρ), by $c = \sqrt{\frac{E}{\rho}}$. Therefore, this effect could potentially be exploited by

selecting a base material with a reduced E_s , resulting in a slower stress wave through the cellular structure and leading to the emergence of rate-dependent effects at lower speeds.

The work in section 4.2.1 and 4.3.4 also provides additional insight into the desirable stress-strain behaviour of the base elastomeric materials. Elastomers with a high instantaneous modulus allow cellular structures produced using them to reach ϵ_{p1} earlier than when

produced with a base material of lower instantaneous modulus (Figure 4.51). As ϵ_d is dictated by geometric self-contact, this ability to reach ϵ_{pl} at lower strains makes the energy absorption of a cellular structure more efficient.

6.2.2 Protect against concussive impacts with cellular structures

As discussed in section 2.1.2.2, mTBI (i.e. concussion) is increasingly being associated with long-term health issues, which motorcycle helmets are not currently capable of addressing. As highlighted in Figure 4.36, between 2.5 m/s and 7.5 m/s, there was little rate-dependence observed in the NF SP structure. Therefore, a helmet produced using the NF SP structure will result in a similar A_{max} value for both of these speeds. Note, EPS has reduced rate-dependence compared to the SP structure (section 4.3.3.3). This similar A_{max} results in the severity of low energy impacts being similar to those of much higher energy.

Increased rate-dependence of the SP structure could allow reduced severity at these lower speeds, resulting in the creation of a helmet that addresses concussion, while still performing to the existing high energy impacts defined in motorcycle helmet standards. This rate-dependence could be achieved by lowering E_s , as described in section 6.2.1, or by decreasing wall thickness, as a link between wall thickness and rate dependence was identified in section 4.3.3.1.

6.2.3 Generation of design tools for rotational criteria

As discussed in section 2.1.2.3, reduction of rotational velocity and acceleration is frequently identified as essential for improved head safety. In the same way that linear impact thresholds (duration and A_{max}) have been interpreted for use in energy absorption diagrams, a design tool could be created for rotational criteria (i.e. acceleration and velocity).

By analysing a cellular structure's shear performance at different angles, a rotation-based design tool could be produced. Utilising this tool, in combination with established rotational injury criteria, could allow the identification of an optimal configuration to reduce rotational injury. Moreover, a combined approach, alongside the linear energy absorption diagrams presented in this thesis, could allow an optimal configuration to be identified for combined linear and rotational performance.

While the numerical simulation of such structures can follow the same approach described in this research, an essential component of such analysis is physical validation. There are limited approaches to analyse combined compression-shear loading quasi-statically, let

alone dynamically. Fortunately, in 2018 the ability to collect such data was demonstrated in the literature, both quasi-statically [217] and dynamically [218]. This experimentation is supported by numerical modelling [219], demonstrating its potential applicability to the approach described in this thesis.

6.2.4 Improving the performance of motorcycle helmet shells

The investigation of improved liner energy mitigation is essential to the production of a safer helmet. However, investigations undertaken through the course of this work have highlighted the inability of the ABS shell to effectively distribute the impact load through the liner material (Figure 4.60). Additionally, preliminary investigations into shell materials also demonstrate the potential performance gains achieved by a stiffer shell (Appendix I). Increasing the stiffness of the helmet shell will lead to increased load distribution, opening access to lower density pads and therefore reduced A_{\max} .

Additionally, as discussed in section 4.4.2.3, preventing fracturing of the shell could result in further improvements to motorcycle helmet multi-impact performance, when combined with liners made from recoverable materials. Re-design of the shell may also allow the identification of a method to reduce its mass, compensating for the increased mass of the elastomeric cellular liner. Achieving a combined goal of increased stiffness, increased resilience, and reduced mass may not be feasible. However, all these variables should still be investigated, alongside studies exploring their relative importance to reducing head injury.

7 Reference list

1. Europe., U.N.E.C.f., *The United Nations Motorcycle Helmet Study*. 2016, United Nations.
2. Administration, N.H.T.S., *Traffic Safety Facts, 2016 Data, Motorcycles*. 2018, U.S. Department of Transportation.
3. Administration, N.H.T.S., *Traffic Safety Facts, 2013 Data, Motorcycles*. 2015, U.S. Department of Transportation.
4. Administration, N.H.T.S., *Fatality Analysis Reporting System*. U.S. Department of Transportation: Washington (DC).
5. Chinn, B., et al., *COST 327 Motorcycle Safety Helmets, final report of the action*. European Cooperation in the Field of Scientific and Technical Research. Belgium, 2001.
6. Wales, S.f., *Motorcycle user casualties, 2016*, N. Statistics, Editor. 2018.
7. Wales, S.f., *Police recorded road accidents, 2018*, N. Statistics, Editor. 2019.
8. Organization, W.H., *Helmets: a road safety manual for decision-makers and practitioners*. 2006.
9. Liu, B.C., et al., *Helmets for preventing injury in motorcycle riders*. Cochrane Database Syst Rev, 2008. **1**(1): p. CD004333.
10. Cook, L.J., et al., *Motorcycle helmet use and head and facial injuries: Crash outcomes in CODES-linked data*. 2009.
11. Rowland, J., et al., *Motorcycle helmet use and injury outcome and hospitalization costs from crashes in Washington State*. American Journal of Public Health, 1996. **86**(1): p. 41-45.
12. Sarkar, S., C. Peek, and J.F. Kraus, *Fatal injuries in motorcycle riders according to helmet use*. J Trauma, 1995. **38**(2): p. 242-5.
13. Administration, N.H.T.S., *Lives and costs saved by motorcycle helmets*. 2017, Department of Transportation: Washington (DC).
14. Administration, N.H.T.S., *2016 Fatal Motor Vehicle Crashes: Overview*. 2017, Department of Transportation.
15. Ankarath, S., et al., *Injury patterns associated with mortality following motorcycle crashes*. Injury, 2002. **33**(6): p. 473-7.
16. Wyatt, J.P., et al., *Injury analyses of fatal motorcycle collisions in south-east Scotland*. Forensic Sci Int, 1999. **104**(2-3): p. 127-32.
17. Goodwin, A.H., et al., *Countermeasures That Work: A Highway Safety Countermeasure Guide for State Highway Safety Offices:: 2015*. 2015, United States. National Highway Traffic Safety Administration.
18. SBRI. *Reducing Motorcyclists' Casualties In Wales*. 2015 01/01/2020]; Available from: https://sbri.innovateuk.org/competition-display-page/-/asset_publisher/E809e7RZ5TZ/content/reducing-motorcyclists-casualties-in-wales/1524978.
19. GB, R.S. *Welsh Government funds motorcyclist safety projects*. 2016 01/01/2020]; Available from: <https://roadsafetygb.org.uk/news/welsh-government-funds-motorcyclist-safety-projects-4922/>.
20. Hurt, H.H., *Motorcycle accident cause factors and identification of countermeasures*. Vol. 2. 1981: The Administration.
21. Alves de Sousa, R., et al., *Assessing the effectiveness of the use of a natural cellular material as safety padding in motorcycle helmet*. Vol. 88. 2011. 580.
22. Fenner Jr, H., et al., *Final Report of Workshop on Criteria for Head Injury and Helmet Standards*. Milwaukee WI: Medical College of Wisconsin and Snell Memorial Foundation, 2005.

23. Shuaeib, F.M., et al., *A new motorcycle helmet liner material: The finite element simulation and design of experiment optimization*. *Materials & Design*, 2007. **28**(1): p. 182-195.
24. Berg, F.A., et al. *Motorcycle impacts into roadside barriers-Real-world accident studies, crash tests and simulations carried out in Germany and Australia*. in *Proceedings of the Nineteenth International Conference on Enhanced Safety of Vehicles*, Washington, DC. 2005.
25. Viano, D.C. and D. Halstead, *Change in Size and Impact Performance of Football Helmets from the 1970s to 2010*. *Annals of Biomedical Engineering*, 2012. **40**(1): p. 175-184.
26. Fernandes, F. and R.A. De Sousa, *Motorcycle helmets—A state of the art review*. *Accident Analysis & Prevention*, 2013. **56**: p. 1-21.
27. UNECE, *22.05 rev. 4: Uniform provision concerning the approval of protective helmets and visors for drivers and passengers of motor cycles and mopeds*, United Nations Economic Commission for Europe. 2002.
28. Gilchrist, A. and N. Mills. *Deformation analysis for motorcycle helmets*. in *Proceedings of the International Research Council on the Biomechanics of Injury conference*. 1993. International Research Council on Biomechanics of Injury.
29. BSI, *BS 6658:1985*, in *Protective Helmets for Vehicle Users*, "British Standard Institution, London. 1985.
30. Gilchrist, A. and N. Mills, *Fast fracture of rubber-toughened thermoplastics used for the shells of motorcycle helmets*. *Journal of materials science*, 1987. **22**(7): p. 2397-2406.
31. DeMarco, A.L., et al., *The impact response of motorcycle helmets at different impact severities*. *Accident Analysis & Prevention*, 2010. **42**(6): p. 1778-1784.
32. Gilchrist, A. and N. Mills, *Protection of the side of the head*. *Accident Analysis & Prevention*, 1996. **28**(4): p. 525-535.
33. Fernandes, F.A. and R.A. De Sousa, *Finite element analysis of helmeted oblique impacts and head injury evaluation with a commercial road helmet*. *Struct. Eng. Mech*, 2013. **48**(5): p. 661-679.
34. Pinnoji, P.K. and P. Mahajan. *Impact analysis of helmets for improved ventilation with deformable head model*. in *IRCOBI Conference-Madrid (Spain)*. 2006.
35. Kostopoulos, V., et al., *Finite element analysis of impact damage response of composite motorcycle safety helmets*. *Composites Part B: Engineering*, 2002. **33**(2): p. 99-107.
36. Fernandes, F., et al., *Finite Element Analysis of Helmeted Impacts and Head Injury Evaluation with a Commercial Road Helmet*. 2013.
37. Walley, S. and J. Field, *Strain rate sensitivity of polymers in compression from low to high rates*. *DYMAT j*, 1994. **1**(3): p. 211-227.
38. Gennarelli, T.A. and L.E. Thibault, *Biomechanics of acute subdural hematoma*. *J Trauma*, 1982. **22**(8): p. 680-6.
39. Gennarelli, T.A., et al., *Diffuse axonal injury and traumatic coma in the primate*. *Ann Neurol*, 1982. **12**(6): p. 564-74.
40. Kleiven, S., *Why most traumatic brain injuries are not caused by linear acceleration but skull fractures are*. *Frontiers in bioengineering and biotechnology*, 2013. **1**: p. 15.
41. Holbourn, A.H.S., *MECHANICS OF HEAD INJURIES*. *The Lancet*, 1943. **242**(6267): p. 438-441.
42. Horgan, T.J. and M.D. Gilchrist, *The creation of three-dimensional finite element models for simulating head impact biomechanics*. *International Journal of Crashworthiness*, 2003. **8**(4): p. 353-366.

43. Kleiven, S., *Finite element modeling of the human head*. 2002, KTH.
44. Takhounts, E.G., et al., *On the development of the SIMon finite element head model*. 2003, SAE Technical Paper.
45. Cory, C.Z., et al., *The potential and limitations of utilising head impact injury models to assess the likelihood of significant head injury in infants after a fall*. Forensic Science International, 2001. **123**(2): p. 89-106.
46. Wauthle, R., et al., *Effects of build orientation and heat treatment on the microstructure and mechanical properties of selective laser melted Ti6Al4V lattice structures*. Additive Manufacturing, 2015. **5**: p. 77-84.
47. Rayne, J., *The Dynamic Behavior of Crash Helmets*. 1972.
48. Hutchinson, T.P., et al. *Protection of the unhelmeted head against blunt impact: The pedestrian and the car bonnet*. in *Proceedings of the Australasian road safety research, policing and education conference*. 2011.
49. Fahlstedt, M., *Numerical accident reconstructions: a biomechanical tool to understand and prevent head injuries*. 2015, KTH Royal Institute of Technology.
50. Rezaei, A., G. Karami, and M. Ziejewski, *Examination of brain Injury thresholds in terms of the severity of head motion and the brain stresses*. Intern Neurotrauma Lett, 2014. **35**.
51. Hoshizaki, T.B., et al., *The development of a threshold curve for the understanding of concussion in sport*. Trauma, 2017. **19**(3): p. 196-206.
52. Bey, T. and B. Ostick, *Second impact syndrome*. Western Journal of Emergency Medicine, 2009. **10**(1): p. 6.
53. Pellman, E.J., et al., *Concussion in Professional Football: Reconstruction of Game Impacts and Injuries*. Neurosurgery, 2003. **53**(4): p. 799-814.
54. Piland, S.G., et al., *Chapter 3 - Protective Helmets in Sports*, in *Materials in Sports Equipment (Second Edition)*, A. Subic, Editor. 2019, Woodhead Publishing. p. 71-121.
55. Lin, M.-R. and J.F. Kraus, *Methodological issues in motorcycle injury epidemiology*. Accident Analysis & Prevention, 2008. **40**(5): p. 1653-1660.
56. Shaheed, M.S. and K. Gkritza, *A latent class analysis of single-vehicle motorcycle crash severity outcomes*. Analytic Methods in Accident Research, 2014. **2**: p. 30-38.
57. Foundation, S., *M2020, 2020 STANDARD FOR PROTECTIVE HEADGEAR 2018*, Snell Foundation.
58. Hardy, W.N., T.B. Khalil, and A.I. King, *Literature review of head injury biomechanics*. International Journal of Impact Engineering, 1994. **15**(4): p. 561-586.
59. Gadd, C.W., *Use of a weighted-impulse criterion for estimating injury hazard*. 1966, SAE Technical Paper.
60. Gurdjian, E.S., V. Roberts, and L.M. Thomas, *Tolerance curves of acceleration and intracranial pressure and protective index in experimental head injury*. Journal of Trauma and Acute Care Surgery, 1966. **6**(5): p. 600-604.
61. Versace, J., *A review of the severity index*. 1971, SAE Technical Paper.
62. NOCSAE, *ND002-13m15 - Standard Performance Specification For Newly Manufactured Football Helmets*. 2015, National Operating Committee On Standards For Athletic Equipment.
63. Mertz, H.J., *Injury risk assessments based on dummy responses*, in *Accidental Injury*. 2002, Springer. p. 89-102.
64. Newman, J. *A generalized acceleration model for brain injury threshold (GAMBIT)*. in *International IRCOBI Conference on the Biomechanics of Impact*. 1986. Zurich, Switzerland.
65. Newman, J.A. and N. Shewchenko, *A proposed new biomechanical head injury assessment function-the maximum power index*. 2000, SAE Technical Paper.

66. Ruan, J.S., T.B. Khalil, and A.I. King, *Finite element modeling of direct head impact*. 1993, SAE Technical Paper.
67. Kang, H.-S., et al., *Validation of a 3D anatomic human head model and replication of head impact in motorcycle accident by finite element modeling*. SAE transactions, 1997: p. 3849-3858.
68. Kimpara, H., et al., *Investigation of anteroposterior head-neck responses during severe frontal impacts using a brain-spinal cord complex FE model*. 2006, SAE Technical Paper.
69. Schwartz, D., et al., *Development of a computationally efficient full human body finite element model*. Traffic injury prevention, 2015. **16**(sup1): p. S49-S56.
70. Takhounts, E.G., et al., *Development of brain injury criteria (BRIC)*. 2013, SAE Technical Paper.
71. Takhounts, E.G., et al. *Kinematic rotational brain injury criterion (BRIC)*. in *Proceedings of the 22nd enhanced safety of vehicles conference. Paper*. 2011.
72. Kimpara, H. and M. Iwamoto, *Mild traumatic brain injury predictors based on angular accelerations during impacts*. Annals of biomedical engineering, 2012. **40**(1): p. 114-126.
73. Kimpara, H., et al., *Head injury prediction methods based on 6 degree of freedom head acceleration measurements during impact*. International Journal of Automotive Engineering, 2011. **2**(2): p. 13-19.
74. Kleiven, S., *Predictors for traumatic brain injuries evaluated through accident reconstructions*. 2007, SAE Technical Paper.
75. Greenwald, R.M., et al., *Head impact severity measures for evaluating mild traumatic brain injury risk exposure*. Neurosurgery, 2008. **62**(4): p. 789-798.
76. Rowson, S. and S.M. Duma, *Brain injury prediction: assessing the combined probability of concussion using linear and rotational head acceleration*. Annals of biomedical engineering, 2013. **41**(5): p. 873-882.
77. Humanetics. *Strasbourg University Finite Element Head Model (SUFEHM)*. 11/10/2019]; Available from: <https://www.humaneticsatd.com/virtual-models/sufehm>.
78. SA/SNZ, AS/NZS 1698-2006: *Protective helmets for vehicle users*. 2006.
79. Administration, N.H.T.S., *49 CFR 571.218 - Standard No. 218; Motorcycle helmets*. 2011, DEPARTMENT OF TRANSPORTATION: Code of Federal Regulations. p. 22390-22396.
80. Gibson, L.J. and M.F. Ashby, *Cellular Solids: Structure and Properties*. 2 ed. Cambridge Solid State Science Series. 1997, Cambridge: Cambridge University Press.
81. Woolam, W.E., *A study of the dynamics of low energy cushioning materials using scale models*. Journal of Cellular Plastics, 1968. **4**(2): p. 79-83.
82. Zhang, J. and M.F. Ashby, *Mechanical selection of foams and honeycombs used for packaging and energy absorption*. Journal of Materials Science, 1994. **29**(1): p. 157-163.
83. Maiti, S., L. Gibson, and M. Ashby, *Deformation and energy absorption diagrams for cellular solids*. Acta metallurgica, 1984. **32**(11): p. 1963-1975.
84. BSI, *BS EN 960:2006 - Headforms for use in the testing of protective helmets*. 2006.
85. Goldstein, J.P., *The effect of motorcycle helmet use on the probability of fatality and the severity of head and neck injuries: a latent variable framework*. Evaluation Review, 1986. **10**(3): p. 355-375.
86. Yee, D. *Average Weight of Human Head*. 09/09/2019]; Available from: <http://danny.oz.au/anthropology/notes/human-head-weight.html>.

87. Hubbard, R.P. and D.G. McLeod, *Definition and development of a crash dummy head*. 1974, SAE Technical Paper.
88. Prabhu, S., V. Raja, and R. Nikhil. *Applications of Cellular Materials—An Overview*. in *Applied Mechanics and Materials*. 2015. Trans Tech Publ.
89. Khosroshahi, S.F., S.A. Tsampas, and U. Galvanetto, *Feasibility study on the use of a hierarchical lattice architecture for helmet liners*. *Materials Today Communications*, 2018. **14**: p. 312-323.
90. Elliott, J., et al., *In-situ deformation of an open-cell flexible polyurethane foam characterised by 3D computed microtomography*. *Journal of materials science*, 2002. **37**(8): p. 1547-1555.
91. Mills, N., *Polymer foams handbook: engineering and biomechanics applications and design guide*. 2007: Elsevier.
92. Castiglioni, A., et al., *Relevant materials parameters in cushioning for EPS foams*. *Colloids and Surfaces A: Physicochemical and Engineering Aspects*, 2017. **534**: p. 71-77.
93. Lam, T. and D. Gates, *Repeated impacts on a motorcycle helmet: What happens after a significant impact?* 2010, SAE Technical Paper.
94. Robinson, M., et al. *Developing Elastomeric Cellular Structures for Multiple Head Impacts*. in *IRCOBI Conference Proceedings*. 2017.
95. Ouellet, S., D. Cronin, and M. Worswick, *Compressive response of polymeric foams under quasi-static, medium and high strain rate conditions*. *Polymer Testing*, 2006. **25**(6): p. 731-743.
96. Krundaeva, A., et al., *Dynamic compressive strength and crushing properties of expanded polystyrene foam for different strain rates and different temperatures*. *Polymer Testing*, 2016. **55**: p. 61-68.
97. Di Landro, L., G. Sala, and D. Olivieri, *Deformation mechanisms and energy absorption of polystyrene foams for protective helmets*. *Polymer Testing*, 2002. **21**(2): p. 217-228.
98. Cui, L., S. Kiernan, and M.D. Gilchrist, *Designing the energy absorption capacity of functionally graded foam materials*. *Materials Science and Engineering: A*, 2009. **507**(1): p. 215-225.
99. Inc., B.L. *Tech Support Doc 0021: Material Properties of Polystyrene and Poly(methyl methacrylate) (PMMA) Microspheres*. 31/05/2019]; Available from: <https://www.bangslabs.com/sites/default/files/imce/docs/TSD%200021%20Material%20Properties%20Web.pdf>.
100. Ramirez, B.J., *Manufacturing and characterization of temperature-stable, novel, viscoelastic polyurea based foams for impact management*. 2017, UCLA.
101. Giudice, J.S., et al., *Development of Open-Source Dummy and Impactor Models for the Assessment of American Football Helmet Finite Element Models*. *Annals of Biomedical Engineering*, 2019. **47**(2): p. 464-474.
102. Harris, C.M. and A.G. Piersol, *Harris' shock and vibration handbook*. Vol. 5. 2002: McGraw-Hill New York.
103. Gent, A.N., *On the relation between indentation hardness and Young's modulus*. *Rubber Chemistry and Technology*, 1958. **31**(4): p. 896-906.
104. Matweb. *Overview of materials for PVC, Flexible grade*. 01/06/2019]; Available from: <http://www.matweb.com/search/datasheet.aspx?matguid=35691707c40445388b94db19e000c50a>.
105. Matweb. *Overview of materials for PVC, Rigid Grade*. 01/06/2019]; Available from: <http://www.matweb.com/search/DataSheet.aspx?MatGUID=69642362cb864d25b8f6eb9d02092ecf>.

106. Gimbel, G. and T.B. Hoshizaki, *A comparison between vinyl nitrile foam and new air chamber technology on attenuating impact energy for ice hockey helmets*. Int J Sports Sci Eng, 2008. **2**(3): p. 154-161.
107. Zhou, Z., et al., *Experimental investigation on the yield behavior of Nomex honeycombs under combined shear-compression*. Latin American Journal of Solids and Structures, 2012. **9**(4): p. 515-530.
108. Goldsmith, W. and J.L. Sackman, *An experimental study of energy absorption in impact on sandwich plates*. International Journal of Impact Engineering, 1992. **12**(2): p. 241-262.
109. Yasui, Y., *Dynamic axial crushing of multi-layer honeycomb panels and impact tensile behavior of the component members*. International Journal of Impact Engineering, 2000. **24**(6): p. 659-671.
110. Brennan-Craddock, J., et al., *The design of impact absorbing structures for additive manufacture*. Journal of Physics: Conference Series, 2012. **382**(1): p. 012042.
111. Helmets, D. *TECHNOLOGY - 6D helmets*. 28/05/19]; Available from: <https://www.6dhelmets.com/innovation/>.
112. Schaedler, T.A., et al., *Designing Metallic Microlattices for Energy Absorber Applications*. Advanced Engineering Materials, 2014. **16**(3): p. 276-283.
113. Keshavarzan, M., et al., *Investigation on the failure mechanism of triply periodic minimal surface cellular structures fabricated by Vat photopolymerization additive manufacturing under compressive loadings*. Mechanics of Materials, 2020. **140**: p. 103150.
114. Abueidda, D.W., et al., *Mechanical properties of 3D printed polymeric cellular materials with triply periodic minimal surface architectures*. Materials & Design, 2017. **122**: p. 255-267.
115. EOS. *PA 2200 Balance 1.0*. 31/05/2019; Available from: <https://eos.materialdatacenter.com/eo/en>.
116. Maskery, I., et al., *Compressive failure modes and energy absorption in additively manufactured double gyroid lattices*. Additive Manufacturing, 2017. **16**: p. 24-29.
117. Mohsenizadeh, M., et al., *Additively-manufactured lightweight Metamaterials for energy absorption*. Materials & Design, 2018. **139**: p. 521-530.
118. Maskery, I., et al., *Insights into the mechanical properties of several triply periodic minimal surface lattice structures made by polymer additive manufacturing*. Polymer, 2018. **152**: p. 62-71.
119. Spoerk, M., et al., *Polypropylene Filled With Glass Spheres in Extrusion-Based Additive Manufacturing: Effect of Filler Size and Printing Chamber Temperature*. Macromolecular Materials and Engineering, 2018. **303**(7): p. 1800179.
120. Prabhu, A.M., *Study of stress relaxation and strain recovery in elastomeric compounds used in pipe seals*. 1991, Loughborough University.
121. Robinson, M., et al., *Mechanical characterisation of additively manufactured elastomeric structures for variable strain rate applications*. Additive Manufacturing, 2019. **27**: p. 398-407.
122. Soe, S.P., et al., *Feasibility of optimising bicycle helmet design safety through the use of additive manufactured TPE cellular structures*. International Journal of Advanced Manufacturing Technology, 2015. **79**(9-12): p. 1975-1982.
123. Moore, J.P. and C.B. Williams. *Fatigue characterization of 3D printed elastomer material*. in *19th Annual International Solid Freeform Fabrication Symposium (SFF)*, Austin, TX, Aug. 2008.
124. Kanyanta, V. and A. Ivankovic, *Mechanical characterisation of polyurethane elastomer for biomedical applications*. Journal of the Mechanical Behavior of Biomedical Materials, 2010. **3**(1): p. 51-62.

125. Yoon, S.h., M. Winters, and C.R. Siviour, *High Strain-Rate Tensile Characterization of EPDM Rubber Using Non-equilibrium Loading and the Virtual Fields Method*. *Experimental Mechanics*, 2016. **56**(1): p. 25-35.
126. Chalivendra, V.B., et al., *Processing and mechanical characterization of lightweight polyurethane composites*. *Journal of Materials Science*, 2003. **38**(8): p. 1631-1643.
127. Wadley, H.N.G., N.A. Fleck, and A.G. Evans, *Fabrication and structural performance of periodic cellular metal sandwich structures*. *Composites Science and Technology*, 2003. **63**(16): p. 2331-2343.
128. Ajdari, A., H. Nayeb-Hashemi, and A. Vaziri, *Dynamic crushing and energy absorption of regular, irregular and functionally graded cellular structures*. *International Journal of Solids and Structures*, 2011. **48**(3-4): p. 506-516.
129. BSI, *BS ISO 37:2017 - Rubber, vulcanized or thermoplastic — Determination of tensile stress-strain properties*. 2017, BSI.
130. BSI, *BS ISO 7743 - Rubber, vulcanized or thermoplastic. Determination of compression stress-strain properties*. 2017, BSI.
131. Axel Products, I., *Testing Brief: Compression or Biaxial Extension?*
132. Sasso, M., et al., *Characterization of hyperelastic rubber-like materials by biaxial and uniaxial stretching tests based on optical methods*. *Polymer Testing*, 2008. **27**(8): p. 995-1004.
133. Day, J. and K. Miller, *Equibiaxial Stretching of Elastomeric Sheets, An Analytical Verification of an Experimental Technique*, in *ABAQUS users' conference*. 2000: Newport, RI. p. 205-220.
134. Kim, B., et al., *A comparison among Neo-Hookean model, Mooney-Rivlin model, and Ogden model for chloroprene rubber*. *International Journal of Precision Engineering and Manufacturing*, 2012. **13**(5): p. 759-764.
135. Timoshenko, S. and J.N. Goodier, *Theory of elasticity*. 1969: McGraw-Hill.
136. Bahuguna, S., R. Marlow, and T. Dalrymple. *Understanding frequency domain viscoelasticity in Abaqus*. in *Proceedings of the Fall 172nd Technical Meeting of the Rubber Division of the American Chemical Society, Cleveland, Ohio, USA*. 2007.
137. Dalrymple, T., J. Choi, and K. Miller. *Elastomer rate-dependence: A testing and material modeling methodology*. in *172nd Technical Meeting of the Rubber Division of the American Chemical Society (ACS), Cleveland, OH, Oct.* 2007.
138. Ogden, R.W., G. Saccomandi, and I. Sgura, *Fitting hyperelastic models to experimental data*. *Computational Mechanics*, 2004. **34**(6): p. 484-502.
139. Mower, T.M. and M.J. Long, *Mechanical behavior of additive manufactured, powder-bed laser-fused materials*. *Materials Science and Engineering: A*, 2016. **651**: p. 198-213.
140. Gorse, S., et al., *Additive manufacturing of metals: a brief review of the characteristic microstructures and properties of steels, Ti-6Al-4V and high-entropy alloys*. *Science and Technology of Advanced Materials*, 2017. **18**(1): p. 584-610.
141. Guide, A.B., *Version 6.13-1*. Dassault Systèmes Simulia Corp., Providence, RI, 2013.
142. Simulia, D.S., *Abaqus Analysis User's Guide, v. 6.13*. Johnston, RI, 2013.
143. Putz, M., et al., *Investigation of Turning Elastomers Assisted with Cryogenic Cooling*. *Procedia CIRP*, 2016. **40**: p. 631-636.
144. Nayak, R. and R. Shetty, *Cutting force and surface roughness in cryogenic machining of elastomer*. 2014.
145. Shih, A.J., M.A. Lewis, and J.S. Strenkowski, *End milling of elastomers—fixture design and tool effectiveness for material removal*. *Journal of Manufacturing Science and Engineering*, 2004. **126**(1): p. 115-123.
146. Thomas, D. and S. Gilbert, *Costs and cost effectiveness of additive manufacturing: A literature review and discussion*. 2015. 1-96.

147. Hopkinson, N. and P. Dicknes, *Analysis of rapid manufacturing—using layer manufacturing processes for production*. Proceedings of the Institution of Mechanical Engineers, Part C: Journal of Mechanical Engineering Science, 2003. **217**(1): p. 31-39.
148. Franchetti, M. and C. Kress, *An economic analysis comparing the cost feasibility of replacing injection molding processes with emerging additive manufacturing techniques*. The International Journal of Advanced Manufacturing Technology, 2017. **88**(9): p. 2573-2579.
149. Ford, S. and T. Minshall, *Invited review article: Where and how 3D printing is used in teaching and education*. Additive Manufacturing, 2019. **25**: p. 131-150.
150. ASTM, *F2792-12a. Standard terminology for additive manufacturing technologies* ASTM International, West Conshohocken, 2012.
151. Bikas, H., P. Stavropoulos, and G. Chryssolouris, *Additive manufacturing methods and modelling approaches: a critical review*. The International Journal of Advanced Manufacturing Technology, 2016. **83**(1): p. 389-405.
152. Zguris, Z., *How mechanical properties of stereolithography 3D prints are affected by UV curing*. Formlabs Inc., Somerville, MA, accessed Mar, 2016. **7**: p. 2017.
153. Colton, J. and B. Blair, *Experimental study of post-build cure of stereolithography polymers for injection molds*. Rapid Prototyping Journal, 1999. **5**(2): p. 72-81.
154. Saari, M., et al. *Additive Manufacturing of Soft and Composite Parts from Thermoplastic Elastomers*. in *Solid Freeform Fabrication Symposium*. Austin, TX: University of Texas at Austin. 2015.
155. Moore, J.P. and C.B. Williams, *Fatigue properties of parts printed by PolyJet material jetting*. Rapid Prototyping Journal, 2015. **21**(6): p. 675-685.
156. Parab, N.D., et al., *Real time observation of binder jetting printing process using high-speed X-ray imaging*. Scientific reports, 2019. **9**(1): p. 2499.
157. Hopkinson, N. and P. Erasenthiran. *High speed sintering-Early research into a new rapid manufacturing process*. in *Solid Freeform Fabrication Symposium*. 2004.
158. Davies, S. *voxeljet announces launch of VX200 High Speed Sintering 3D printer*. TCT Magazine 2017 [cited 2019 02/09/2019]; Available from: <https://www.tctmagazine.com/3d-printing-news/voxeljet-vx200-high-speed-sintering-3d-printer/>.
159. Voxeljet. *High Speed Sintering as a 3D printing process: flexible, customer-oriented and versatile*. Voxeljet [cited 2019 03/09/2019]; Available from: <https://www.voxeljet.com/anwendungen/funktionsmodelle/whitepaper-voxeljet-high-speed-sintering/>.
160. Deckard, C.R., *Apparatus for producing parts by selective sintering*. 1997, Google Patents.
161. Tofail, S.A.M., et al., *Additive manufacturing: scientific and technological challenges, market uptake and opportunities*. Materials Today, 2018. **21**(1): p. 22-37.
162. Boissonneault, T. *DuPont introduces new Zytel and Hytrel pellets and filaments for 3D printing*. 2019 3/6/19]; Available from: <https://www.3dprintingmedia.network/dupont-new-zytel-hytrel-pellets-filaments-3d-printing/>.
163. JACKSON, B. *BASF AND INNOFIL3D EXPAND ULTRAFUSE RANGE OF FILAMENTS WITH ESD SAFE AND FLEXIBLE MATERIALS*. 3D printing industry 2019 [cited 2019 03/09/2019]; Available from: <https://3dprintingindustry.com/news/basf-and-innofil3d-expand-ultrafuse-range-of-filaments-with-esd-safe-and-flexible-materials-154990/>.

164. Crump, S.S., *Apparatus and method for creating three-dimensional objects*. 1992, Google Patents.
165. Zander, N.E., M. Gillan, and R.H. Lambeth, *Recycled polyethylene terephthalate as a new FFF feedstock material*. *Additive Manufacturing*, 2018. **21**: p. 174-182.
166. Hart, K.R., J.B. Frketic, and J.R. Brown, *Recycling meal-ready-to-eat (MRE) pouches into polymer filament for material extrusion additive manufacturing*. *Additive Manufacturing*, 2018. **21**: p. 536-543.
167. Woern, A.L., et al., *RepRapable Recyclebot: Open source 3-D printable extruder for converting plastic to 3-D printing filament*. *HardwareX*, 2018. **4**: p. e00026.
168. Ilkgün, Ö., *Effects of production parameters on porosity and hole properties in laser sintering rapid prototyping process*. 2005, The Graduate School of Natural and Applied Sciences of Middle East Technical
169. Cooke, W., et al., *Anisotropy, homogeneity and ageing in an SLS polymer*. *Rapid Prototyping Journal*, 2011. **17**(4): p. 269-279.
170. Van Hooreweder, B., et al., *Microstructural characterization of SLS-PA12 specimens under dynamic tension/compression excitation*. *Polymer Testing*, 2010. **29**(3): p. 319-326.
171. Shaw, B. and S. Dirven. *Investigation of porosity and mechanical properties of nylon SLS structures*. in *2016 23rd International Conference on Mechatronics and Machine Vision in Practice (M2VIP)*. 2016.
172. Wittbrodt, B. and J.M. Pearce, *The effects of PLA color on material properties of 3-D printed components*. *Additive Manufacturing*, 2015. **8**: p. 110-116.
173. Laureto, J., et al., *Thermal properties of 3-D printed polylactic acid-metal composites*. *Progress in Additive Manufacturing*, 2017. **2**(1): p. 57-71.
174. Aniwaa. *PROMAKER P1000*. 27/06/19]; Available from: <https://www.aniwaa.com/product/3d-printers/prodways-promaker-p1000/>.
175. Prodways. *ProMaker P1000*. 27/06/19]; Available from: <https://www.prodways.com/en/industrial-3D-printers/promaker-p1000/>.
176. Statistics, N., *QUARTERLY ENERGY PRICES - Quarter 4 2018*, E.I.S. Department for Business, Editor. 2019.
177. Feng, L., Y. Wang, and Q. Wei, *PA12 Powder Recycled from SLS for FDM*. *Polymers*, 2019. **11**(4): p. 727.
178. Rigid.ink. *The Ultimate 3D Print Quality Troubleshooting Guide 2019*. 27/06/19]; Available from: <https://rigid.ink/pages/ultimate-troubleshooting-guide>.
179. Simplify3D. *Print Quality Troubleshooting Guide*. 27/06/19]; Available from: <https://www.simplify3d.com/support/print-quality-troubleshooting/>.
180. Bates, S.R.G., I.R. Farrow, and R.S. Trask, *3D printed polyurethane honeycombs for repeated tailored energy absorption*. *Materials & Design*, 2016. **112**: p. 172-183.
181. Simplify3D. *Scars on Top Surface*. 27/06/19]; Available from: <https://www.simplify3d.com/support/print-quality-troubleshooting/scars-on-top-surface/>.
182. Ninjatek. *Technical Specifications: NinjaFlex® 3D Printing Filament*. 03/06/19]; Available from: <https://ninjatek.fppsites.com/wp-content/uploads/2018/10/NinjaFlex-TDS.pdf>.
183. Soe, S., *Energy absorption characteristics of additively manufactured TPE cellular structures*. 2015.
184. Diabase. *How To Print Flexible Filament*. 2017 27/06/19]; Available from: <https://flexionextruder.com/print-flexible-filament/>.
185. NinjaTek. *NinjaFlex*. 27/06/19]; Available from: <https://ninjatek.com/ninjaflex/>.
186. Treloar, L.R.G., *The physics of rubber elasticity*. 1975: Oxford University Press, USA.

187. Bergstrom, J.S., *Mechanics of solid polymers: theory and computational modeling*. 2015: William Andrew.
188. BSI, *BS 903-5:2004 - Physical testing of rubber. Guide to the application of rubber testing to finite element analysis*. 2004, BSI: BSI.
189. Harris, J.A., *Additively manufactured metallic cellular materials for blast and impact mitigation*. 2018, University of Cambridge.
190. Hale, S. *Should Tetrahedral Elements Be Avoided In Explicit Dynamics Analysis?* 2013 12/09/2019]; Available from: <https://caeai.com/blog/should-tetrahedral-elements-be-avoided-explicit-dynamics-analysis>.
191. Diehl, T. *Using Advanced Energy Methods to Enhance FEA and Experiments*. 2012 12/09/2019]; Available from: http://www.simulia.com/SCCProceedings2012/content/presentations/Diehl_Bodie_5222012.pdf.
192. ABAQUS. *Overview of ABAQUS/Explicit*. 03/06/19]; Available from: <https://imechanica.org/files/0-overview%20Explicit.pdf>.
193. Yang, L. *A study about size effects of 3D periodic cellular structures*. in *Proceedings of the 27th International Solid Freeform Fabrication (SFF) Symposium, Austin, TX*. 2016.
194. Maskery, I., et al., *Effective design and simulation of surface-based lattice structures featuring volume fraction and cell type grading*. *Materials & Design*, 2018. **155**: p. 220-232.
195. Ninjatek. *Technical Specifications: Cheetah™ 3D Printing Filament*. 03/06/19]; Available from: <https://ninjatek.fppsites.com/wp-content/uploads/2018/10/Cheetah-TDS.pdf>.
196. Song, B., et al., *Compressive and tensile stress–strain responses of additively manufactured (AM) 304L stainless steel at high strain rates*. *Journal of Dynamic Behavior of Materials*, 2017. **3**(3): p. 412-425.
197. Marlow, R., *A general first-invariant hyperelastic constitutive model*. *Constitutive Models for Rubber*, 2003: p. 157-160.
198. Tobajas, R., E. Ibartz, and L. Gracia. *A comparative study of hyperelastic constitutive models to characterize the behavior of a polymer used in automotive engines*. in *Proceedings of the 2nd International Electronic Conference on Materials*. 2016.
199. Lee, S., et al., *Dynamic failure of metallic pyramidal truss core materials – Experiments and modeling*. *International Journal of Plasticity*, 2006. **22**(11): p. 2118-2145.
200. DuPont. *DuPont™ Hytrel® 3D4100FL NC010*. 03/06/19]; Available from: https://www.dupont.com/content/dam/dupont/products-and-services/plastics-polymers-and-resins/plastics-polymers-and-resins-landing/documents/Hytrel_3D4100FL_NC010.pdf.
201. Ouckama, R. and D.J. Pearsall, *Impact performance of ice hockey helmets: head acceleration versus focal force dispersion*. *Proceedings of the Institution of Mechanical Engineers, Part P: Journal of Sports Engineering and Technology*, 2012. **226**(3-4): p. 185-192.
202. Dadbakhsh, S., et al. *Effect of powder size and shape on the SLS processability and mechanical properties of a TPU elastomer*. in *Physics Procedia*. 2016. Elsevier.
203. Kobayashi, T., et al., *Application of Thermoplastic Polyester Elastomer for Honeycomb Shock Absorbing Components*.
204. D’Mello, R.J. and A.M. Waas, *Synergistic energy absorption in the axial crush response of filled circular cell honeycombs*. *Composite Structures*, 2012. **94**(5): p. 1669-1676.

205. Adams, R., et al., *A novel pathway for efficient characterisation of additively manufactured thermoplastic elastomers*. *Materials & Design*, 2019. **180**: p. 107917.
206. Bates, S.R.G., I.R. Farrow, and R.S. Trask, *Compressive behaviour of 3D printed thermoplastic polyurethane honeycombs with graded densities*. *Materials & Design*, 2019. **162**: p. 130-142.
207. Caserta, G., *The use of honeycomb in the design of innovative helmets*, in *Aeronautics*. 2012, Imperial College London: Imperial College London.
208. Baekeland, L.H., *Method of making insoluble products of phenol and formaldehyde*. 1909, Google Patents.
209. Frazier, W.E., *Metal Additive Manufacturing: A Review*. *Journal of Materials Engineering and Performance*, 2014. **23**(6): p. 1917-1928.
210. Soe, S.P., et al., *Mechanical characterisation of Duraform® Flex for FEA hyperelastic material modelling*. *Polymer Testing*, 2014. **34**: p. 103-112.
211. Ahn, S.-H., et al., *Anisotropic material properties of fused deposition modeling ABS*. *Rapid prototyping journal*, 2002. **8**(4): p. 248-257.
212. Karim, M., Z. Zhang, and Y. Zhu, *Prediction of Nonlinear Viscoelastic Recovery of Thermoplastic Polymers using Abaqus Parallel Rheological Framework (PRF) Model*. *Science in the Age of Experience*, Boston, 2016.
213. Khajehsaeid, H., et al., *A visco-hyperelastic constitutive model for rubber-like materials: A rate-dependent relaxation time scheme*. *International Journal of Engineering Science*, 2014. **79**: p. 44-58.
214. Thorn, D.R., H.H. Hurt Jr, and T.A. Smith. *Motorcycle helmet test headform and test apparatus comparison*. in *Proceedings of the 16th ESV Conference, Windsor, ON, Canada*. 1998. Citeseer.
215. Huston, R. and J. Sears, *Effect of protective helmet mass on head/neck dynamics*. 1981.
216. O'Connor, P.J., *Motorcycle helmets and spinal cord injury: helmet usage and type*. *Traffic injury prevention*, 2005. **6**(1): p. 60-66.
217. Ling, C., et al., *Deformation response of EPS foam under combined compression-shear loading. Part I: Experimental design and quasi-static tests*. *International Journal of Mechanical Sciences*, 2018. **144**: p. 480-489.
218. Ling, C., et al., *Deformation response of EPS foam under combined compression-shear loading. Part II: High strain rate dynamic tests*. *International Journal of Mechanical Sciences*, 2018. **145**: p. 9-23.
219. Ling, C., P. Cardiff, and M.D. Gilchrist, *Mechanical behaviour of EPS foam under combined compression-shear loading*. *Materials Today Communications*, 2018. **16**: p. 339-352.

A Appendices

I. Shell element investigation

Solid quadratic tetrahedral elements have been shown to have a high correlation with mechanical testing in this research (section 4.2.3.3). However, they are computationally expensive. Comparatively, shell elements simplify the simulation setup by not requiring the physical modelling of wall thickness, in addition to being more computationally efficient. However, these efficiencies are based on assumptions regarding element boundary conditions, which bring the appropriateness of shell element for modelling thicker components into question.

Due to the computational efficiencies that shell elements offer, a preliminary study was undertaken to investigate their accuracy. Three Schwarz primitive (SP) configurations with $t:l$ ratios of 0.05:1, 0.1:1 and 0.15:1, consisting of $3*3*3$ unit cells and a cell length (l) of 10 mm, were investigated using solid and shell elements. As the final objective of this work was to produce a helmet to the requirements of UNECE 22.05, constant displacement was applied over a duration that resulted in compression at 7.5 m/s. The default ABAQUS mesh size was used. The results of this investigation are presented in Figure A.1.

For all configurations investigated, the shell elements resulted in notably higher ϵ_d . As the $t:l$ ratio increased, the shell elements generated increasingly higher ϵ_d over the solid elements. This difference was most notable for the configuration with a $t:l$ ratio of 0.15:1, where ϵ_d increased by 37%, compared to an increase of only 8% for a $t:l$ ratio of 0.05:1. Additionally, for a $t:l$ ratio of 0.1:1, the energy capacity of shell elements was 16% lower than that of solid elements, and for a $t:l$ ratio of 0.15:1 it was 34% lower.

Of the configurations investigated, only the $t:l$ ratio of 0.05:1 demonstrated good agreement between the shell and solid elements. If the wall thickness exceeded this $t:l$ ratio, then the stress generated and ϵ_d became inaccurate, resulting in under-prediction of the energy absorption capacity.

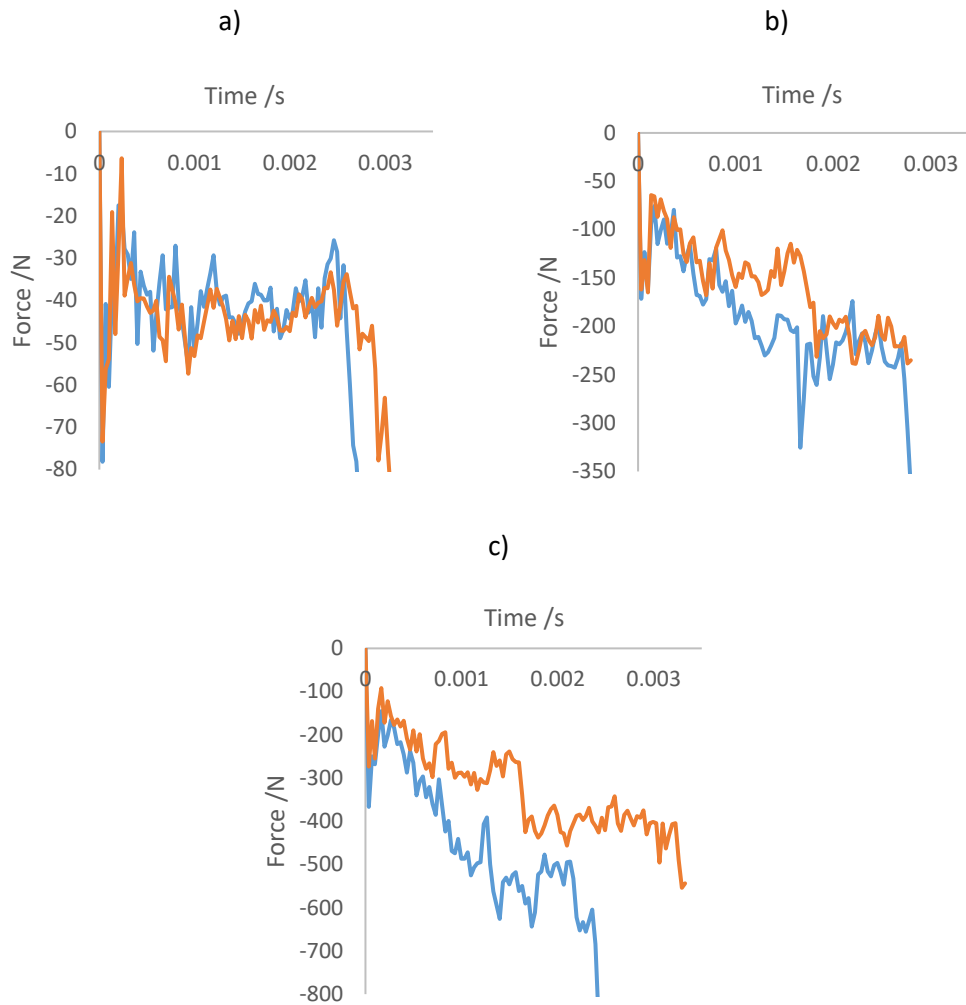


Figure A.1. Simulated force-time curves for NF SP pads using solid (blue), and shell (orange), elements, a) $t:l = 0.05:1$, b) $t:l = 0.1:1$, c) $t:l = 0.15:1$

II. Raw simulated response of the NF SP structure for the generation of energy absorption diagrams

The force-time curves for the simulations that produced the SP energy absorption diagram are shown in Figure A.2 through to Figure A.7. These curves are presented with and without filtering, which was used to remove generated noise, to highlight its effect. As described in section 3.3.3, the SP configurations investigated all consisted of $3*3*3$ unit cells, with $l = 10$ mm.

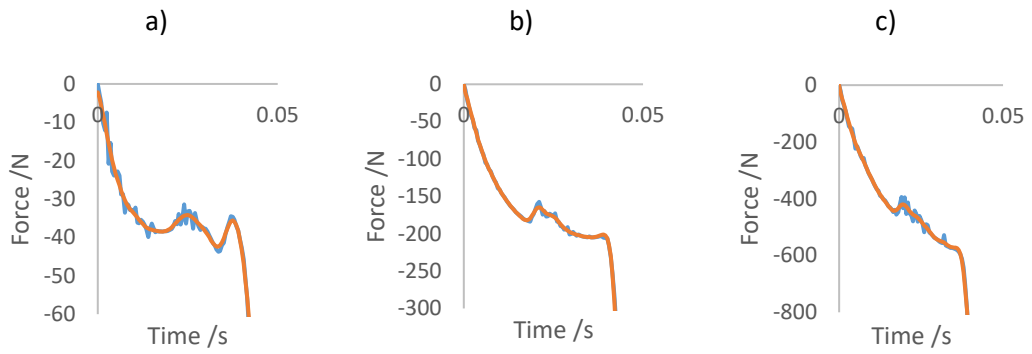


Figure A.2. Unfiltered (blue) and filtered (orange) simulated force-time curves for SP configurations, at 0.5 m/s and, a) $t:l = 0.05:1$, b) $t:l = 0.1:1$, c) $t:l = 0.15:1$

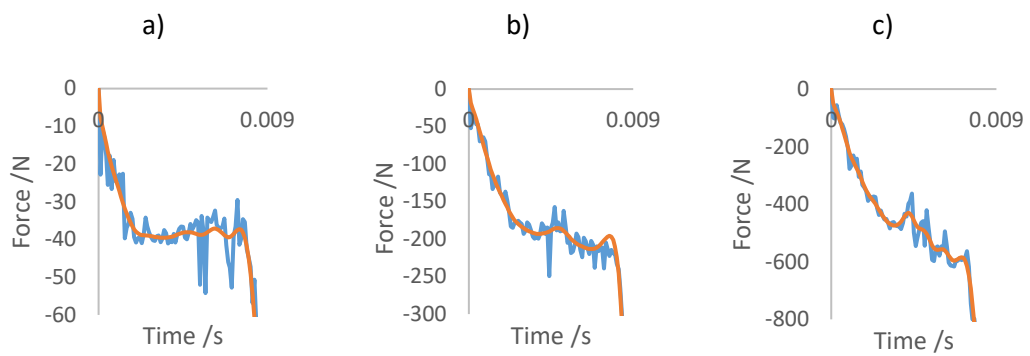


Figure A.3. Unfiltered (blue) and filtered (orange) simulated force-time curves for SP configurations, at 2.5 m/s and, a) $t:l = 0.05:1$, b) $t:l = 0.1:1$, c) $t:l = 0.15:1$

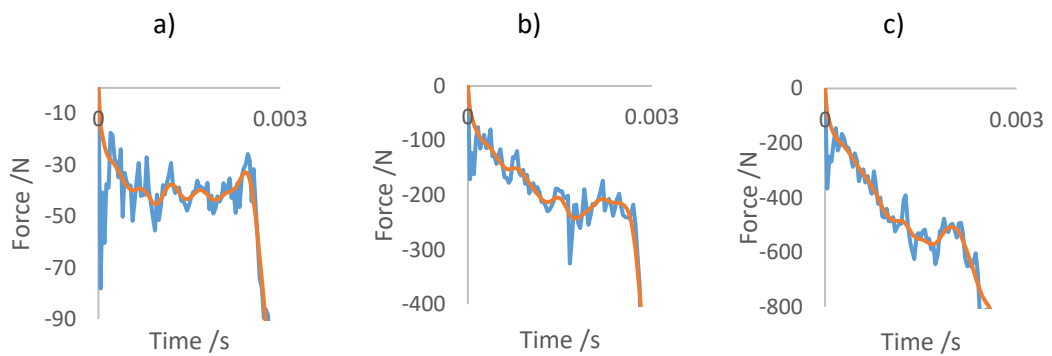


Figure A.4. Unfiltered (blue) and filtered (orange) simulated force-time curves for SP configurations, at 7.5 m/s and, a) $t:l = 0.05:1$, b) $t:l = 0.1:1$, c) $t:l = 0.15:1$

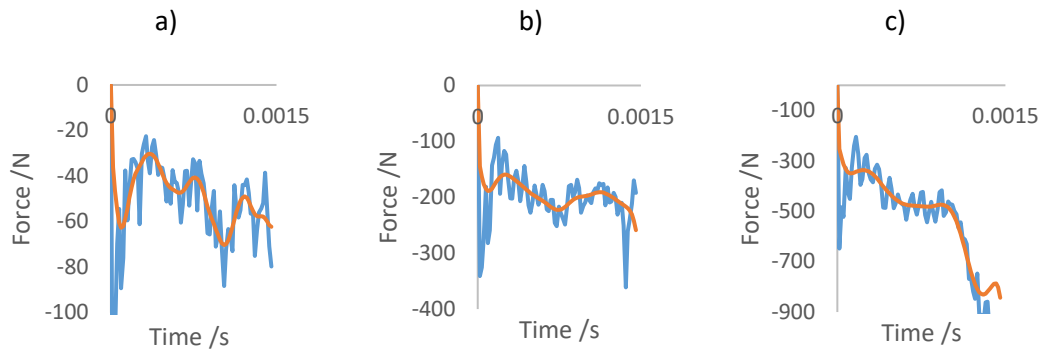


Figure A.5. Unfiltered (blue) and filtered (orange) simulated force-time curves for SP configurations, at 13.4 m/s and, a) $t:l = 0.05:1$, b) $t:l = 0.1:1$, c) $t:l = 0.15:1$

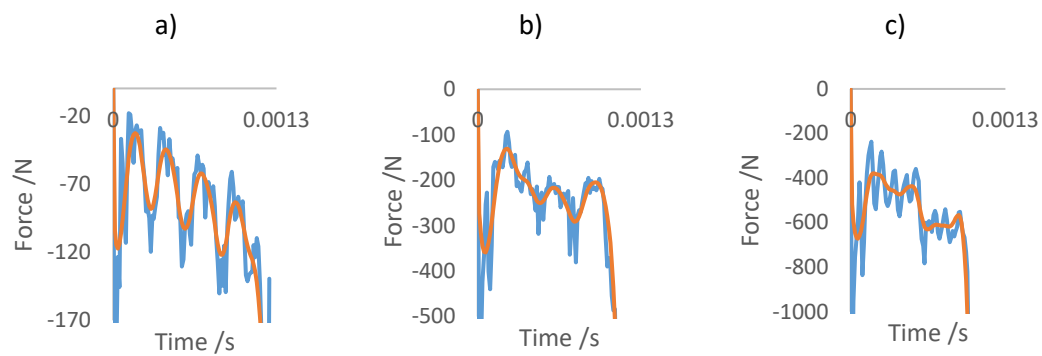


Figure A.6. Unfiltered (blue) and filtered (orange) simulated force-time curves for SP configurations, at 20 m/s and, a) $t:l = 0.05:1$, b) $t:l = 0.1:1$, c) $t:l = 0.15:1$

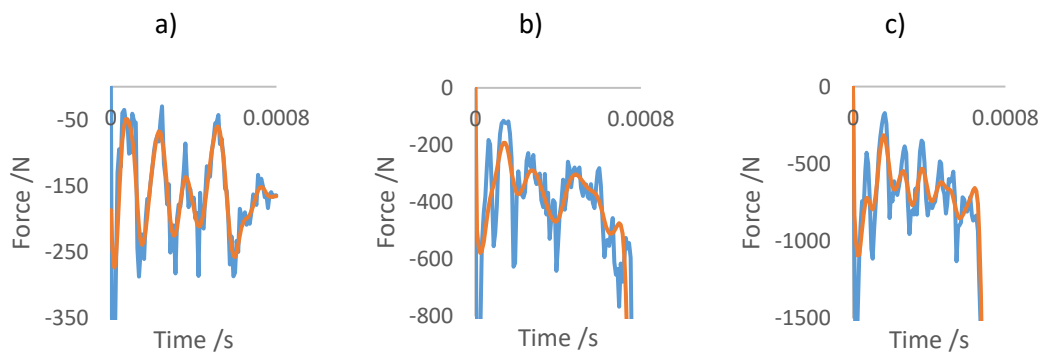


Figure A.7. Unfiltered (blue) and filtered (orange) simulated force-time curves for SP configurations, at 31.3 m/s and, a) $t:l = 0.05:1$, b) $t:l = 0.1:1$, c) $t:l = 0.15:1$

III. Raw data for the dynamic experimental compression of NF and CH cubes

This section presents the raw data generated when performing drop tower experimentation on NF (Figure A.8) and CH (Figure A.9) pads. The experimental approach to generate this data is described in section 3.3.1.3.

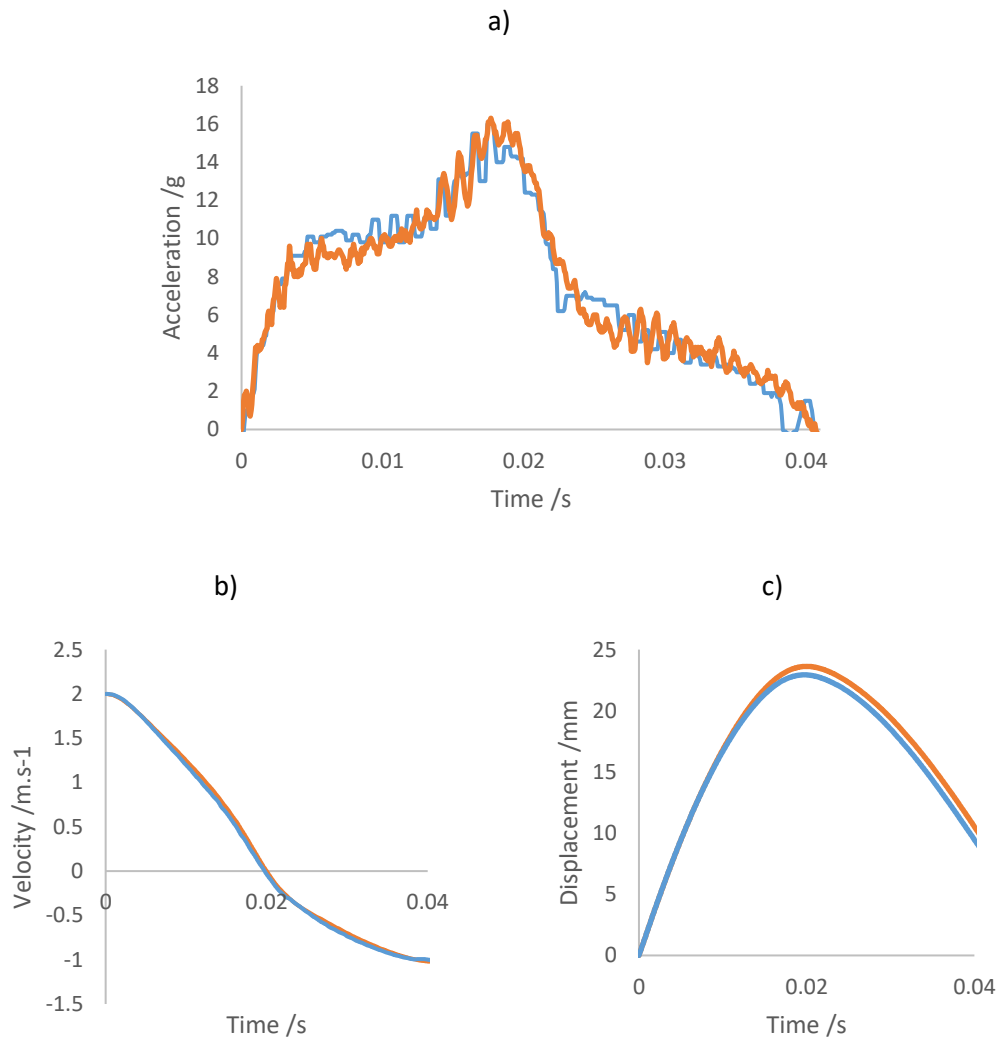


Figure A.8. Experimental dynamic compression of NF SP pads: a) acceleration-time curve, b) integrated velocity-time curve, c) integrated displacement-time curve

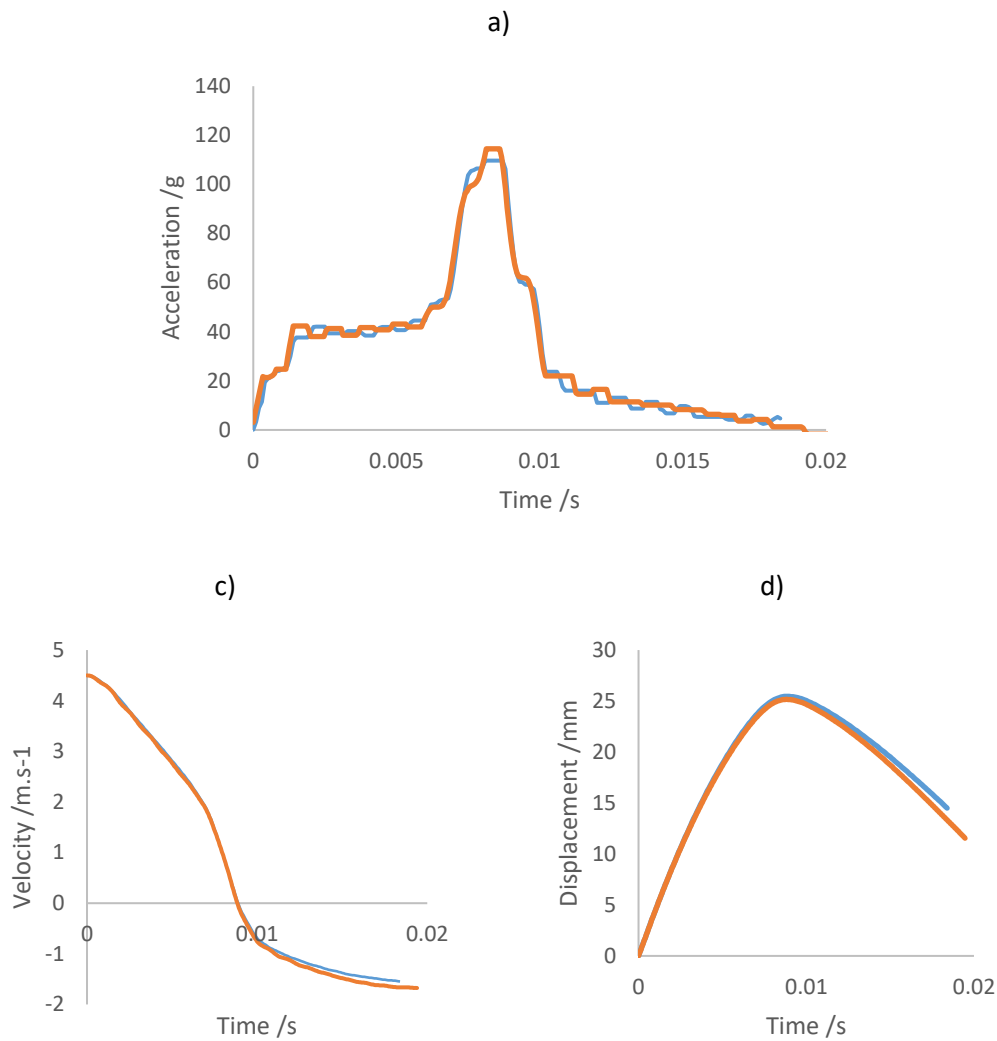


Figure A.9. Experimental dynamic compression of CH SP pads: a) acceleration-time curve, b) velocity-time curve (via integration), c) displacement-time curve (via double integration)

The CoR for the NF SP pad was 0.5 and 0.37 for the CTH pads. These CoR values demonstrate that elastomeric SP structures do not return incoming energy, but instead absorb 50 - 63% of it. It should be noted that this testing was performed to overcompress the SP structure past ϵ_d . Exceeding ϵ_d is indicative of a cellular structure's features starting to engage in self-contact (section 4.2.1). Consequently, if the SP structure was used efficiently (deformation $< \epsilon_d$), this CoR could change.

IV. Investigating shell stiffness

This section describes a brief investigation performed to identify the indicative performance of increasing the helmet shell stiffness. Therefore, the goal was not that the simulation was accurate, but the identification of the relative change in performance associated with an increase in stiffness. To ensure this investigation was bounded in reality, an existing motorcycle helmet shell material was investigated to provide this increased stiffness.

In addition to acrylonitrile butadiene styrene (ABS), motorcycle helmet shells are also constructed from fibre-reinforced materials. A study was found that investigated the simulation of carbon fabric reinforced polyester (CFRP) helmet shells [35]. This study took measurements from existing helmets to identify that fibre-reinforced helmet shells had an average thickness of 2 mm. Additionally, the material properties displayed in Table A.1 were extracted from this study.

Table A.1. Material properties used for CFRP, from [35]

	Density /kg.m ³	Poisson's ratio	Young's Modulus /GPa
CFRP	1.8	0.4	61.3

While the study explored the use of an orthotropic damage material model, a simplified linear elastic material model was used to model CFRP in this investigation. As described at the beginning of the section, the intention is not an accurate simulation of the CFRP shell, but identification of the relative performance that might be achieved using a stiffer shell.

Simulations were undertaken using an identical set of SP pads, with two separate shells. The first was modelled to the same specification as the 3 mm ABS shell used in this research (section 3.4.2.2). The second shell was modelled using the same approach, except instead of a 3 mm ABS section a 2 mm CFRP material section was applied to the shell [35]. The two simulations were undertaken at impact point B (UNECE 22.05 [27]) at 7.5 m/s and are presented in Figure A.10.

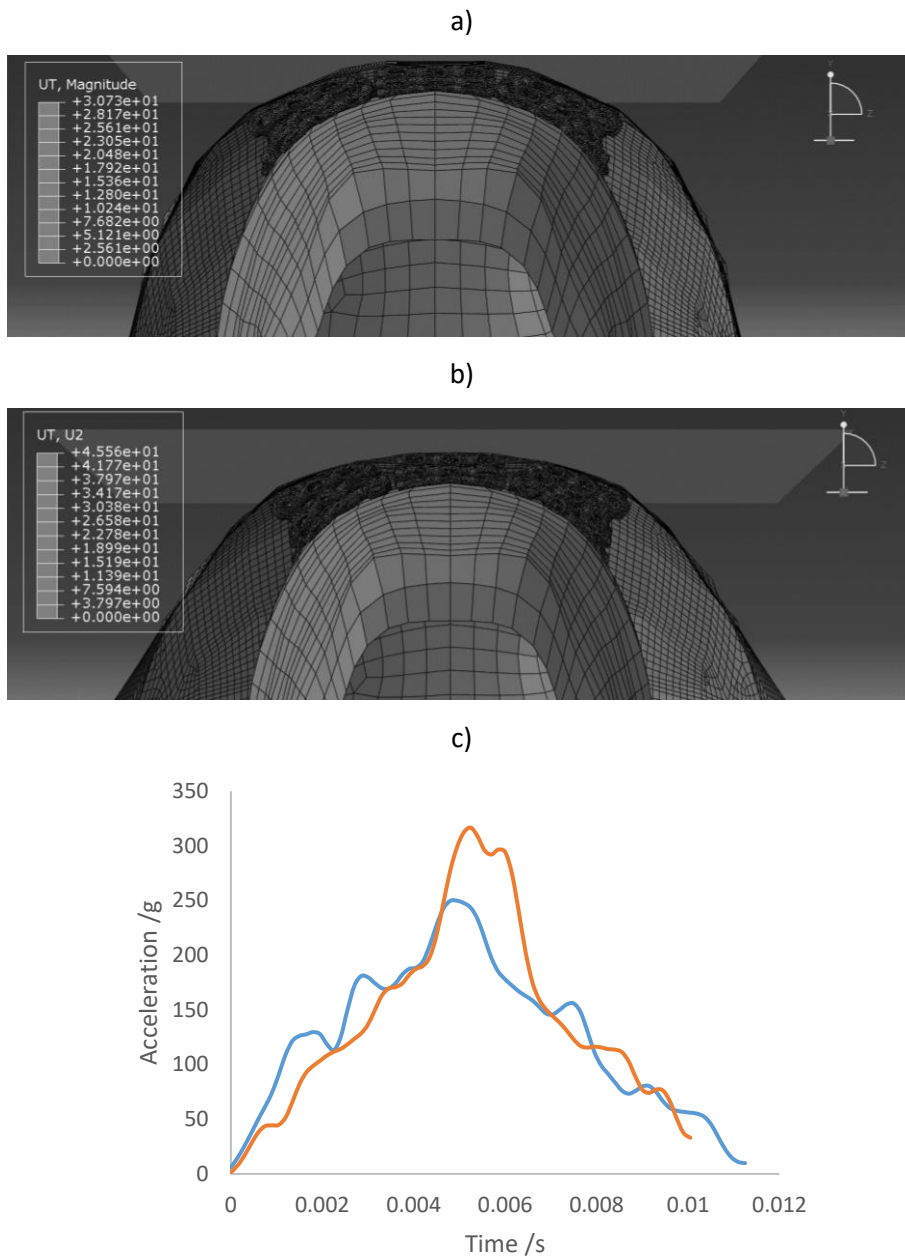


Figure A.10. Deformation of ABS and CFRP shells a) CFRP deformation at maximum compression, b) ABS deformation at maximum compression, c) comparison of acceleration-time curves with CFRP (blue) and ABS (orange) shells

Examining Figure A.10 a and b, the difference in load distribution can be visually identified, with the CFRP shell spreading the load more evenly into the underlying pads. The effect of this can be identified in Figure A.10c, where A_{max} for the CFRP shell is $\sim 22\%$ lower. It should be noted that fibre-reinforced materials are subject to damage, potentially making them less capable of multi-impact mitigation than ABS. Therefore, while this initial investigation has indicated the benefit of increased shell stiffness, the selection of materials in future work should consider both their E_s and resilience.

V. Helmet reverse analysis

A BOX-BX1 helmet was used in this research to provide a surrogate shell for the prototype SP liner, as well as to provide a comparative EPS response. It was used as a surrogate helmet by removal of the EPS liner, enabling insertion of the SP pads.

During removal of the EPS liner, it was sectioned to enable measurement of the variation in the liner thickness at impact points B, R and P (UNECE 22.05 [27]). Additionally, holes were bored into the side of the liner to assess the thickness of the liner at impact point X. As the helmet shell was required for testing the SP pads, no destructive measurements (e.g. sectioning) were taken from it. Instead, measurements were taken around the circumference of the helmet shell to establish its average thickness. All measurements were taken using Vernier callipers.

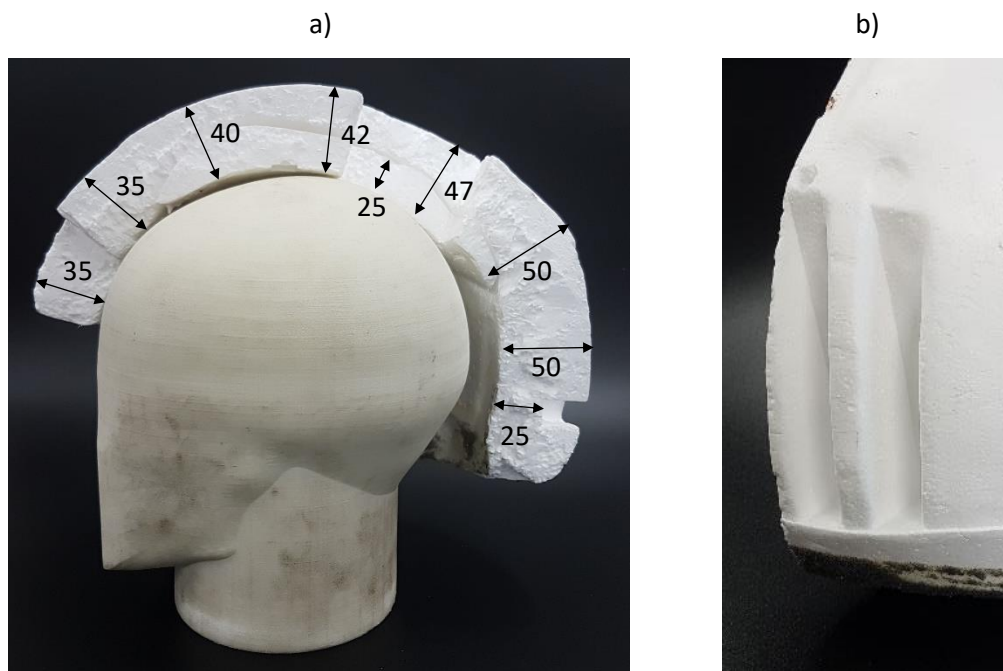


Figure A.11. EPS helmet liner removed from BOX BX-1 helmet a) side view of CSA through sagittal plane b) oblique view of fins moulded into the rear of the helmet

An insert of lower density EPS was used at point P (crown) and was attached to the main liner using adhesive. The only other design features were fins moulded into the back of the liner, as can be seen in Figure A.11b.

The energy-absorbing liner was removed, and a cross-section was made through the sagittal plane, as can be seen in Figure A.11a. The liner thickness through this cross-section

was non-uniform, with overall thicknesses ranging from ~35 – 50 mm. Additionally, the liner thickness at point X was measured at 40 mm. The shell thickness around the brim of the helmet was consistent at ~3 mm and was marked “ABS” on its interior surface.

Markings on the helmet liner components implied that the main liner had a density of 40 kg/m³, and the insert at point P had a density of 24 kg/m³. The overall helmet mass (e.g. visor, shell, straps) was measured at 1,486 g, and the overall mass of the complete liner was 238 g.

Compared to the average liner thickness of 35 mm and the average density of 55 kg/m³ identified in section 2.1.1, the EPS liner in the BOX BX-1 helmet was thicker and of a lower density. This discrepancy can be explained by thinner liners requiring higher density cellular structure to absorb the same amount of energy, as discussed in section 2.1.1.1. The thickness and material used for the shell were in-line with the average values identified in section 2.1.1.1.

VI. Experimental observations during testing of the helmet

This section serves to record any general observations that were made during the testing of the prototype and EPS filled helmets. The high-speed videography of this experimentation is presented, with brief descriptions. This information is included to support discussion in this research and to provide insight into the testing of motorcycle helmets, as limited examples or discussion of the ABS shell behaviour was found in the literature.

For all high-speed videography, as the helmet impacted the anvil, the ABS shell appeared to fluctuate significantly. Additionally, throughout the impact, the ABS shell directly under the impact point appeared to flatten completely. This flattening can be seen in Figure A.12 through to Figure A.14.

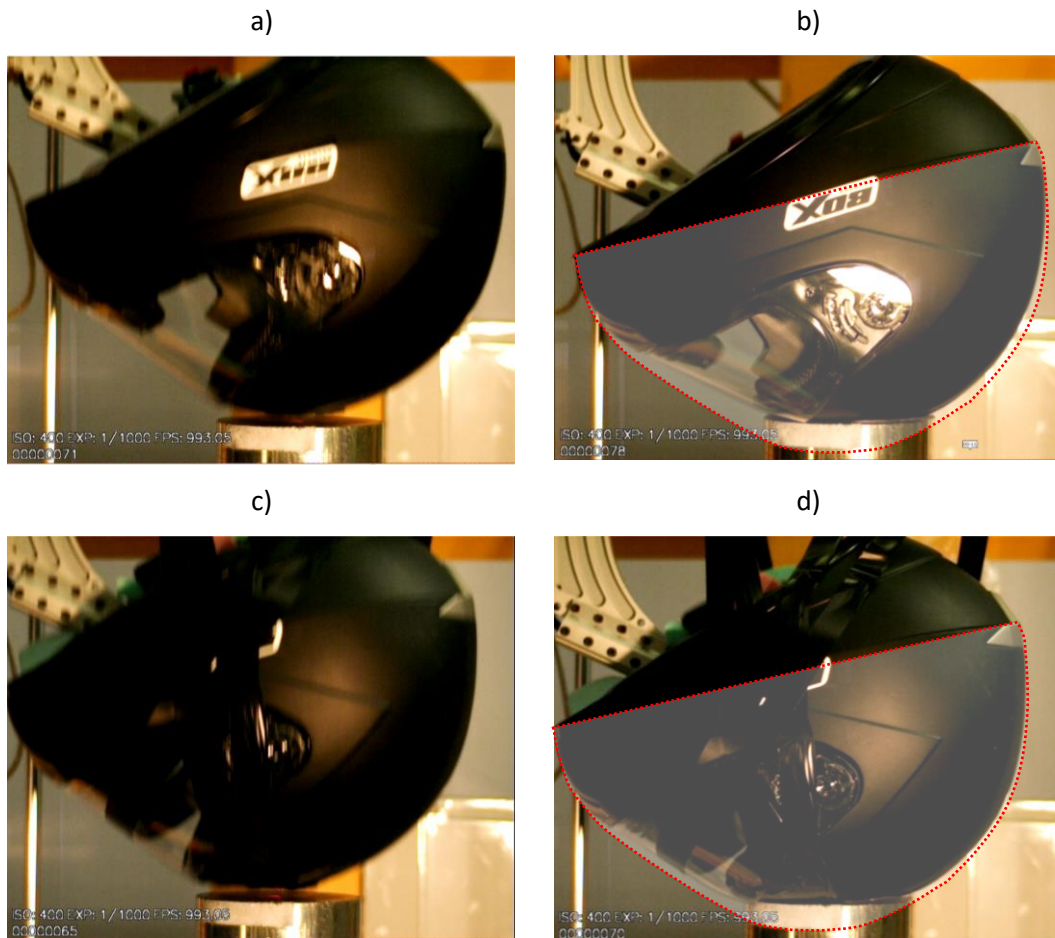


Figure A.12. High-speed videography of impact, at point B. a) EPS filled helmet pre-impact, b) EPS filled helmet at maximum compression, c) SP filled helmet pre-impact, d) SP filled helmet at maximum compression

For point B (Figure A.12), much of the deformation in the shell was focussed directly at the impact point. The region above the visor area flexed inwards towards the centre of the helmet, and there was little noticeable deformation elsewhere. This behaviour was observed in both the EPS and SP helmet shells.

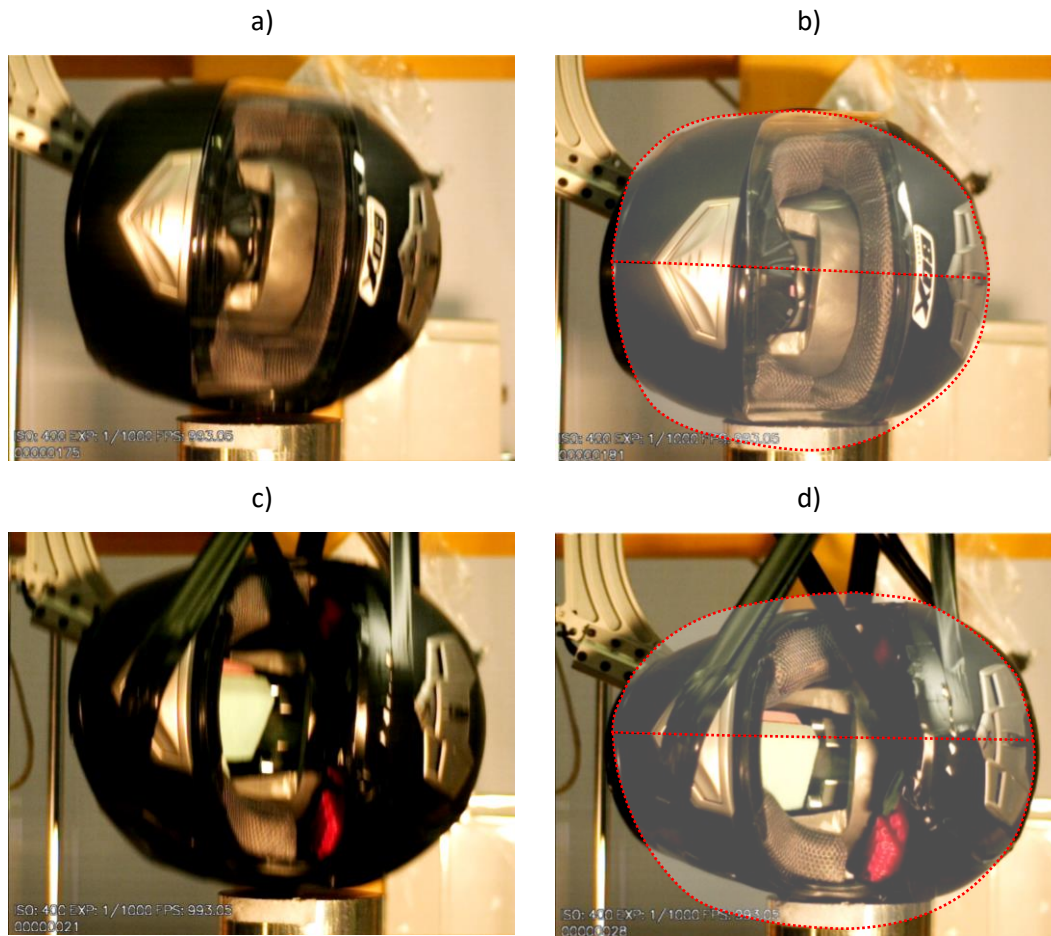


Figure A.13. High-speed videography of impact, at point X, a) EPS filled helmet pre-impact, b) EPS filled helmet at maximum compression, c) SP filled helmet pre-impact, d) SP filled helmet at maximum compression

For impact point X (Figure A.13), the EPS helmet shell compresses in line with the impact direction. During this compression, the visor region appeared to flex open perpendicularly to the impact direction, returning to its original shape as the helmet rebounded from the anvil. The SP helmet shell demonstrated similar behaviour to that of the EPS filled helmet. However, in addition to the deformation at the impact site, additional flexure was observed in the chin bar (causing the visor region to ‘open’) and in the shell on the opposite side of the helmet to the impact site.

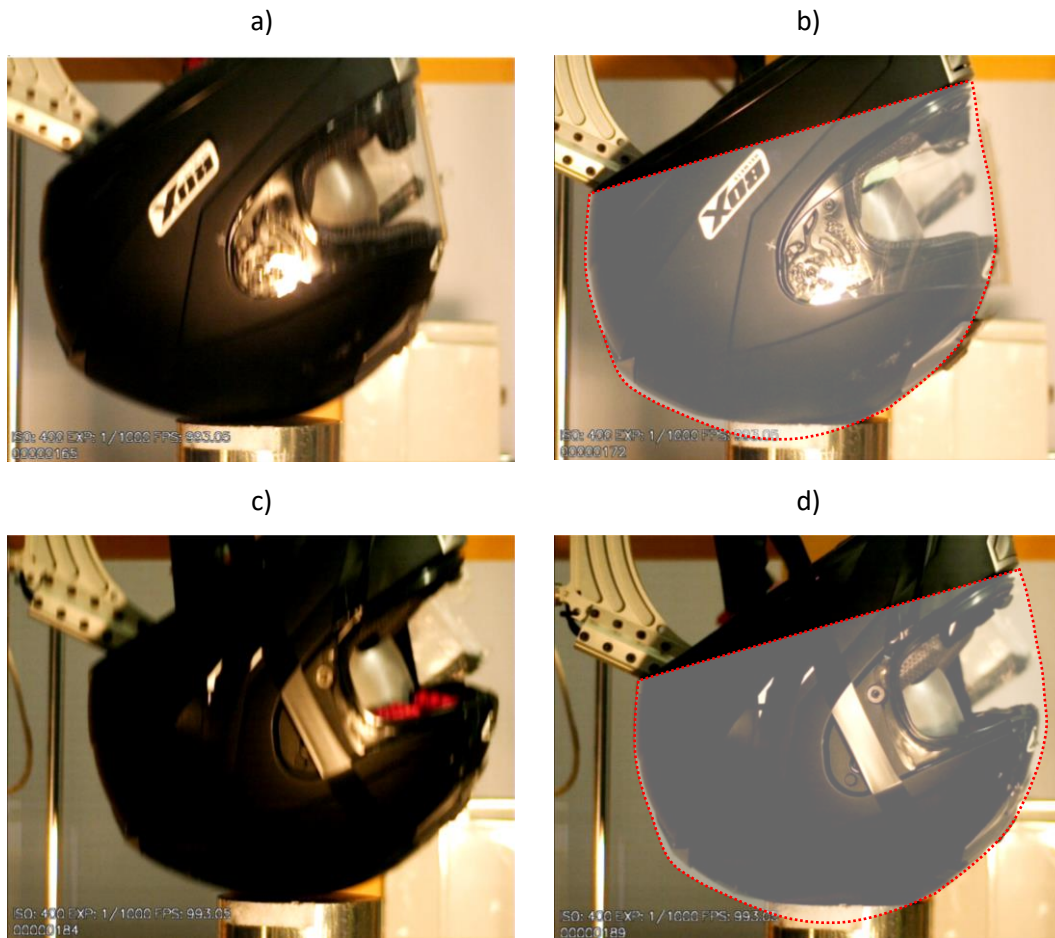


Figure A.14. High-speed videography of impact at point P. a) EPS filled helmet pre-impact, b) EPS filled helmet at maximum compression, c) SP filled helmet pre-impact, d) SP filled helmet at maximum compression

For the impact at point P (Figure A.14), both the EPS and SP lined helmet shells demonstrated similar behaviour, with the shell flattening at the impact site and little deformation elsewhere on the helmet.

For impact point X (Figure A.13), the increased deformation of the SP filled helmet shell, was likely due to the replacement of the contiguous EPS liner. The continuous nature of the EPS liner adds rigidity around the circumference of the helmet, which would appear to inhibit the additional flexing observed in the SP helmet. At point X, there appears to be an additional deformation on the opposite side of the helmet to the impact site. However, the examination of Figure A.12 through Figure A.14 demonstrates comparable deflection of the shell at the impact site for all points, suggesting this contiguous liner has limited benefit.

During impact testing, both the EPS and SP filled helmets fractured, with cracks propagating from vents located at the front and rear of the helmet shell (Figure A.15).



Figure A.15. Photos of the crack which propagated in the SP filled helmet's shell, after multi-impacts at, a) front, b) rear

After the first impact for the SP helmet, at point B, a crack was identified in the ABS shell. This crack appeared to have propagated from ventilation slots (which appeared machined into the shell) to the front edge of the helmet. A similar crack was identified after the first impact at point R. The crack at point R was more severe and propagated from the rear vents, along a profiled ridge in the helmet shell, to the lower edge of the shell. No other structural damage was observed in subsequent impacts. For the EPS helmet, a crack was observed after the first impact at point B; however, no crack propagated at point R.

The cracks at point B revealed that the shell had been non-uniformly thickened towards the vent (helmet edge = 3 mm, vent = ~6 mm). There was no apparent thickening over the length of the crack at point R (as can be seen in Figure A.15b).

In addition to the severe structural damage shown in Figure A.15, less severe damage was also observed during impacts. The quick-release mechanism used to control the opening of the visor was shattered during impacts for the replaced SP helmet. Additionally, for both helmets, the visor detached from the quick-release mechanism during all impacts. After the destruction of the quick-release mechanism, the visor was taped in place using PTFE tape for the remainder of the impacts.